HAL
open science

Linear and Nonlinear Numerical Methods for Real-World Inverse Problems of Time-Domain Electromagnetic Active Shaping - From Theory to Experiment

Ali Al Ibrahim

To cite this version:

Ali Al Ibrahim. Linear and Nonlinear Numerical Methods for Real-World Inverse Problems of Time-Domain Electromagnetic Active Shaping - From Theory to Experiment. Electromagnetism. Université Clermont Auvergne, 2021. English. NNT : 2021UCFAC001 . tel-03544968

HAL Id: tel-03544968

https://theses.hal.science/tel-03544968

Submitted on 27 Jan 2022

HAL is a multi-disciplinary open access archive for the deposit and dissemination of scientific research documents, whether they are published or not. The documents may come from teaching and research institutions in France or abroad, or from public or private research centers.

L'archive ouverte pluridisciplinaire **HAL**, est destinée au dépôt et à la diffusion de documents scientifiques de niveau recherche, publiés ou non, émanant des établissements d'enseignement et de recherche français ou étrangers, des laboratoires publics ou privés.

UNIVERSITÉ CLERMONT AUVERGNE
ECOLE DOCTORALE SCIENCES POUR L'INGÉNIEUR
INSTITUT PASCAL
LABORATOIRE DE MATHÉMATIQUES BLAISE PASCAL

Linear and Nonlinear Numerical Methods for Real-World Inverse Problems of Time-Domain Electromagnetic Active Shaping

From Theory to Experiment

Doctoral dissertation in Engineering Sciences (Electronics and Systems) presented by **Ali Al Ibrahim** and submitted in fulfillment of the requirements for the degree ***Doctor of Clermont Auvergne University***.

This dissertation is defended on the 28th of January 2021 and reviewed by the committee composed of:

Mme F. Paladian	Professeur des Universités, IP, Clermont Fd, France,	Président du jury
M. F. Rachidi	Professeur des Universités, EPFL, Lausanne, Suisse,	Rapporteur
M. X. Ferrières	Directeur de Recherche, ONERA, Toulouse, France,	Rapporteur
M. M. Kafal	Ingénieur-Chercheur, CEA, Paris, France,	Examinateur
M. C. Jullien	Ingénieur-Chercheur, SAFRAN, Toulouse, France,	Examinateur
M. P. Bonnet	Professeur des Universités, IP, Clermont Fd, France,	Directeur de thèse
M. C. Chauvière	Maître de Conférences, LMBP, Clermont Fd, France,	Encadrant
Mme V. Beauvois	Ingénieure de Recherche, Institut Montefiore, Liège, Belgique,	Invitée

—Version submitted on February 15, 2021 —

Dedication

This thesis is dedicated to my parents Hussein and Fatima. I hope that this achievement will complete the dream you had for me all those many years ago when you choose to give me the best education you could.

Acknowledgements

THIS is a pivotal and emotional milestone in my life. I would like to stop here for some moments to express my gratitude to those without whom I would not be the way I am today.

I owe my deepest gratitude to my thesis supervisor Prof. Pierre Bonnet for providing guidance, encouragement, support, and advice throughout this work. Thank you for lighting my first candle in the scientific research. I will always be honored that I had a supervisor like you not only for your intellectual level but also for your human side.

I am deeply grateful to my thesis co-supervisor Dr. Cédric Chauvière for his devoted time to guide me during these three years. Thank you for your precious comments, and help as well as your availability, support, and kindness.

I would like also to thank Prof. Farhad Rachidi, professor of universities at the École Polytechnique Fédérale de Lausanne (EPFL), and Prof. Xavier Ferrières, research director at the Office National d'Etudes et de Recherches Aérospatiales (ONERA) for accepting to be the reviewers of my thesis manuscript. Equally, I would like to thank Prof. Françoise Paladian, professor of universities at Institut Pascal laboratory, Dr. Moussa Kafal, research engineer at CEA, Dr. Charles Jullien, research engineer at Safran Electrical & Power, and Eng. Véronique Beauvois, research engineer at Institut Montefiore for giving me the pleasure to examine my defense.

I want to thank Prof. Evelyne Gil, the head of Institut Pascal, Vanessa Chaudron, administrative officer, and the CEM group members Sébastien G., Sébastien L., Kamal, Khalil, Christophe, Kofi, Claire for welcoming me with high hospitality. Thank you for all the scientific and nonscientific discussions we had and for maintaining the best cordial working environment for me.

Many thanks to the trainees, doctoral and postdoctoral students that I met in the CEM group, Abdelaziz, Achraf, Mohamed, Eric, Zied, Asma, and for sure Amélie, Salwa, Imane, Ghida with whom I had lunch and coffee breaks. Thanks for being real daily supporters. I wish you more success in your future career.

I want to take the opportunity to heartwarmingly thank all my friends, especially Janwa, Janah, Hassan, Amani for being my second family in France, Ayman & Yara, Mojtaba, Mohammad K., Hadi H., Kamal, Jessica, Hussein S., Hadi N., Lara, Francine, Didier and his family Florence, Laura, Alicia for their frequent support, my fun-run partner Daoud and tartare partner Bob for their solidarity during the last stages of my thesis. The list elongates but I cannot miss thanking Asaad, Mohammad A., Hussein F. M., Hussein H. M., Haidar, and Ali T. Thank you all for the time spent together.

This dream would not come true without the love, trust, and support of my family. I am forever grateful to my dearest dad Hussein and one-of-a-kind mom Fatima for their immense love, encouragement, and endless patience. Thank you both for teaching me to never give up and giving me the strength to chase my dreams. My sisters Soso, Farah, Malak, my little brother Ahmad, and my brother-in-law Rached deserve my wholehearted thanks as well.

"Thoroughly conscious ignorance is the prelude to every real advance in science."

– James Clerk Maxwell

Contents

Acknowledgements

Acronyms

Abstract

Résumé

Résumé Etendu en Français **1**

General Introduction **13**

1 Electromagnetic Source Identification: State of the Art and Context **21**

1.1 Source Identification Techniques 22
1.1.1 Equivalent source models 22
1.1.2 Inverse-source problems 25
1.1.3 Optimal control of partial differential equations 31
1.1.4 Time-reversal method 32
1.2 Wire Diagnosis 37
1.2.1 Reflectometry-based techniques 38
1.2.2 Time-reversal imaging techniques 40
1.3 Settings: Electromagnetic Wave Propagation 42
1.3.1 Maxwell's equations 42
1.3.2 Telegrapher's equations 47
1.4 Conclusion 50

2 Source Identification in Linear Systems: The LCCF Method 53
2.1 LCCF Concept 54
2.1.1 Basic LCCF method 55
2.1.2 Numerical illustrations in wiring networks 58
2.1.3 Numerical illustrations in free space environments . . 64
2.2 TR vs. LCCF 69
2.2.1 Lossless network 69
2.2.2 Lossy network 74
2.3 Source Properties Modifications 77
2.3.1 Duration of source emission 77
2.3.2 Source filtering 84
2.3.3 Amplitude constraints 89
2.4 Composed Sources and Complex Targets 91
2.5 Conclusion 92

3 Generalized LCCF and Software Correction Application 95
3.1 Generalized LCCF Method 96
3.1.1 Numerical illustrations in wiring networks 97
3.1.2 Numerical illustrations in free space environments . . 103
3.2 Software Correction of Faulty Lossy Linear Networks 106
3.2.1 Soft fault 111
3.2.2 Hard fault 112
3.2.3 Multiple faults 112
3.2.4 External defect 116
3.2.5 Multiple faults and external defects 116
3.3 Conclusion 119

4 Source Identification in Nonlinear Systems: Newton's Method and the NLLSQ Solver 121
4.1 Time-Domain Source Identification in Nonlinear Media 122
4.1.1 Theory: Newton's method and the NLLSQ solver . . . 122
4.1.2 Numerical illustrations in wiring networks 125
4.2 Software Correction of Faulty Lossy Nonlinear Networks . . . 135
4.2.1 Soft fault 136
4.2.2 Hard fault 137
4.2.3 Multiple faults 138
4.2.4 External defect 139

4.2.5 Multiple faults and external defects 140
4.3 Conclusion 141

5 Experimental Validation: The LCCF Method 145
5.1 Experimental LCCF method 146
5.2 Source Identification in Wiring Networks 149
5.2.1 Experimental setup 150
5.2.2 Simple network configuration 151
5.2.3 Complex network configuration 157
5.3 Software Correction in Wiring Networks 162
5.3.1 Soft fault 162
5.3.2 Hard fault 165
5.3.3 Multiple faults 166
5.4 Enhanced Spatial Control of Microwave Plasma in a Reverberant Cavity 169
5.4.1 Experimental setup 169
5.4.2 Plasma control by the TR method 171
5.4.3 Plasma control by the LCCF method 173
5.5 Conclusion 178

Conclusion 181

Bibliography 185

List of Publications 203

Acronyms

EMC ElectroMagentic Compatibility 21
IPs Inverse Problems 25
IMPs Inverse-Medium Problems 26
IOPs Inverse-Obstacle Problems 26
IESSPs Inverse Equivalent Surface-Source Problems 26
ISPs Inverse-Source Problems 26
FD Frequency Domain 31
TD Time Domain 31
FFT Fast Fourier Transform 31
IFFT Inverse Fast Fourier Transform 31
PDEs Partial Differential Equations 31
HUM Hilbert Uniqueness Method 31
TR Time-Reversal 32
AC Anechoic Chamber 33
TRM Time-Reversal Mirrors 34
MSRC Mode Stirred Reverberation Chamber 34
ESN Equivalent Surface Network 35
TREC Time-Reversal Electromagnetic Chamber 35
LCCF Linear Combination of Configuration Field 53
TDR Time-Domain Reflectometry 39

FDR Frequency-Domain Reflectometry 39
TRO Time-Reversal Operator 40
EDORT Enhanced DORT 40
TR-MUSIC Time-Reversal MUltiple SIgnal Classification 40
FDTD Finite-Difference Time-Domain 44
PEC Perfect Electric Conductor 47
ABC Absorbing Boundary Condition 47
TLs Transmission Lines 48
TEM Transverse ElectroMagnetic 48
MPPI Moore-Penrose Pseudo-Inverse 58
RE Relative Error 60
LLSQ Linear Least-SQuares 89
SC Software Correction 95
NM Newton's Method 121
NLLSQ NonLinear Least-SQuares 121
NLPs NonLinear Problems 122
AWG Arbitrary Waveform Generator 150

Abstract

In this work, we solve time-domain effective inverse problems to shape the electromagnetic fields in linear and nonlinear media. Electromagnetic active shaping is essential for imposing predefined fields at fixed positions or suppressing undesired radiations and replace them with intentional ones. In linear media, we improve and generalize the Linear Combination of Configuration Field (LCCF) method to identify the temporal sources that shape voltage/current or fields at one or more spatial points. In nonlinear media, we propose alternative methods, namely Newton's method and the nonlinear least-squares solver, to shape electromagnetic fields after showing the inefficiency of the LCCF in the presence of nonlinear elements. Particularly, we apply these ideas in linear and nonlinear defective wiring networks to introduce a new paradigm called the *Software Correction (SC)*. The SC cancels the unintentional perturbations resulting from both faults inherent in the network lines and coupling external defects. It compensates for their effects regardless of their number, position, and nature. With a view to consider experimental tests in the linear case, constraints are added to the LCCF problem to comply with some physical limitations encountered during experiments. Practically, two main applications are conducted. The SC process is first tested in faulty networks, then a three-dimensional application for shaping electromagnetic fields is conducted to control the nanosecond microwave plasma in a reverberant cavity.

Keywords: electromagnetic interference control, source identification, time-domain analysis, fault, transmission line.

Résumé

DANS ce travail, nous résolvons des problèmes inverses non triviaux dans le domaine temporel pour contrôler les champs électromagnétiques dans des milieux linéaires et non linéaires. Le contrôle actif électromagnétique est essentiel pour imposer des champs prédéfinis à des positions fixes ou supprimer les radiations indésirables et les remplacer par des radiations intentionnelles. Dans les médias linéaires, nous améliorons et généralisons la méthode *Linear Combination of Configuration Field (LCCF)* pour identifier les sources temporelles qui contrôlent la tension/courant ou les champs en un ou plusieurs points spatiaux. Dans les milieux non linéaires, nous proposons des méthodes alternatives, à savoir la méthode de Newton et le solveur des moindres carrés non linéaires, pour contrôler les champs électromagnétiques après avoir illustré l'inefficacité de la LCCF en présence d'éléments non linéaires. En particulier, nous appliquons ces idées dans des réseaux de câbles défectueux linéaires et non linéaires pour introduire un nouveau paradigme appelé *Software Correction (SC)*. Le SC annule les perturbations non intentionnelles résultant à la fois des défauts inhérents aux lignes du réseau et du couplage des défauts externes. Il compense leurs effets quels que soient leur nombre, leur position et leur nature. En vue d'envisager des tests expérimentaux dans le cas linéaire, des contraintes sont ajoutées au problème LCCF pour se conformer à certaines limitations physiques rencontrées lors des expérimentations. En pratique, deux applications principales sont menées. Le procédé SC est d'abord testé dans des réseaux défectueux, puis une application tridimensionnelle de contrôle actif des champs électromagnétiques est conduite pour contrôler le plasma micro-onde nanoseconde dans une cavité réverbérante.

Mots clés: contrôle des interférences électromagnétiques, identification de sources, analyse temporelle, défaut, ligne de transmission.

Résumé Etendu en Français

Introduction

AVEC la prolifération de différents appareils électroniques, divers problèmes liés au domaine de la Compatibilité Electro-Magnétique (CEM) sont apparus. Ces appareils émettent des radiations intentionnelles ou non intentionnelles qui peuvent interférer, entraînant des effets parfois catastrophiques. Pour cette raison, la nécessité de rendre compatible leur fonctionnement et de gérer leurs rayonnements émissifs devient nécessaire. Pour répondre à ce besoin, de nombreuses solutions ont été proposées pour protéger les équipements et maintenir leurs performances élevées telles que des blindages. De même, l'identification de source électromagnétique qui produit les champs souhaités peut également être une solution afin de remplacer les émissions indésirables par celles souhaitées ou bien les radiations complexes par leurs équivalents.

Différentes méthodes ont été développées pour identifier les sources électromagnétiques telles que les méthodes basées sur le principe d'équivalence ou les algorithmes génétiques, les problèmes inverses, l'optimisation, etc. Si ces méthodes se sont montrées efficaces pour résoudre des problèmes dans le domaine fréquentiel, elles présentent néanmoins des inconvénients (consommation de temps élevée, difficultés de mise en œuvre, ou réalisations expérimentales impossibles). Comme solution alternative, la méthode de Retournement Temporel (TR) (Figure 1) est parmi les méthodes qui peuvent être plus simples et efficaces pour identifier le profil des sources directement dans le domaine temporel. Les applications du TR sont nombreuses et ont été étudiées dans les réseaux de lignes de transmission et les environnements réverbérants. Malheureusement, le TR se révèle moins

efficace lorsqu'il s'agit de résoudre des problèmes avec pertes ou d'imposer des conditions complexes sur les caractéristiques temporelles (durée ou la forme) du champ électromagnétique imposé.

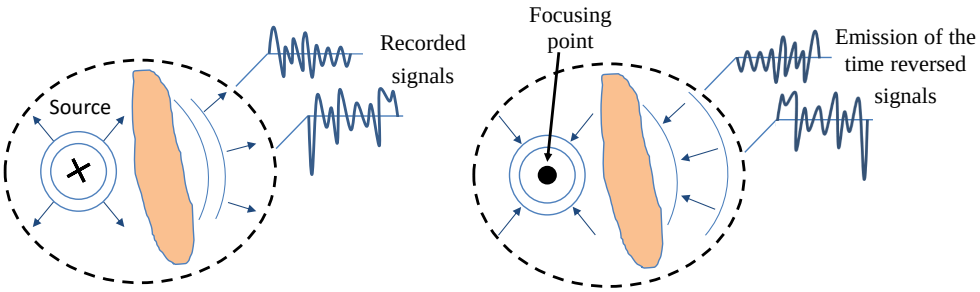

Figure 1: *Principe du retournement temporel.*

La plupart des travaux réalisés jusqu'à présent sur le TR soulèvent de nombreuses questions sans réponse ou insuffisamment répondues. Notamment, lorsqu'il s'agit d'identifier des sources sans connaissances préalables des caractéristiques du milieu, de traiter des milieux non linéaires, ou de contrôler simultanément les champs électromagnétiques en plusieurs points spatiaux. Pour surmonter ces limitations dans cette thèse, nous développons/utilisons des techniques alternatives qui identifient les sources électromagnétiques dans le domaine temporel. L'objectif est de contrôler (imposer ou annuler) les champs électromagnétiques dans les milieux linéaires et non linéaires. Différentes applications numériques et expérimentales ont été menées dans les cas unidimensionnels (réseaux de câblage) et tridimensionnels (cavités) pour valider les résultats.

Identification des sources dans des systèmes linéaires: la méthode LCCF

La méthode *Linear Combination of Configuration Field* (LCCF) est une méthode simple et efficace qui permet d'identifier le profil temporel d'une source électromagnétique satisfaisant à des propriétés particulières pour une cible donnée (champ, tension ou courant) dans un milieu linéaire. La LCCF ne dépend ni de la topologie du système ni de ses caractéristiques, toutefois elle dépend uniquement de la réponse impulsionnelle du système entre

le point source et le point récepteur. Le problème LCCF peut s'écrire sous forme matricielle

$$\mathbf{A}\mathbf{x} = \mathbf{F}, \tag{1}$$

où $\mathbf{A}$ est la matrice de caractérisation construite sur la base de la réponse impulsionnelle, $\mathbf{x}$ est le signal à calculer et $\mathbf{F}$ est la cible à imposer au point de réception. Au point source, nous injectons un signal calculé $\mathbf{x}$ qui se propage, interfère et peut être déformé en raison de discontinuités et d'inhomogénéités dans le milieu linéaire. Un récepteur placé à un autre point enregistre le signal détecté dans le but d'obtenir $\mathbf{F}$ sur un temps cible donné (Figure 2).

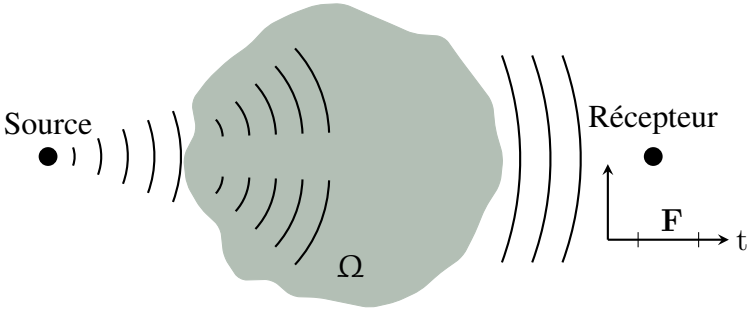

Figure 2: *Le principe de la méthode LCCF.*

Nous avons amélioré et généralisé la méthode LCCF pour contrôler les champs électromagnétiques en M points spatiaux sur le temps cible en utilisant N générateurs de source. La méthode LCCF généralisée est basée sur la résolution du système linéaire suivant:

$$\begin{pmatrix} \mathbf{A}_{11} & \cdots & \mathbf{A}_{1N} \\ \vdots & \ddots & \vdots \\ \mathbf{A}_{M1} & \cdots & \mathbf{A}_{MN} \end{pmatrix} \begin{pmatrix} \mathbf{x}_1 \\ \vdots \\ \mathbf{x}_N \end{pmatrix} = \begin{pmatrix} \mathbf{F}_1 \\ \vdots \\ \mathbf{F}_M \end{pmatrix}. \tag{2}$$

Quelque soit $i \in \{1, \cdots, M\}$ et $j \in \{1, \cdots, N\}$, chaque sous-matrice $\mathbf{A}_{ij}$ est la matrice de caractérisation entre le point source j at le point récepteur i, $\mathbf{x}_j$ est le signal à calculer émise par le générateur j et $\mathbf{F}_i$ est la cible souhaitée au point récepteur i sur le temps cible. Des illustrations numériques dans des réseaux de câblage et des cavités (anéchoïques et

réverbérations) montrent que la LCCF est indépendant des phénomènes physiques intervenant lors de la propagation (atténuation, dispersion, réflexions multiples, absorption, etc.).

Comme le contrôle actif des champs électromagnétiques est une tâche commune des techniques TR et LCCF, nous positionnons la LCCF par rapport au TR. Les deux méthodes sont comparées pour montrer la supériorité de la LCCF sur le TR. En général, cette comparaison est valable dans les cas unidimensionnels (réseaux de câblage) et tridimensionnels (cavités). Le Tableau 1 résume la comparaison du TR et de la LCCF.

Méthodes / Propriétés	TR	LCCF
Points d'accès	≥ 2 (Surface de Huygens en théorie)	2
Contrôler des champs complexes	Pas efficace	Efficace
Caractéristiques du médium	Dépendant et nécessite des étapes supplémentaires	Indépendante
Contrôler plusieurs points spatiaux	Pas efficace	Efficace

Table 1: *Comparaison entre les techniques TR et LCCF.*

Les caractéristiques temporelles de la source calculée par la méthode LCCF peuvent parfois, en raison notamment de la fréquences très élevées, empêcher son application expérimentale. Pour cette raison, nous proposons deux manières pour diminuer la valeur de la fréquence maximale de la source: filtration *a posteriori* et filtration *a priori*. La filtration a posteriori consiste à filtrer la source après son calcul, alors que la filtration a priori consiste à ajouter des contraintes au problème qui agissent comme un filtre sur la source. Après comparaison des résultats, la filtration *a priori* se révèle plus efficace que la filtration *a posteriori* en termes de calcul des sources plus adaptées aux expérimentations avec de faibles erreurs relatives.

Enfin, comme certains équipements utilisent des signaux dont les amplitudes se situent entre deux valeurs spécifiques, nous ajoutons un autre type

de contraintes en utilisant le solveur linéaire des moindres carrés qui spécifie l'amplitude maximale et minimale de la source. Après avoir comparé les résultats de la résolution du problème LCCF avec et sans contraintes, nous soulignons l'importance d'ajouter des contraintes au problème afin de calculer des sources réalisables expérimentalement. L'utilisation de ces contraintes dépend du type de problème traité.

Application du *software correction*

Inévitablement, les fils sont exposés à des contraintes naturelles, mécaniques ou thermiques (par exemple, humidité, corrosion, échauffement, etc.) qui réduisent leur durée de vie et causent leurs dégradations. Ces défauts peuvent être francs (circuits ouverts et courts-circuits) ou non francs (frottements, dommages d'isolation, fissures, effilochage, etc.) impactant le blindage, l'immunité ou l'émissivité des fils (Figure 3).

Figure 3: *Défauts francs (image de gauche) et non francs (image de droite) apparaissant dans les réseaux de câblage.*

Pour de nombreuses raisons telles que la sûreté, la sécurité et les performances optimales des systèmes de câblage, de nombreuses techniques (les techniques basées sur la réflectométrie et l'imagerie par retournement temporel) ont été développées pour anticiper, détecter l'apparition ou localiser de défauts électriques dans les réseaux de câblage. Malheureusement, le processus de détection et localisation des défauts, à savoir le processus de dépannage ou *hardware correction*, entraîne de nombreux inconvénients (l'arrêt inattendu du système, une consommation excessive de temps et d'argent, etc.). La situation s'aggrave lorsque les défauts sont localisés dans des zones difficiles d'accès, telles que les zones radioactives dans les centrales nucléaires ou les satellites dans l'espace, donc absolument

inaccessibles aux processus de maintenance.

Alternativement, nous introduisons un nouveau paradigme appelé le *Software Correction (SC)*. Le processus du SC tolère les défauts et les gère comme faisant partie de la topologie du réseau sans avoir besoin d'accéder à leur emplacement ou de récupérer des informations les concernant. Il est défini comme le traitement numérique permettant de tolérer à distance les défauts de câblage des réseaux de communication sans aucune intervention physique. Ce processus est indépendant des nombres, natures et positions des défauts qui peuvent apparaître dans le réseau. Dans les réseaux de câblage se comportant de manière linéaire, la méthode LCCF est utilisée pour amener le SC au réseau de câblage défectueux.

Parfois le réseau fonctionne mal lorsqu'il est exposé à des défauts de couplage externes. Il peut s'agir d'un champ électromagnétique externe qui se couple le réseau le long d'une longueur de câble non blindé conduisant à des surtensions/surcourants et à une dégradation des performances. Cependant, cela n'entrave pas le fonctionnement du SC qui reste applicable même avec ce type de défauts. Le SC souffre de certaines limitations: les réseaux de communication transférant des données sont considérés uniquement et non les réseaux de puissance, en plus une connaissance préalable de la sortie saine et l'accès à une extrémité libre pour brancher un récepteur sont toujours nécessaires.

La LCCF montre une applicabilité élevée pour traiter les problèmes linéaires afin de contrôler les champs électromagnétiques. Cependant, les problèmes de compatibilité électromagnétique (CEM) sont principalement non linéaires en raison de la présence massive de circuits non linéaires (par exemple amplificateur de puissance, commutateur, multiplicateur, mélangeur, etc.) basés sur des éléments passifs (par exemple des diodes) ou actifs (par exemple des transistors). Malheureusement, notre étude montre que la LCCF fonctionne mal une fois qu'un composant non linéaire est introduit dans le système. Par conséquent, d'autres techniques sont nécessaires pour contrôler les champs électromagnétiques dans les milieux non linéaires.

Identification des sources dans des systèmes non linéaires: méthode de Newton et le solveur NLLSQ

Dans les réseaux de câblage non linéaires, nous utilisons deux techniques, à savoir la méthode de Newton (NM) et le solveur moindres carrés non linéaires "nonlinear least-squares (NLLSQ)", pour identifier le profil temporel des sources qui produiraient un signal cible prédéfini sur le temps cible. NM et NLLSQ sont des algorithmes itératifs qui convergent vers la source à calculer. Pour les deux méthodes, on part d'un point de départ initial et on s'arrête lorsque la variation est inférieure à un seuil fixe. En effet, NM est basé sur le calcul des dérivées de la matrice jacobienne, alors que le NLLSQ est basé sur l'algorithme Levenberg-Marquardt.

Nous voulons appliquer les mêmes idées présentées précédemment pour le câblage des réseaux, mais cette fois, avec la présence d'éléments non linéaires. En particulier, nous voulons contrôler les tensions/courants dans les réseaux de câbles non linéaires et amener une *Software Correction (SC)* lorsque des défauts apparaissent dans leurs lignes. Des applications numériques ont été illustrées pour montrer l'applicabilité des méthodes NM et NLLSQ dans les réseaux de câblage avec pertes non linéaires.

Différents niveaux d'atténuation ont été considérés où NM et le NLLSQ continuent de fonctionner correctement et imposent efficacement la tension/courant souhaité au temps cible. Les deux méthodes non linéaires sont indépendantes de la topologie et des caractéristiques du réseau ainsi que de son niveau de non-linéarité. Cela implique que les deux algorithmes ne reposent ni sur la complexité du réseau (nombre de lignes et de jonctions, caractéristiques, charges, etc.), ni sur les réflexions multiples intervenant lors de la propagation, ni sur les niveaux d'atténuations ou dispersions.

Après avoir comparé les méthodes NM et NLLSQ dans des conditions similaires, le solveur NLLSQ semble être plus efficace que NM pour imposer une cible spécifiée sur un temps cible fixe car il offre une précision plus élevée avec moins de temps CPU. De plus, NM nécessite un point de départ pas trop éloigné de la solution; sinon, l'algorithme diverge. Souvent, le signal calculé est caractérisé par son profil complexe, ce qui rend difficile de deviner le point de départ. Pour cette raison, nous nous appuyons sur le solveur

NLLSQ uniquement pour le SC d'un réseaux de câblage non linéaires avec perte défectueux.

Le SC dans le cas non linéaire est défini de la même manière que le cas linéaire. En utilisant le solveur NLLSQ, nous voulons tolérer les défauts et compenser leurs effets dans les réseaux défectueux avec perte se comportant de manière non linéaire. Similaire au cas linéaire, le SC dans le cas non linéaire est également indépendant des nombres, natures et positions des défauts potentielles qui apparaissent dans les lignes du réseau. De plus, le réseau peut parfois être perturbé par des défauts externes, mais cela n'entrave pas le fonctionnement du SC.

Validation expérimentale dans les réseaux de câblage: la méthode LCCF

Pour appliquer la méthode LCCF expérimentalement en milieux linéaires, nous mettons à niveau la LCCF pour se conformer à certaines limitations physiques rencontrées lors des expériences. Ces limitations sont représentées par la difficulté à récupérer la réponse impulsionnelle résultant de l'injection impratique du signal Dirac pour construire la matrice de caractérisation $\mathbf{A}$. Comme solution alternative, nous considérons la réponse de tout signal incident qui pourrait être réalisé expérimentalement pour construire une autre matrice $\tilde{\mathbf{A}}$, la matrice LCCF dans la base non canonique. Cela signifie que nous résolvons le système LCCF sur une base non canonique, puis en utilisant des concepts simples d'algèbre linéaire, nous pouvons passer à la base canonique par une matrice de passage. Le système LCCF à résoudre est alors

$$\begin{cases} \tilde{\mathbf{A}}\tilde{\mathbf{x}} = \mathbf{F}, \\ \mathbf{x} = \mathbf{P}\tilde{\mathbf{x}}. \end{cases} \tag{3}$$

Dans un premier temps, nous présentons les équipements utilisés lors des tests: le générateur de signaux arbitraires (AWG) et l'oscilloscope. Ensuite, nous utilisons la méthode LCCF améliorée pour identifier le profil temporel de la source dans un réseau simple de câbles coaxiaux sur un point fixe afin

d'imposer le signal cible souhaité sur le temps cible. En considérant le même réseau avec des caractéristiques plus complexes, nous identifions une autre source qui imposerait le signal souhaité sur le temps cible. Malheureusement, la source calculée nécessite des contraintes d'amplitude car elle dépasse la limite maximale comprise par l'AWG. Pour cette raison, nous résolvons ce problème LCCF avec des contraintes d'amplitude pour satisfaire cette limitation intégrée de l'AWG.

Dans un autre test expérimental, nous augmentons la complexité de la topologie du réseau en ajoutant plus de lignes et de jonctions pour tester l'applicabilité expérimentale de la méthode LCCF lorsqu'il s'agit de contrôler la tension/courant à plusieurs points du réseau. La LCCF a réussi à imposer des signaux cibles identiques et différents à deux points spatiaux sur un intervalle de temps prédéfini.

Dans les réseaux de câblage défectueux, nous considérons des réseau avec des caractéristiques et des topologies différentes pour appliquer le processus SC. Un ou plusieurs défauts francs ou non francs sont introduits dans les lignes des réseaux. La méthode LCCF présente une efficacité élevée pour la rectification des sorties en deux points spatiaux différents malgré la présence des défauts. Les résultats du SC expérimental montrent que les mêmes signaux en deux points de mesure sont enregistrés avant et après l'introduction d'un ou plusieurs défauts francs et non francs.

Validation expérimentale dans une cavité réverbérante: la méthode LCCF

Dans le cadre d'une application expérimentale tridimensionnelle de la méthode LCCF, elle peut être utilisée pour améliorer le contrôle des plasmas micro-onde dans une cavité réverbérante. Ce travail est une collaboration entre l'Université Clermont Auvergne (Institut Pascal) et l'Université Paul Sabatier de Toulouse, France (laboratoires LAPLACE et ISAE-SUPAERO). Après avoir présenté la configuration expérimentale de la cavité, on utilise les deux techniques TR et LCCF pour contrôler les plasmas dans la cavité. Les deux techniques sont ensuite comparées pour montrer les limites de la méthode TR et comment elles pourraient être surmontées par la méthode LCCF.

Dans un premier temps, nous utilisons la technique TR pour contrôler les plasmas en un point spatial de la cavité, noté $\mathbf{r}_p$. Cela peut être fait en focalisant un champ électrique qui a une forme de pic à $\mathbf{r}_p$. En effet, le TR montre une grande efficacité pour focaliser ce champ et générer des plasmas au point souhaité. Malheureusement, le TR conduit inévitablement à une augmentation de l'amplitude du champ électrique aux points voisins de $\mathbf{r}_p$, noté $\mathbf{r}_z$, provoquant l'apparition de décharges parasites à $\mathbf{r}_z$ (Figure 4). La technique TR échoue à empêcher l'apparition de ces décharges à $\mathbf{r}_z$ car cela nécessite de contrôler le champ électrique à plusieurs positions spatiales, $\mathbf{r}_p$ et $\mathbf{r}_z$, simultanément.

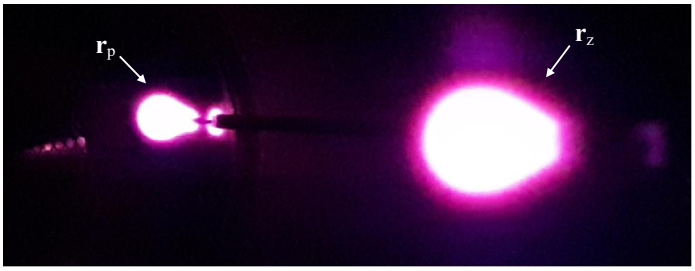

Figure 4: *Résultats expérimentaux: le TR réussit à activer les plasmas à* $\mathbf{r}_p$ *et échoue à empêcher leur apparition à* $\mathbf{r}_z$.

Alternativement, nous utilisons la méthode LCCF (généralisée) en raison de sa capacité à contrôler les champs électromagnétiques en plusieurs points spatiaux simultanément. Cela peut être fait en imposant un champ électrique élevé à $\mathbf{r}_p$ et le niveau le plus bas possible de champ électrique à $\mathbf{r}_z$. La LCCF active efficacement les plasmas à $\mathbf{r}_p$ et empêche son apparition à $\mathbf{r}_z$ (Figure 5).

Conclusion

L'objectif principal de cette thèse est de contrôler des champs électromagnétiques dans le domaine temporel dans des milieux linéaires et non linéaires. Cela se fait en développant/utilisant des méthodes numériques pour identifier le profil temporel des sources qui, lorsqu'elles sont injectées, produisent le signal souhaité à des points spatiaux donnés sur le temps

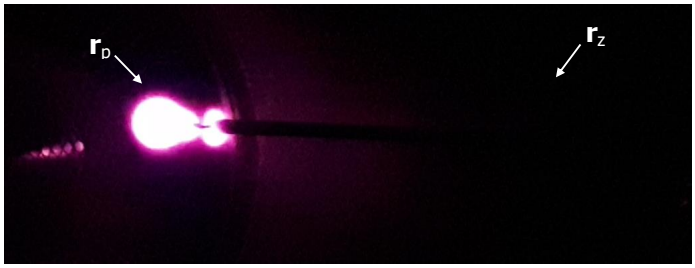

Figure 5: *Résultats expérimentaux: la méthode LCCF réussit simultanément à activer les plasmas à* $\mathbf{r}_p$ *et à empêcher leur apparition à* $\mathbf{r}_z$.

cible prédéfini. Les méthodes ont été testées dans des conditions complexes parfois dans des réseaux de câblage et d'autres fois dans des environnements d'espace libre. En fait, elles montrent une grande efficacité de contrôler des champs électromagnétiques indépendamment des topologies du milieu étudiées en se basant uniquement sur le signal détecté par le point de réception. Dans le contexte des réseaux de câblage défectueux linéaires et non linéaires, le paradigme *Software Correction (SC)* a été introduit pour compenser les effets des défauts. De plus, des validations expérimentales ont été effectuées dans des réseaux de câblage linéaire pour tester à la fois le contrôle actif des tensions/courants et le SC. Finalement, dans une cavité réverbérante linéaire, nous améliorons le contrôle spatial des plasmas micro-ondes en contrôlant les champs électromagnétiques aux positions spatiales souhaitées.

General Introduction

ELECTROMAGNETISM is an area of major importance in physical science that involves all the phenomena of interaction between electricity and magnetism. In 1865, after J. C. Maxwell introduced his equations, electromagnetism became an active field in scientific research. Numerous problems have been resolved and many natural phenomena have been explained based on Maxwell's principles in different domains, such as optical, radio, and electric technologies. In particular, diverse issues related to the field of ElectroMagnetic Compatibility (EMC) have emerged, especially after the proliferation of different electronic devices. These devices emit intentional or unintentional radiations that may interfere, leading to catastrophic effects (fires, damages, etc.). For this reason, the need to compatibilize their functioning and manage their emissive radiations become necessary.

Many European governments have adopted strict laws since 1992, forcing all the importers and manufacturers to certify that their electronic products are electromagnetically compatible. In any electromagnetic environment, the EMC is the ability of electrical devices and systems to function within their tolerance range when exposed to unintentional generation and reception of electromagnetic energy or when operational equipment is physically damaged. Therefore, it is necessary to cancel or limit the level of these undesired emissions and check the sufficient immunity of the devices to any external interference to minimize their susceptibility.

A classical solution may be to use electromagnetic shielding to protect the equipment from interfering radiations. Due to the heavyweights and high expenses of the shields, some researchers and engineers have devoted much

effort to model and characterize the radiated fields to improve the systems' designs. Others developed theoretical studies and experiments to reduce (or cancel, if possible) all kinds of electric or magnetic disturbances to protect and maintain the high performance of the systems. For example, generating electromagnetic fields in opposition to the disturbances can be a solution. For that, the electromagnetic source identification that produces the desired fields to substitute unintentional emissions by desired ones or complex radiations by their equivalents is necessary [1–3].

Source identification problems have triggered the interest of scientists in the last decades. In the frequency-domain analysis, different methods based on the equivalence principle substitute complex real sources by equivalent radiating electric or magnetic dipoles [4]. These methods characterize elemental sources surrounding an electronic device to emit radiations equivalent to that emitted by the device itself. More recently, genetic algorithm-based techniques have been used to find a set of elemental electric or magnetic sources that replace radiating dipoles [5]. Similarly, identifying electromagnetic sources to replace any unintentional field with the desired one is also an interesting challenge in inverse-source problems.

Inverse-source problems are the processes of estimating data that may not be obtained by direct measurements. They are defined as computing, from a set of observable results, the casual input parameters of the physical system that produced them. Unfortunately, inverse-source problems have shown signs of instability, ill-posedness, and ill-conditionality. Then, researchers resorted to mathematical tools to solve optimization problems [6] and partial differential equations that would successfully identify electromagnetic sources. Although these methods have shown to be efficient in the frequency domain [7], they have presented some limitations in the time domain [8]. However, developing time-domain methods has become essential due to the large numbers of real-world time-dependent problems. Moreover, nonlinearities, which are common EMC problems, are easier to handle in the time domain.

Among the alternative methods that may be more simple and efficient at determining the profile of the sources directly in the time domain is the Time-Reversal (TR) method. In 1990, M. Fink and his team introduced the novel

time-domain approach TR to refocus acoustic and electromagnetic waves by reversing in time a system's response signals [9]. The TR process consists of two stages: in the first phase, an electromagnetic pulse is emitted at a point in the space, and its resulting electromagnetic fields are recorded by an opening array called the Time-Reversal Mirrors (TRM). Secondly, the recorded fields are simultaneously re-emitted by the TRM in reverse chronology. During the last three decades, in-depth TR analyses have been carried out to study its aspects in different environments. By proposing the refocusing of an electromagnetic wave, both spatially and temporally, this method opens up a wide field of possible applications (electromagnetic attacks on a target, detection, discrete communication, etc.). Particularly, among the interesting applications of the TR is the active shaping of electromagnetic fields.

Despite the interesting results delivered by the TR, a surrounding source surface is required to avoid information losses [10]. Due to the difficult emission of several signals simultaneously, many studies have been conducted to maintain the high refocusing quality using as few sources as possible to be placed at the optimal spatial positions in the medium. Unfortunately, some positions may be located in hard-to-access areas for both emitting and recording signals. If not, the equipment used in some experiments are bulky or too large and allows conducting *in situ* measurements only; thus, they cannot be placed at the optimal source positions. On top of that, the TR demonstrates to be less reliable when tackling lossy problems or when imposing complex conditions on the duration or the form of the imposed electromagnetic field [11]. All these reasons result in poor refocusing quality and justify the importance of developing new time-domain techniques to shape electromagnetic fields independently of the topology of the medium and the position of the source(s) or receiver(s) as well.

The applications of the TR are plentiful and have been investigated in transmission line networks and reverberant environments [12]. In a reverberant cavity, refocusing electromagnetic fields using the TR has recently been applied to real physical problems, such as plasma generation [13]. As a matter of fact, the aforementioned limitations of the TR appear more clearly when shaping electromagnetic fields to enhance the local generation of nanosecond microwave plasma. Although several types of surface-wave launchers were proposed to generate large, dense, and uniform plasma, the

location of the generated plasma is fixed once and for all, occupying the entire cavity volume [14–24]. Instead, a new kind of microwave plasma source was recently proposed by the authors in [13] to generate local plasma at a predefined position using the TR method. In fact, the TR succeeds in generating plasma locally; however, the generation of plasma elsewhere remains uncontrolled. In other terms, the TR efficiently activates plasma on the desired position, but it may not prevent the appearance of plasma at the neighboring points. Thus, we emphasize the importance of developing new time-domain techniques that simultaneously control the electromagnetic fields in three dimensions at several spatial points.

The TR process may also deal with detecting and locating faults in power line [25, 27, 136] and transmission line networks [28] due to their effect on modifying the EMC characteristics of any system. Unavoidably, a cable in a network will show signs of weakness attributed to either external factors (mechanical aggression, chemical contamination, humidity, etc.) or internal reasons (heating, corrosion, insulation damage, cracks, frays, etc.) affecting the immunity and emissivity of the wires. The most common methods used today for detecting and locating faults in transmission line networks are the reflectometry-based techniques. Although they are generally well suited to detect and locate electrical faults, reflectometry-based techniques show some limitations when dealing with soft faults, complex, or lossy networks [29]. In many cases, the TR and reflectometry-based techniques detect and locate faults that may not be repaired due to external factors such as hard-to-access zones. For example, a network presenting faults at its parts located in a radioactive zone or a faulty network of a satellite in outer space. Alternatively, new paradigms dedicated to tolerate the faults in cables become necessary.

Thesis objectives and scopes

Our study focuses on developing numerical methods to solve linear and nonlinear inverse-source problems directly in the time domain. In linear media, we improve the Linear Combination of Configuration Field (LCCF), while in nonlinear media, we use Newton's Method (NM) and the NonLinear Least-SQuares (NLLSQ) solver. In complex linear and nonlinear media, the developed numerical methods identify the temporal profile of source signals to shape and impose desired electromagnetic fields or to suppress

unintentional ones at some spatial points over a given duration. In all our computations, we do not switch to the frequency domain, except for some analyses and interpretations of the computed signals, to avoid numerical difficulties resulting from the use of the Fast Fourier Transform (FFT) and its inverse; the computations are carried out in reference to time only.

Practically, our contributions deals with the electrical faults appearing in transmission line networks. Applications of the developed/used methods can include the fault tolerance of faulty lossy wiring networks behaving linearly or nonlinearly. The aim is not to locate or characterize these faults, but to tolerate their appearance and treat them as a part of the network without any physical intervention. We seek to tolerate the faults independently of their number, position, and nature. This introduced paradigm is called the *Software Correction (SC)*.

In the linear case, the ultimate objective of our study is to experimentally test and validate the time-domain electromagnetic shaping in one-dimensional and three-dimensional environments. For this purpose, we add constraints to the LCCF problem to modify the temporal characteristics of the source. The modified sources comply with the built-in limitations of the equipment used. In wiring networks, both the voltage/current active shaping and the SC experiments are conducted. In a three-dimensional linear inverse-source problem, our efforts focus on enhancing the controllability of nanosecond microwave plasma in a reverberant cavity using the TR and the LCCF methods. The LCCF and the TR abilities are compared to shape electromagnetic fields under complex conditions. This comparison shows the advantages that the LCCF may bring over the TR.

Thesis outline

The following thesis is composed of five chapters:

Chapter 1 will be an overview of the context of our study. We will list the different common methods used to identify electromagnetic sources in both the time-domain and frequency-domain analyses, along with illustrating their major advantages and limitations. Then, we will present the general principles of the techniques used to detect, locate, and diagnose electrical

faults in cables. We will focus on the importance of such techniques and the limitations they encounter. The last section will describe the settings and tools used in all the numerical simulations throughout this dissertation.

Chapter 2 will present the basic version of the LCCF method to shape electromagnetic fields in the time domain at a single spatial point using one source generator. After explaining its theory, the LCCF will be supported by numerical examples in wiring networks and free space environments to illustrate its applicability in any linear medium. After that, the LCCF will be compared to the TR to show its superiority in shaping electromagnetic fields. For future experimental considerations, we will finally add constraints to the LCCF problem to modify the properties of the computed source.

Chapter 3 will provide an improvement of the LCCF method to control several spatial points using one or more source generators. After presenting the generalized theory, numerical examples will be illustrated in wiring networks and free space environments to show that the generalized LCCF is still efficient at shaping electromagnetic fields. An interesting application of the LCCF method in the context of defective wiring networks will be introduced. We will propose a new paradigm to compensate for the effects of the defects regardless of their number, nature, and position.

Chapter 4 will show that the LCCF is inefficient at shaping electromagnetic fields in nonlinear media. Alternatively, two methods will be proposed to identify the temporal source that would impose a predefined voltage or current at a single position on any wiring network over an interval of time. After explaining the corresponding theories, both methods will be supported by numerical examples to illustrate their efficiency in nonlinear media. After comparing the two methods, the most efficient one will be selected to compensate for the effects of the defects in nonlinear defective networks regardless of their number, nature, and position.

Chapter 5 will deal with the experimental validation of the LCCF method in one and three dimensions to test its robustness. For specific considerations, the LCCF theory will first be adapted, then applied to different wiring network configurations to shape electromagnetic fields. After simulating faults of different natures and numbers in the lines of the wiring networks, we

will show how the effects of these faults could be compensated to recover the healthy outputs again. In a final interesting three-dimensional experiment, the LCCF method is used to enhance the spatial control of nanosecond microwave plasma in a linear cavity.

Remark: In this thesis, all the numerical simulations were conducted by the multi-paradigm numerical computing software *Matlab*.

1

Electromagnetic Source Identification: State of the Art and Context

We begin the first chapter by reviewing the state of the art of the different approaches developed earlier in the field of ElectroMagentic Compatibility (EMC) to identify electromagnetic sources. In the frequency-domain analysis literature, we recall the existing methods, such as the equivalent source models and the inverse-source problems, then we state their advantages and limitations. However, as we are more interested in the time-domain analysis, we focus on existing time-domain methods based on the optimal control of partial differential equations. We remind about the limitations of the optimal control before stepping forward to recall other more efficient and simple time-domain approaches, such as the time-reversal method to shape electromagnetic fields at a point in a domain of interest. In detail, we review the time-reversal progress over the last few years, its advantages, and drawbacks.

An essential part of our work focuses on electrical faults that may appear in wiring networks. That is why, in another section, we present the existing wire diagnosis tools, namely the most common reflectometry-based techniques and the time-reversal imaging methods, to detect, locate, and diagnose electrical faults in wiring networks. We shed light on the importance of these tools in diagnosing wires, the advantages they may provide, and the limitations that may deteriorate their proper performance.

At the end of each section, we raise controversial (unanswered or not adequately answered) questions that will be considered throughout the upcoming chapters. These questions position our work in the state of the art described in this chapter and highlight the objectives of this thesis. Finally, we describe our work settings after reporting its context, then list the different tools to be used during our numerical simulations. As this thesis is applied to electromagnetism, it is essential to present Maxwell's equations that describe the propagation of electromagnetic waves in any medium and the telegrapher's equations that govern the propagation of voltage and current in wiring networks. To solve Maxwell's and the telegrapher's equations, we describe the numerical method preferentially used throughout this study, namely the finite-difference time-domain method.

1.1 Source Identification Techniques

In electromagnetic theory, the source identification problem may be formulated to find sources that produce a prescribed radiation pattern in a region of interest. For a long time, source identification problems have been receiving considerable attention from researchers and have been arising in various research studies and engineering applications [1–3]. Different methods were developed in the literature to model few equivalent radiating electric or magnetic sources to predict, replace, or substitute real complex ones. This section will present the different existing methods proposed earlier in EMC to identify electromagnetic sources in either the frequency-domain or time-domain analysis. For each approach, we will determine the witnessed advantages and limitations.

1.1.1 Equivalent source models

The equivalent source models characterize a set of equivalent elemental sources encircling an electronic device that radiates the same electromagnetic fields as the device itself. Several techniques based on the equivalence principle were put forward by many scientists and engineers [4]. The equivalence principle states that a field in a lossless region can be determined from a surface enclosure of current densities. To give the equivalence principle's main lines, we consider Figure 1.1 where the electric $\mathbf{E}$ and magnetic $\mathbf{H}$ fields out-

side a closed surface S are obtained by placing adequate electric and magnetic current densities on S, taking into account the boundary conditions. The surface S separates between the inner volume V_1 surrounded by S and the outer volume V_2 outside S. In the initial problem, a source represented by an electric current density $\mathbf{J}_1$ and a magnetic current density $\mathbf{M}_1$ radiates in V_1 to produce $\mathbf{E}$ and $\mathbf{H}$. According to the equivalence principle, this problem can be replaced by an equivalent one: new sources ($\mathbf{J}_S$ and $\mathbf{M}_S$) are placed on the surface of S to produce the same fields $\mathbf{E}$ and $\mathbf{H}$ in V_2 and null electromagnetic fields in V_1.

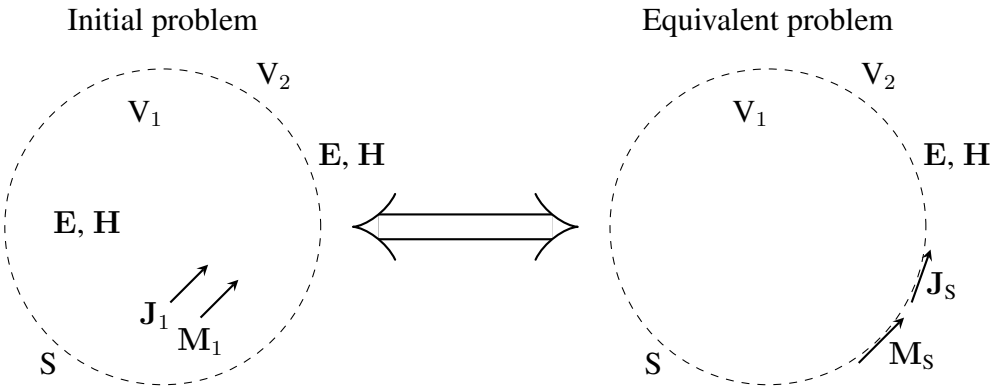

Figure 1.1: *Equivalence principle concept: the source inside the enclosed volume V_1 radiates to produce the electric $\mathbf{E}$ and magnetic $\mathbf{H}$ fields. This problem is replaced by an equivalent one; we identify sources on the enclosure of V_1 that produce the same $\mathbf{E}$ and $\mathbf{H}$ in V_2 after their radiation.*

In antennas studies, a physical model based on the multipole expansion was introduced to represent the electromagnetic emissions in system-level analysis [30]. This model gives a convenient representation with a low number of parameters determined by measurements or simulations. Moreover, neural networks were also applied to source identification problems to recognize basic printed circuit board configurations using its magnetic near-field spectra and radiated far-field emissions [31]. In other studies, researchers relied on the equivalent current approach in antenna design to calculate the far-field from the near-field radiation based on different methods, such as the modal expansion, the integral equation, and the conjugate gradient [6,32–34]. Despite the interesting results, the systems solved by these models are generally ill-conditioned; thus, they may be solved by different methods,

such as the singular value decomposition or the iterative conjugate gradient. Nonetheless, their main drawback, unfortunately, lies in their computational costs [35]. In [36–38], matrix inversion methods were proposed to find the parameters of the equivalent radiation model. Although they showed high speed in calculations since only a linear system has to be solved, several time-consuming measurements are required to find an accurate model that may require different information beforehand.

Alternatively, the model parameters for EMC applications in many other works were calculated based on optimization tools [5, 39–45]. In [5], the binary genetic algorithm optimization method was used to simulate antennas from near-field distribution by a set of infinitesimal dipoles. Regué *et al.* used the genetic algorithms to identify the source distribution and predict the far-field radiations [39]. De Daran *et al.* modeled the coupling phenomena on an electronic board and evaluated the radiated emissions [40]. The authors in [41] presented a methodology to substitute radiating dipoles for real sources. Another methodology in [42] was introduced for radiating source identification of power electronic devices based on substituting a set of elemental magnetic dipoles for the natural systems. Moreover, other genetic algorithm-based techniques were also developed to predict the radiation from shielding enclosures using near-field scan data [43] or model electromagnetic emissions of a printed circuit board [44]. Although a reduced number of dipoles may construct these models, their computational time is massive, especially when high numbers of dipoles are required. That is why Benyoubi *et al.* proposed a fast technique taking advantage of the matrix inversion and optimization methods to enhance the computational time [45].

Most of the equivalent source models, especially the matrix inversion methods, may be viewed as solving inverse problems. In the next section, we give a detailed definition of the inverse problems and particularly the inverse-source problems from a mathematical perspective. Similar to what preceded, identifying electromagnetic sources to replace any undesired field by a desired one in inverse-source problems is also an interesting EMC issue [46, 47].

1.1.2 Inverse-source problems

Inverse Problems (IPs) are the process to determine some physical parameters from recorded or desired measurements and observations of a studied physical event. They are widely spread in different domains: acoustics, radar, signal processing, EMC, etc. IPs usually start with the effects called *measurements* or *data* and then calculate their causes called *parameters*. More precisely, they determine an operator called *measurement operator* that maps the data and parameters of the studied problem (see Figure 1.2).

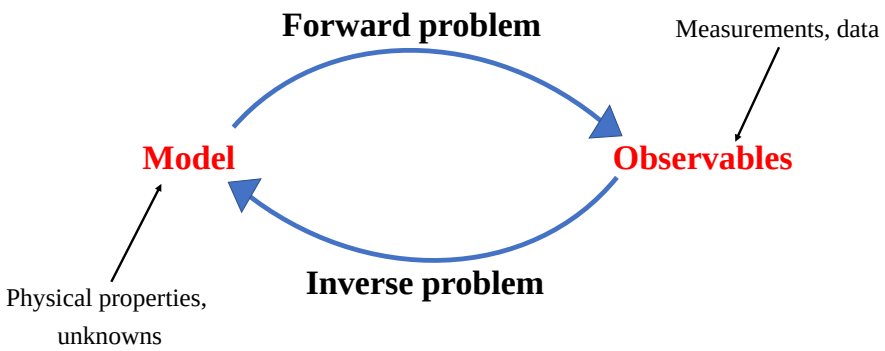

Figure 1.2: *Forward and inverse problems.*

An injective measurement operator means that the acquired data uniquely characterize the parameters. Often, this inversion amplifies errors in measurements, which we refer to as noise, enhancing the instability of the model. In 1923, the French mathematician J. S. Hadamard introduced the idea of well-posed inverse problems. Any mathematical model of a certain physical phenomenon should satisfy the following three properties to achieve its well-posedness

1. A solution exists,
2. The solution is unique,
3. The solution behavior changes continuously with the initial conditions.

In mathematical modeling, IPs are often not well-posed or ill-posed in the sense of Hadamard. An ill-posed IP is a problem in which at least one of the

above conditions is not satisfied. In the scattering theory, IPs are categorized into: Inverse-Medium Problems (IMPs), Inverse-Obstacle Problems (IOPs), Inverse Equivalent Surface-Source Problems (IESSPs), Inverse-Source Problems (ISPs), etc. For fixed electromagnetic sources, the IMPs and the IOPs rebuild the topology of the studied medium or determine the positions and shapes of the built-in scatterers to obtain the desired radiation pattern at an observation point based on the scattering of the incoming source radiations. However, for fixed medium and scatterers, the IESSPs and the ISPs identify a surface-source enclosure or some source-points in the space equivalent to a real source. After radiation, the identified sources scatter to generate the desired pattern at the observation point. Figure 1.3 represents the different types of IPs; however, in this thesis, we are only interested in ISPs.

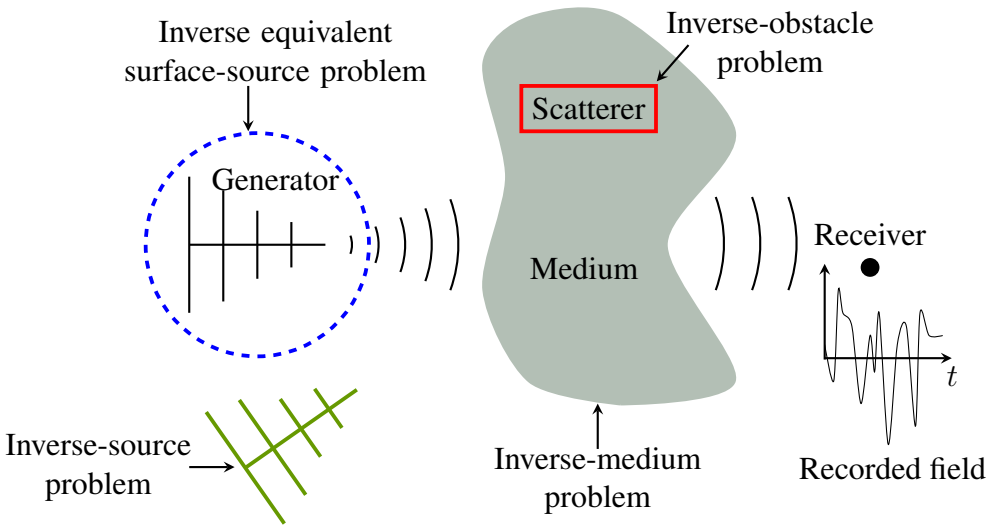

Figure 1.3: *Different inverse problems: inverse-medium problems, inverse-obstacle scattering problems, inverse equivalent surface-source problems, inverse-source problems.*

ISPs have long been an active field of research in various scientific and industrial areas, such as antenna design and synthesis, biomedical imaging, and photo-acoustic tomography [48]. As an important research topic in the inverse scattering theory, they have continuously attracted much attention from many researchers and engineers. In essence, ISPs identify sources

that would give rise to prescribed radiation fields at one or more spatial positions. As a part of IPs or the so-called *inverse crime* [49, 50], ISPs are equally ill-posed due to either the nonuniqueness or the instability of the solution (conditions 2 and 3). In general, their solutions are not unique at a fixed frequency due to the existence of nonradiating sources, where the field is identically zero outside a finite region [51–53]. For this reason, the source requires additional constraints to obtain a unique solution, such as picking up the solution with a minimum L^2 norm, i.e., minimum energy solution [54]. Similarly, the instability of the solution is also a challenging issue in mathematical computations, where a small data change might lead to considerable errors in computations.

For a fixed frequency, researchers have invested much effort to solve the ISPs for Helmholtz's equation [55, 56]. The instability of such models refers to the exponential decay of the singular eigenvalues of the forward operator. Then, to overcome the complications of the nonuniqueness and instability of the solution, an efficient alternative approach is to use multifrequency data instead of a single frequency. By taking measurements at multiple frequencies, a mathematical study was introduced on the stability of the ISP for Helmholtz's equation [57]. In what follows, we describe this study to formulate the ISP for Helmholtz's equation using multiple frequencies.

Let Ω be a smooth domain in $\mathbb{R}^d$ ($d = 2$ or 3) of boundary $\Gamma = \partial\Omega$. For all $\mathbf{r} \in \mathbb{R}^d$, denote by $B_\rho = \left\{\mathbf{x} \in \mathbb{R}^d : |\mathbf{x}| < \rho\right\}$ the d-dimensional open ball of radius ρ and center $\mathbf{r}$ (see Figure 1.4). We consider the ISP to determine an unknown source $\mathbf{S} = \mathbf{S}(\mathbf{r}, t)$ of the homogeneous Helmholtz's equation

$$\nabla^2 \mathbf{\Phi} + k^2 \mathbf{\Phi} = \mathbf{S}, \tag{1.1}$$

knowing that $\mathbf{\Phi} = \mathbf{\Phi}(\mathbf{r}, t)$ may be any radiated field (electric, magnetic, sound, elastic, etc.) at a position $\mathbf{r} \in \Omega$ and an instant t, whereas k is the wavenumber of $\mathbf{\Phi}$. The source $\mathbf{S} = \mathbf{S}(\mathbf{r}, t) \in \left(L^2(\Omega)\right)^3$ has a compact support V_0. The field $\mathbf{\Phi}$ satisfies the Sommerfeld radiation condition

$$\lim_{|\mathbf{r}| \to +\infty} |\mathbf{r}|^{\frac{d-1}{2}} \left(\partial_{|\mathbf{r}|} \mathbf{\Phi} - ik\mathbf{\Phi}\right) = \mathbf{0}. \tag{1.2}$$

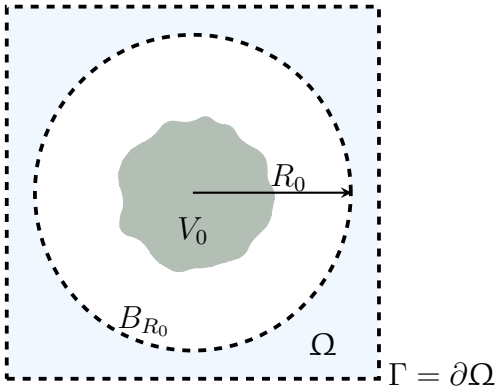

Figure 1.4: *Problem geometry of the inverse-source problem.*

We define the Green function $\mathscr{G}(\mathbf{x}, k)$ in the whole space as

$$\mathscr{G}(\mathbf{x}, k) = \begin{cases} -\dfrac{i}{4} H_0^{(1)}(k\mathbf{x}) & \text{if } d = 2, \\ -\dfrac{e^{ikx}}{4\pi\mathbf{x}} & \text{if } d = 3, \end{cases} \tag{1.3}$$

where $H_0^{(1)}(kx)$ is the Hankel function of the first kind with order 0. Then, there exists a unique solution $\Phi(\mathbf{r})$ satisfying both Helmholtz's equation (1.1) and the radiation condition (1.2)

$$\mathbf{\Phi}(\mathbf{r}, t) = \int_\Omega \mathscr{G}(|\mathbf{r} - \mathbf{x}|, k)\, \mathbf{S}(\mathbf{x}, t) d\mathbf{x}. \tag{1.4}$$

The forward problem (1.4) allows to introduce the ISP for Helmholtz's equation. Assuming that $\exists R_0 > 0$ such that $\overline{V}_0 \subset B_{R_0} \subset \Omega$, the multifrequency ISP is to reconstruct the source from the measured radiated field $\mathbf{\Phi}(\mathbf{r})$ on the boundary Γ ($\mathbf{r} \in \Gamma$), $\forall k \in [0, k_0]$, where k_0 is a fixed frequency.

Further studies focused on increasing the stability for the ISP of the three-dimensional Helmholtz's equation [58, 59]. The introduced method is based on the Huygens principle [1], limited to the assumption of a particular form of the source, and requires the Dirichlet and Neumann boundary data to

[1] The field at any point of the domain may be computed from the fields on a closed surface surrounding the sources.

gain stability. These limitations were overcome by Li *et al.* after introducing an alternative approach in [59] to obtain the same results for the two and three-dimensional Helmholtz's equation by removing the source assumption and Neumann boundary data, i.e., it requires only Dirichlet data.

Studies on the stability of the ISP for Helmholtz's equation were accomplished in various domains, such as elastics, acoustics, optics, etc., whereas little work focused on the stability of ISP for electromagnetic waves. Based on a low-frequency asymptotic analysis of the time-harmonic Maxwell's equations, the authors in [60] formulated and solved the ISP to reconstruct dipole sources in a heterogeneous medium showing uniqueness and stability. The uniqueness and nonuniqueness of the ISP for Maxwell's equations were argued by R. Albanese *et al.* in [46]. Other analyses on solving ISPs for hyperbolic systems using Carleman estimates could be found in [61–64]. Unfortunately, no stability results were demonstrated for the ISP of Maxwell's equations in a general setting until 2019.

Recently, a new study initialized the mathematical analysis and provided the first results on the stability of the ISP for electromagnetic waves [65]. This study was inspired by the ISP of Helmholtz's equation to extend an approach that handles the more complicated Maxwell's equations. They gave a detailed theory about the uniqueness and the increasing stability of the ISP to reconstruct the radiating electric current density from multiple frequencies data. In a homogeneous medium, we consider the time-harmonic Maxwell's equations, where $\mathbf{\Phi}$ is the electric $\mathbf{E}$ (in $\mathrm{V/m}$) or magnetic field $\mathbf{H}$ (in $\mathrm{A/m}$)

$$\nabla \times \mathbf{E} - ik\mathbf{H} = \mathbf{0}, \tag{1.5}$$

$$\nabla \times \mathbf{H} + ik\mathbf{E} = \mathbf{J}. \tag{1.6}$$

Assume now that the source $\mathbf{S}$ is the electric current density $\mathbf{J} \in \left(L^2(\Omega)\right)^3$ having a compact support V_0. To make the direct problem well-posed, it requires the Silver-Müller condition

$$\lim_{|\mathbf{r}|\to+\infty} \left[(\nabla \times \mathbf{E}) \times \mathbf{r} - ik\,|\mathbf{r}|\,\mathbf{E}\right] = \mathbf{0}. \tag{1.7}$$

After multiplying equation (1.6) by ik, we substitute equation (1.5) in (1.6)

yielding the decoupled Maxwell's system for the electric field $\mathbf{E}$ in $\mathbb{R}^3$

$$\nabla^2\mathbf{E} - k^2\mathbf{E} = ik\mathbf{J}. \tag{1.8}$$

It is known that there is a unique solution that satisfies both Maxwell's system (1.8) and the Silver-Müller condition (1.7) [66]

$$\mathbf{E}\left(\mathbf{r}, t\right) = \int_{\Omega} \mathscr{G}_M\left(\left|\mathbf{r} - \mathbf{x}\right|, k\right) \mathbf{J}(\mathbf{x}, t) d\mathbf{x}, \tag{1.9}$$

where $\mathscr{G}_M\left(\mathbf{x}, k\right)$ is the Green's tensor for Maxwell's system (1.8) defined in [65]. In a similar way, if we eliminate the electric field $\mathbf{E}$, we may prove in $\mathbb{R}^3$ that

$$\Delta\mathbf{H} + k^2\mathbf{H} = -\nabla \times \mathbf{J}. \tag{1.10}$$

The system (1.10) has a unique solution

$$\mathbf{H}\left(\mathbf{r}, t\right) = -\int_{\Omega} \mathscr{G}\left(\left|\mathbf{r} - \mathbf{x}\right|, k\right) \mathbf{I}_3 \cdot \nabla \times \mathbf{J}(\mathbf{x}, t) d\mathbf{x}, \tag{1.11}$$

where $\mathbf{I}_3$ is the 3×3 identity matrix. The forward problems (1.9) and (1.11) allows to introduce the ISPs for Maxwell's equations. Assuming that $\exists R_0 > 0$ such that $\overline{V}_0 \subset B_{R_0} \subset \Omega$, the multifrequency ISP is to reconstruct the electric current density from the measured fields $\mathbf{E}$ and $\mathbf{H}$ on the boundary Γ $(\mathbf{r} \in \Gamma)$, $\forall k \in [0, k_0]$, where k_0 is a fixed frequency.

G. Bao *et al.* addressed the uniqueness and nonuniqueness of the ISP solution for the electromagnetic waves. They showed that the multifrequency data can uniquely determine $\mathbf{J}$ if $\nabla \cdot \mathbf{J} = 0$. Then, they went further in their analysis to discuss the uniqueness results by studying the variational equation relating the unknown current density to the data. In detail, they distinguished between the possible unique identification of $\mathbf{J}$ and its impossible identification using multiple frequencies and Dirichlet boundary data. The stability estimations of the problem consist of the data discrepancy and the high-frequency tail. Bao and his collaborators concluded that the ill-posedness of the ISP decreases as the data frequency increases.

The stability of the ISP for electromagnetic waves is limited to data available on the total border area (Huygens principle) and may not deal

with limited aperture data. Add to that, the analytical Green tensors are not available anymore in heterogeneous media; thus, the study may be applied only in homogeneous media. Despite the few surveys on the uniqueness and stability of ISPs in electromagnetism, their mathematical theories are still complicated. The effect of this complication is the increasing price to pay for the implementation complexities. In addition to that, the ISP for electromagnetic waves was analyzed in the Frequency Domain (FD), and according to the best of our knowledge, it was never investigated directly in the Time Domain (TD), which is rather more difficult due to the requirement of all frequency samples to gain better stability. Therefore, other alternative techniques focusing on the time-domain analysis may be more suitable, such as the optimal control of partial differential equations, for example.

What advantages may the time-domain analysis offer over the frequency-domain analysis? In the TD, the wideband data are available from one model computation; however, many frequency samples are required to obtain equivalent data in the FD. The time-domain analysis allows us to avoid numerical errors resulting from the use of the Fast Fourier Transform (FFT) and the Inverse Fast Fourier Transform (IFFT) algorithms when switching from the TD to the FD and vice versa. In fact, the electromagnetic fields may be controlled in the TD at specified periods as opposed to the FD, where the control occurs for the whole time process. Moreover, we are interested in analyzing nonlinear systems that are difficult to handle in the FD, so the time analysis seems more convenient.

1.1.3 Optimal control of partial differential equations

Partial Differential Equations (PDEs) may be used to describe a wide variety of physical phenomena, such as sound, heat, diffusion, electrostatics, electromagnetics, elasticity, gravitation and quantum mechanics, etc. The optimal control drives the solution of the PDEs understudy to a predefined state. The optimal control theory may be applied to the PDEs that govern the propagation of waves, such as Maxwell's equations. Besides fitting problems in the FD [7], the optimal control theory may also deal with problems in the TD. In 1988, J. L. Lions introduced a new time-domain method known as the Hilbert Uniqueness Method (HUM) to build an appropriate control that leads a system from its initial state to a rest state at a given time $T > 0$ [67].

The HUM was illustrated numerically in [8], where the authors clearly pointed out the transiency of the reached state. This transiency occurs when reaching a nonrest state at a chosen time T, where the wave inevitably continues propagating. Although the HUM method may find the right control time sequence to drive the system from the initial state to the rest state in simple settings, it is found that the HUM may not tackle realistic and complex configurations. Similar to the numerical algorithms for the boundary control of wave equations, the HUM approach depends on the space discretization and starts to diverge as the step tends to zero due to high-frequency oscillations [68]. Although several regularization techniques have been proposed [68–70], the robustness of the HUM method for the time T and the geometry discretization is still under study. Practically, the concerned method starts to fail with ultra-high-frequency electromagnetic fields due to the unreachable bandwidth of most common EMC generators and amplifiers to achieve a reasonable control time T. Another limitation could be the need for prior knowledge of the transient noise in the system, which may not be achievable in practice.

The optimal control of PDEs is a general method that is difficult to implement due to the complex underlying mathematical theory. Moreover, it shows intrinsic experimental limitations to shape electromagnetic fields in the TD. For these reasons, the research work focused on other recent time-domain methods that may be more simple and efficient at shaping electromagnetic fields, such as the time-reversal method.

1.1.4 Time-reversal method

In 1990, the Time-Reversal (TR) method was first proposed in acoustics by M. Fink and his team [9], then tends to focus more on EMC [12, 25, 71, 72]. The TR for the electromagnetic wave equation

$$\frac{1}{c^2}\frac{\partial^2 \mathbf{\Phi}}{\partial t^2} = \Delta \mathbf{\Phi} \tag{1.12}$$

($\mathbf{\Phi}$ stands for the electric $\mathbf{E}$ or magnetic $\mathbf{H}$ fields) is based on the principle of their reciprocity in a lossless stationary medium. From a mathematical point of view, if the equation (1.12) admits $\mathbf{\Phi}(\mathbf{r}, t)$ as a solution, then $\mathbf{\Phi}(\mathbf{r}, -t)$

is also a solution. This may be physically interpreted as the existence of a "reverse" solution due to the absence of the first-order derivative in the equation (1.12). In other words, the reverse of $\mathbf{\Phi}(\mathbf{r}, t)$ in the TD would precisely retrace the path of the original wave back toward the source point; the retro-propagation of the waves is based on the reversibility of the wave equation (1.12) in time. The field $\mathbf{\Phi}(\mathbf{r}, t)$ is the divergent wave, which is usually called the scattered field, whereas $\mathbf{\Phi}(\mathbf{r}, -t)$ is the convergent wave that refocuses on the source point.

To better understand the concept of the TR in EMC, Figure 1.5 is considered. A generator radiates an electromagnetic source that propagates through an inhomogeneous and discontinuous medium. As a result, the incident waves experience distortion before ending to an array of probes surrounding the source, where each records the signal it detects over a long interval of time. This is the first step of the TR, known as the recording step. Following step one, the recorded signals are time-reversed and synchronously re-emitted, each by its corresponding probe. Traveling back in time, the emitted waves retrace the original path back through the medium and refocus on the source point. This step is known as the time-reversal and re-emission step.

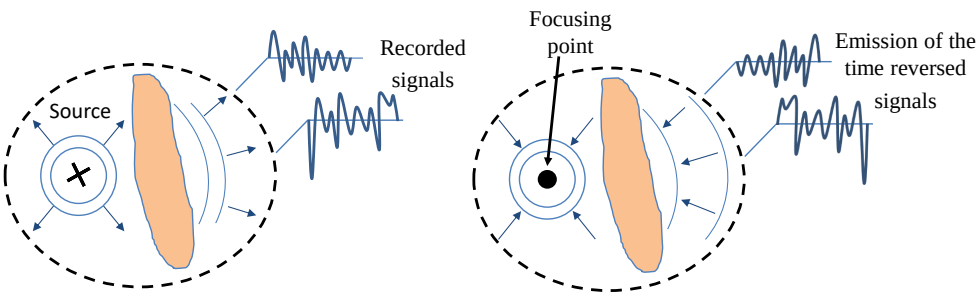

Figure 1.5: *Time-reversal principle: the source radiates through an inhomogeneous medium before ending to an array of probes surrounding the source. The divergent waves are recorded, time-reversed, and synchronously re-emitted to refocus on the source point.*

Practically, the free space propagation is simulated by an Anechoic Chamber (AC) that absorbs the electromagnetic waves through its walls [73].

In ACs, a closed TR cavity is not feasible, even though it presents an ideal refocusing concept through any inhomogeneous medium. From an experimental point of view, the infinite number of probes enclosing the source has to be limited to an opening array forming the Time-Reversal Mirrors (TRM). Note that each probe has its own electronics (amplifier, generator, receiver, digital memory, etc.) to synthesize the inverted temporal signals stored in the memory. Compared to the original source, the quality of refocusing is affected by the number of the considered probes; the decrease in the angular aperture makes it possible to realize the TRM; however, it causes information losses and poor refocusing quality. The TR of electromagnetic waves was experimentally validated, presenting complexities and high costs [72]. Indeed, a simultaneous re-emission of several signals is a very difficult task and may not be easily achieved; that is why, the TRM should be composed of as few probes as possible without reducing the refocusing quality.

Considering a few probes in free space has to be substituted by an increase in the medium complexity to collect much information on the wave propagation in the first phase of the TR [10, 74]. Interestingly, in a reflective cavity, such as the Mode Stirred Reverberation Chamber (MSRC) [75, 76], a TRM composed of a single probe is enough to attain an excellent refocusing. Actually, the characteristics of such a cavity allow us to benefit from the multiple reflections and re-reflections experienced by the waves on the metallic walls of the chamber. The information represented by the echoes collected using a single probe is sufficient to realize a TR experiment.

Although the TR method is still applicable in a lossy reverberant chamber [77–79], introducing wall losses should be carefully considered since the environment is not completely reversible in this case [80]. Moreover, the TRM efficiency may be improved in the MSRC mode by acting on the recording duration of the incoming signals and identifying the optimal source location [81, 82]. Apart from the refocusing quality, an important limitation of the TR is the need for an emitting source at the refocusing position; otherwise, there is no wave refocusing. This disadvantage is problematic for different EMC applications when such a position is inaccessible. In general, sources are not supposed to radiate intentionally; they are not active (transmit mode) as described before, whereas they are defects that behave passively (echo mode) to reflect an incident wave. This reality has been treated based

on the equivalence principle described in Section 1.1.1 after adding extra antennas called Equivalent Surface Network (ESN) and placed around the passive source [83, 84] (see Figure 1.6).

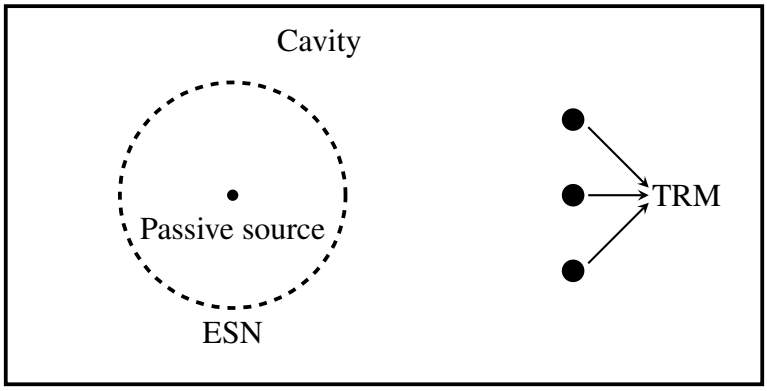

Figure 1.6: *Time-Reversal Electromagnetic Chamber: extra antennas are placed around the passive source based on the equivalence principle.*

This problem is called the Time-Reversal Electromagnetic Chamber (TREC) and introduced by A. Cozza in [85] as an alternative approach to the standard TR. The TREC uses the multipath propagation to control wavefronts and their directions in complex environments. As opposed to the standard TR, the TREC works well when it comes to controlling the wavefront directions. Despite its interesting results, the TREC still presents some limitations regarding the type or the number of antennas used to form the ESN. Also, common testings in EMC, such as generating a plane wave of any arbitrary direction, may not be achieved by the TREC; the transverse shape of the refocused wavefronts is always cylindrical or spherical. Indeed, although the back-propagated waves impinging the ESN will also impinge the center of the inner volume, it is unfortunate that no guarantees were provided about the accuracy in amplitude and shape of the wavefronts once reaching the center of the inner volume.

Besides all the limitations mentioned above for the TR and TREC, some general questions may also be raised.

- If no prior knowledge is provided about the characteristics of the

medium (reverberating, lossy, dispersive, etc.), how could this influence the TR applicability?

- What are the optimal positions of the source and the TRM to deliver a high quality refocusing? If determined, how to attain the optimal TR performance if these positions are inaccessible? It is worth noting that many common EMC applications work in nondestructive testings, where the probe could only be placed at one side of the cavity.

- Refocusing at the source point may generate unintentional electromagnetic fields in its neighborhood. How can the TR simultaneously control the electromagnetic fields at several points of the cavity to cancel these fields?

- Wide variety of nonlinear problems occupy a substantial space of the EMC applications. How can the TR behave in such a case with low and high nonlinearity levels?

In this dissertation, we are interested in identifying electromagnetic sources in the TD in guided wave and free space propagation. The objective is to impose/cancel desired/undesired electromagnetic fields in linear and nonlinear media. In the linear case, a new technique called the Linear Combination of Configuration Field (LCCF) is developed in later chapters. The LCCF will be examined in detail, then validated numerically and experimentally. Interestingly, we will also compare the LCCF to the TR, under the title "TR vs. LCCF", in guided wave and free space propagation. Such a comparison will show the superiority of the LCCF method to shape electromagnetic fields in the TD. After proving the inapplicability of the LCCF in nonlinear systems, other methods, such as Newton's method and the nonlinear least-squares solver, will be used to identify the temporal sources that generate the desired field at a definite position in the nonlinear medium. The developed/used techniques, for the linear and nonlinear cases, are proposed as alternative approaches to overcome the above arguable questions.

In guided wave propagation, the developed/used techniques in this thesis are found to fit wire diagnosis problems, especially when electrical faults appear in wiring networks. In the following, we review the state of the art of

the existing methods to detect, locate, and diagnose electrical faults in wiring networks.

1.2 Wire Diagnosis

Unavoidably, wires are subjected to natural, mechanical, or thermal stresses (e.g., humidity, corrosion, heating, etc.) that reduce their lifespan and cause their damage [86]. Moreover, the degradation resulting from the excessive use and maintenance of wires leads to the appearance of faults in wiring networks. These faults may be hard ones (open and short circuits) or soft ones (chafing, insulation damage, cracks, frays, etc.) impacting the shielding, immunity, or emissivity of wires (see Figure 1.7). In fact, maintaining soft or hard faults is of equal importance as soft faults will evolve to hard ones sooner or later. This evolution is critical since hard faults may jeopardize the functioning of the overall system causing data breaks and fires.

Figure 1.7: *Hard (left image [source]) and soft (right image [source]) faults appearing in wiring networks.*

The increase in the length of cables makes it difficult, if not impossible, to locate faults manually after being detected. That is why the researchers turned their attention to develop different approaches to detect and locate faults in wiring networks. In EMC, as the faults may modify the EMC properties of any system, fault detection and location in wires have occupied a wide area in EMC studies [87–89]. In what follows, we will give the main lines of the many different methods developed to detect and locate electrical faults in wiring networks. This section will review the reflectometry-based and the time-reversal imaging techniques, but it is worth mentioning that other nonreflectometry-based approaches, such as the visual inspection,

radiographic inspections, capacitive and inductive methods, etc. also exist. Related results may be found in [89–92], where the authors pointed out the limitations of these methods, such as the need for complete access to the network, treatment of only one fault nature (either soft or hard and not both), failure with complex networks, or cable disconnection from the network, etc.

1.2.1 Reflectometry-based techniques

Reflectometry is a high-frequency technique of investigation that has triggered the interest of scientists in diverse applications, such as radar systems, where it has been extensively used to detect and measure the distance to a target (see Figure 1.8). The reflectometry concept consists of sending a signal into the system to be diagnosed; this signal propagates in the medium, where a portion of its energy returns back to the injection point once it hits an obstacle. The reflected signal analyzed to the incident one carries information about the system and the encountered obstacle.

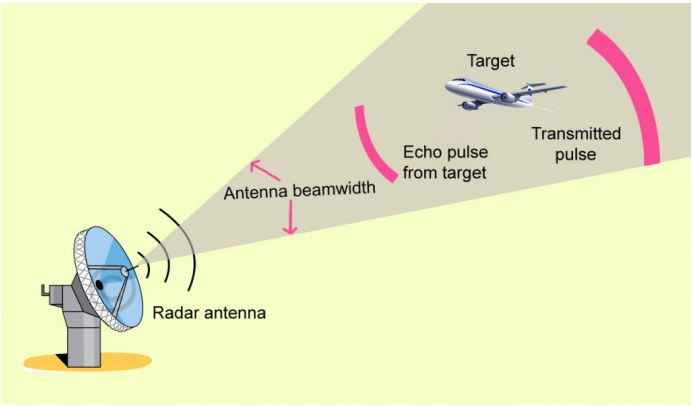

Figure 1.8: *Reflectometry principle in radar systems [source].*

While numerous wiring diagnosis methods have been developed, reflectometry-based techniques are still in the center stage of research and applications to solve transmission lines problems. Similar to the three-dimensional reflectometry, the reflectometry principle in wires is described as follows: a high-frequency voltage signal V_{inc} is sent down the wire, where it propagates, reflects due to the impedance discontinuities (faults), and returns back to the point of incidence. Denoting by V_{ref} the reflected voltage

signal, the reflection is measured by the voltage reflection coefficient

$$\Gamma = \frac{V_{\mathrm{ref}}}{V_{\mathrm{inc}}} = \frac{Z_{\mathrm{L}} - Z_{\mathrm{C}}}{Z_{\mathrm{L}} + Z_{\mathrm{C}}}, \tag{1.13}$$

where Z_{C} is the characteristic impedance of the line and Z_{L} is the impedance of the fault. The reflection coefficient lies in $[-1, 1]$ such that -1 is the reflection coefficient for a short circuit, whereas 1 is the reflection coefficient for an open circuit. Multiplying the measured time delay between V_{inc} and V_{ref} by the velocity of propagation indicates the distance to the fault from the point of incidence. The larger the reflection coefficient, the easier it is to distinguish between the fault reflectometry signature and the noise. Accordingly, open or short circuits may be observed by the reflectometry, while soft anomalies may not [29, 93].

In the context of detecting and locating faults in wires, the reflectometry-based methods are divided into two main categories: Time-Domain Reflectometry (TDR) and Frequency-Domain Reflectometry (FDR). The TDR methods use a short rise time voltage step or pulse as the incident signal and rely on the analysis of the reflected signal in the TD [94–97], whereas the FDR methods use stepped frequency sine waves to measure their frequency, magnitude, and phase in order to find the distance to a fault [98–100]. The different reflectometry methods differ in the form of the injected signal or in the post-processing techniques used to extract information from the reflected signal.

The TDR methods are more expensive than the FDR methods; however, they are simpler to implement with higher noise immunity. Both TDR and FDR techniques show limitations in locating soft faults since the amplitudes of the signal reflected when reaching these faults are low enough and may be comparable to the noise level. The complication arises when attenuations are introduced to the problem as they lower the amplitudes of the reflected signal traveling toward the point of incidence. Add to that, reflectometry-based techniques are well suited for single cable configurations and not for complex ones since the reflections and re-reflections resulting from the junctions, discontinuities, mismatched loads, etc., mask the echoes of the faults. Although recent studies combine the reflectometry-based technique with neural networks and genetic algorithms to detect, locate and characterize multiple

soft faults in complex networks, they also present some limitations, such as requiring prior knowledge of the network's topology and the massive computational time for training the neural network [101]. We point out the necessity to repeat the training once the network undergoes any modification. Then, to address the soft faults in complex networks, the time-reversal imaging techniques were introduced.

1.2.2 Time-reversal imaging techniques

The methods used in imaging scatterers in generic media may be adapted to guided wave propagation analysis in wiring networks. Assume that we define N test ports on the network, the time-reversal imaging for wiring networks relies on finding a differential scattering matrix $\mathbf{S}$ to compute the Time-Reversal Operator (TRO) $\mathbf{K} = \mathbf{S}\mathbf{S}^{\dagger}$, such that $\dagger$ is the Hermitian transpose. The scattering matrix (also called baselined scattering matrix) $\mathbf{S}$ is the difference between the scattering matrices of the healthy and faulty systems. The importance of baselining is to remove all the common echoes (connectors, junctions, etc.) between the healthy and faulty networks and keep only the echoes resulting from the potential faults [102]. As the last step, the nonnegligible eigenvalues computed by the eigenvalue decomposition of $\mathbf{K}$ gives the number of faults that appeared in the system.

After detecting the number of faults in the network, studies focused on the analysis of the TRO to specify their location. The decomposition of the time-reversal operator (DORT) (the French acronym of *Décomposition de l'Opérateur de Retournement Temporel*) method was first transposed to transmission lines in [103]. Although DORT technique shows to be efficient at locating the most severe fault existing in the wiring system, Kafal *et al.* highlighted its inability to resolve multiple faults separately due to their strong coupling *via* guided wave propagation [104]. For this reason, they improved the DORT method to an enhanced version- called Enhanced DORT (EDORT)- in order to locate multiple soft faults in complex networks [104, 105]. To better specify the fault location, the Time-Reversal MUltiple SIgnal Classification (TR-MUSIC) was used to locate faults with submillimeter precision [106]. TR-MUSIC is an efficient single-frequency fault-detection technique capable of locating single or multiple soft faults in complex networks. In [107], it was shown that the quality of MUSIC

processing starts to degrade with noisy data. Unfortunately, in real-life systems, the associated equipment is always subjected to natural noise or signals, which may degrade the MUSIC processing quality. To overcome this limitation, the authors in [108] have proposed an alternative multifrequency TR-MUSIC processing to locate soft faults accurately despite the presence of the noise.

Both EDORT and TR-MUSIC see the network as a black box during the whole process, where the interventions occur only at the N extremities. These techniques showed their ability to locate soft faults in complex networks and were experimentally validated in the cited references above. Nevertheless, the set of N extremities may frequently be located in hard-to-access areas making it difficult to construct the parameters of $\mathbf{S}$. Furthermore, EDORT and TR-MUSIC may only address problems to locate soft faults and not hard ones as opposed to reflectometry-based techniques.

Yet, wire diagnosis methods still raise the following questions:

- How could they locate identical or ambiguous faults in symmetric networks in the absence of information about their configurations and characteristics?
- How do they perform when multiple soft and hard faults simultaneously appear in networks?
- How could their performance be affected in the presence of losses, dispersion, or an entire corroded cable?
- Are they still applicable in networks behaving nonlinearly?
- What is the advantage of detecting and locating faults inaccessible to maintenance processes?

In the following chapters, we will introduce a novel temporal paradigm to deal with electrical faults in wiring networks called the *software correction* process. We will give its detailed definition and show its applicability along with the limitations it witnesses in linear and nonlinear media. In fact, the software correction is an alternative process for locating faults in wiring networks and does not raise any of the above controversial questions for wire diagnosis.

As our work lies entirely in the TD, it seems essential to recall the time-dependent equations of electromagnetic wave propagation. In free space environments, we describe Maxwell's equations that govern the behavior of electromagnetic fields in three-dimensional media. However, in wiring networks, we review the telegrapher's equations that describe the propagation of voltage and current in wiring networks. Equally important, we also describe the numerical method used to numerically solve Maxwell's and the telegrapher's equations as well as the considered boundary and stability conditions.

1.3 Settings: Electromagnetic Wave Propagation

1.3.1 Maxwell's equations

J. C. Maxwell's equations are a set of coupled partial differential equations that form the base of classical electromagnetism governing the evolution of electric and magnetic fields in a domain of interest. In fact, the charge and the current density, together with the electromagnetic field, determine the electromagnetic phenomena in any medium. At a space point $\mathbf{r} \in \mathbb{R}^3$ and an instant of time t, the electromagnetic field is determined by four-vector fields, namely: the electric field $\mathbf{E} = \mathbf{E}(\mathbf{r}, t)$ (in $\mathrm{V/m}$), the magnetic field $\mathbf{H} = \mathbf{H}(\mathbf{r}, t)$ (in $\mathrm{A/m}$), the electric flux density $\mathbf{D} = \mathbf{D}(\mathbf{r}, t)$ (in $\mathrm{C/m^2}$), and the magnetic flux density $\mathbf{B} = \mathbf{B}(\mathbf{r}, t)$ (in T). Maxwell's equations may be divided into four laws

- Faraday's law:
$$\nabla \times \mathbf{E} + \frac{\partial \mathbf{B}}{\partial t} = 0, \tag{1.14}$$
- Ampère's law:
$$\nabla \times \mathbf{H} - \frac{\partial \mathbf{D}}{\partial t} = \mathbf{J}, \tag{1.15}$$
- Gauss's law:
$$\nabla \cdot \mathbf{D} = \rho, \tag{1.16}$$
- and Gauss's law for magnetism:
$$\nabla \cdot \mathbf{B} = 0. \tag{1.17}$$

The charge density ρ (in $\mathrm{C/m^3}$) and the electric current density $\mathbf{J}$ (in $\mathrm{A/m^2}$) are linked by

$$\nabla \cdot \mathbf{J} + \frac{\partial \rho}{\partial t} = 0. \tag{1.18}$$

Constitutive laws link the fields and the flux densities; likewise, Ohm's law correlates the current density and the electric field. A linear medium is characterized by the three functions $\varepsilon = \varepsilon(\mathbf{r})$, $\mu = \mu(\mathbf{r})$, and $\sigma = \sigma(\mathbf{r})$ representing the local electric permittivity (in $\mathrm{F/m}$), magnetic permeability (in $\mathrm{H/m}$), and electric conductivity (in $\mathrm{S/m}$) of the medium, respectively, and defined as follows:

$$\mathbf{D} = \varepsilon \mathbf{E}, \tag{1.19}$$

$$\mathbf{B} = \mu \mathbf{H}, \tag{1.20}$$

$$\mathbf{J} = \sigma \mathbf{E}. \tag{1.21}$$

Substituting equations (1.19) and (1.21) in (1.15) gives

$$\nabla \times \mathbf{H} = \sigma \mathbf{E} + \varepsilon \frac{\partial \mathbf{E}}{\partial t}, \tag{1.22}$$

where $\varepsilon \frac{\partial \mathbf{E}}{\partial t}$ is called the displacement current density. After combining equations (1.14) and (1.22), we obtain the following propagation equations of the fields $\mathbf{E}$ and $\mathbf{H}$ in a linear medium:

$$\Delta \mathbf{E} - \mu\varepsilon \frac{\partial^2 \mathbf{E}}{\partial t^2} = \mu \frac{\partial \mathbf{J}}{\partial t} + \frac{1}{\varepsilon} \nabla \rho, \tag{1.23}$$

$$\Delta \mathbf{H} - \mu\varepsilon \frac{\partial^2 \mathbf{H}}{\partial t^2} = -\nabla \cdot \mathbf{J}. \tag{1.24}$$

The equations (1.23) and (1.24) are usually solved numerically and not analytically in most cases. Doing so, various solvers were developed, such as the finite-difference time-domain [109, 110], discontinuous Galerkin [111–113], finite volume [114, 115], etc. In this dissertation, we use the finite-difference time-domain scheme to solve the propagation equations.

Finite-difference time-domain scheme

The Finite-Difference Time-Domain (FDTD) is an efficient method for solving Maxwell's equations numerically. This method makes it possible to take into account the phenomena of propagation and interaction of electromagnetic waves in complex homogeneous or inhomogeneous environments in the presence or absence of conductive and/or dielectric scatterers.

Assume that any vector in $\mathbb{R}^3$ is written as $\mathbf{U} = (U_x, U_y, U_z)$. In a Cartesian coordinate system, Maxwell's equations (1.14) and (1.22) are equivalent to the following system of scalar equations:

$$\begin{cases} \dfrac{\partial B_x}{\partial t} = \dfrac{\partial E_y}{\partial z} - \dfrac{\partial E_z}{\partial y}, \\ \dfrac{\partial B_y}{\partial t} = \dfrac{\partial E_z}{\partial x} - \dfrac{\partial E_x}{\partial z}, \\ \dfrac{\partial B_z}{\partial t} = \dfrac{\partial E_x}{\partial y} - \dfrac{\partial E_y}{\partial x}, \\ \dfrac{\partial D_x}{\partial t} = \dfrac{\partial H_z}{\partial y} - \dfrac{\partial H_y}{\partial z} - J_x, \\ \dfrac{\partial D_y}{\partial t} = \dfrac{\partial H_x}{\partial z} - \dfrac{\partial H_z}{\partial x} - J_y, \\ \dfrac{\partial D_z}{\partial t} = \dfrac{\partial H_y}{\partial x} - \dfrac{\partial H_x}{\partial y} - J_z. \end{cases} \tag{1.25}$$

Denote by Δx, Δy and Δz the space steps in the x, y and z-directions, respectively. Any triplet $(i, j, k) \in \mathbb{N}^3$ corresponds to a grid point of the space $(i\Delta x, j\Delta y, k\Delta z)$ in the orthonormal system $(Oxyz)$. For the sake of simplicity, we will use the notation $\mathbf{U}(\mathbf{r}, t) = \mathbf{U}[(i\Delta x, j\Delta y, k\Delta z); n\Delta t] = \mathbf{U}^n(i, j, k)$, where Δt is the time step of discretizaion.

The system (1.25) is solved numerically using an explicit scheme of time and space, such as the FDTD. Based on Taylor's finite expansion, K. S. Yee in [110] evaluated the derivatives by the central finite difference approxima-

tions below

$$\frac{\partial \mathbf{U}^n(i,j,k)}{\partial t} = \frac{\mathbf{U}^{n+\frac{1}{2}}(i,j,k) - \mathbf{U}^{n-\frac{1}{2}}(i,j,k)}{\Delta t} + \mathcal{O}\left(\Delta t^2\right), \tag{1.26}$$

$$\frac{\partial \mathbf{U}^n(i,j,k)}{\partial x} = \frac{\mathbf{U}^n(i+\frac{1}{2},j,k) - \mathbf{U}^n(i-\frac{1}{2},j,k)}{\Delta x} + \mathcal{O}\left(\Delta x^2\right). \tag{1.27}$$

This scheme is a second-order scheme of time and space. The components of $\mathbf{E}$ and $\mathbf{H}$ are shown in the schematic Figure 1.9 for a single cubic grid voxel or the so-called Yee's lattice.

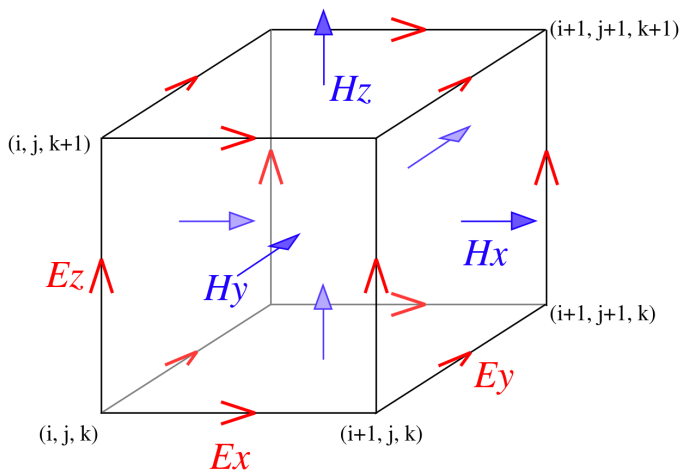

Figure 1.9: *Yee's lattice [source].*

The $\mathbf{E}$-components are in the middle of the edges of the lattice, whereas the $\mathbf{H}$-components are in the center of the faces. All the components are computed according to a Leapfrog scheme at time intervals separated by $\frac{1}{2}\Delta t$. That is to say, if the $\mathbf{E}$-components are computed at the instants $n\Delta t$, the $\mathbf{H}$-components are then computed at the instants $\left(n+\frac{1}{2}\right)\Delta t$. Actually, the finite difference equations for the first three equations of system (1.25) may

be similarly constructed. As an example, we write for the first equation

$$\frac{B_x^{n+\frac{1}{2}}\left(i,j+\frac{1}{2},k+\frac{1}{2}\right)-B_x^{n-\frac{1}{2}}\left(i,j+\frac{1}{2},k+\frac{1}{2}\right)}{\Delta t}=\frac{E_y^n\left(i,j+\frac{1}{2},k+1\right)}{\Delta z}-\frac{E_y^n\left(i,j+\frac{1}{2},k\right)}{\Delta z}-\frac{E_z^n\left(i,j+1,k+\frac{1}{2}\right)-E_z^n\left(i,j,k+\frac{1}{2}\right)}{\Delta y}. \tag{1.28}$$

For the fourth equation of the system (1.25), the finite difference equation is

$$\frac{D_x^n\left(i+\frac{1}{2},j,k\right)-D_x^{n-1}\left(i+\frac{1}{2},j,k\right)}{\Delta t}=\frac{H_z^{n-\frac{1}{2}}\left(i+\frac{1}{2},j+\frac{1}{2},k\right)}{\Delta y}-\frac{H_z^{n-\frac{1}{2}}\left(i+\frac{1}{2},j-\frac{1}{2},k\right)}{\Delta y}-\frac{H_y^{n-\frac{1}{2}}\left(i+\frac{1}{2},j,k+\frac{1}{2}\right)-H_y^{n-\frac{1}{2}}\left(i+\frac{1}{2},j,k-\frac{1}{2}\right)}{\Delta z}+J_x^{n-\frac{1}{2}}\left(i+\frac{1}{2},j,k\right), \tag{1.29}$$

and the finite difference equations for the last two equations of system (1.25) are constructed in the same way as the equation (1.29).

Stability conditions

Because of its explicit nature, the FDTD method requires a stability condition. For computational stability, it is necessary to satisfy a relation between the time and space steps called Courant-Friedrichs-Lewy (CFL) condition that states

$$\Delta t \leq \frac{1}{c\sqrt{\frac{1}{\Delta x^2}+\frac{1}{\Delta y^2}+\frac{1}{\Delta z^2}}}, \tag{1.30}$$

where c is the speed of the wave propagation in the considered medium.

Despite the existence of many improved FDTD versions, such as the unconditional stable FDTD [116–122], conformal FDTD [123–125], etc., we use the basic FDTD scheme developed in *Matlab* within the EMC group to illustrate all the numerical methods and their applications described in this thesis.

Boundary conditions

Boundary conditions control the behavior of electromagnetic waves at the frontier of the domain of interest. One of the most common boundary conditions used in EMC is the Perfect Electric Conductor (PEC), which encloses the electromagnetic waves in the domain and causes their total reflection once reaching the boundary. In our work, the PEC condition takes the form

$$\begin{cases} \mathbf{n} \times \mathbf{E} = \mathbf{0}, \\ \mathbf{H} \cdot \mathbf{n} = 0, \end{cases} \tag{1.31}$$

where $\mathbf{n}$ is the outward normal unit vector to the boundary.

Another boundary condition type is the Absorbing Boundary Condition (ABC) that absorbs the waves as soon as they reach the border of the domain, preventing any type of reflection. In this thesis, we use the Mur ABC to simulate the free space environment [126]. Mur's technique adds multiplying coefficients to the borders of the domain to cancel the reflected waves and, therefore, simulate the free space environment. The performance of this condition is relatively modest (spurious reflected waves); however, it is still simple to implement. Also, we point to the existence of more recent boundary conditions methods, such as the perfect-matched layer [127]; nevertheless, Mur's technique remains adequate as long as the methods used/developed in this work function properly.

1.3.2 Telegrapher's equations

The emergence of electrical operations has geared the indispensable use of electrical cables in nearly all modern systems. Electrical cables are extensively used nowadays for the functioning of most systems and devices by transferring necessary information (power, signals, commands, etc.) to their destinations to guarantee the normal functioning and optimal performance of the system.

Simple time-domain wiring models may be implemented in three-dimensional codes, such as Richard Holland's thin wiring model [128]. The associated equations of each model may be discretized either by the finite difference or finite volume [114] schemes. More sophisticated

transmission-line models may be considered, but combining them with three-dimensional codes is complex as they mainly deal with wired problems. In the context of our work, we consider, the simplest case of Transmission Lines (TLs) without spatial coupling. The objective is to illustrate the relevance of the numerical methods used/developed in guided wave propagation.

The formalism of the TLs is based on the computation of the Transverse ElectroMagnetic (TEM) wave propagation modes. More precisely, it is based on the computation of the quasi-TEM mode of the waves along wires. That is to say, the electromagnetic fields, modeled by this approach, are all restricted to directions normal to the direction of propagation. This assumption implies that the transverse dimensions of the cables are small compared to the wavelength. The unknowns of the electromagnetic field $\mathbf{E}$ and $\mathbf{H}$ are then replaced by the more intuitive notions in the case of TLs: the voltage V and the current I. The numerical study is then carried out on the evolution of these quantities as a function of time and their curvilinear abscissas.

At high frequencies, a single TL may be modeled by four parameters that form the distributed-element model [129]. The propagation and coupling phenomena are represented by the distributed components: the inductance L and the capacity C, whereas the losses phenomena are represented by the resistance R and the conductance G. The length of each elementary component (a short segment of the TL) is denoted by Δz and supposed to be small enough with respect to the emitted wave wavelength. The four parameters of the distributed-element model called the primary line constants, rule the behavior of a TL at high frequencies. In general, they depend on the frequency; however, in the context of our work, the primary line constants are considered frequency-independent. We note that the two-conductor line model in Figure 1.10 extends to multiwire lines without any difficulties [130].

We apply Kirchhoff law on V and I of the circuit of Figure 1.10 to obtain the differential equations that describe their instantaneous evolution in the TL

$$\frac{\partial V}{\partial z} + L\frac{\partial I}{\partial t} + R \times I = 0, \tag{1.32}$$

$$\frac{\partial I}{\partial z} + C\frac{\partial V}{\partial t} + G \times V = 0, \tag{1.33}$$

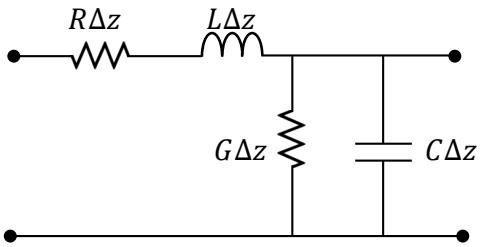

Figure 1.10: *Schematic representation of the elementary component of a transmission line.*

where $V = V(z,t)$ [resp. $I = I(z,t)$] is the voltage (resp. current) at a position z and an instant t. After combining the two equations (1.32) and (1.33), we obtain the telegrapher's equations

$$\frac{\partial^2 V}{\partial z^2} = LC\frac{\partial^2 V}{\partial t^2} + (RC + LG)\frac{\partial V}{\partial t} + RGV, \tag{1.34}$$

$$\frac{\partial^2 I}{\partial z^2} = LC\frac{\partial^2 I}{\partial t^2} + (RC + LG)\frac{\partial I}{\partial t} + RGI. \tag{1.35}$$

The equations (1.34) and (1.35) have been solved using many analytical and numerical methods. In the next section, we use the one-dimensional FDTD scheme to solve the telegrapher's equations in the TD numerically.

One-dimensional FDTD scheme

By keeping the same notation for the space and time steps as in Section 1.3.1, we denote by $V^n(k)$ [resp. $I = I^n(k)$] the voltage (resp. current) at a point $k\Delta z$ and an instant $n\Delta t$. Here, as for the fields $\mathbf{E}$ and $\mathbf{H}$ of Maxwell's equations, V and I are defined according to a grid of points in time and space. Then, Taylor's finite expansion is used again to write the equations (1.32)

and (1.33) as follows:

$$V^{n+1}(k) = -\frac{2\Delta t}{(G\Delta t + 2C)\Delta z}\left[I^{n+\frac{1}{2}}(k) - I^{n+\frac{1}{2}}(k-1)\right] - \frac{G\Delta t - 2C}{G\Delta t + 2C}V^{n}(k), \tag{1.36}$$

$$I^{n+\frac{1}{2}}(k) = -\frac{2\Delta t}{(R\Delta t + 2L)\Delta z}\left[V^{n}(k+1) - V^{n}(k)\right] - \frac{R\Delta t - 2L}{R\Delta t + 2L}I^{n-\frac{1}{2}}(k). \tag{1.37}$$

Stability conditions

As in three dimensions, Δt and Δz must satisfy a stability criterion given by

$$\Delta t \leq \frac{\Delta z}{c}. \tag{1.38}$$

The numerical tools used in this thesis have been presented and will be used in all the simulations and applications illustrated in the next chapters.

1.4 Conclusion

In this chapter, an overview of different methods developed earlier to identify electromagnetic sources in both the frequency-domain and time-domain analysis was presented. The proper functioning along with the limitations of each method were described. Then, we compared the facilities provided by the time-domain analysis to that of the frequency-domain analysis and showed the importance of identifying electromagnetic sources in the time domain rather than the frequency domain. In another section, as dealing with faulty wiring networks is an essential part of this thesis, we presented the main well-known methods to detect, locate, and diagnose electrical faults in wiring networks, especially the reflectometry-based and time-reversal imaging techniques. Although they show excellent performances to locate faults, the proper functioning of each technique is confined to specific nature of the detected faults, whether hard or soft. Each section was ended by a set of unanswered or partially answered questions about the applicability and the functioning of the existing methods. Different techniques will be proposed in the upcoming chapters to overcome these questions in linear and

nonlinear media.

Finally, we presented all the necessary tools employed during this thesis. We recalled the time-dependent Maxwell's and telegrapher's equations that govern the propagation of electromagnetic fields in free space environments or voltage/current in wiring networks. We also described the finite-difference time-domain solver used throughout all our numerical simulations to solve Maxwell's and the telegrapher's equations numerically.

2

Source Identification in Linear Systems: The LCCF Method

In this chapter, we present the Linear Combination of Configuration Field (LCCF) method that provides a way to identify the temporal profile of an electromagnetic source satisfying particular properties for a given target (field, voltage, or current) in a linear medium. At first, we present the theoretical part of the method and show how one could control an electromagnetic field at a single spatial point over a time interval. Then, we run numerical simulations in lossless and lossy wiring networks as well as anechoic and reverberant three-dimensional environments to illustrate the applicability of the LCCF method.

As shaping electromagnetic fields is a common task for the Time-Reversal (TR) and the LCCF techniques, both methods are compared to show the superiority of the LCCF over the TR. Mathematically, the LCCF may always compute a source, if it exists; however, this source may not physically be satisfying due to some physical inconveniences. For this reason, constraints are added to the LCCF problem to improve the physical properties of the source. In the last section, we address a useful application of the constrained LCCF method to replace an undesired field by a desired one. Finally, we conclude this chapter and open the horizons to improve and generalize the LCCF technique and consequently widen its applications in the next chapter.

2.1 LCCF Concept

Let $[0, t_n]$ be the time interval during which a signal is emitted and received, where $t_n = n\Delta t > 0$ $(n \in \mathbb{N}^*)$ is the last instant of time to be specified. For all $t \in [0, t_n]$, the source generator G emits a discrete signal $\mathbf{x} = [x(0), x(1), \cdots, x(n)] \in \mathbb{R}^{n+1}$ that propagates, interferes, and may be distorted due to discontinuities and inhomogeneities in the linear medium Ω. A receiver R, placed at a fixed point called the *receiver point*, records the detected discrete signal $\mathbf{y} = [y(0), y(1), \cdots, y(n)] \in \mathbb{R}^{n+1}$ over $[0, t_n]$.

Assume that we want to identify $\mathbf{x}$ that controls $\mathbf{y}$ at an instant of time t_q. Controlling $\mathbf{y}$ at t_q means to impose a predefined target field F at t_q, i.e., $y(q) = F$. For physical considerations, $t_q \gg 0$; t_q may be any instant of time after R starts to detect signals. The process to impose F is detailed as follows:

- In Ω, we inject the unit impulse (also called the standard basis vector) $\mathbf{e}_1 = [1, 0, \cdots, 0]$ at $t_0 = 0$ by G. At the R-level, the scalar value of the impulse response $\mathbf{h}_1$ at t_q is recorded and denoted by $h_1(q)$.
- Similarly, we inject the same impulse as before, but delayed by one step of time $(t_0 + \Delta t)$, i.e., $\mathbf{e}_2 = [0, 1, 0, \cdots, 0]$. Then, the second scalar value of the impulse response $\mathbf{h}_2$ is recorded at t_q and denoted by $h_2(q)$.

  $\vdots$
- Similarly, we inject the same impulse as before, but delayed by n steps of time $(t_0 + n\Delta t)$, i.e., $\mathbf{e}_{n+1} = [0, \cdots, 0, 1]$. Then, the $(n+1)$th scalar value of the impulse response $\mathbf{h}_{n+1}$ is recorded at t_q and denoted by $h_{n+1}(q)$.
- Finally, due to the linearity of the time-invariant system, injecting the impulses $\mathbf{e}_1, \mathbf{e}_2, \cdots, \mathbf{e}_{n+1}$ simultaneously $(\mathbf{e}_1 + \mathbf{e}_2 + \cdots + \mathbf{e}_{n+1})$ produce the sum of the impulse responses $h_1(q) + h_2(q) + \cdots + h_{n+1}(q)$ previously obtained at t_q.

The problem to be solved is represented in an *inverse* form. We generate a target scalar field F at t_q from a linear combination of

the fields $h_1(q), h_2(q), \cdots, h_{n+1}(q)$ recorded after injecting the impulses at different instants of time separated by Δt. In other words, we look for unknown scalars $\lambda_0, \cdots, \lambda_n$ that satisfy the linear relation $F = \lambda_0 \cdot h_1(q) + \cdots + \lambda_n \cdot h_{n+1}(q)$. Assume that $\lambda_0, \cdots, \lambda_n$ exist, then the quantity F may be obtained after the emission of a source $\mathbf{x} = \lambda_0 \cdot \mathbf{e}_1 + \cdots + \lambda_n \cdot \mathbf{e}_{n+1}$. This implies that the scalars $\lambda_0, \cdots, \lambda_n$ are the components of $\mathbf{x}$, i.e., $x(0) = \lambda_0, \cdots, x(n) = \lambda_n$. Hence, we write

$$F = \begin{bmatrix} h_1(q) & h_2(q) & \cdots & h_{n+1}(q) \end{bmatrix} \begin{pmatrix} x(0) \\ x(1) \\ \vdots \\ x(n) \end{pmatrix}. \tag{2.1}$$

The linear combination of equation (2.1) is not unique as different amplitude superimposition scenarios may be built to produce the target F. To demonstrate the nonuniqueness of the solution, we consider this simple counterexample: given the impulse responses $h_1(q) = h_2(q) = 1$ and $h_3(q) = -1$, suppose that the desired target amplitude at t_q is $F = 2$, then different solutions for $\mathbf{x}$ may be $(0, 1, -1)$ or $(2, 0, 0)$. As a result, source $\mathbf{x}$ is not unique.

In a linear medium, identifying a source to create a scalar field at an instant t_q seems easy and trivial. On the other hand, if the objective is to create a field at an interval of time and not only an instant, the problem becomes more complicated. Recently, a new approach called the LCCF method was designed to impose a predefined field over a given duration of time. We first start by describing the settings of the problem, then give a detailed formulation of the LCCF method.

2.1.1 Basic LCCF method

In [131, 132], the authors introduced a novel technique called the Linear Combination of Configuration Field (LCCF) to identify the temporal source that would shape electromagnetic fields in any linear medium at an interval of time. This time interval is called the *target time* and denoted by $[t_q, t_f] = [q\Delta t, f\Delta t] \subseteq [0, t_n]$, $(q, f) \in \mathbb{N}^* \times \mathbb{N}^*$. To understand the concept of the LCCF method, we consider its schematic setup represented

below in Figure 2.1.

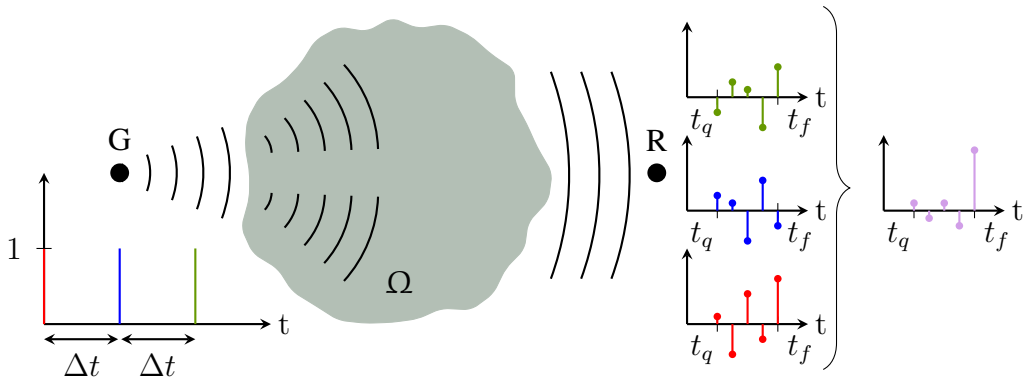

Figure 2.1: *LCCF concept: the desired field is a linear combination of the impulse responses obtained over the target time* $[t_q, t_f]$.

We endeavor to find a source $\mathbf{x}$ that imposes a target field $\mathbf{F} = (F_0, \cdots, F_{f-q})$ over $[t_q, t_f]$, i.e., $\mathbf{y}_{/[t_q,t_f]} = \mathbf{F}$, where $\mathbf{y}_{/[t_q,t_f]} = [y(q), \cdots, y(f)]$ are the amplitudes of $\mathbf{y}$ over $[t_q, t_f]$. Based on the interpretation given to yield equation (2.1), similar justifications can be considered to compute $\mathbf{x}$, the solution of the following system of equations:

$$\begin{cases} F_0 = x(0) \cdot h_1(q) + x(1) \cdot h_2(q) + \cdots + x(n) \cdot h_{n+1}(q), \\ F_1 = x(0) \cdot h_1(q+1) + x(1) \cdot h_2(q+1) + \cdots + x(n) \cdot h_{n+1}(q+1), \\ \quad \vdots \\ F_{f-q} = x(0) \cdot h_1(f) + x(1) \cdot h_2(f) + \cdots + x(n) \cdot h_{n+1}(f). \end{cases} \tag{2.2}$$

To reduce the dimension of the system (2.2), and consequently the computational costs, the amplitudes $x(f+1), \cdots, x(n)$ of $\mathbf{x}$ emitted at $t \in]t_f, t_n]$ are set to 0. This is due to the fact that $x(f+1), \cdots, x(n)$ hit R at an instant $t > t_f$; thus, they have no impact on $\mathbf{y}$ over $[t_q, t_f]$. To control $\mathbf{y}$ over $[t_q, t_f]$, the longest possible duration to emit $\mathbf{x}$ is $[0, t_f]$, that is to say

$\mathbf{x} = [x(0), \cdots, x(f), 0, \cdots, 0]$. Henceforth, we denote by $\mathbf{x}$ the part of the signal which is not identically zero, i.e., $\mathbf{x} = [x(0), \cdots, x(f)]$. In a matrix form, we write

$$\underbrace{\begin{pmatrix} h_1(q) & h_2(q) & \cdots & h_{f+1}(q) \\ h_1(q+1) & h_2(q+1) & \cdots & h_{f+1}(q+1) \\ \vdots & \vdots & & \vdots \\ h_1(f) & h_2(f) & \cdots & h_{f+1}(f) \end{pmatrix}}_{\mathbf{A} \in \mathbb{M}_{(f-q+1)\times(f+1)}} \begin{pmatrix} x(0) \\ x(1) \\ \vdots \\ x(f) \end{pmatrix} = \begin{pmatrix} F_0 \\ F_1 \\ \vdots \\ F_{f-q} \end{pmatrix} \tag{2.3}$$

$$\iff \mathbf{A}\mathbf{x} = \mathbf{F}.$$

The system (2.3) is called the LCCF linear system. Practically, only one simulation is required to construct $\mathbf{A}$. We emit $\mathbf{e}_1$ by G and record, by means of R, the impulse response $\mathbf{h}_1$ for the entire time interval $[0, t_n]$, referred to as the *configuration field*. The recorded amplitudes $h_1(q), \cdots, h_1(f)$ are set to the first column of $\mathbf{A}$. For $k = \{2, \cdots, f+1\}$, the rest columns $[h_k(q), \cdots, h_k(f)]^T$ are the delay of $[h_1(q), \cdots, h_1(f)]^T$ by $(k-1)$-zeroes, i.e.,

$$\begin{pmatrix} h_k(q) \\ \vdots \\ h_k(f) \end{pmatrix} = \begin{cases} [h_1(q-k+1), \cdots, h_1(f-k+1)]^T & \text{for } 1 \le k \le q+1, \\ [\mathbf{0}_{k-q-1}, h_1(0), \cdots, h_1(f-k+1)]^T & \text{for } q+1 \le k \le f+1, \end{cases}$$

where $\mathbf{0}_{k-q-1}$ is the zero vector of length $k-q-1$. Explicitly, $\mathbf{A}$ may be written as

$$\mathbf{A} = \begin{pmatrix} h_1(q) & h_1(q-1) & \cdots & h_1(0) & 0 & \cdots & 0 \\ \vdots & h_1(q) & & \vdots & h_1(0) & \ddots & \vdots \\ \vdots & \vdots & & \vdots & \vdots & \ddots & 0 \\ h_1(f) & h_1(f-1) & \cdots & h_1(f-q) & h_1(f-q-1) & \cdots & h_1(0) \end{pmatrix}. \tag{2.4}$$

The matrix $\mathbf{A}$ of the LCCF system characterizes the medium between the two fixed G-point and R-point. Actually, the number of rows of $\mathbf{A}$ represents the duration of the target time $[t_q, t_f]$, whereas the number of its columns

represents the duration of the source $\mathbf{x}$. The matrix $\mathbf{A}$ is not square (more columns than rows) and said to be rank-deficient. Thereupon, the system (2.3) may be solved for $\mathbf{x}$ in the least square sense by premultiplying both sides by $\mathbf{A}^T$, the transpose of $\mathbf{A}$. The matrix $\mathbf{A}^T\mathbf{A}$ is ill-conditioned; thus, its inversion $\left(\mathbf{A}^T\mathbf{A}\right)^{-1}$ is numerically unstable due to its large condition number $\kappa(\mathbf{A}^T\mathbf{A})$. A large $\kappa(\mathbf{A}^T\mathbf{A})$ indicates that a small change in the coefficients of $\mathbf{A}$ may lead to larger changes in the output $\mathbf{F}$. To stabilize the new LCCF system, a convenient solution may be to use Moore-Penrose Pseudo-Inverse (MPPI) in order to minimize the norm $\left\|\mathbf{A}^T\mathbf{A}\mathbf{x} - \mathbf{A}^T\mathbf{F}\right\|$ [133]. Among the infinite solutions, MPPI picks a source $\mathbf{x}$ of the smallest norm (lowest possible amplitudes), which seems to be a reasonable choice from an experimental point of view. However, numerical tests have shown that MPPI computes a source of an amplitude order $\mathcal{O}(10^3)$ to create an electric field of an amplitude order $\mathcal{O}(1)$. Alternatively, a better solution would be to regularize the matrix $\mathbf{A}$ using the Tikhonov regularization technique [134], then the system becomes

$$\left(\mathbf{A}^T\mathbf{A} + \epsilon\mathbf{I}\right)\mathbf{x} = \mathbf{A}^T\mathbf{F}, \tag{2.5}$$

where $\mathbf{I}$ is the identity matrix. The Tikhonov parameter $\epsilon > 0$ is heuristically chosen to be small enough so as not to distort the solution. We note that much work has been achieved for designing strategies to find optimal values of ϵ, in certain senses, and solve other problems related to Tikhonov regularization [70], but this is not our objective in this thesis.

Remark: In this chapter, voltage signals are considered for illustrations and applications in wiring networks; however, current signals could be considered in a similar way.

2.1.2 Numerical illustrations in wiring networks

Identifying sources may be applied to any medium, such as wiring networks. In guided wave propagation, we seek to identify the temporal profile of a source that leads to imposing a given target voltage at a point of the network over a predefined target time. For illustration purposes, after describing the network setup, the LCCF process is first applied to a lossless network, then we go one step further to introduce different attenuation levels and show that the LCCF remains applicable.

Problem settings

The considered medium of propagation is an aerial network Ω made up of unshielded two-conductor uniform cables. The topology and characteristics of Ω (number, lengths, impedance, loads of lines, etc.) are chosen arbitrarily. For example, let Ω be the network of Figure 2.2 composed of two nodes and five point-to-point Transmission Lines. Table 2.1 displays their respective number l, length z, characteristic impedance Z_{C}^{l}, and load impedance Z_{L}^{l} for $l \in \{1, ..., 5\}$.

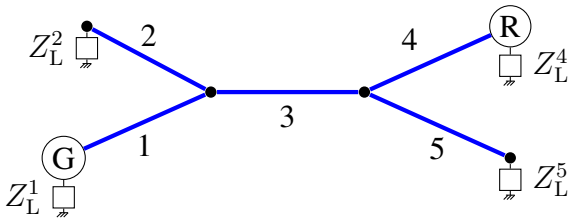

Figure 2.2: *Network configuration.*

Line Nb. l	z (in m)	Z_{C}^{l} (in Ω)	Z_{L}^{l} (in Ω)
1	7	50	50
2	6	50	0
3	7	50	-
4	3	50	50
5	5	50	30

Table 2.1: *Characteristics of the network.*

Considering an RLCG model, a standard one-dimensional FDTD scheme is used to solve the telegrapher's equation (see Chapter 1 Section 1.3.2). The total duration of the simulations is $[0, t_n] = [0, 1422\Delta t]$. The time step $\Delta t = 3.16 \times 10^{-10}\,\mathrm{s}$ and the space step $\Delta z = 0.1\,\mathrm{m}$ are selected in a way that satisfies the stability criterion (1.38).

The generator G and the receiver R are respectively placed at the start node of line 1 and the termination of line 4, knowing that they can still be placed

at any point on the network. Actually, any target time and target signal may be chosen to apply the LCCF method. Here, we choose to impose a Gaussian pulse over the target time $[t_q, t_f] = [500\Delta t, 920\Delta t]$, for example. The Gaussian pulse is denoted by $\mathbf{G}_1$ ($\mathbf{F} = \mathbf{G}_1$) and has maximum amplitude $+1\,\mathrm{V}$. A Gaussian function of maximum amplitude β is denoted by G_β and has the following form:

$$G_\beta(t) = \beta.\exp\left[-\left(\frac{t-t_c}{\sigma}\right)^2\right], \tag{2.6}$$

where t_c is the position of the center of the peak and σ controls the width of $\mathbf{G}_\beta = [G_\beta(0), \cdots, G_\beta(f-q)]$. By taking $t_c = 210\Delta t$ and $\sigma = 20\Delta t$, $\mathbf{G}_1$ is plotted in blue sky in Figure 2.4b. The considered Tikhonov parameter for the LCCF method is $\epsilon = 10^{-9}$.

Lossless network

For the sake of simplicity, assume that no losses are added to the lines of Ω ($R = G = 0$). We apply the LCCF method to identify the signal $\mathbf{x}$ injected by G that propagates in Ω, leading R to record $\mathbf{G}_1$ over $[t_q, t_f]$. Then, we build the characterization matrix $\mathbf{A}$ according to formula (2.4) before solving the simple LCCF linear system

$$\left(\mathbf{A}^T\mathbf{A} + \epsilon\mathbf{I}\right)\mathbf{x} = \mathbf{A}^T\mathbf{G}_1. \tag{2.7}$$

The image of $\mathbf{A}$ represented in Figure 2.3 shows its diagonal constancy, where each of its descending diagonals from left to right remains constant.

We solve system (2.7) and show the computed nontrivial source $\mathbf{x}$ in Figure 2.4a. After its emission, the voltage $\mathbf{y}$ is recorded by R and represented in Figure 2.4b. Obviously, $\mathbf{y}_{/\left[t_q,t_f\right]} = \mathbf{G}_1$ for $t \in [t_q, t_f]$ lying between the two dashed lines in the same figure. We may define the Relative Error (RE) between any target field $\mathbf{F}$ and an obtained field $\mathbf{y}_{/\left[t_q,t_f\right]}$ as

$$\mathrm{RE}\left(\mathbf{F}, \mathbf{y}_{/\left[t_q,t_f\right]}\right) = \frac{\left\|\mathbf{F} - \mathbf{y}_{/\left[t_q,t_f\right]}\right\|_2}{\|\mathbf{F}\|_2}, \tag{2.8}$$

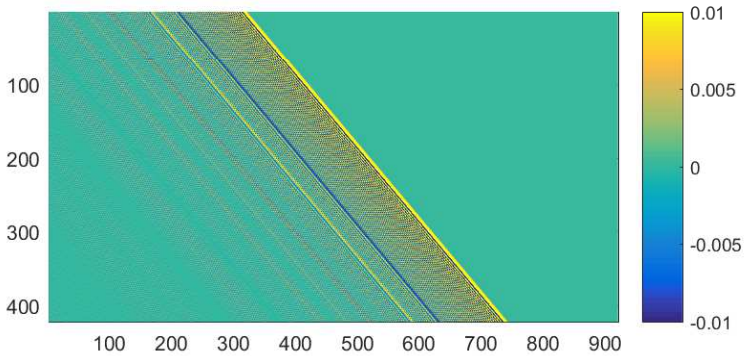

Figure 2.3: *Image of the LCCF characterization matrix* $\mathbf{A}$.

where $\|.\|_2$ is the Euclidean norm. In this example, the relative error between the target voltage $\mathbf{G}_1$ and the obtained voltage $\mathbf{y}_{/\left[t_q,t_f\right]}$ is about RE $= 2.85 \times 10^{-7}$. We point out that the voltage $\mathbf{y}$ is uncontrolled for all $t \in [0, t_n] \setminus [t_q, t_f]$.

Lossy network

Losses in any medium are inevitable in reality; that is why it is vital to show the applicability of the LCCF in the presence of losses. In wiring networks, the signals attenuate while propagating from one point to another, causing amplitude reductions. In this section, we demonstrate the fact that the LCCF method remains efficient when the lines of Ω are resistive ($R \neq 0$) without taking into account the frequency-dependent losses. For the different attenuation levels, we show that the LCCF successfully generates $\mathbf{G}_1$ at the R-point without any additional treatments or excessive computational costs in comparison to the lossless problem illustrated previously. The considered attenuation levels are represented in the first two columns of Table 2.2; the first column indicates the chosen level of attenuation, while the second one shows the amplitude reductions resulting from each level.

For each attenuation level, we characterize Ω by constructing the new LCCF matrix $\mathbf{A}$ based on the new impulse response of the lossy network. Recall that we may not reuse the impulse response of the lossless network as the system has to be re-characterized once it undergoes any modification (losses

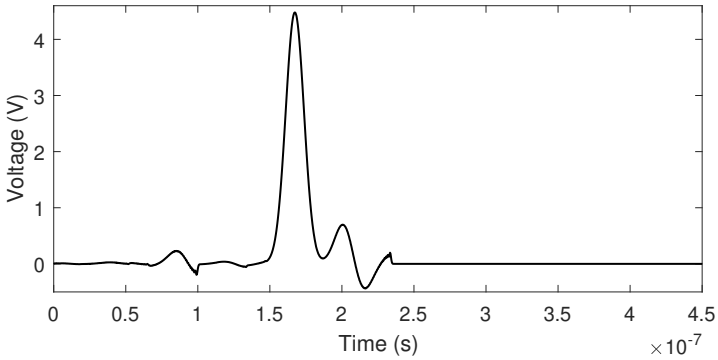

(a) Source $\mathbf{x}$ computed by the LCCF method.

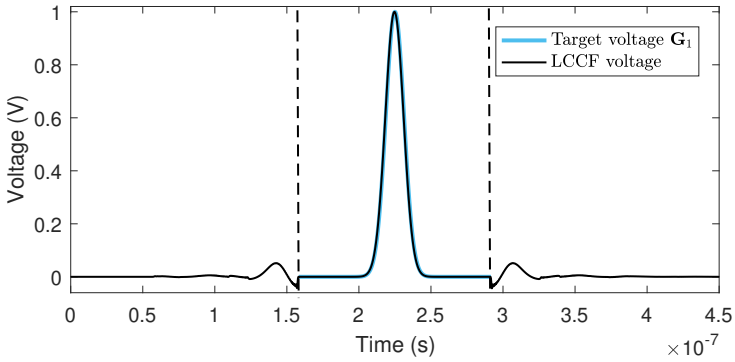

(b) Voltage signal $\mathbf{y}$ recorded after injecting $\mathbf{x}$.

Figure 2.4: *Signal* $\mathbf{x}$ *propagates through the lossless network to control the voltage at the termination of line* 4*. After its emission, the receiver R records the signal* $\mathbf{y}$*, where the desired target voltage* $\mathbf{G}_1$ *is recorded over the target time* $[t_q, t_f] = [1.58 \times 10^{-7}, 2.9 \times 10^{-7}]$ *lying between the two dashed lines.*

in this case). Theoretically, we expect that the LCCF computes sources of the same profile as the source of the lossless problem (Figure 2.4a), but with higher amplitudes relative to the attenuation levels to compensate for the amplitude reductions.

For the lossy problem, the dimension of the LCCF system is equal to the dimension of the system for the lossless problem. In fact, this dimension depends only on the duration of the target time $[t_q, t_f]$ taken the same in both

problems. Therefore, no excessive computational costs or additional treatments are required to apply the LCCF method after introducing losses. The only difference between the lossless and the lossy problems is the need to record different impulse responses. After separate LCCF processes at different attenuation levels, the sources are computed and represented in Figure 2.5a. The receiver R records the output voltage signals represented in Figure 2.5b.

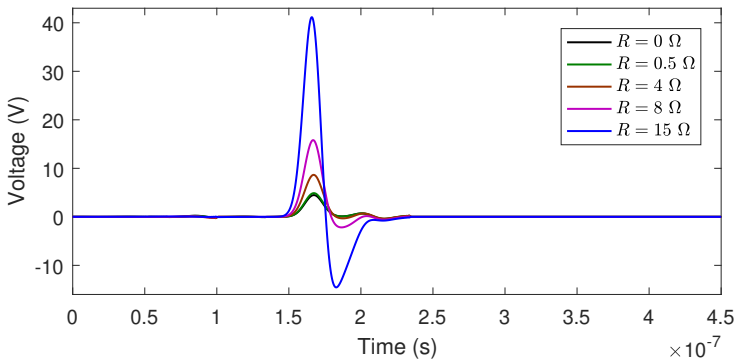

(a) Sources $\mathbf{x}$ computed by the LCCF method at different attenuation levels.

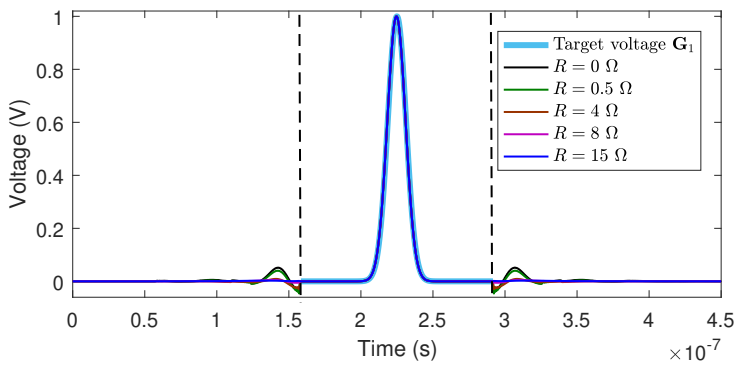

(b) Voltage signals $\mathbf{y}$ recorded after separately injecting the sources $\mathbf{x}$ at different attenuation levels.

Figure 2.5: *After several LCCF processes at different attenuation levels, the signals* $\mathbf{x}$ *separately propagate through the lossy network to control the voltage at the termination of line* 4*. After their emissions, the receiver R records the signals* $\mathbf{y}$*, where the desired target voltage* $\mathbf{G}_1$ *is obtained over the target time* $[t_q, t_f] = [1.58 \times 10^{-7}, 2.9 \times 10^{-7}]$ *lying between the two dashed lines.*

The LCCF processes successfully produce $\mathbf{G}_1$ at the R-point over $[t_q, t_f]$ with the REs represented in the last column of Table 2.2. We note that the dispersion is treated similarly as attenuation, where the LCCF keeps its proper functioning to generate the desired target voltage over the target time.

Resistance (in Ω/m)	Amplitude reductions (in %)	RE $\left(\mathbf{G}_1, \mathbf{y}_{/\left[t_q, t_f\right]}\right)$
0.5	8.53	3.36×10^{-7}
4	50.13	3.74×10^{-7}
8	74.42	2.77×10^{-7}
15	91.66	1.96×10^{-6}

Table 2.2: *Effect of the different attenuation levels on the LCCF method.*

2.1.3 Numerical illustrations in free space environments

The LCCF method may also be applied to free space environments. In free space propagation, we want to identify the temporal behavior of a field source to impose a predefined target field at a spatial point over a target interval of time. In what follows, anechoic and reverberant cavities are considered to show that the LCCF is a general method with the possibility to be applied in any linear medium.

Problem settings

For example, the considered medium is a $5\,\mathrm{cm} \times 4\,\mathrm{cm} \times 3\,\mathrm{cm}$ cavity denoted by Ω and represented in Figure 2.6, where ten scatterers are placed arbitrarily. The FDTD scheme (see Chapter 1 Section 1.3.1) is used to solve Maxwell's equations. The total duration of the simulations is $[0, t_n] = [0, 1422\Delta t]$. The time step $\Delta\mathrm{t} = 3.85 \times 10^{-12}\,\mathrm{s}$ and the space step $(\Delta x, \Delta y, \Delta z) = (0.2\,\mathrm{cm}, 0.2\,\mathrm{cm}, 0.2\,\mathrm{cm})$ are selected in a way that satisfies the stability criterion (1.30). Without loss of generality, any component of the electric $\mathbf{E} = (E_x, E_y, E_z)$ or magnetic $\mathbf{H} = (H_x, H_y, H_z)$ field may be considered to illustrate the LCCF method. Accordingly, we choose the first component of the electric field E_x for this purpose.

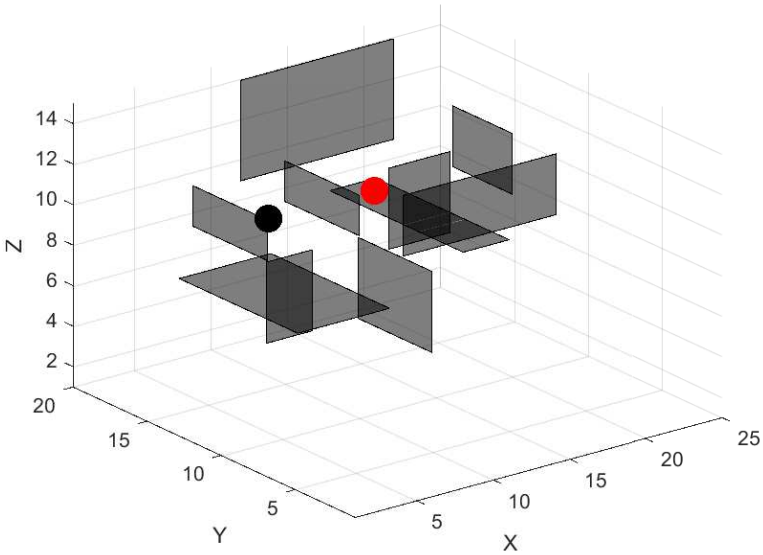

Figure 2.6: *Cavity configuration used in simulations.*

The generator G is placed at $(6\Delta x, 12\Delta y, 11\Delta z)$ (see the black point in Figure 2.6) and the receiver R is placed at $(11\Delta x, 10\Delta y, 12\Delta z)$ (see the red point in Figure 2.6), although they could still be placed at any point in the cavity. For example, the duration of the target time is about 420-time steps, i.e., $[t_q, t_f] = [500\Delta, 920\Delta t]$. The target electric field is chosen to be the Gaussian pulse $\mathbf{G}_1$ (2.6) represented by the blue sky signal in Figure 2.7b. The considered Tikhonov parameter for this problem is $\epsilon = 10^{-12}$.

Anechoic cavity

Firstly, we consider the cavity with absorbent walls. The LCCF method is used to identify the signal $\mathbf{x}$ injected by G that propagates in Ω, leading R to record $\mathbf{G}_1$ over $[t_q, t_f]$. After characterizing the cavity by the impulse response to construct the matrix $\mathbf{A}$, we solve the simple linear system

$$\left(\mathbf{A}^T\mathbf{A} + \epsilon\mathbf{I}\right)\mathbf{x} = \mathbf{A}^T\mathbf{G}_1. \tag{2.9}$$

Figure 2.7a shows the source $\mathbf{x}$ computed by the LCCF method. The source $\mathbf{x}$ is simple but nontrivial as to compensate for the reflections and re-reflections resulting from the scatterers. After its emission, the electric field $\mathbf{y} = \mathbf{E}_x = [E_x(0), \cdots, E_x(n)]$ is recorded by R and represented in Figure 2.7b. Obviously, $\mathbf{y}_{/[t_q,t_f]} = \mathbf{G}_1$ for $t \in [t_q, t_f]$, where $[t_q, t_f]$ lies between the two dashed lines in the same figure. The relative error (2.8) between the target and the obtained electric fields is estimated at RE $= 1.14 \times 10^{-8}$.

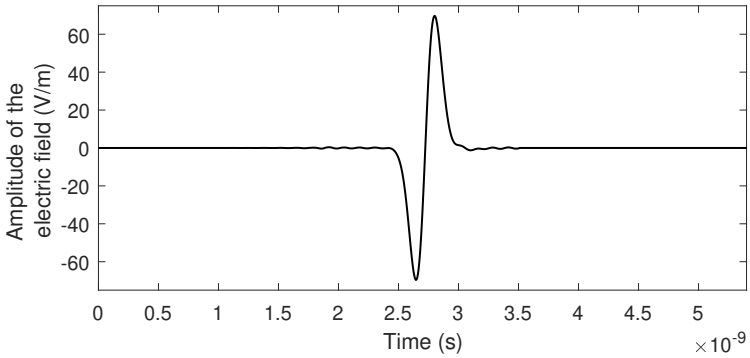

(a) Source $\mathbf{x}$ computed by the LCCF method.

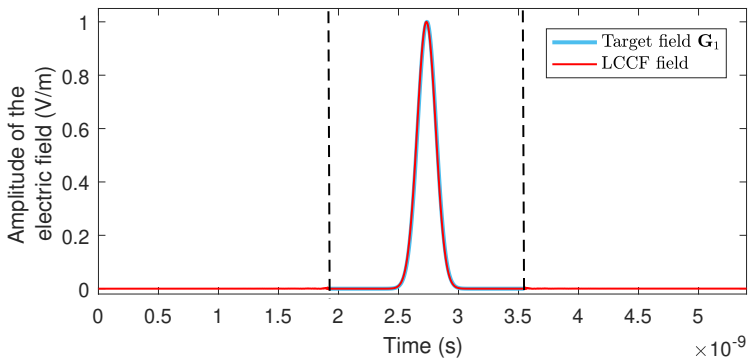

(b) Electric signal $\mathbf{y}$ recorded after injecting $\mathbf{x}$.

Figure 2.7: *Signal* $\mathbf{x}$ *propagates through the anechoic cavity to control the electric field at the receiver point. After its emission, the receiver R records the signal* $\mathbf{y}$*, where the desired target electric field* $\mathbf{G}_1$ *is recorded over the target time* $[t_q, t_f] = [1.92 \times 10^{-9}, 3.54 \times 10^{-9}]$ *lying between the two dashed lines.*

Reverberant cavity

Let Ω be the reverberant cavity where the waves perfectly reflect once reaching its walls. Still, the LCCF efficiently generates the target field $\mathbf{G}_1$ at the R-point without any additional treatments or excessive computational costs compared to the problem of the anechoic cavity. After re-characterizing Ω, the new computed source is represented in Figure 2.8a. The receiver R records the electric signal represented in Figure 2.8b with an RE $= 7.1 \times 10^{-9}$ (2.8). The LCCF, in this case, computes a more complex source to compensate for the reflections resulting from the scatterers and the walls of Ω as well. We note that $\mathbf{y}$ is uncontrolled for all $t \in [0, t_n] \setminus [t_q, t_f]$.

One and three-dimensional examples were illustrated to show that the LCCF method may identify the temporal source to control the voltage/current or field at a point of any linear media. The complexity of the computed sources refers to the occurring multiple reflections and re-reflections. It is also important to highlight that the LCCF is independent of the topology of the studied media: cartography, number or length of lines, characteristic impedance, load impedance in networks, and position of scatterers, environments in cavities. Moreover, the LCCF is independent of the numerical technique used for temporal or spatial discretizations. In fact, the studied system may be viewed as a black box regardless of all the physical phenomena occurring during propagation (attenuation, dispersion, multiple reflections, absorption, etc.). The LCCF relies on nothing else than the impulse response between the source-receiver points.

As a matter of fact, the LCCF performs better in complex media than with simple ones, such as networks composed of a single cable. To better understand the reason behind this kind of performance, we should differentiate between the complex and simple media from an LCCF point of view. This difference lies in the reflections and re-reflections taking place in these media, knowing that in complex media more reflections and re-reflections occur due to junctions and ramifications in wiring networks or scatterers in cavities. After emitting the unit impulse to construct the LCCF matrix $\mathbf{A}$, the LCCF method benefits from these reflections to recover a nonsparse or "rich" impulse response that better characterizes the system. Consequently, a rich impulse response reduces the sparsity of $\mathbf{A}$. From a mathematical point of

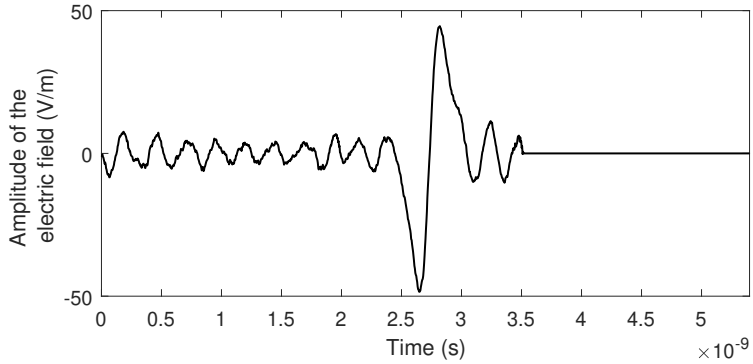

(a) Source $\mathbf{x}$ computed by the LCCF method.

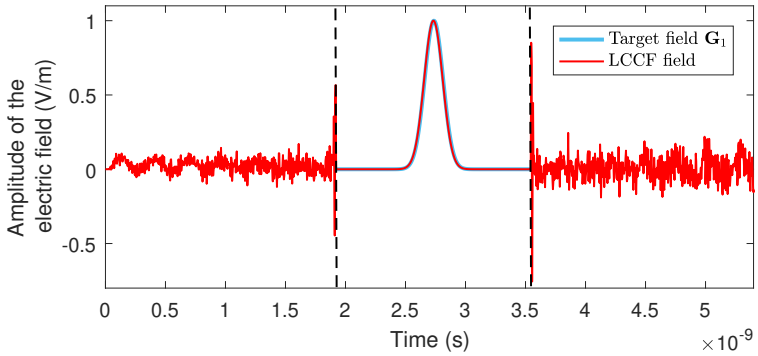

(b) Electric signal $\mathbf{y}$ recorded after injecting $\mathbf{x}$.

Figure 2.8: *Signal* $\mathbf{x}$ *propagates through the reverberant cavity to control the electric field at the receiver point. After its emission, the receiver R records the signal* $\mathbf{y}$*, where the desired target electric field* $\mathbf{G}_1$ *is recorded over the target time* $[t_q, t_f] = [1.92 \times 10^{-9}, 3.54 \times 10^{-9}]$ *lying between the two dashed lines.*

view, as the sparsity of $\mathbf{A}$ decreases, the chance to obtain zero columns in $\mathbf{A}$, thus in $\mathbf{A}^T\mathbf{A}$, decreases as well. A kth zero column in $\mathbf{A}^T\mathbf{A}$ means that the component $x(k-1)$ of the source $\mathbf{x}$ does not contribute to the solution of the LCCF system (2.5) and may be set to zero. We recall that the number of rows or columns of the square matrix $\mathbf{A}^T\mathbf{A}$ represents the duration of the source $\mathbf{x}$. Assuming that some columns of $\mathbf{A}^T\mathbf{A}$ are zeroes, then some components of $\mathbf{x}$ corresponding to these columns are also zeroes. As a result, the sparsity

of $\mathbf{x}$ increases. A sparse source $\mathbf{x}$ faces difficulties in producing the target $\mathbf{F}$ over $[t_q, t_f]$.

In Chapter 1, we presented the TR technique to refocus waves at a spatial point to generate the desired field. This common objective with the LCCF makes it interesting to compare both methods. In the next section, we list the limitations of the TR and the advantages that the LCCF method could bring over the TR in wiring networks with lossless and lossy lines. The carried out comparison and the obtained results may also be generalized to three-dimensional problems.

2.2 TR vs. LCCF

This section compares the Time-Reversal (TR) method to the LCCF method in wiring networks. For this purpose, we consider the same network Ω with the same cartography and characteristics as Section 2.1.2 (Figure 2.2 and Table 2.1).

2.2.1 Lossless network

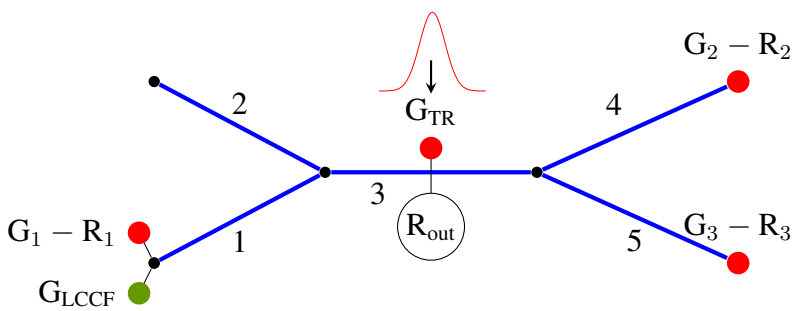

Figure 2.9: *Placement of the generators and receivers for the TR and the LCCF processes.*

First of all, no losses are considered in the lines of Ω ($R = G = 0$) to show that the weak points of the TR are not limited to lossy problems only. Here, the TR and LCCF methods are compared to produce a predefined target voltage over a duration of $120\Delta t$. For the TR process, we use a generator G_{TR}

placed at the midpoint of line 3 to inject a signal represented by the Gaussian pulse $\mathbf{G}_1$ (2.6) with $t_c = 30\Delta t$ and $\sigma = 5\Delta t$ (see the blue sky signal in Figure 2.10b). The pulse $\mathbf{G}_1$ propagates, reflects, and re-reflects through Ω due to the mismatched loads, ending to the three receivers R_1, R_2, and R_3 placed at the three extremities of the network, as indicated in Figure 2.9. We point out that no recordings are required for the TR process at the end of line 2 since the signal totally reflects once reaching this termination; thus, no information is lost at this extremity. The recorded signals are reversed in time, then re-emitted simultaneously by the generators G_1, G_2, and G_3, each placed at the same level of the corresponding receiver. The re-emitted signals retrace the path of the source back through Ω to refocus $\mathbf{G}_1$ at the midpoint of line 3. The time-reversal refocusing of $\mathbf{G}_1$ is recorded over $[t_q, t_f] = [620\Delta t, 740\Delta t]$ by the receiver R_{out} and represented in red in Figure 2.10b. The relative error (2.8) between the target and the refocused signal is about RE $= 7.16 \times 10^{-3}$. On the other hand, we assume for the LCCF method that the source generator G_{LCCF} is placed the start node of line 1. After solving the LCCF linear system to compute the source $\mathbf{x}$ represented in Figure 2.10a, the output voltage is recorded by R_{out} and represented in dark blue in Figure 2.10b. The relative error (2.8) for the LCCF process is estimated at RE $= 2.04 \times 10^{-9}$.

In general, the interventions at all the extremities of Ω are required for the TR method to work properly (Huygens surface). We note that it is unnecessary to intervene at the open-circuited or short-circuited extremities, where the voltage is perfectly reflected, such as the termination of line 2 in the above example. In this case, prior knowledge of the characteristics of the network is required to specify the intervention points. Practically, the TR malfunctions if at least one of its extremities absorbs the voltage partially or totally and is found to be inaccessible or accessible with an impossible placement of any equipment (generator or receiver) due to their heavyweight or voluminousness, for instance. Nevertheless, the LCCF method still works properly with access to only one point of the network corresponding to the source point that may be placed anywhere and without the requirement of neither Huygens surface nor prior knowledge of the impedance characteristics. Actually, these characteristics are included in the impulse response used to characterize the network. In the considered example, the points of access (generators and receivers) of Ω for the TR are represented by red

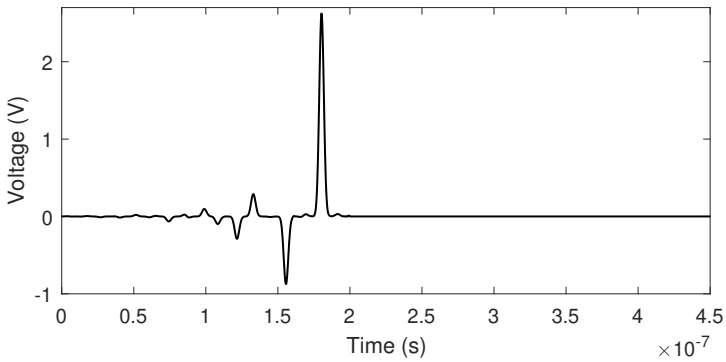

(a) Source $\mathbf{x}$ computed by the LCCF method.

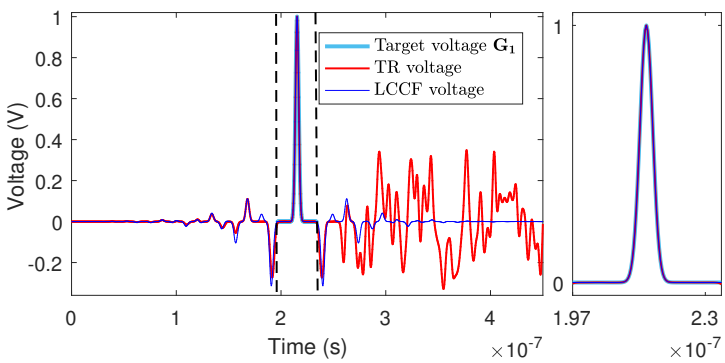

(b) Voltage signals $\mathbf{y}$ recorded after injecting the LCCF source $\mathbf{x}$ and the TR back-propagated signals.

Figure 2.10: *TR back-propagated signals and the LCCF signal* $\mathbf{x}$ *propagate through the lossless network to refocus/control the voltage at the midpoint of line* 3. *After their separate emissions, the receiver* R_{out} *records the signals* $\mathbf{y}$, *where the desired target voltage* $\mathbf{G}_1$ *is obtained over the refocusing/target time* $[t_q, t_f] = [1.95 \times 10^{-7}, 2.34 \times 10^{-7}]$ *lying between the two dashed lines. The small figure represents the signals zoomed over* $[t_q, t_f]$.

circles, whereas the point of access of the LCCF is chosen to be an extremity, for instance, and represented by a green circle in Figure 2.9. Generally, not considering all the extremities to apply the TR method causes information losses and leads to an improper refocusing of $\mathbf{G}_1$. Figure 2.11 refers to the deteriorated refocusing of $\mathbf{G}_1$ when considering 1, 2, and 3 extremities of Ω successively during a numerical TR process. We may note that the LCCF is less expensive than the TR in terms of equipment from an experimental point of view.

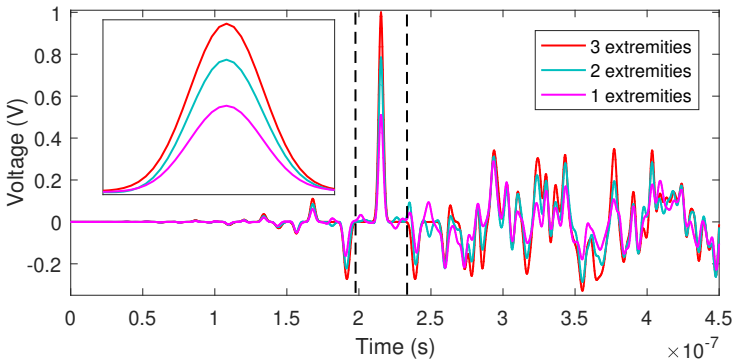

Figure 2.11: *During separate TR processes in a lossless network, not considering all the absorbent extremities causes information losses and leads to an improper refocusing of* $\mathbf{G}_1$. *The small figure represents the signals zoomed over the refocusing time* $[1.95 \times 10^{-7}, 2.34 \times 10^{-7}]$.

To produce a simple target voltage, such as $\mathbf{G}_1$ in a lossless network Ω, the TR and the LCCF have shown to be remarkably effective. However, this cannot be generalized to produce any target voltage, especially complex ones. Let us denote by $\mathbf{S}_1$ the 1–periodic sinusoidal signal of maximum amplitude $+1\,\mathrm{V}$. The general form of a sinusoidal function $S_\beta(t)$ of maximum amplitude β is

$$S_\beta(t) = \beta \sin(2\pi \ell t), \tag{2.10}$$

such that ℓ denotes the frequency of the function and $\mathbf{S}_1 = [S_1(0), S_1(1), \cdots]$. By taking $\ell = 31.6\,\mathrm{MHz}$, we now consider $\mathbf{G}_1$ followed by $\mathbf{S}_1$ as the new complex target voltage. The new target voltage is denoted by $\mathbf{G}_1\mathbf{S}_1$ and represented in blue sky in Figure 2.12b. After

applying the TR and the LCCF processes, their output signals are respectively displayed in red and dark blue in Figure 2.12b, while Figure 2.12a represents the computed LCCF source $\mathbf{x}$.

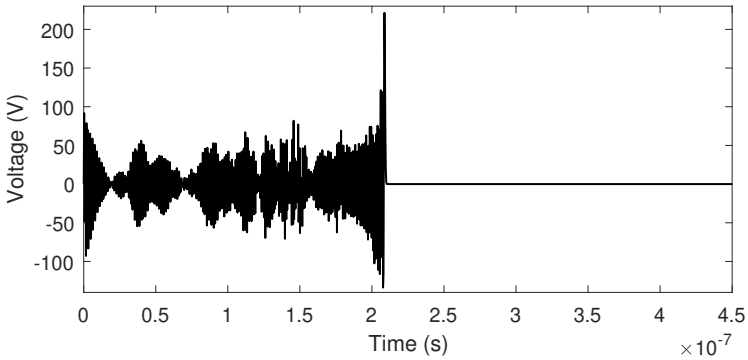

(a) Source $\mathbf{x}$ computed by the LCCF method.

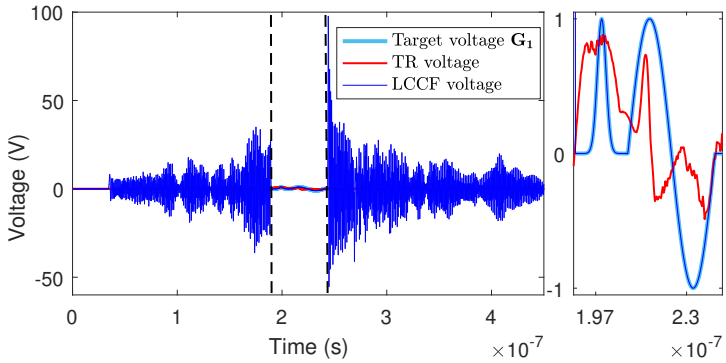

(b) Voltage signals $\mathbf{y}$ recorded after injecting the LCCF source $\mathbf{x}$ and the TR back-propagated signals.

Figure 2.12: *TR back-propagated signals and the LCCF signal* $\mathbf{x}$ *propagate through the lossless network to refocus/control the voltage at the midpoint of line* 3. *After their separate emissions, the receiver* R_{out} *records the signals* $\mathbf{y}$. *For the LCCF process, the desired complex target voltage* $\mathbf{G}_1\mathbf{S}_1$ *is obtained over the target time* $[t_q, t_f] = [1.95 \times 10^{-7}, 2.34 \times 10^{-7}]$ *(the interval between the two dashed lines), whereas the TR fails in refocusing* $\mathbf{G}_1\mathbf{S}_1$ *over* $[t_q, t_f]$. *The small figure represents the signals zoomed over* $[t_q, t_f]$.

Obviously, the LCCF succeeds in generating the desired complex target voltage, unlike the TR that fails in refocusing $\mathbf{G}_1\mathbf{S}_1$ at the midpoint of line 3.

The relative error (2.8) between the target signal and the signal obtained by the LCCF over $[t_q, t_f] = [600\Delta t, 770\Delta t]$ is about RE $= 8.66 \times 10^{-4}$. As a result, the TR shows to be inefficient at refocusing a complex target voltage at a single point in a lossless network. Unlikely, the LCCF method succeeds in generating any voltage profile at any fixed point on the network.

In general, the comparison "TR vs. LCCF" remains valid in three-dimensional cases, where the Time-Reversal Mirrors (TRM) could not be placed at the optimal positions due to inaccessible volumes inside the cavity, for example, leading to poor refocusing quality. An alternative solution could be to work remotely using the LCCF method, where only one source point is required with the possibility to be placed anywhere. Often, when working in irreversible media, a single TRM is not sufficient to obtain a good refocusing due to the absorbent walls, but one probe is enough for the LCCF method to generate the desired target field as demonstrated in Section 2.1.3. Hence, still in three dimensions, the LCCF is less costly than the TR in terms of equipment needed to realize experimental manipulations. Another key point, the LCCF may generate more complex target fields that may not be feasible by the TR. In the next section, we go further and introduce arbitrary losses to the problem to compare the TR and LCCF methods.

2.2.2 Lossy network

Comparing the TR and the LCCF in lossy media is also an interesting problem. It is important to distinguish between the amplitude losses resulting from the signal propagation and the information losses resulting from the irreversibility of the media due to the absorbent walls (extremities in the wiring networks) treated in the previous section. These types of losses could not be treated in the same way; we have shown in the previous section the need to access each leaky extremity of the voltage in a TL network to obtain a good refocusing when dealing with information losses. In this section, we only focus on amplitude losses to prove the superiority of the LCCF over the TR without claiming that the TR does not work in this case [135]. We apply and compare the TR and the LCCF methods for generating a simple target voltage in a lossy medium after both methods have proven their efficiency in lossless media. We show that the TR requires additional treatments to compensate for the amplitude losses, unlike the LCCF, where no additional

steps are required.

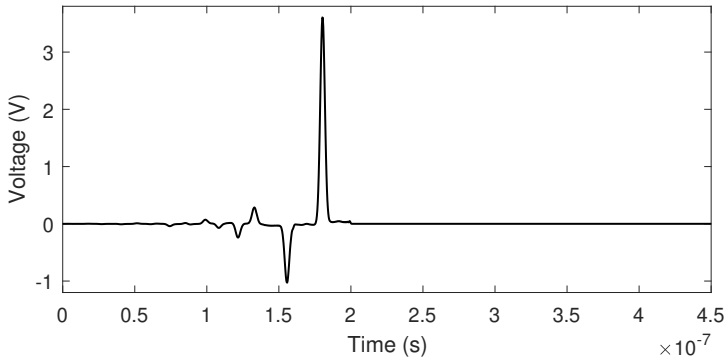

(a) Source $\mathbf{x}$ computed by the LCCF method.

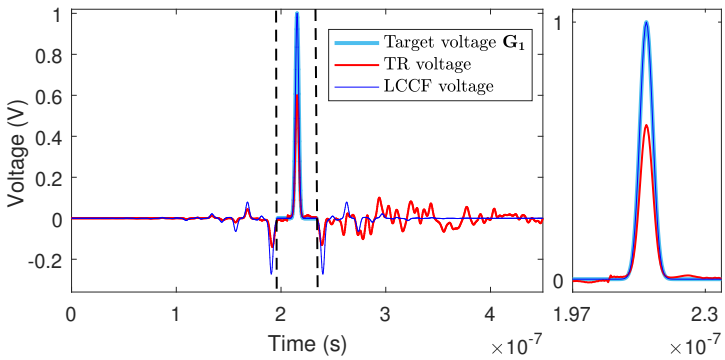

(b) Voltage signals $\mathbf{y}$ recorded after injecting by the LCCF source $\mathbf{x}$ and the TR back-propagated signals.

Figure 2.13: *TR back-propagated signals and the LCCF signal* $\mathbf{x}$ *propagate through the lossy network to refocus/control the voltage at the midpoint of line* 3*. After their separate emissions, the receiver* R_{out} *records the signals* $\mathbf{y}$*, where the desired target voltage* $\mathbf{G}_1$ *is recorded over the refocusing/target time* $[t_q, t_f] = [1.95 \times 10^{-7}, 2.34 \times 10^{-7}]$ *lying between the two dashed lines. Unlikely, the TR fails in refocusing* $\mathbf{G}_1$*. The small figure represents the signals zoomed over* $[t_q, t_f]$*.*

Here, losses are introduced to the lines of Ω by modifying the values of the resistance $R = 0.1\,\Omega/\mathrm{m}$ and the conductance $G = 0.001\,\mathrm{S/m}$, causing

amplitude reductions by 36.68%. For the sake of simplicity, we do not take into account frequency-dependent losses. We compare the LCCF and the TR methods for generating the same target voltage $\mathbf{G}_1$ (2.6) at a single point of Ω. The TR technique fails in refocusing $\mathbf{G}_1$ due to the amplitude reductions resulting from the losses after the propagation back and forth of the signals (see the red signal in Figure 2.13b). Such losses result in lowering the amplitudes of the refocusing peak at the midpoint of line 3. In contrast, the LCCF method computes the new source of Figure 2.13a to be emitted by $\mathrm{G}_{\mathrm{LCCF}}$, leading the receiver $\mathrm{R}_{\mathrm{out}}$ to record the voltage represented in dark blue in Figure 2.13b. The LCCF successfully produces $\mathbf{G}_1$ at the midpoint of line 3 over $[t_q, t_f]$. The relative error (2.8) between $\mathbf{G}_1$ and the obtained voltage by the LCCF over $[t_q, t_f]$ is about RE $= 3.95 \times 10^{-9}$.

For the TR method, a simple solution, in this case, is to increase the energy of the detected signals at the receiver points in the first phase; however, this requires prior knowledge of the attenuation level presented in Ω. In many experimental tests, it may not be possible to increase the amplitudes of the back-propagated signals due to equipment limitations. Another solution is to use lossy back-propagation models to compensate for the effects of losses [136]. The situation worsens for the TR when dealing with lossy-dispersive media as dispersion may distort the form of the signal; therefore, different treatments are required. Without additional treatments, it is not possible to refocus a proper target voltage/current or field at the source point using the standard TR method. In general, the TR method requires prior knowledge of the characteristics of the medium, whether it is lossy, dispersive, reversible, absorbent, etc. to select (or not) the appropriate treatments to be taken. However, the LCCF is totally independent of the medium characteristics. As a matter of fact, the impulse response used to characterize the system implicitly includes all these propagative information to be compensated during an LCCF process. To sum up, Table 2.3 below summarizes the "TR vs. LCCF" comparison and shows the advantages of the LCCF over the TR to shape electromagnetic fields at a spatial point over a time interval.

The computational results in Sections 2.1 and 2.2 are encouraging enough and may pave the way for experimental validation, as we will see in the last chapter of this dissertation. Nonetheless, not all the computed sources by the

Properties \ Methods	TR	LCCF
Access points*	≥ 2 (Huygens surface in theory)	2
Shaping complex fields	Not efficient	Efficient
Medium's characteristics	Dependent and requires additional steps	Independent

$(*)$: The access points correspond to the required number of points used to place generators and receivers.

Table 2.3: *Comparison between the TR and the LCCF techniques.*

LCCF may experimentally be realized due to their physical characteristics (amplitudes, frequencies, etc.); otherwise, they become costly or even experimentally unachievable. To fill this gap between numerical and experimental validation, we take an intermediate step towards improving the sources by adding constraints to the LCCF problem, as we will see in the following.

2.3 Source Properties Modifications

This section is dedicated to showing that the LCCF method still gives interesting results under certain conditions, namely *constraints*, to be satisfied by the computed solution. These constraints may modify the source properties to obey some limitations one may encounter during experiments. At first, we adjust the source period of emission by specifying the first and the last emission instants. Further, constraints are added to the problem to filter the source, then restrict its amplitudes between two predefined maximal and minimal values.

2.3.1 Duration of source emission

Let $t_p = p\Delta t$ and $t_z = z\Delta t$ $[(p, z) \in \mathbb{N}^2]$ be the first and the last instants of the source emission, respectively. In Section 2.1.1, the LCCF method has been presented to identify the source $\mathbf{x} \in \mathbb{R}^{(f+1)}$ emitted for the longest possible time duration from $t_p = 0$ to $t_z = t_f$. Only in this section we will employ the notation $\mathbf{x} = \mathbf{x}_{0\to f}$ to put this feature in appearance. We develop

the LCCF technique to identify the source $\mathbf{x}_{p\to z}$ emitted over $[t_p, t_z]$, where $0 \leq t_p \ll t_q$ and $t_p \ll t_z \leq t_f$. Doing so, we modify the LCCF matrix $\mathbf{A}$ in a way to satisfy this condition. To start emitting the source at t_p, we inject the unit pulse $\mathbf{e}_{p+1} = [0, \cdots, 0, 1, 0, \cdots, 0]$ to record the impulse response $\mathbf{h}_{p+1}$ that will be used to build the first column of $\mathbf{A}$. Then, we proceed exactly in the same diagonal constancy as previously described in formula (2.4) to build the rest columns. In particular, the case of $p = 0$ refers to the theory of Section 2.1.1, where the unit pulse $\mathbf{e}_1$ is injected to record $\mathbf{h}_1$. Concerning the emission duration of the source, it is represented by the number of columns of $\mathbf{A}$. Then, it is sufficient to choose the first $z - p + 1$ columns. Therefore, the matrix $\mathbf{A} \in \mathbb{M}_{(f-q+1)\times(z-p+1)}$ may generally be written as

$$\mathbf{A}_{ij} = \begin{pmatrix} h_{p+1}(q) & h_{p+1}(q-1) & \cdots & \cdots & \cdots & h_{p+1}(q+p-z) \\ \vdots & h_{p+1}(q) & \ddots & & & \vdots \\ \vdots & \vdots & \ddots & & & \vdots \\ h_{p+1}(f) & h_{p+1}(f-1) & \cdots & h_{p+1}(q) & \cdots & h_{p+1}(f+p-z) \end{pmatrix}. \tag{2.11}$$

The matrix $\mathbf{A}$ should not extend straight up, i.e., the number of rows should not exceed the number of columns. In fact, the integers p and z could not be chosen randomly, at least they should be selected in a way that allows a physical computation of the source to impose the target field $\mathbf{F}$. That is to say, the duration of emitting the source is long enough to cover the entire duration of the target time $(z - p + 1 \geq f - q + 1)$. After regularization, the LCCF system to be solved is

$$\left(\mathbf{A}^T\mathbf{A} + \epsilon\mathbf{I}\right)\mathbf{x}_{p\to z} = \mathbf{A}^T\mathbf{F}. \tag{2.12}$$

Emitting $\mathbf{x}_{p\to z}$ leads the receiver R to recording the signal $\mathbf{y}_{p\to z}$, such that $\mathbf{y}_{p\to z}/_{\left[t_q, t_f\right]} = \mathbf{F}$.

Problem settings

Assume that the network Ω has the same cartography as before but with different characteristics, as seen below in Figure 2.14 and Table 2.4. The reason behind changing the characteristics of Ω is to show that any arbitrary length of lines, load, and impedance characteristics may be considered to

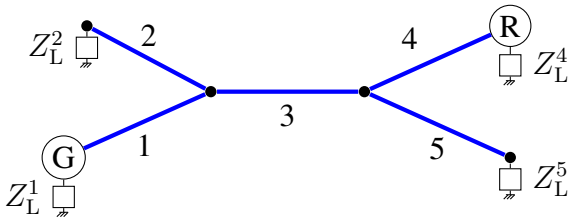

Figure 2.14: *Network configuration.*

Line Nb. l	z (in m)	Z_{C}^l (in Ω)	Z_{L}^l (in Ω)
1	5	50	50
2	6	50	0
3	4	50	0
4	5	50	50
5	8	50	0

Table 2.4: *New characteristics of the network.*

apply the LCCF method. Losses are added to the lines of Ω by taking $R = 0.1\,\Omega/\mathrm{m}$ and $G = 0.001\,\mathrm{S/m}$, causing amplitude reductions by 36.68%. For the sake of simplicity, we do not take into account frequency-dependent losses. The network Ω, with its new characteristics, will be used in the numerical applications in the rest of this chapter.

The source generator G is placed at the start node of line 1 and a receiver R is placed at the termination of line 4. The target voltage is chosen to be the Gaussian pulse $\mathbf{G}_1$ (2.6) with $t_c = 75\Delta t$, $\sigma = 10\Delta t$ (see the blue sky signal in Figure 2.15b) and the target time $[t_q, t_f] = [450\Delta t, 600\Delta t]$. We first apply the LCCF method to identify the source $\mathbf{x}_{0\to f}$ that leads R to recording $\mathbf{G}_1$ over $[t_q, t_f]$ without any constraints. Figure 2.15a shows the computed source and its output signal $\mathbf{y}_{0\to f}$ recorded by R is represented in Figure 2.15b. In this case, the relative error (2.8) is about RE $= 1.43 \times 10^{-6}$.

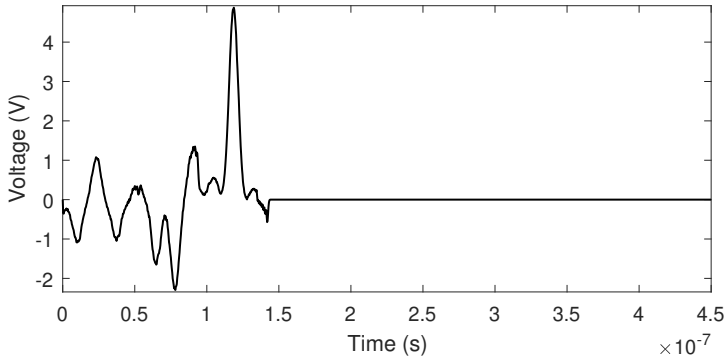

(a) Source $\mathbf{x}_{0\to f}$ emitted over $[0, f\Delta t]$.

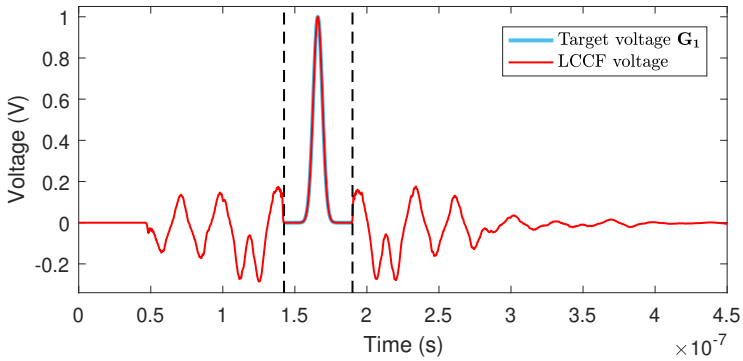

(b) Voltage signal $\mathbf{y}$ recorded after injecting $\mathbf{x}_{0\to f}$.

Figure 2.15: *After the emission of the source* $\mathbf{x}_{0\to f}$*, the receiver R records the signal* $\mathbf{y}$*, where* $\mathbf{y}_{/[t_q,t_f]} = \mathbf{G}_1$ *over the target time* $[t_q, t_f] = [1.42 \times 10^{-7}, 1.9 \times 10^{-7}]$ *lying between the two dashed lines.*

Numerical applications

We have seen in Figure 2.15a how the LCCF method could compute a source $\mathbf{x}_{0\to f}$ emitted over the time interval $[0, t_f] = [0, f\Delta t]$ to generate $\mathbf{G}_1$ over $[t_q, t_f]$. In the next step, the LCCF is applied to compute a source $\mathbf{x}_{p\to z}$ to be emitted between two specified instants $p\Delta t$ and $z\Delta t$, such that after its emission, the output signal $\mathbf{y}_{p\to z} = \mathbf{G}_1$ over $[t_q, t_f]$. Here, we present the first example with a short source emission duration and a second example with a shorter duration.

Example 1: We set $p = 100$ and $z = 400$, then the LCCF computes a source $\mathbf{x}_{100\to400}$. Its emission by G leads to recording the signal $\mathbf{y}_{100\to400}$ that matches $\mathbf{G}_1$ over $[t_q, t_f]$. The signals $\mathbf{x}_{100\to400}$ and $\mathbf{y}_{100\to400}$ are represented in red in Figure 2.16. The relative error (2.8) in this example is RE $= 2.86 \times 10^{-6}$.

Example 2: We set $p = 200$ and $z = 360$ to compute the source $\mathbf{x}_{200\to360}$. Its emission generates the signal $\mathbf{y}_{200\to360}$ that matches $\mathbf{G}_1$ over $[t_q, t_f]$. The signals $\mathbf{x}_{200\to360}$ and $\mathbf{y}_{200\to360}$ are displayed in gray in Figure 2.16. The relative error (2.8) in this example is RE $= 8.02 \times 10^{-4}$.

To analyze our results, the sources $\mathbf{x}_{100\to400}$ and $\mathbf{x}_{200\to360}$ seem to be chaotic. Using the Fast Fourier Transform (FFT), the frequency spectra of $\mathbf{x}_{100\to400}$ and $\mathbf{x}_{200\to360}$ are computed and plotted in Figure 2.17 to show their frequencies. The presented high frequencies raise our attention to go deeper into our study as they result in costly or unachievable sources during experimental validation. Up to now, the LCCF technique does not take into account the physical characteristics of the computed source (frequencies, amplitudes, etc.). In fact, the LCCF with a short source emission duration usually finds a mathematical true solution; however, this solution may not necessarily be considered in experiments due to physical considerations or equipment limitations.

Moreover, shortening the source emission duration may lead to computing sources of high amplitudes compared to the amplitudes of the desired target voltage. In *Example 2*, the amplitudes of $\mathbf{x}_{200\to360}$ are not in the same order of magnitude as $\mathbf{G}_1$; they vary over a wide range -89.88 and $+67.73\,\mathrm{V}$ to generate $\mathbf{G}_1$ of maximum amplitude $+1\,\mathrm{V}$. Not only the source amplitudes suffer from this disorder, but also the output voltage $\mathbf{y}_{200\to360}$ does not remain in the same order of magnitude as $\mathbf{G}_1$ in the neighborhood of $[t_q, t_f]$, i.e., they vary between -11.53 and $+11.19\,\mathrm{V}$, $\forall\, t \in [0, t_n] \setminus [t_q, t_f]$.

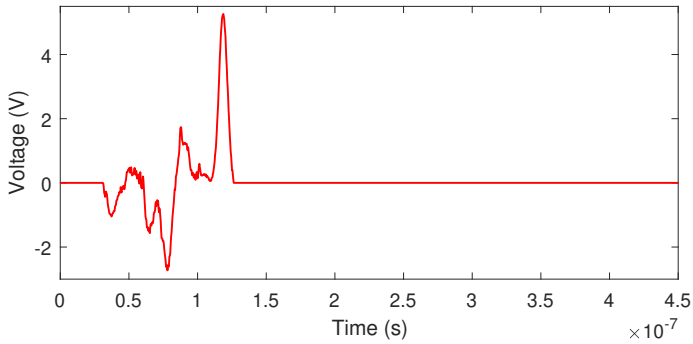

(a) Source $\mathbf{x}_{100\to400}$ emitted over $[100\Delta t, 400\Delta t]$.

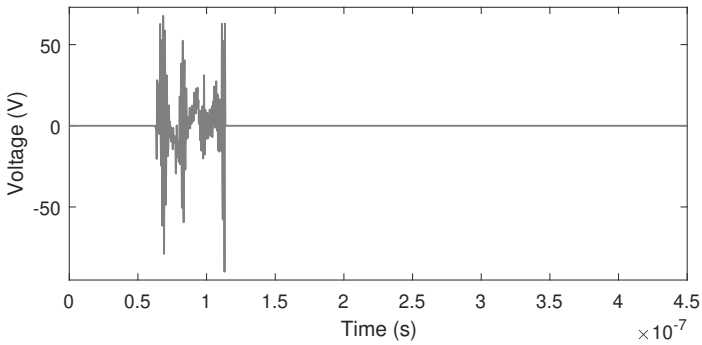

(b) Source $\mathbf{x}_{200\to360}$ emitted over $[200\Delta t, 360\Delta t]$.

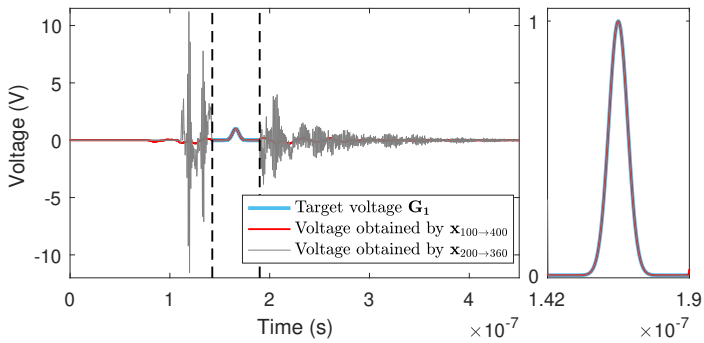

(c) Voltage signals $\mathbf{y}$ recorded after injecting $\mathbf{y}_{100\to400}$ and $\mathbf{y}_{200\to360}$.

Figure 2.16: *After the separate emission of the sources* $\mathbf{x}_{100\to400}$ *and* $\mathbf{x}_{200\to360}$*, the receiver R records the signals* $\mathbf{y}$*, where* $\mathbf{y}_{/[t_q,t_f]} = \mathbf{G}_1$ *over the target time* $[t_q, t_f] = [1.42\times10^{-7}, 1.9\times10^{-7}]$ *lying between the two dashed lines. The small figure represents the signals zoomed over* $[t_q, t_f]$.

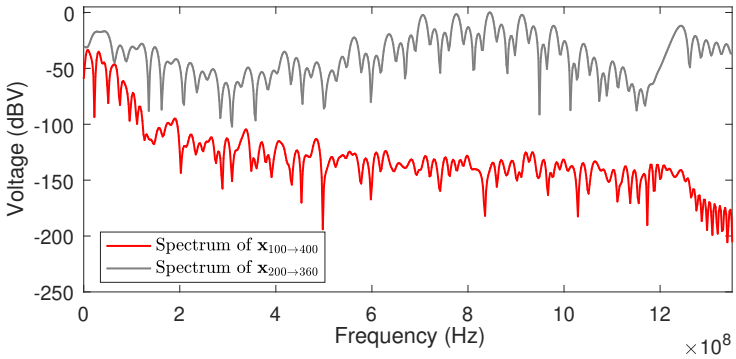

Figure 2.17: *Spectra of the signals* $\mathbf{x}_{100\to400}$ *and* $\mathbf{x}_{200\to360}$.

Accordingly, to avoid these undesirable behaviors, we may improve the signals $\mathbf{x}_{100\to400}$ and $\mathbf{x}_{200\to360}$ in a way to satisfy all the following four conditions:

1. Low relative error between the target and the obtained voltages,

2. Low maximum frequency of the source,

3. The amplitudes of the source are in the same order of magnitude as the target voltage,

4. The amplitudes of the output signal obtained in the neighborhood of $[t_q, t_f]$ are in the same order of magnitude as the target voltage imposed over $[t_q, t_f]$.

We put signal $\mathbf{x}_{100\to400}$ understudy and propose two possibilities of improvement to satisfy the above conditions. Then, the best possibility will be selected and applied to signal $\mathbf{x}_{200\to360}$ to show the efficiency of the LCCF at computing signals that are experimentally realizable.

Remark: In the rest of this chapter, we will only deal with signals with restricted emission duration between $p\Delta t$ and $z\Delta t$. Then we will assume that $\mathbf{x} = \mathbf{x}_{p\to z}$ and $\mathbf{y} = \mathbf{y}_{p\to z}$ to avoid complex notation.

2.3.2 Source filtering

In this section, we present two types of filtering: *a posteriori* filtering and *a priori* filtering. First, we start by presenting the theoretical part of each process, then we reconsider *Example 1* to filter the computed source $\mathbf{x}_{100\to400}$.

After solving the LCCF system (2.12), the source $\mathbf{x} = \mathbf{x}_{p\to z}$ is computed, then filtered using a moving average filter, which typically takes the form:

$$x^{(\rho)}(k) = \frac{1}{\rho}\Big[x\left(k-\frac{\rho}{2}\right)+\cdots+x\left(k-1\right)+x\left(k+1\right)+\cdots+x\left(k+\frac{\rho}{2}\right)\Big], \tag{2.13}$$

where

- $x^{(\rho)}(k)$ is the smoothed value for the kth data point, $\forall k \in \{0,\cdots,z-p\}$,
- $\rho > 0$ is an even integer to be heuristically chosen. It represents the number of neighboring points on both sides of $\mathbf{x}$. The parameter ρ is called the *linear filtering level* or *span*.

Note that the choice of ρ is a compromise between the smoothness of $\mathbf{x}^{(\rho)}$ and the resulting relative error. In essence, increasing the filtering level of $\mathbf{x}^{(\rho)}$ leads to an increase in the degradation of the obtained voltage $\mathbf{y}^{(\rho)}$ ($\mathbf{y} = \mathbf{y}_{p\to z}$) over $[t_q, t_f]$. As a consequence, the relative error increases relatively.

In *Example 1*, we apply the formula (2.13) to the computed source $\mathbf{x}$ with $\rho = 2$. The filtered signal $\mathbf{x}^{(2)} = \mathbf{x}^{(2)}_{100\to400}$ is computed and represented in blue in Figure 2.18a. After its injection, the obtained voltage $\mathbf{y}^{(2)}_{100\to400}$ is recorded by the receiver R and displayed in blue in Figure 2.18b. *A posteriori* filtering keeps the amplitudes of $\mathbf{x}^{(2)}$ and $\mathbf{y}^{(2)}$ in the same order of magnitude as $\mathbf{G}_1$; the amplitudes of $\mathbf{x}^{(2)}$ vary between -2.66 and $+5.2\,\mathrm{V}$, while the amplitudes of $\mathbf{y}^{(2)}$ vary between -0.29 and $+0.22\,\mathrm{V}$ over $[0, t_n] \setminus [t_q, t_f]$. By the FFT, the spectrum of $\mathbf{x}^{(2)}$ is computed and displayed in blue in Figure 2.19. Notably, *a posteriori* filtering did not lead to significant progress in computing a source $\mathbf{x}^{(2)}$ whose maximum frequency is less than that of $\mathbf{x}$. More importantly, the relative error (2.8) between the target voltage $\mathbf{G}_1$ and $\mathbf{y}^{(2)}$

has remarkably increased from 2.86×10^{-6} to 3.58×10^{-2} with the lowest span ($\rho = 2$). Increasing ρ would compute a smoother source with a lower maximum frequency; however, it may highly deform the output voltage between t_q and t_f after its injection. The increase in the relative error contradicts condition (1) and highlights the impractical improvement of $\mathbf{x}$ using *a posteriori* filtering.

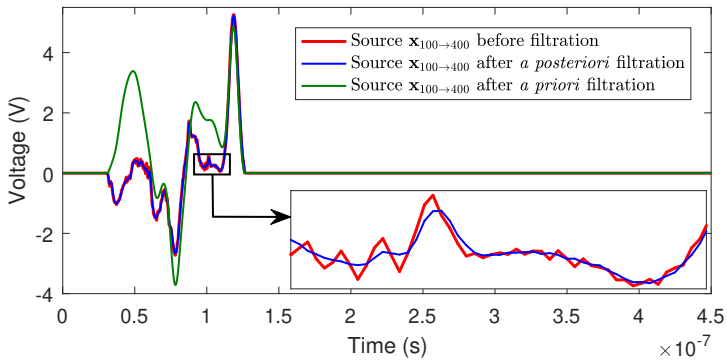

(a) Source $\mathbf{x}_{100\to400}$ before filtering, and after *a posteriori* and *a priori* filtering. The small figure shows the effect of *a posteriori* filtering on $\mathbf{x}_{100\to400}$.

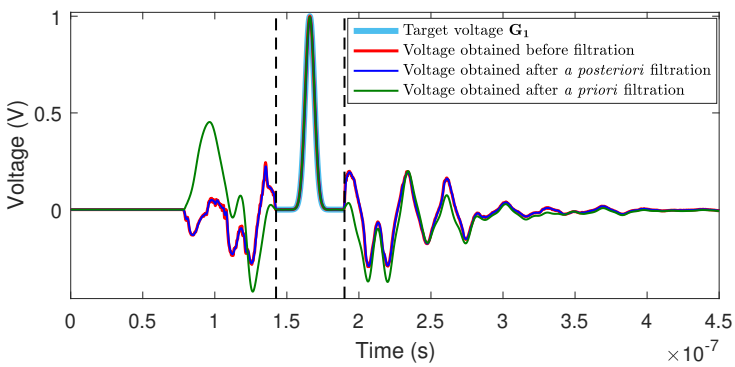

(b) Voltage signal $\mathbf{y}_{100\to400}$ recorded after injecting $\mathbf{x}_{100\to400}$ before and after filtering.

Figure 2.18: *After separate emissions of the filtered sources, the receiver R records the signals* $\mathbf{y}^{(2)}_{100\to400}$, *which are similar to* $\mathbf{G}_1$ *over the target time* $[t_q, t_f] = [1.42 \times 10^{-7}, 1.9 \times 10^{-7}]$ *lying between the two dashed lines.*

Alternatively, constraints are then added to the LCCF system (2.12), acting as a filter on the source $\mathbf{x}$. These constraints satisfy the filter of formula (2.13) and compute a smooth and low-frequency source. Such constraints may be written in a matrix-vector form $\mathbf{B}\mathbf{x}^{(\rho)} = 0$ ($\mathbf{B}$ is the squared matrix of filtering) and added to the system (2.12), which becomes

$$\left(\mathbf{A}^T\mathbf{A} + \mathbf{B}^T\mathbf{B} + \epsilon\mathbf{I}\right)\mathbf{x}^{(\rho)}_{p\to z} = \mathbf{A}^T\mathbf{F}. \tag{2.14}$$

By referring to *Example 1*, we choose $\rho = 2$, similar to *a posteriori* filtering, to obtain comparable results. In this case, $\mathbf{B}$ is a tridiagonal matrix with 1 on its diagonal and $-\frac{1}{2}$ on its upper and lower diagonals. The filtered source $\mathbf{x}^{(2)}$ is then computed and displayed in green in Figure 2.18a. After its emission, the voltage signal $\mathbf{y}^{(2)}$ is recorded at the receiver point and represented in green in Figure 2.18b. Similar to *a posteriori* filtering, the amplitudes of $\mathbf{x}^{(2)}$ and $\mathbf{y}^{(2)}$ remain in the same order of magnitude as $\mathbf{G}_1$ varying between -3.71 and $+4.87\,\mathrm{V}$ for $\mathbf{x}^{(2)}$, whereas they vary between -0.42 and $+0.45\,\mathrm{V}$ for $\mathbf{y}^{(2)}$ over $[0, t_n] \setminus [t_q, t_f]$. As opposed to *a posteriori* filtering, the relative error (2.8) with *a priori* filtering stands at $\mathrm{RE} = 3.42 \times 10^{-4}$, which highlights acceptable degradation over $[t_q, t_f]$. After plotting the frequency spectrum of $\mathbf{x}^{(2)}$ (see the green signal in Figure 2.19), adding filtering constraints to the LCCF system computes a source $\mathbf{x}^{(2)}$ whose maximum frequency is less than that of $\mathbf{x}$.

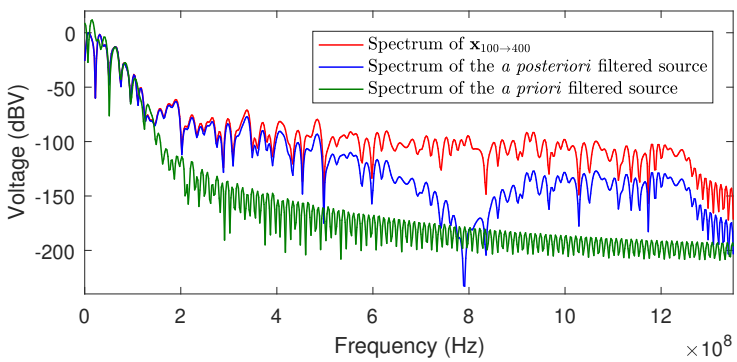

Figure 2.19: *Spectra of the signal* $\mathbf{x}_{100\to400}$ *before filtering, and after a posteriori and a priori filtering.*

Accordingly, *a priori* filtering satisfies the conditions (1), (2), (3), and (4) and shows to be an efficient improvement of the source $\mathbf{x}$. As observed in Figure 2.19, with *a priori* filtering, the maximum frequency of the solution decreases more significantly than with *a posteriori* filtering. Then, *a priori* filtering is selected as the best choice and applied to more critical cases, such as *Example 2*. *A priori* filtered source $\mathbf{x}^{(2)} = \mathbf{x}^{(2)}_{200\to360}$ and its produced voltage $\mathbf{y}^{(2)} = \mathbf{y}^{(2)}_{200\to360}$ are represented in green in Figure 2.20.

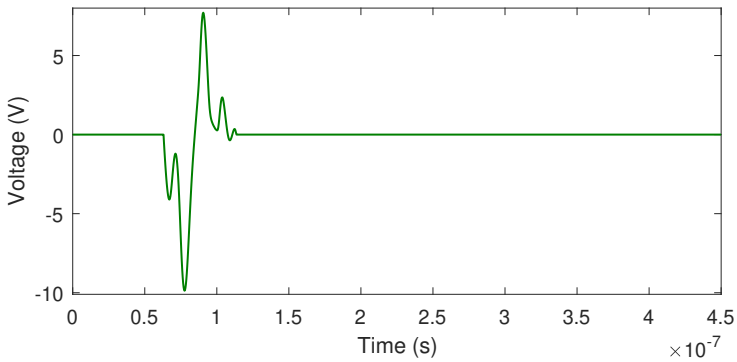

(a) Source $\mathbf{x}_{200\to360}$ after *a priori* filtering.

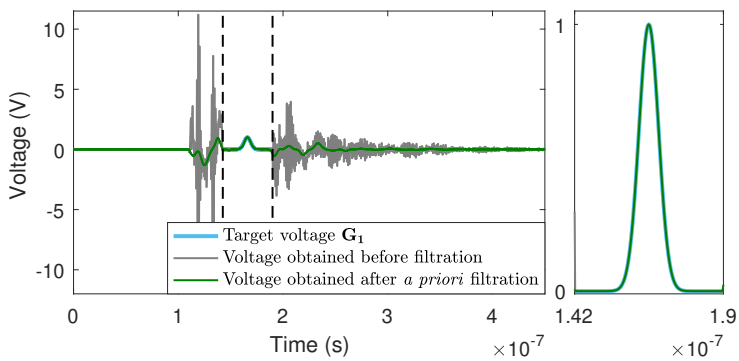

(b) Voltage signal $\mathbf{y}_{200\to360}$ recorded after injecting $\mathbf{x}_{200\to360}$ before and after *a priori* filtering.

Figure 2.20: *After the emission of a priori filtered source* $\mathbf{x}^{(2)}_{200\to360}$*, the receiver R records the signal* $\mathbf{y}^{(2)}_{200\to360}$*, which is similar to* $\mathbf{G}_1$ *over the target time* $[t_q, t_f] = [1.42\times10^{-7}, 1.9\times10^{-7}]$ *lying between the two dashed lines. The small figure represents the signals zoomed over* $[t_q, t_f]$*.*

After *a priori* filtering, the amplitudes of $\mathbf{x}^{(2)}$ vary between -9.87 and $+7.7\,\mathrm{V}$, while they varied between -89.88 and $+67.73\,\mathrm{V}$ before. Similarly, the amplitudes of $\mathbf{y}^{(2)}$ vary between -1.3 and $+0.95\,\mathrm{V}$ over $[0, t_n] \setminus [t_q, t_f]$, whereas they varied between -11.53 and $+11.19\,\mathrm{V}$ before. This implies that the amplitudes of $\mathbf{x}^{(2)}$ and $\mathbf{y}^{(2)}$ remain in the same order of magnitude as $\mathbf{G}_1$ $(+1\,\mathrm{V})$. In this example, the relative error (2.8) is about $\mathrm{RE} = 1.4 \times 10^{-2}$, indicating adequate accuracy. To check the maximum frequency of $\mathbf{x}^{(2)}$, we plot its frequency spectrum in green in Figure 2.21. As expected, *a priori* filtering computes a source $\mathbf{x}^{(2)}$ whose maximum frequency is less than that of $\mathbf{x}_{200\to360}$. As aforementioned, the LCCF method with filtering constraints is efficient at computing low-frequency sources. This fact is illustrated more clearly in *Example 2*, as the unconstrained source $\mathbf{x}_{200\to360}$ is highly chaotic.

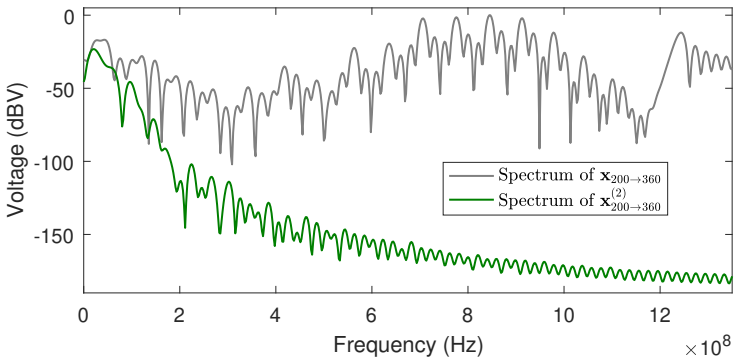

Figure 2.21: *Spectra of the signal* $\mathbf{x}_{200\to360}$ *before and after a priori filtering.*

Table 2.5 sums up the general results obtained by *a posteriori* filtering and *a priori* filtering to improve any computed source. Although *a priori* filtering may modify the amplitudes and reduce the maximum frequency of the computed source, these modifications stay random and uncontrolled. For the moment, we could not solve the LCCF system for a source whose amplitudes are restricted to specified minimal and maximal values. Unfortunately, it happens sometimes that adding filtering constraints to the LCCF method reduces the amplitudes of the smooth source, but this reduction is not always sufficient. In such a case, adding another type of constraint that specifies the minimal and maximal amplitude values of the source could be necessary.

filtering	Condition (1)	Condition (2)	Condition (3)	Condition (4)
A posteriori	✗	✗	✓	✓
A priori	✓	✓	✓	✓

Table 2.5: *General comparison between a posteriori and a priori filtering to improve the computed source.*

2.3.3 Amplitude constraints

Subsequently, we show how the amplitudes of the signal may be restricted between two predefined lower and upper vector bounds denoted by $\mathbf{l}_b$ and $\mathbf{u}_b$, respectively. Solving the LCCF system (2.14) with amplitude constraints is equivalent to find a source that minimizes

$$\left\| \left(\mathbf{A}^T\mathbf{A} + \mathbf{B}^T\mathbf{B} + \epsilon\mathbf{I}\right) \mathbf{x}_{p\to z}^{(\rho)} - \mathbf{A}^T\mathbf{F} \right\|_2^2, \text{ such that } \mathbf{l}_b \leq \mathbf{x}_{p\to z}^{(\rho)} \leq \mathbf{u}_b. \quad (2.15)$$

This problem may be solved using the linear Linear Least-SQuares (LLSQ) solver with bound constraints. The LLSQ solver uses the trust-region-reflective algorithm, which is a subspace trust-region technique based on the interior-reflective Newton's method [137]. The algorithm generates strictly feasible iterations converging, in the limit, to a local solution. Each iteration involves the approximate solution of a large linear system using the method of preconditioned conjugate gradients.

In *Example 1*, after *a priori* filtering of the source, we assume that we are only interested in a source whose amplitudes lie in $[-3, 4]$, i.e., $\mathbf{l}_b = -\mathbf{3}$ and $\mathbf{u}_b = \mathbf{4}$. The LLSQ algorithm converges with 1809 iterations to compute the new source $\mathbf{x}_{\mathrm{CSTR}}^{(2)}$ represented by the magenta signal in Figure 2.22a. After its injection, the voltage $\mathbf{y}_{\mathrm{CSTR}}^{(2)}$ is recorded by R and displayed in magenta in Figure 2.22b. The computational time taken by the algorithm to achieve convergence is $25.5\,\mathrm{s}$ with an relative error (2.8) about RE $= 2.8 \times 10^{-2}$.

Recalling about the definition of $\mathbf{x}_{\mathrm{CSTR}}^{(2)}$, it is a source that is emitted over a predefined duration, filtered, and constrained to specified upper and lower bounds. In the presence of all these restrictions, an relative error (2.8) equivalent to 2.8×10^{-2} might be accepted. Imposing amplitude constraints

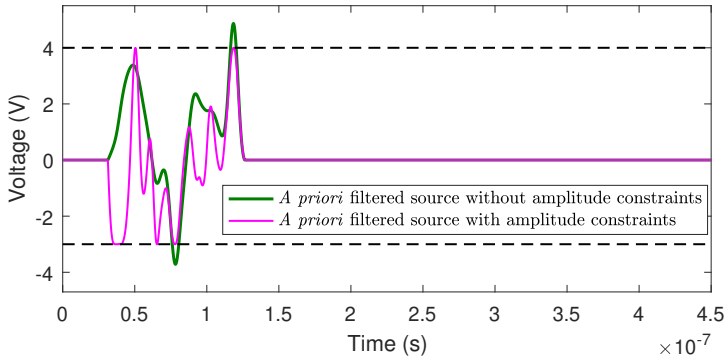

(a) Source $\mathbf{x}^{(2)}_{100\to400}$ before and after adding amplitude constraints.

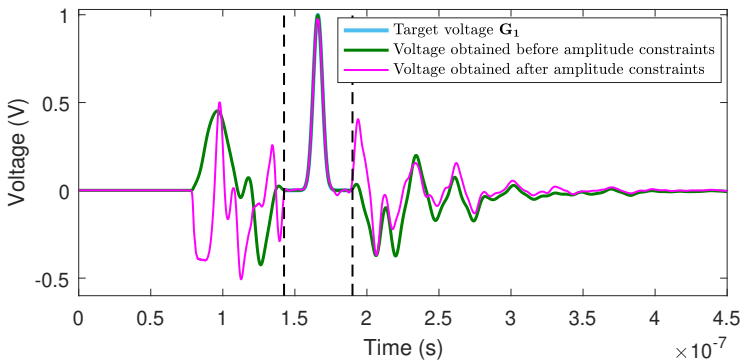

(b) Voltage signal $\mathbf{y}^{(2)}_{100\to400}$ recorded after injecting $\mathbf{x}^{(2)}_{100\to400}$ before and after adding amplitude constraints.

Figure 2.22: *After the emission of the amplitude-constrained source* $\mathbf{x}^{(2)}_{\mathrm{CSTR}}$ *over* $[100\Delta t, 400\Delta t]$, *the receiver R records the signal* $\mathbf{y}^{(2)}_{\mathrm{CSTR}}$, *which is similar to* $\mathbf{G}_1$ *over the target time* $[t_q, t_f] = [1.42\times10^{-7}, 1.9\times10^{-7}]$ *lying between the two dashed lines.*

on $\mathbf{x}^{(2)}_{100\to400}$ is not that easy since the latter already obeys two restrictions on its emission duration and smoothness. Then, adding severe amplitude constraints in such a case would highly increase the relative error and deform the voltage obtained over $[t_q, t_f]$; that is why we chose nonstrict constraints on the amplitudes. Another LCCF problem with stiffer amplitude constraints might be found in [138].

Imposing stiffer constraints on the amplitudes requires removing other restrictions or reducing their severity. In a nutshell, we have to compromise between the source emission duration and added constraints to satisfy the four conditions (1), (2), (3), and (4) mentioned earlier in this section. The constraints of the LCCF method may serve as tools that can be used when necessary. The use of such constraints is problem-dependent.

2.4 Composed Sources and Complex Targets

Identifying sources to replace a field by another one could also be an interesting application for the LCCF. Here, we show that such a technique may produce not only simple target fields (such as Gaussian or sine pulses), but also complex ones over longer periods. Denote by $\mathbf{s}_{\text{init}}$ an initial source placed anywhere in the medium, emitted over $[0, r\Delta t]$, and excites the medium at every single point. The receiver R records the output signal $\mathbf{y}_{\text{init}}$ produced by $\mathbf{s}_{\text{init}}$, where the set of amplitudes of $\mathbf{y}_{\text{init}}$ over $[t_q, t_f]$ is denoted by $\mathbf{U}$ $\left(\mathbf{y}_{\text{init}}/_{[t_q,t_f]} = \mathbf{U}\right)$. We want to identify the source emitted after $\mathbf{s}_{\text{init}}$, such that the output voltage $\mathbf{y}_{\text{init}}/_{[t_q,t_f]} = \mathbf{F}$, i.e., we replace $\mathbf{U}$ by $\mathbf{F}$. Basically, applying the LCCF as previously described fails in doing so as the computed source interferes with the reflected and re-reflected signals resulting from the injection of $\mathbf{s}_{\text{init}}$. Before generating $\mathbf{F}$ over $[t_q, t_f]$, we take an earlier step to cancel $\mathbf{U}$ created by $\mathbf{s}_{\text{init}}$ over $[t_q, t_f]$. Due to the superposition theorem that is always valid in linear media, the LCCF system (2.12) is modified as follows:

$$\left(\mathbf{A}^T\mathbf{A} + \epsilon\mathbf{I}\right)\mathbf{x}_{p\to z} = \mathbf{A}^T\left(-\mathbf{U} + \mathbf{F}\right). \tag{2.16}$$

Considering the same settings and setup as Section 2.3.1, we assume that Ω is excited by $\mathbf{s}_{\text{init}} = \mathbf{G}_1$ (2.6) with $t_c = 75\Delta t$ and $\sigma = 10\Delta t$ emitted over $[0, 130\Delta t]$ ($r = 130$) by the generator G, for example (see the black signal in Figure 2.23b). After injecting $\mathbf{G}_1$, its output voltage $\mathbf{y}_{\text{init}}$ is recorded by the receiver R and represented in Figure 2.23a. Assume that the complex target voltage $\mathbf{F}$ is the blue sky signal of Figure 2.23a to be imposed over the target time $[t_q, t_f] = [450\Delta, 987\Delta t]$. Then, we look for the source emitted

after $\mathbf{G}_1$ to cancel $\mathbf{U}$ and impose $\mathbf{F}$ over $[t_q, t_f]$.

For $t_p = 160\Delta t$ and $t_z = f\Delta t$, the source $\mathbf{x} = \mathbf{x}_{160\to f}$ is computed and represented in red in Figure 2.23b. Injecting $\mathbf{x}$ after $\mathbf{G}_1$ replaces the voltage $\mathbf{U}$ by $\mathbf{F}$ over $[t_q, t_f]$, as illustrated in Figure 2.23c with an RE $= 1.07 \times 10^{-3}$ (2.8). In this case, the signal $\mathbf{x}$ is chaotic; thus, lowering its maximum frequency requires filtering constraints. After adding such constraints to the problem, the signal $\mathbf{x}^{(2)}$ (blue signal in Figure 2.23b) is computed, which in turn produces the blue signal in Figure 2.23c at the R-level. With *a priori* filtering, the relative error (2.8) slightly increases to 8.69×10^{-3}. We note that this problem does not necessitate amplitude constraints.

2.5 Conclusion

We began this chapter by recalling the main lines of the LCCF technique, which is capable of effectively identifying a source to control a field in any linear medium over a specified time interval. This idea was supported by numerical applications in lossless and lossy wiring networks as well as anechoic and reverberant free space environments. Later, we compare the LCCF and the time-reversal for shaping electromagnetic fields in a linear medium, then present the advantages that the former could bring over the latter. Due to some limitations encountered during experiments, constraints are added to the LCCF problem to control the first and last instants of the source emission, reduce the maximum frequency of the source by filtering, and control its maximal and minimal bounds. We gathered all the necessary ideas together in an interesting application for the LCCF method in the last section. We showed that the LCCF method might substitute an undesired voltage by an intentional one with and without filtering constraints. The idea of this application will be used in the next chapter after improving the LCCF method. More applications will be presented to show the interest of the generalized LCCF when applied to electromagnetic interference problems.

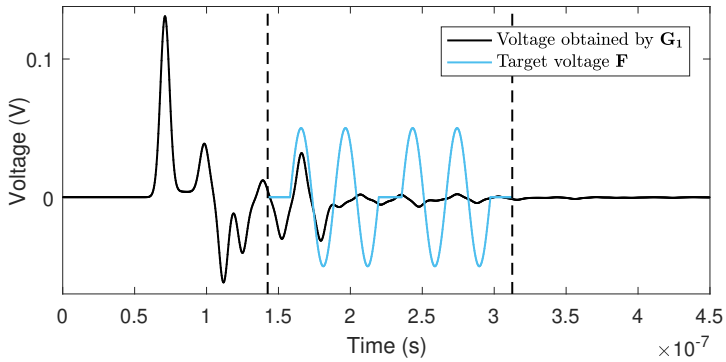

(a) Voltage signal $\mathbf{y}_{\text{init}}$ recorded after injecting the initial pulse $\mathbf{G}_1$.

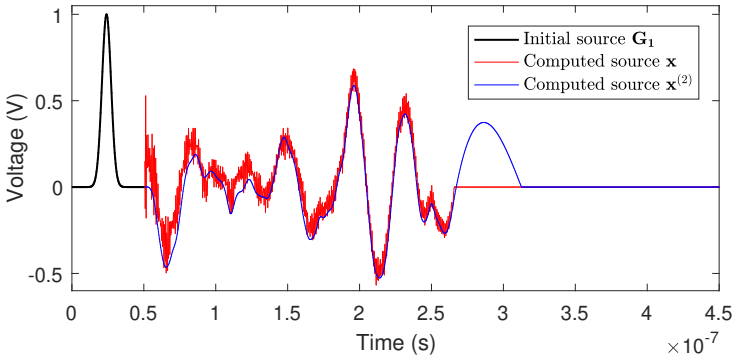

(b) Composed source $\mathbf{G}_1 + \mathbf{x}_{160\to f}$ before and after *a priori* filtering.

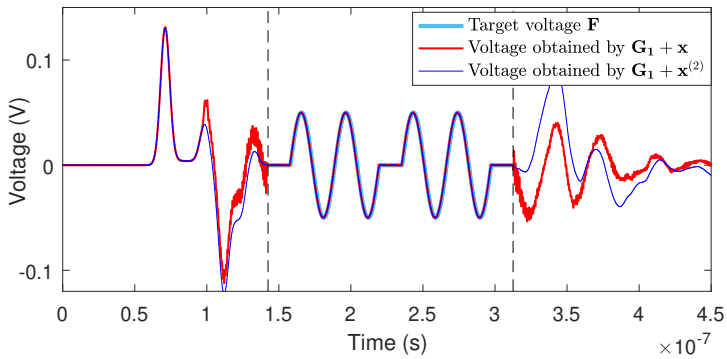

(c) Voltage signals recorded after injecting $\mathbf{G}_1 + \mathbf{x}_{160\to f}$ before and after filtering.

Figure 2.23: *After the emission of the composed source* $\mathbf{G}_1 + \mathbf{x}_{160\to f}$ *before and after a priori filtering, the receiver R records a signal, which is similar to* $\mathbf{G}_1$ *over the target time* $[t_q, t_f] = [1.42 \times 10^{-7}, 1.9 \times 10^{-7}]$ *lying between the two dashed lines.*

3

Generalized LCCF and Software Correction Application

THE Linear Combination of Configuration Field (LCCF) method is generalized to identify several temporal sources that control the voltage/current or field at one or more spatial points in the time domain. The generalized LCCF technique is first presented, followed by numerical illustrations in lossy wiring networks as well as anechoic and reverberant three-dimensional environments.

Electrical wires deliver safety and control operations to various wiring systems, so any shortening in their performance due to the appearance of faults might be dreadful from an economic point of view or in terms of lives. For this reason, researchers innovated and developed various wire diagnosis techniques to detect, locate, and diagnose the different faults in communication networks. Sometimes, these techniques are inefficient or suffer from limitations that reduce their proper functioning. Here, we introduce an interesting application for the generalized LCCF method called the Software Correction (SC) in wiring networks. The SC suppresses any unintentional perturbation resulting from the presence of any number of faults regardless of their position and nature. The acronym "LCCF" may refer to both the basic and the generalized versions of the LCCF method without specifying the used LCCF version. Simply, as long as we deal with one source generator and one receiver, we use the basic LCCF; otherwise, we use the generalized LCCF.

3.1 Generalized LCCF Method

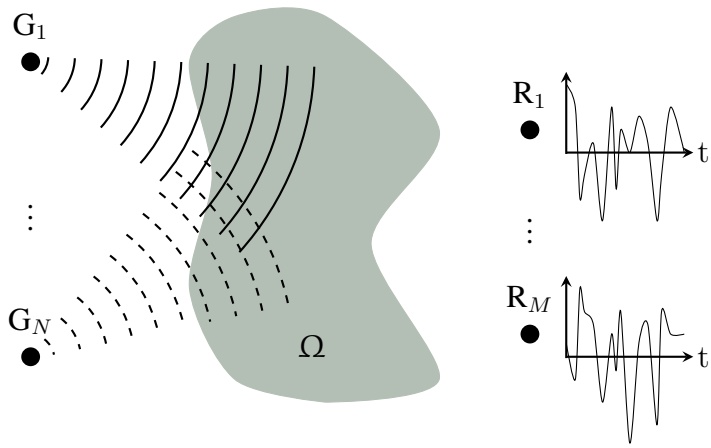

Figure 3.1: *Schematic setup of the LCCF method: the source generators emit signals that propagate and interfere through a linear medium, and perhaps being distorted by inhomogeneities in the medium. Each receiver records the signal it detects.*

Consider the schematic setup of the generalized LCCF method represented in Figure 3.1. For all $t \in [0, t_n]$, the source generators $\mathrm{G}_1, \cdots, \mathrm{G}_N$ emit $N \in \mathbb{N}^*$ nonnull input signals $\mathbf{x}_1, \cdots, \mathbf{x}_N$, respectively. For all $j \in \{1, \cdots, N\}$, $\mathbf{x}_j = [x_j(0), \cdots, x_j(n)] \in \mathbb{R}^{n+1}$. The signals $\mathbf{x}_1, \cdots, \mathbf{x}_N$ propagate, interfere and may be distorted due to discontinuities and inhomogeneities in the linear medium. A set of $M \in \mathbb{N}^*$ receivers $\mathrm{R}_1, \cdots, \mathrm{R}_M$ are placed at M distinct points, where each records the signal it detects over $[0, t_n]$. Let $\mathbf{y}_1, \cdots, \mathbf{y}_M \in \mathbb{R}^{n+1}$ be the output signals detected by $\mathrm{R}_1, \cdots, \mathrm{R}_M$, respectively. The general aim of the LCCF method is to identify $\mathbf{x}_1, \cdots, \mathbf{x}_N$ that may simultaneously control $\mathbf{y}_1, \cdots, \mathbf{y}_M$ over the target time $[t_q, t_f] = [q\Delta t, f\Delta t]$. Controlling $\mathbf{y}_1, \cdots, \mathbf{y}_M$ means to impose predefined target fields $\mathbf{F}_1, \cdots, \mathbf{F}_M$ at the M points over $[t_q, t_f]$. That is to say, $\mathbf{y}_{i/_{[t_q,t_f]}} = [y_i(q), \cdots, y_i(f)] = \mathbf{F}_i$, where $\mathbf{y}_{i/_{[t_q,t_f]}}$ are the amplitudes of $\mathbf{y}_i$ over $[t_q, t_f]$, $\forall i \in \{1, \cdots, M\}$. To reduce the computational costs, we avoid the calculation of $\mathbf{x}_{j/_{]t_f,t_n]}}$ and set them to 0 since they reach the receiver points after t_f having no influence over $[t_q, t_f]$. For the sake of sim-

plicity, we denote by $\mathbf{x}_j$ the part of the signal that is not identically zero, i.e., $\mathbf{x}_j = [x_j(0), \cdots, x_j(f)]$. The generalized LCCF method is based on solving the following linear system:

$$\mathbf{A}\mathbf{x} = \mathbf{F}, \tag{3.1}$$

where

- $\mathbf{x} = (\mathbf{x}_1, \cdots, \mathbf{x}_N)$ with $\mathbf{x}_j \in \mathbb{R}^{f+1}$ the vector to be computed containing the discrete data of the source emitted by G_j,
- $\mathbf{F} = (\mathbf{F}_1, \cdots, \mathbf{F}_M)$ with $\mathbf{F}_i \in \mathbb{R}^{f-q+1}$ the vector representing the discrete data of the target field imposed at R_i-point over $[t_q, t_f]$ after emitting $\mathbf{x}_1, \cdots, \mathbf{x}_N$,
- $\mathbf{A} = \begin{pmatrix} \mathbf{A}_{11} & \cdots & \mathbf{A}_{1N} \\ \vdots & \ddots & \vdots \\ \mathbf{A}_{M1} & \cdots & \mathbf{A}_{MN} \end{pmatrix}$ is a block matrix with $\mathbf{A}_{ij} \in \mathbb{M}_{(f-q+1)\times(f+1)}$ the rectangular real matrix that characterizes the medium between the two fixed G_j-point and R_i-point. Each A_{ij} is constructed according to the formula (2.4) based on the impulse response $(\mathbf{h}_1)_{ij}$ recorded by R_i after G_j injects $\mathbf{e}_1$. In general, the total number of simulations required to construct $\mathbf{A}$ is $N \times M$.

Similar to the basic LCCF, the generalized LCCF system (3.1) is also not square and may be solved for $\mathbf{x}$ in the least square sense by premultiplying both sides by $\mathbf{A}^T$. Then, we use Tikhonov regularization [134] to stabilize the new LCCF system

$$\left(\mathbf{A}^T\mathbf{A} + \epsilon\mathbf{I}\right)\mathbf{x} = \mathbf{A}^T\mathbf{F}. \tag{3.2}$$

Remark: In this chapter, voltage signals are considered for illustrations and applications in wiring networks; however, current signals can be considered in a similar way.

3.1.1 Numerical illustrations in wiring networks

We consider an aerial network Ω made up of unshielded two-conductor uniform cables. The topology and characteristics of Ω (number, lengths,

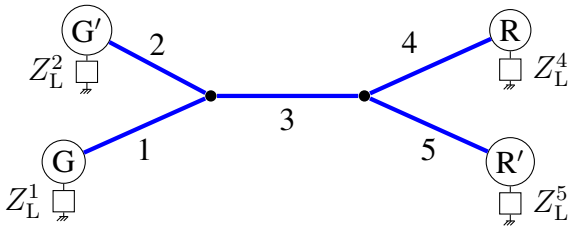

Figure 3.2: *Network configuration.*

Line Nb. l	z (in m)	Z_{C}^{l} (in Ω)	Z_{L}^{l} (in Ω)
1	5	50	50
2	6	50	0
3	4	50	-
4	5	50	50
5	8	50	50

Table 3.1: *Characteristics of the network.*

impedance, and loads of lines, etc.) may be chosen arbitrarily. For example, assume that Ω is the network of Figure 3.2 composed of two nodes and five point-to-point transmission lines. Table 3.1 represents their respective numbers l, lengths z, characteristic impedance Z_{C}^{l}, and load impedance Z_{L}^{l} for $l \in \{1, ..., 5\}$. For the sake of simplicity, no losses are considered in the lines of Ω. Losses are added to the lines of Ω by taking $R = 4\,\Omega$, causing amplitude reductions by 50.13%. Here, we do not take into account frequency-dependent losses.

As in the previous chapter, we consider an RLCG model, where a standard one-dimensional FDTD scheme is used to solve the telegrapher's equation (see Chapter 1 Section 1.3.2). The time step $\Delta t = 3.16 \times 10^{-10}\,\mathrm{s}$ and the space step $\Delta z = 0.1\,\mathrm{m}$ are selected in a way that satisfies the stability criteria (1.38). The total duration of the simulations is $[0, t_n] = [0, 1422\Delta t]$. We illustrate the generalized LCCF technique with two numerical examples. The objective is to show that the LCCF method still gives excellent results when several source generators or signal receivers are introduced to Ω. The considered Tikhonov parameter for the LCCF method is $\epsilon = 10^{-9}$.

One source generator and two receivers

The first illustration shows that the LCCF may simultaneously control multiple points of Ω over $[t_q, t_f]$ using a single source. Assume that a source generator G is placed at the start node of line 1 and two receivers, R and R′, are respectively placed at the terminations of lines 4 and 5 (see Figure 3.2). The aim is to identify a voltage source $\mathbf{x}$ that propagates through Ω, driving R and R′ to record two different target signals over $[t_q, t_f] = [450\Delta t, 600\Delta t]$. For R, we choose the Gaussian target voltage $\mathbf{G}_1$ (2.6) to be the corresponding target voltage, where $t_c = 210\Delta t$ and $\sigma = 20\Delta t$, whereas we choose the sinusoidal signal $\mathbf{S}_1$ (2.10) for R′, i.e., $\mathbf{F}_1 = \mathbf{G}_1$ and $\mathbf{F}_2 = \mathbf{S}_1$. The LCCF system (3.2) is then reduced to

$$\left[\begin{pmatrix}\mathbf{A}_{11}\\ \mathbf{A}_{21}\end{pmatrix}^T \begin{pmatrix}\mathbf{A}_{11}\\ \mathbf{A}_{21}\end{pmatrix} + \epsilon\mathbf{I}\right]\mathbf{x} = \begin{pmatrix}\mathbf{A}_{11}\\ \mathbf{A}_{21}\end{pmatrix}^T \begin{pmatrix}\mathbf{G}_1\\ \mathbf{S}_1\end{pmatrix}. \tag{3.3}$$

The LCCF characterization matrix $\mathbf{A} = \begin{pmatrix}\mathbf{A}_{11}\\ \mathbf{A}_{21}\end{pmatrix}$ is represented in Figure 3.3.

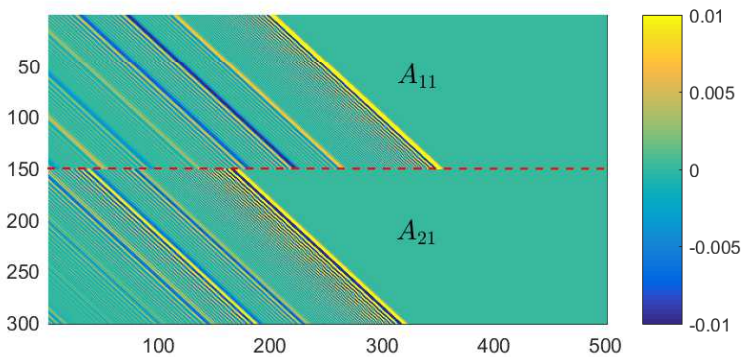

Figure 3.3: *Image of the LCCF characterization matrix* $\mathbf{A}$ *(*1 *generator and* 2 *receivers).*

After solving the above system (3.3), the complex source $\mathbf{x}$ is computed and represented in Figure 3.4a. Its emission by G leads R (resp. R′) to recording the voltage signal $\mathbf{y}$ (resp. $\mathbf{y}'$) represented in Figure 3.4b (resp. 3.4c). The small figures represent $\mathbf{y}$ and $\mathbf{y}'$ zoomed over the target time $[t_q, t_f] = [1.42 \times 10^{-7}, 1.9 \times 10^{-7}]$. It is obvious that $\mathbf{y}_{[t_q,t_f]} = \mathbf{G}_1$

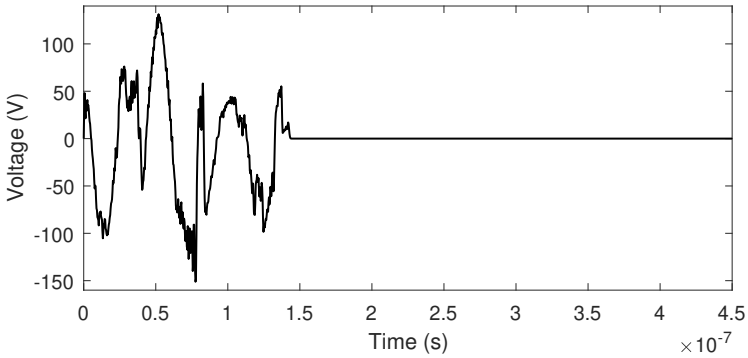

(a) Source $\mathbf{x}$ computed by the LCCF method.

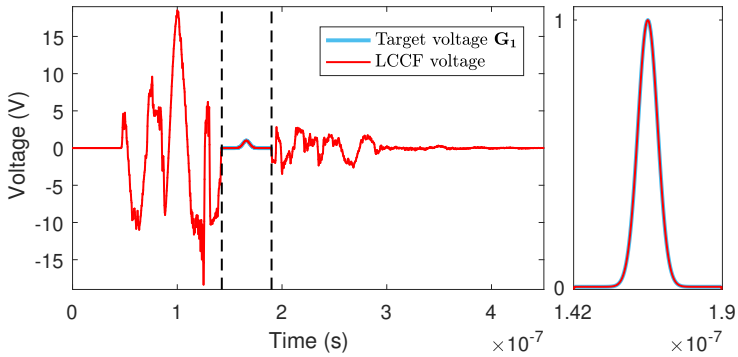

(b) Voltage signal $\mathbf{y}$ recorded after injecting $\mathbf{x}$.

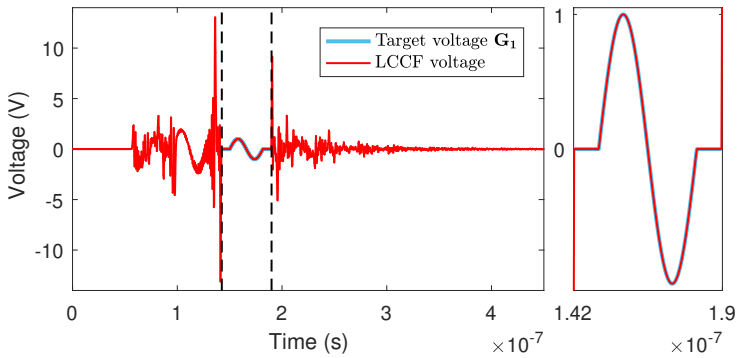

(c) Voltage signal $\mathbf{y}'$ recorded after injecting $\mathbf{x}$.

Figure 3.4: *Source* $\mathbf{x}$ *propagates through the network to control the voltage simultaneously at the terminations of lines* 4 *and* 5. *After its emission, the receiver R (resp. R′) records the signal* $\mathbf{y}$ *(resp.* $\mathbf{y}'$*) where the desired target voltage* $\mathbf{G}_1$ *(resp.* $\mathbf{S}_1$*) is recorded over the target time.*

and $\mathbf{y}'_{[t_q,t_f]} = \mathbf{S}_1$. The Relative Errors (REs) (2.8) in this case are $\mathrm{RE}\left(\mathbf{G}_1, \mathbf{y}_{[t_q,t_f]}\right) = 1.89 \times 10^{-4}$ and $\mathrm{RE}\left(\mathbf{S}_1, \mathbf{y}'_{[t_q,t_f]}\right) = 1.26 \times 10^{-3}$.

Two source generators and two receivers

Considering a more complex problem, we show how the LCCF technique may identify multiple sources to control multiple receiver points of Ω by imposing distinct target voltages. A second generator G′ is placed at the start node of line 2. We determine the temporal profiles of two sources $\mathbf{x}$ and $\mathbf{x}'$ generated by G and G′, respectively. The considered target signals are still the same at the R and R′-levels as previously described. The LCCF system (3.2) becomes

$$\left[\begin{pmatrix}\mathbf{A}_{11} & \mathbf{A}_{12}\\ \mathbf{A}_{21} & \mathbf{A}_{22}\end{pmatrix}^T \begin{pmatrix}\mathbf{A}_{11} & \mathbf{A}_{12}\\ \mathbf{A}_{21} & \mathbf{A}_{22}\end{pmatrix} + \epsilon\mathbf{I}\right]\begin{pmatrix}\mathbf{x}_1\\ \mathbf{x}_2\end{pmatrix} = \begin{pmatrix}\mathbf{A}_{11} & \mathbf{A}_{12}\\ \mathbf{A}_{21} & \mathbf{A}_{22}\end{pmatrix}^T \begin{pmatrix}\mathbf{G}_1\\ \mathbf{S}_1\end{pmatrix}. \tag{3.4}$$

The corresponding LCCF characterization matrix $\mathbf{A} = \begin{pmatrix}\mathbf{A}_{11} & \mathbf{A}_{12}\\ \mathbf{A}_{21} & \mathbf{A}_{22}\end{pmatrix}$ is represented in Figure 3.5.

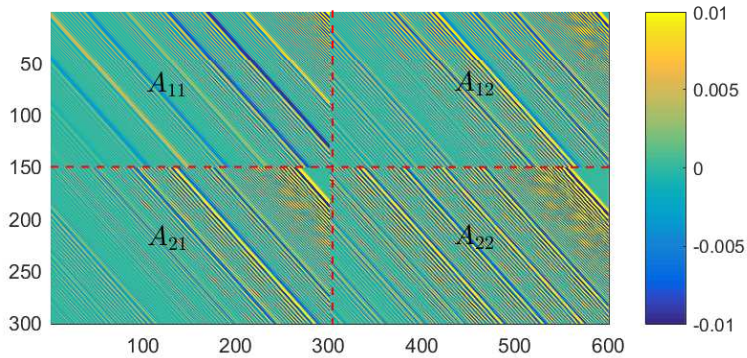

Figure 3.5: *Image of the LCCF characterization matrix* $\mathbf{A}$ *(2 generators and 2 receivers).*

The above system is solved, then two complex sources, $\mathbf{x}$ and $\mathbf{x}'$, are computed and represented in Figures 3.6a and 3.6b. After emitting $\mathbf{x}$ and $\mathbf{x}'$ simultaneously, R (resp. R′) records the voltage $\mathbf{y}$ (resp. $\mathbf{y}'$) represented in Figure 3.6c (resp. 3.6d). The small figures represent $\mathbf{y}$ and $\mathbf{y}'$ zoomed over

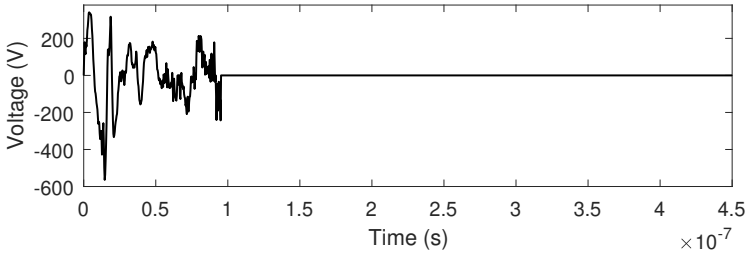

(a) Source $\mathbf{x}$ computed by the LCCF method.

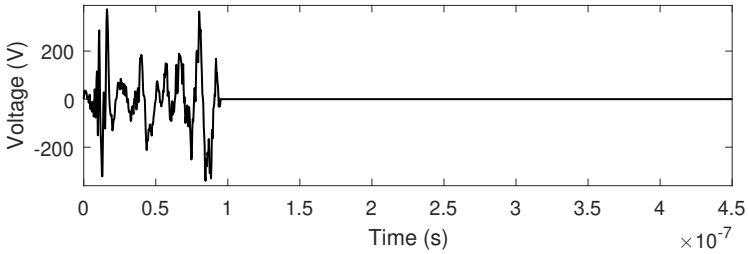

(b) Source $\mathbf{x}'$ computed by the LCCF method.

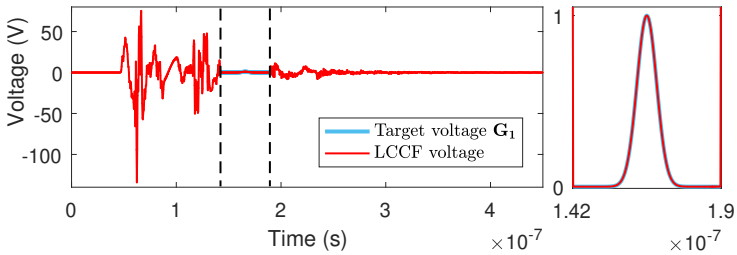

(c) Voltage signal $\mathbf{y}$ recorded by R after injecting $\mathbf{x}$ and $\mathbf{x}'$ simultaneously.

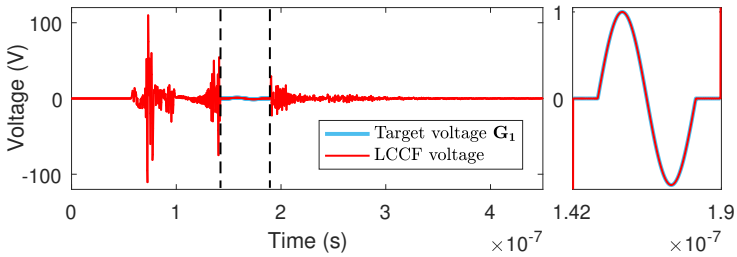

(d) Voltage signal $\mathbf{y}'$ recorded by R′ after injecting $\mathbf{x}$ and $\mathbf{x}'$ simultaneously.

Figure 3.6: *Sources* $\mathbf{x}$ *and* $\mathbf{x}'$ *propagate through the network to control the voltage simultaneously at the terminations of lines* 4 *and* 5*. After their emission, the receiver R (resp. R′) records the signal* $\mathbf{y}$ *(resp.* $\mathbf{y}'$*) where the desired target voltage* $\mathbf{G}_1$ *(resp.* $\mathbf{S}_1$*) is recorded over the target time.*

the target time $[t_q, t_f] = [1.42 \times 10^{-7}, 1.9 \times 10^{-7}]$. The signals impose $\mathbf{G}_1$ and $\mathbf{S}_1$ at the terminations of lines 4 and 5, respectively. The relative errors (2.8) recorded in this example are RE $\left(\mathbf{G}_1, \mathbf{y}_{[t_q,t_f]}\right) = 1.57 \times 10^{-3}$ and RE $\left(\mathbf{S}_1, \mathbf{y}'_{[t_q,t_f]}\right) = 1.92 \times 10^{-3}$. We note that any attenuation level may still be selected without affecting the applicability of the generalized LCCF method. This idea was successfully tested in Chapter 2 Section 2.1.2. We have shown the existence of a linear relation between the sources computed at different attenuation levels.

3.1.2 Numerical illustrations in free space environments

In the $5\,\mathrm{cm} \times 4\,\mathrm{cm} \times 3\,\mathrm{cm}$ cavity Ω represented in Figure 3.7, we use the FDTD scheme (see Section 1.3.1) to solve Maxwell's equations. The total duration of the simulations is $[0, t_n] = [0, 1422\Delta t]$. The time step $\Delta \mathrm{t} = 3.85 \times 10^{-12}\,\mathrm{s}$ and the space step $(\Delta x, \Delta y, \Delta z) = (0.2\,\mathrm{cm}, 0.2\,\mathrm{cm}, 0.2\,\mathrm{cm})$ are selected in a way that satisfies the stability criteria (1.30). As an example, the first component of the electric field E_x is chosen to illustrate the LCCF method; however, any electric or magnetic component may still be considered.

Assume that two source generators G and G′ are placed at $(6\Delta x, 12\Delta y, 11\Delta z)$ and $(15\Delta x, 5\Delta y, 13\Delta z)$ (see the black points in Figure 3.7), whereas two receivers R and R′ are placed at $(11\Delta x, 10\Delta y, 12\Delta z)$ and $(4\Delta x, 12\Delta y, 7\Delta z)$ (see the red points in Figure 3.7). The generators and the receivers may be placed anywhere in the cavity. We use the LCCF method to identify electric sources $\mathbf{x}$ and $\mathbf{x}'$ in the TD to impose the target electric field $\mathbf{G}_1$ (2.6) ($t_c = 210\Delta t$ and $\sigma = 20\Delta t$) at two different spatial points over $[t_q, t_f] = [500\Delta, 920\Delta t]$. The target signal $\mathbf{G}_1$ is represented in blue sky in Figures 3.8c and 3.8d ($\mathbf{F}_1 = \mathbf{F}_2 = \mathbf{G}_1$). Here, the Tikhonov parameter for the LCCF method is $\epsilon = 10^{-12}$.

Anechoic cavity

After applying the LCCF process, the sources $\mathbf{x}$ and $\mathbf{x}'$ are computed and represented in Figures 3.8a and 3.8b, respectively. After a simultaneous emission of the sources, each by its corresponding generator, the electric fields $\mathbf{y}$ and $\mathbf{y}'$ are recorded by R and R′, then represented in Figures 3.8c and 3.8d. The small

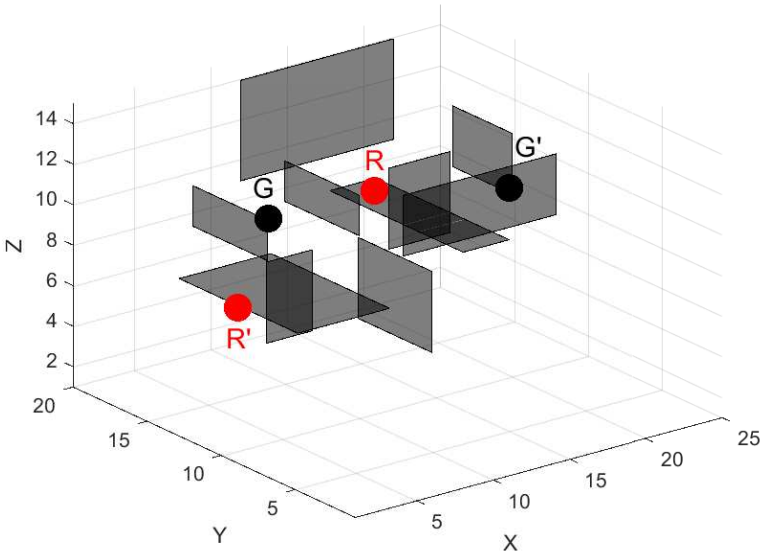

Figure 3.7: *Cavity configuration used in simulations.*

figures represent $\mathbf{y}$ and $\mathbf{y}'$ zoomed over $[t_q, t_f] = [1.92 \times 10^{-9}, 3.54 \times 10^{-9}]$. In fact, $\mathbf{y}_{/_{[t_q,t_f]}} = \mathbf{y}'_{/_{[t_q,t_f]}} = \mathbf{G}_1$ for $t \in [t_q, t_f]$, where $[t_q, t_f]$ lies between the two dashed lines in Figure 3.8. The relative errors between the target and the obtained electric fields are 4.15×10^{-6} for R and 3.38×10^{-6} for R′.

Reverberant cavity

Let Ω now be the reverberant cavity in which the waves are totally reflected once reaching the walls. We re-characterize Ω to compute the new sources $\mathbf{x}$ and $\mathbf{x}'$ represented in Figures 3.9a and 3.9b. The receivers R and R′ record the electric signals $\mathbf{y}$ and $\mathbf{y}'$ represented in Figure 3.9c and 3.9d. The small figures represent $\mathbf{y}$ and $\mathbf{y}'$ zoomed over $[t_q, t_f] = [1.92 \times 10^{-9}, 3.54 \times 10^{-9}]$. It is obvious that $\mathbf{y}$ and $\mathbf{y}'$ are almost the target signal $\mathbf{G}_1$ over $[t_q, t_f]$. The relative errors between $\mathbf{G}_1$ and the obtained electric fields are estimated at 2.77×10^{-6} for R and 1.37×10^{-5} for R′.

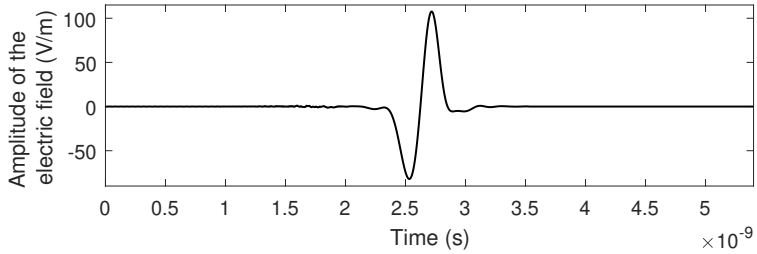

(a) Source $\mathbf{x}$ computed by the LCCF method.

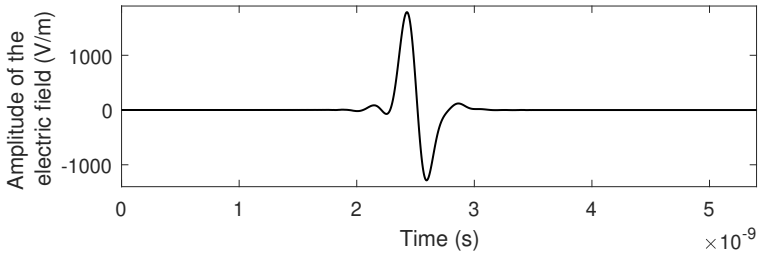

(b) Source $\mathbf{x}'$ computed by the LCCF method.

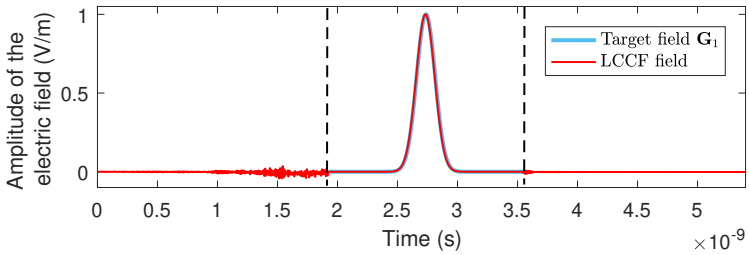

(c) Electric signal $\mathbf{y}$ recorded by R after injecting $\mathbf{x}$ and $\mathbf{x}'$ simultaneously.

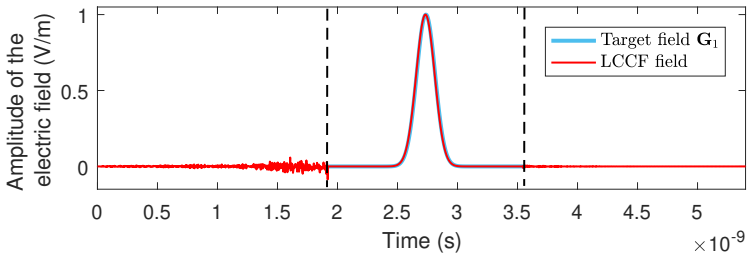

(d) Electric signal $\mathbf{y}'$ recorded by R$'$ after injecting $\mathbf{x}$ and $\mathbf{x}'$ simultaneously.

Figure 3.8: *Signals* $\mathbf{x}$ *and* $\mathbf{x}'$ *propagate through the anechoic cavity to control the electric field at the receiver points. After their emission, the receivers R and R$'$ record the signals* $\mathbf{y}$ *and* $\mathbf{y}'$ *where the desired target electric field* $\mathbf{G}_1$ *is recorded over the target time.*

For each case of the anechoic or reverberant cavity, the two sources computed by the LCCF are nontrivial as it is difficult to define a trajectory for their interference and interaction inside the cavity. In both cases, $\mathbf{y}$ and $\mathbf{y}'$ are uncontrolled $\forall\ t \in [0, t_n] \setminus [t_q, t_f]$. However, in a reverberant medium, the LCCF computes more complex sources to compensate for the reflections resulting from the scatterers and the walls of Ω as well.

The advantages of the generalized LCCF are similar to its basic version discussed and analyzed in Chapter 2. Whether in its basic or generalized forms, the LCCF is always independent of the topology of the studied medium. The medium is always viewed as a black box without any prior knowledge of all the occurring physical phenomena (attenuation, dispersion, multiple reflections, absorption, etc.). The LCCF relies solely on the impulse responses between the source points and the receiver points. Interestingly, the LCCF may be applied to many activities in EMC. In particular, it maybe used with communication systems that are often exposed to faults, causing their malfunctioning. In the following, we introduce a new process called the *software correction* to address such faults. Then, numerical examples are illustrated to show the applicability of such a process.

3.2 Software Correction of Faulty Lossy Linear Networks

For many reasons such as safety, security, and optimal performance in wiring systems, numerous techniques have been developed to anticipate or detect the occurrence of electrical faults in wiring networks. Fault detection is often used to shut down electrical systems and prevent exposure to all kinds of risks or damages. After detecting the faults, the intervention of other methods, such as the reflectometry-based [99], TR-imaging [103], and FasTR [139] techniques, adopted to locating and diagnosing faults in power and transmission line networks becomes essential. The ultimate objective behind wire diagnosis is to repair these faults to preserve the optimal performance of the system in the shortest time and with the smallest investment. This process is called the hardware correction or troubleshooting as it requires a close-up physical treatment.

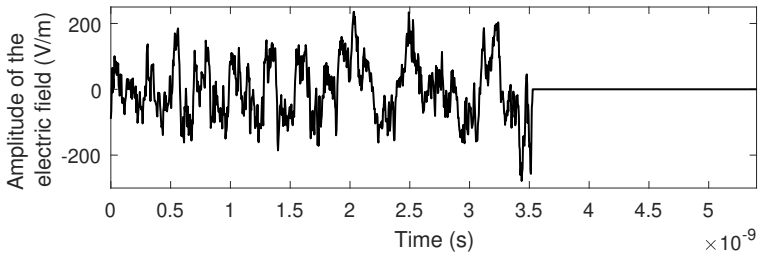

(a) Source $\mathbf{x}$ computed by the LCCF method.

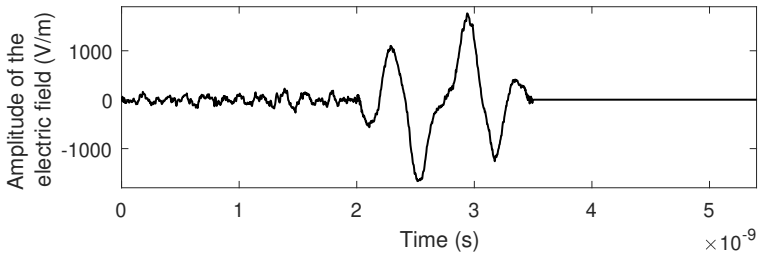

(b) Source $\mathbf{x}'$ computed by the LCCF method.

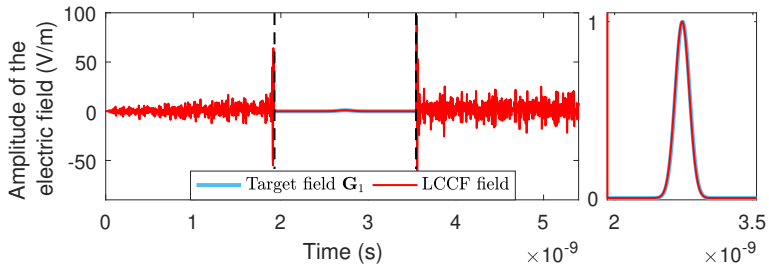

(c) Electric signal $\mathbf{y}$ recorded by R after injecting $\mathbf{x}$ and $\mathbf{x}'$ simultaneously.

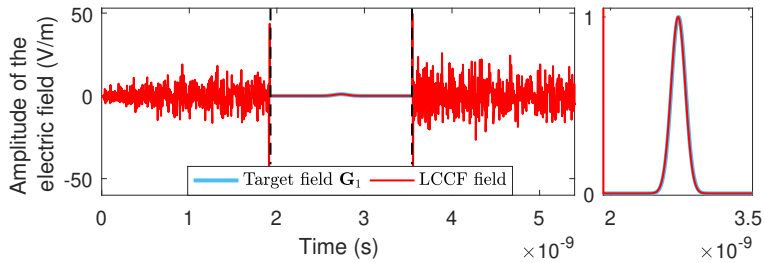

(d) Electric signal $\mathbf{y}'$ recorded by R′ after injecting $\mathbf{x}$ and $\mathbf{x}'$ simultaneously.

Figure 3.9: *Signals* $\mathbf{x}$ *and* $\mathbf{x}'$ *propagate through the reverberant cavity to control the electric field at the receiver points. After their emission, the receivers R and R′ record the signals* $\mathbf{y}$ *and* $\mathbf{y}'$ *where the desired target electric field* $\mathbf{G}_1$ *is recorded over the target time.*

Unfortunately, many drawbacks can be highlighted from the troubleshooting process. Firstly, after detecting the presence of the faults, unexpected shutdown of the system during the detection-maintenance period may waste time and money. Secondly, repairing the faults is also money and time consuming, such as the drilling or submarine processes needed to access faults inherent in underground or undersea cables. Thirdly, the situation worsens when faults are located in hard-to-access areas, such as radioactive zones in nuclear plants or satellites in outer space, thus absolutely inaccessible to maintenance processes.

Alternatively, other paradigms are required, such as the Software Correction (SC) process, to tolerate the faults and handle them as a part of the network's topology without the need to access their location or to recover information about them. The SC can be achieved by adding new input signals to the faulty networks to satisfy the following:

- Compensate for the effects of the faults,
- Ensure a proper signal transmission to preserve the optimal performance of the networks,
- Force the faulty networks to function as the healthy ones.

The SC is defined as the digital processing to remotely tolerate the faults in wiring communication networks without any physical intervention. It may be used in the following two cases:

- Faults that can be located by the wire diagnosis techniques, but
  - Not immediately accessible to maintenance processes, such as faults in underground or undersea cables. Once the faults are detected, shutting down the system is no longer necessary during the detection-maintenance period. However, the SC can serve as a temporary solution and preserve the optimal performance of the system away from any critical consequence during this period.
  - Inaccessible to maintenance processes, such as faults located in radioactive zones in nuclear plants or satellites in outer space.

- Faults that may not be located by the wire diagnosis techniques due to many reasons such as the ambiguity in symmetric networks, complex networks, "blind spot[1]", etc.

The SC process is independent of the topology of the studied network regardless of its linear behavior (resistors, capacitors, inductors, etc.). We emphasize that the independence of the network's topology and characteristics includes its complexity (cartography, number of lines, and junctions), impedance (characteristic and load), as well as the multiple reflections, attenuation, and dispersion occurring in the network during signals propagation. Moreover, the SC is also independent of the number, nature, and location of the potential faults that may appear in the network. During the SC process, the tested network is considered as a black box during the whole process, where the interventions occur only at the source point(s) and the receiver point(s).

In the sequel, the LCCF method is used to bring an SC to the faulty network denoted by Ω' with resistive loads. The faulty network Ω' has the same topology and characteristics as the healthy network Ω, but with the presence of one or more faults inherent in its lines. In this section, we illustrate the SC with three examples when Ω' presents a soft fault, a hard fault (short circuit or open circuit), and multiple faults (hard and soft) placed at random positions to show that the SC process is independent of the nature, number and position of the fault(s). Then, we show that the applicability of the SC process is not only confined to faults inherent in the network's lines, but defects resulting from external sources can also be compensated. In these illustrations, we consider voltage signals to apply the SC process; however, current signals can also be considered in a similar way.

Problem settings

For example, we assume that Ω is the complex network represented in Figure 3.10 composed of two nodes and six point-to-point lines with the

[1]In the avionic industry, a significant source of error in reflectometry is referred to as the "blind spot" that occurs with cables of relatively short lengths. This is usually caused by the fact that the reflected signal overlaps the incident one as a result of the momentary time delay.

characteristics represented in Table 3.2 (line number l, line length z, characteristic impedance Z_{C}^{l}, load impedance Z_{L}^{l}) and losses chosen arbitrarily, the resistance $R = 0.025\,\Omega/\mathrm{m}$ for instance. For the sake of simplicity, we do not take into account frequency-dependent losses. Actually, any attenuation level may certainly be considered, although the chosen value of the resistance provides a low level of attenuation coefficient ($\alpha = 0.0022\,\mathrm{dB/m}$), causing information losses by 5.36%. As a matter of fact, the higher the attenuation level, the better the SC works since high losses completely attenuate some reflections resulting from the faults before reaching the receiver point, especially those of low amplitudes. Consequently, it limits the liability of the SC to cancel the anomalies. For illustration purposes, assume that the attenuation level introduced to the network is high enough in which a signal sent down the wire is completely attenuated before reaching the receiver point. Then, the recorded signals at this point in the presence or absence of the faults are null. As a result, the SC is ineffective in such particular case. This can easily be noticed when addressing soft faults with high losses as they create only small impedance changes on the wire.

Considering an RLCG model, the telegrapher's equations are solved using a standard one-dimensional FDTD scheme, as described in Chapter 1 Section 1.3.2, to compute the voltage at the receiver points. The total duration of the simulations is $[0, t_n] = [0, 1422\Delta t]$ ($n = 1422$), where $\Delta t = 3.9 \times 10^{-9}\,\mathrm{s}$ and $\Delta z = 0.1\,\mathrm{m}$ are chosen in a way that satisfies the stability criteria (1.38). The SC may be applied over any target time $[t_q, t_f] \subseteq [0, t_n]$; however, in this chapter, the SC process is addressed over the entire time interval ($[t_q, t_f] = [0, t_n]$), which is significantly more complicated than considering a short period of time.

We discuss the linear SC process by using one source generator G and two receivers (R and R′) that may be placed at any points on Ω. For instance, we choose the start node of line 1 and the terminations of lines 4 and 5 as the positions of G, R, and R′, respectively. The Tikhonov parameter considered in this section is $\epsilon = 10^{-9}$. To show the impact of the fault(s), we record the voltage signals at the receiver points after two separate injections of a Gaussian pulse $\mathbf{G}_2$ (2.6) ($t_c = 40\Delta t$ and $\sigma = 8\Delta t$) in the healthy Ω and the faulty Ω' networks. For $\lambda = \{1, 2\}$, we denote by $\mathbf{V}_{\mathrm{H}}^{\lambda}$ the healthy voltage signal recorded by the receivers after injecting $\mathbf{G}_2$ in Ω; however, we denote

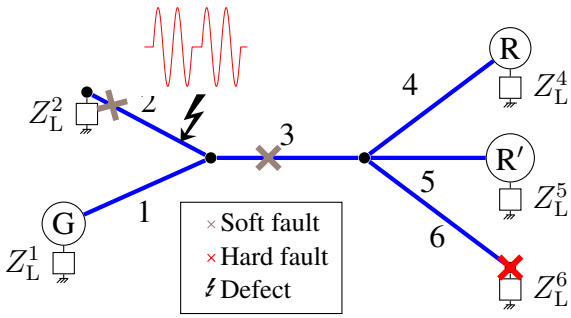

Figure 3.10: *Configuration of the linear network used during the SC process.*

Line Nb. l	z (in m)	Z_C^l (in Ω)	Z_L^l (in Ω)
1	1	50	50
2	3	50	∞
3	4	50	-
4	8	50	50
5	5	50	50
6	7	50	0

Table 3.2: *Characteristics of the healthy linear network.*

by $\mathbf{V}_F^\lambda$ the faulty voltage signal recorded by the receivers after injecting $\mathbf{G}_2$ in Ω'.

3.2.1 Soft fault

Assume that a soft fault has appeared in line 2 at $2.5\,\mathrm{m}$ distance from the first junction of Ω. The fault is represented by a gray X-mark in the network of Figure 3.10. The healthy signals $\mathbf{V}_H^1$ and $\mathbf{V}_H^2$ are respectively displayed in green in Figures 3.11b and 3.11c, while the faulty signals $\mathbf{V}_F^1$ and $\mathbf{V}_F^2$ are represented in blue in the same figures. These slight output distortions at the receiver levels refer to the effect of the soft fault. Using the LCCF method, we now solve the linear system

$$\left[\begin{pmatrix}\mathbf{A}_{11}\\ \mathbf{A}_{21}\end{pmatrix}^T\begin{pmatrix}\mathbf{A}_{11}\\ \mathbf{A}_{21}\end{pmatrix}+\epsilon\mathbf{I}\right]\mathbf{x}=\begin{pmatrix}\mathbf{A}_{11}\\ \mathbf{A}_{21}\end{pmatrix}^T\begin{pmatrix}\mathbf{V}_H^1\\ \mathbf{V}_H^2\end{pmatrix}. \tag{3.5}$$

for $\mathbf{x}$. The new signal $\mathbf{x}$ is the source to be identified and added to $\mathbf{G}_2$ to eliminate the disturbances caused by the fault (see Figure 3.11a). After its injection, the corrected voltage signals $\mathbf{V}_{\mathrm{C}}^1$ and $\mathbf{V}_{\mathrm{C}}^2$ are recorded by R and R′, then represented in red in Figures 3.11b and 3.11c, respectively. For all λ, the signal $\mathbf{V}_{\mathrm{C}}^{\lambda}$ is similar to $\mathbf{V}_{\mathrm{H}}^{\lambda}$ with relative errors (2.8) RE $(\mathbf{V}_{\mathrm{H}}^1, \mathbf{V}_{\mathrm{C}}^1) = 1.46\times 10^{-7}$ and RE $(\mathbf{V}_{\mathrm{H}}^2, \mathbf{V}_{\mathrm{C}}^2) = 1.43 \times 10^{-7}$.

3.2.2 Hard fault

In Ω, a hard fault is simulated by modifying the load impedance Z_{L}^6 from 0 to $\infty\,\Omega$ (see the red X-mark in Figure 3.10), then Ω' is the short-circuited network at the termination of line 6. After injecting $\mathbf{G}_2$, the healthy signal $\mathbf{V}_{\mathrm{H}}^1$ (resp. $\mathbf{V}_{\mathrm{H}}^2$) and the faulty signal $\mathbf{V}_{\mathrm{F}}^1$ (resp. $\mathbf{V}_{\mathrm{F}}^2$) are respectively displayed in green and blue in Figure 3.12b (resp. 3.12c). In fact, the hard faults generate perturbations of greater amplitudes than those of soft ones; that is why it is important to rectify the outputs in such cases. Accordingly, the same LCCF system (3.5) is solved after re-characterizing Ω'. Hence, the new source $\mathbf{x}$ is identified (see Figure 3.12a) and sent down in Ω' to produce the corrected signals $\mathbf{V}_{\mathrm{C}}^1$ and $\mathbf{V}_{\mathrm{C}}^2$. Notably, $\mathbf{V}_{\mathrm{H}}^{\lambda}$ and $\mathbf{V}_{\mathrm{C}}^{\lambda}$ are almost identical with the relative errors (2.8) RE $(\mathbf{V}_{\mathrm{H}}^1, \mathbf{V}_{\mathrm{C}}^1) = 1.54 \times 10^{-7}$ and RE $(\mathbf{V}_{\mathrm{H}}^2, \mathbf{V}_{\mathrm{C}}^2) = 1.51 \times 10^{-7}$.

3.2.3 Multiple faults

The situation worsens when multiple faults appear in Ω. We assume that two soft faults are inherent in lines 2 and 3 at $2.5\,\mathrm{m}$ and $1.5\,\mathrm{m}$ distances from the first junction, respectively. Add to that, a hard fault (open circuit) is simulated at the termination of line 6. The soft faults are represented by gray X-marks, while the red X-mark in Figure 3.10 represents the hard fault. The disturbances resulting from the faults are shown in Figures 3.13b and 3.13c as the differences between the healthy and the faulty signals. After re-characterizing Ω' to solve the LCCF system (3.5), the new source $\mathbf{x}$ is computed and represented in Figure 3.13a. Its injection in Ω' leads to recording the corrected signal $\mathbf{V}_{\mathrm{C}}^1$ by R and $\mathbf{V}_{\mathrm{C}}^2$ by R′. Remarkably, $\mathbf{V}_{\mathrm{H}}^1$ and $\mathbf{V}_{\mathrm{C}}^1$ coincide for the entire time domain with a relative error (2.8) RE $(\mathbf{V}_{\mathrm{H}}^1, \mathbf{V}_{\mathrm{C}}^1) = 4.33 \times 10^{-7}$. Similarly, $\mathbf{V}_{\mathrm{H}}^2$ and $\mathbf{V}_{\mathrm{C}}^2$ are indistinguishable with RE $(\mathbf{V}_{\mathrm{H}}^2, \mathbf{V}_{\mathrm{C}}^2) = 4.24 \times 10^{-7}$.

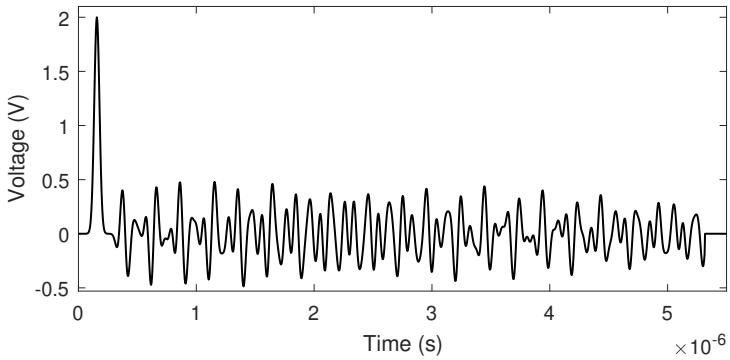

(a) Source $\mathbf{x}$ to tolerate the soft fault.

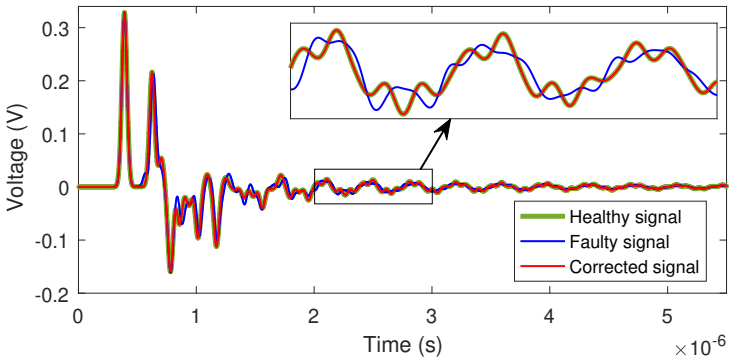

(b) Healthy, faulty and corrected voltage signals at the R-level.

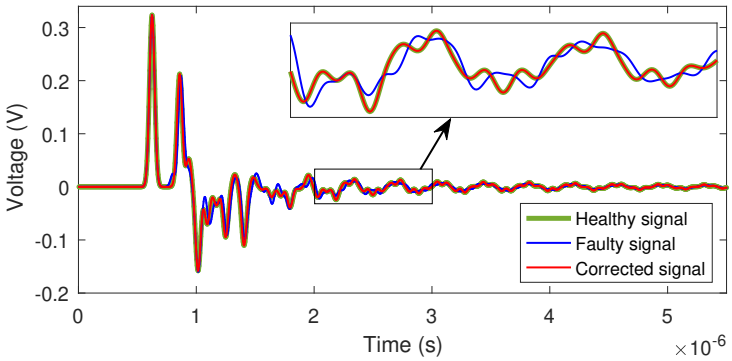

(c) Healthy, faulty and corrected voltage signals at the R′-level.

Figure 3.11: *Software correction of a faulty network presenting a single soft fault.*

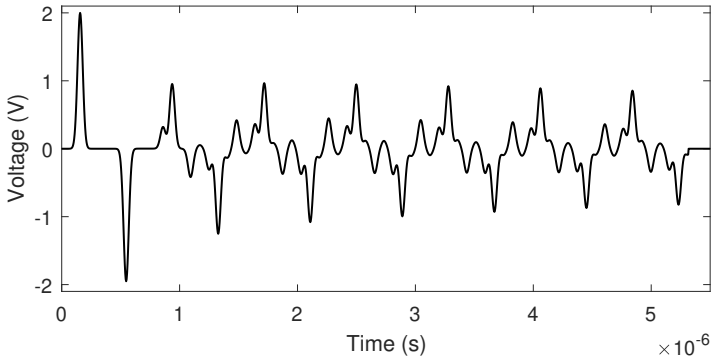

(a) Source $\mathbf{x}$ to tolerate the hard fault.

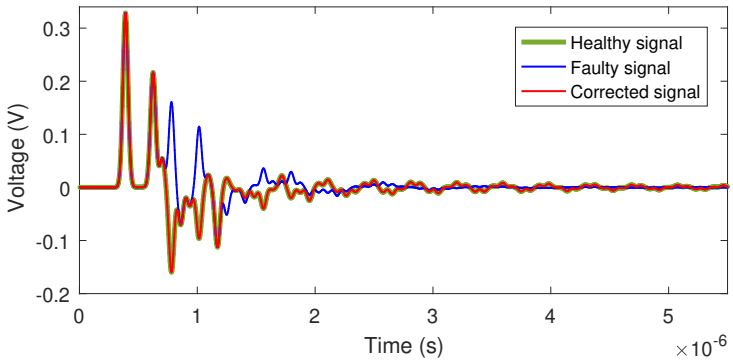

(b) Healthy, faulty and corrected voltage signals at the R-level.

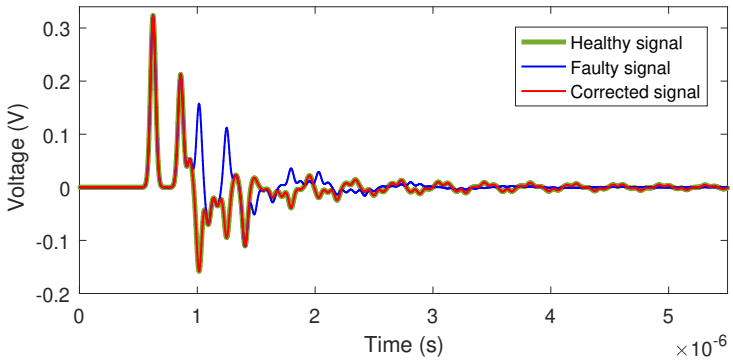

(c) Healthy, faulty and corrected voltage signals at the R′-level.

Figure 3.12: *Software correction of a linear faulty network presenting a single hard fault.*

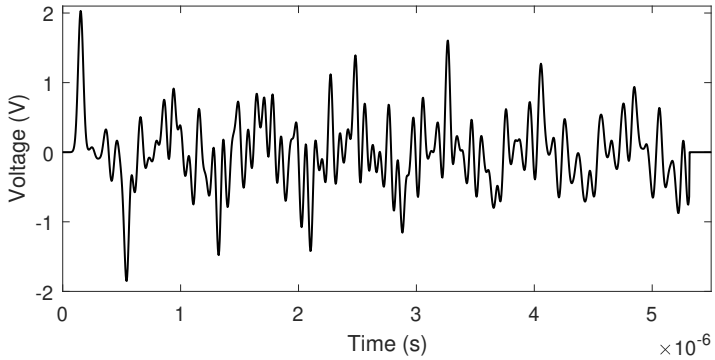

(a) Source $\mathbf{x}$ to tolerate the multiple faults.

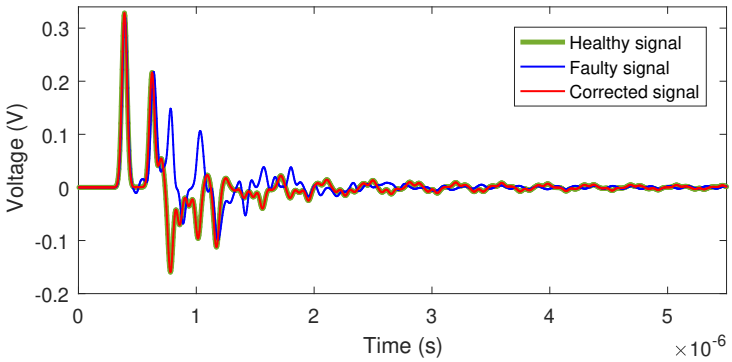

(b) Healthy, faulty and corrected voltage signals at the R-level.

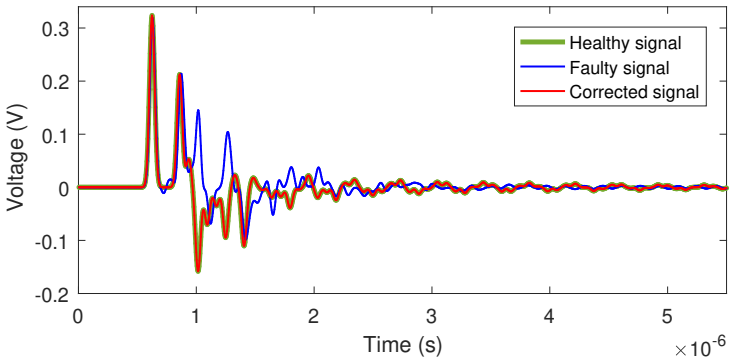

(c) Healthy, faulty and corrected voltage signals at the R′-level.

Figure 3.13: *Software correction of a linear faulty network presenting multiple faults.*

3.2.4 External defect

A defect may be any type of transient voltage perturbation. It could be an external electromagnetic field that couples the network along an unshielded cable length, leading to overvoltages and degradation in performance. Assume that a defect is generated by an external radiator and couples Ω at $1\,\mathrm{m}$ distance from the first junction along the second line, as represented in Figure 3.10. In fact, we deal with defects of constant profiles, i.e., the radiator keeps emitting the same signal without any changes. These defects can take any form; for example, we suppose that the defect is the red signal represented in Figure 3.10. The distortions caused by this interference at the receiver levels are represented in Figures 3.14b and 3.14c. Using the LCCF, we correct the faulty outputs by identifying the temporal source to be emitted by G (see Figure 3.14a). The relative errors (2.8) between the healthy and the corrected signals are $\mathrm{RE}\left(\mathbf{V}_{\mathrm{H}}^{1}, \mathbf{V}_{\mathrm{C}}^{1}\right) = 8.89 \times 10^{-6}$ and $\mathrm{RE}\left(\mathbf{V}_{\mathrm{H}}^{2}, \mathbf{V}_{\mathrm{C}}^{2}\right) = 8.78 \times 10^{-6}$.

3.2.5 Multiple faults and external defects

When faults and defects meet together to perturb Ω, the SC process remains applicable. Assume that Ω suffers from the multiple faults described earlier and a defect coupling the network at $1\,\mathrm{m}$ distance from the first junction along line 2. The SC process is displayed in Figure 3.15 where the outputs are corrected despite their high distortions. The relative errors (2.8) in this case are $\mathrm{RE}\left(\mathbf{V}_{\mathrm{H}}^{1}, \mathbf{V}_{\mathrm{C}}^{1}\right) = 4.02 \times 10^{-4}$ and $\mathrm{RE}\left(\mathbf{V}_{\mathrm{H}}^{2}, \mathbf{V}_{\mathrm{C}}^{2}\right) = 3.96 \times 10^{-4}$.

The SC process may be applied to any defective system regardless of the number, nature (soft/hard or external), and position of the faults or defects. In [140–142], we considered other network topology and successfully corrected the faulty outputs in the presence of faults and defects of different nature and position. Only communication networks transferring data are considered for rectifications and not power systems that transmit electrical energy. Although no information about the network topology is required for the SC, prior knowledge of the healthy output and a free extremity to branch a receiver are always needed. It is interesting to highlight the possibility of adding constraints (see Chapter 2 Section 2.3.2) to the SC problem to filter the source when defects couple the network and distort its outputs [142]. When a hard fault appears on the linking source-receiver path, the SC stops working as no signal is detected by the receiver. For example, if line 3 is cut at any of its

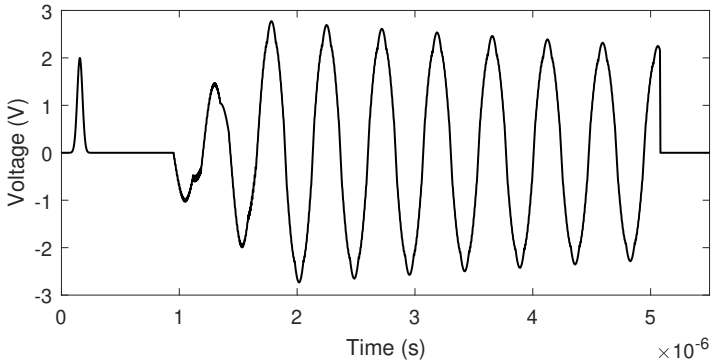

(a) Source $\mathbf{x}$ to tolerate the defect.

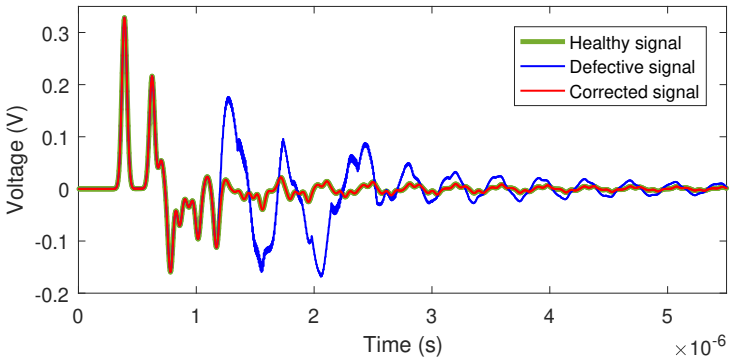

(b) Healthy, faulty and corrected voltage signals at the R-level.

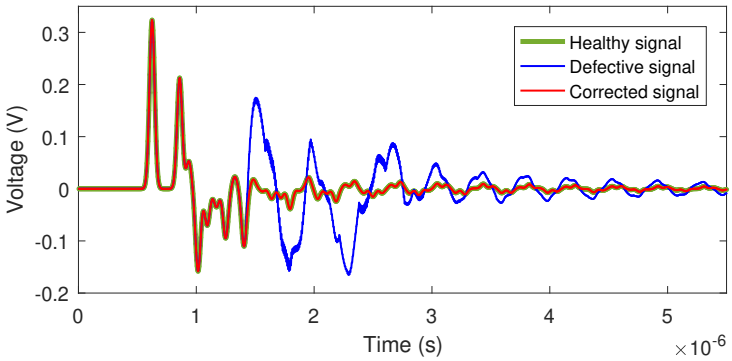

(c) Healthy, faulty and corrected voltage signals at the R′-level.

Figure 3.14: *Software correction of a defective network coupled by an external interfering signal.*

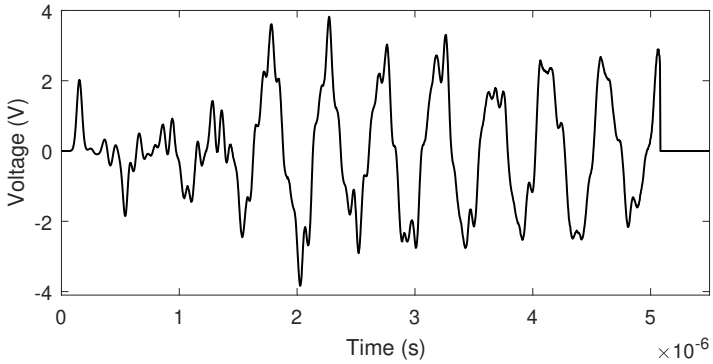

(a) Source $\mathbf{x}$ to tolerate the inherent faults and the external defect.

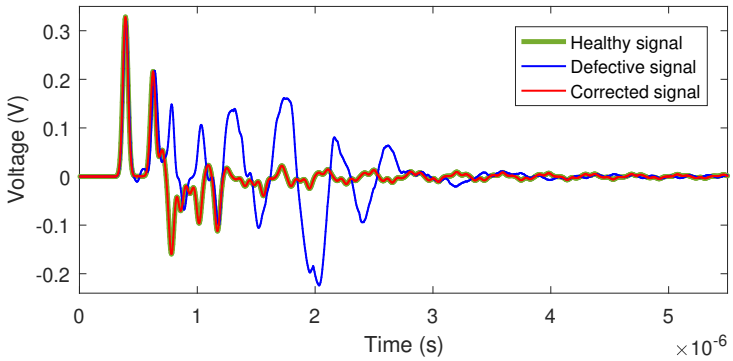

(b) Healthy, faulty and corrected voltage signals at the R-level.

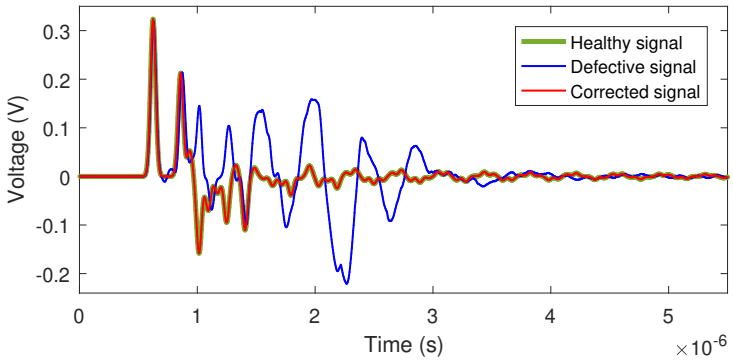

(c) Healthy, faulty and corrected voltage signals at the R′-level.

Figure 3.15: *Software correction of a defective network coupled by an interfering signal with multiple faults inherent in its lines.*

points, the SC process is not applicable anymore, in such a particular case, and other alternative wire diagnosis techniques are required to locate the fault(s). These techniques may necessitate prior knowledge of the network's topology. Not only the SC process may be an application for the LCCF method, but such a technique may also be applied in the field of signal integrity. A simple example is illustrated in [138].

3.3 Conclusion

We generalized the LCCF method in a way to identify the temporal behaviors of one or more sources to control one or more voltage/current or field signals in any linear media. General numerical applications in lossy networks as well as anechoic and reverberant chambers were illustrated to show the applicability of the generalized LCCF independently of the topology of the studied medium. In another section, we described an interesting application for the LCCF method in faulty networks, called the software correction, to tolerate the faults and compensate for their effects. Three numerical examples were treated to address the different aspects of faults inherent in the lines of the wiring networks (soft, hard, or multiple faults). Furthermore, we showed that the software correction process remains applicable when the networks are exposed to external interfering defects. In essence, the software correction is independent of the position, number, and nature of the potential faults or defects.

The results obtained in this chapter are encouraging enough and show that the LCCF is a promising method that paves the path for two additional studies. The first study discusses the possibility of realizing the LCCF method and its applications experimentally. Further researches are required on the sensitivity of the LCCF in the presence of noise, although few results have been obtained in [143]. This study will be addressed in the last chapter of this dissertation, where a detailed analysis will be given about the LCCF method's robustness in one and three-dimensional environments.

Due to the importance of nonlinear EMC problems, the second study identifies the temporal sources in nonlinear media. For this reason, we test the LCCF method when nonlinear elements are introduced to the wiring net-

works. The next chapter will reveal whether the LCCF remains valid in nonlinear wiring networks or not. If not, we will try to propose other alternative methods that may resolve nonlinear problems in EMC. The Chapters 3 and 4 are identically designed except that the former tackles linear wiring networks, whereas the latter deals with nonlinear ones.

4

Source Identification in Nonlinear Systems: Newton's Method and the NLLSQ Solver

PROBLEMS in ElectroMagnetic Compatibility (EMC) are mainly nonlinear due to the massive presence of nonlinear circuits (e.g. power amplifier, switch, multiplier, mixer, etc.) based on passive (e.g. diodes) or active (e.g. transistors) elements. Different methods have focused on characterizing systems and objects of those problems [144–146]. In this chapter, Newton's Method (NM) and the NonLinear Least-SQuares (NLLSQ) method are used to identify the temporal profile of an electromagnetic source that satisfies particular properties for a given target (field, voltage, or current) at a single spatial point of the medium over a time interval. Although both techniques may be described for any nonlinear medium, our illustrating examples are only confined to wiring networks. First of all, we test the Linear Combination of Configuration Field (LCCF) method presented previously to show its malfunctioning once nonlinear elements are introduced to the system. Afterward, numerical applications show the applicability of NM and the NLLSQ solver in lossless and lossy wiring networks to determine the effect of low and high attenuation levels on their applicability.

We gather our ideas to bring a Software Correction (SC) to faulty nonlinear complex networks with losses introduced to its lines. We highlight our ability to correct the faulty outputs during the SC process regardless of the numbers, positions, and nature of the potential faults. In the last application, we apply the SC in the presence of signals emitted by a radiating source which

couple the network at unshielded parts. Finally, the chapter draws some conclusions and gives some perspectives.

4.1 Time-Domain Source Identification in Nonlinear Media

Here, we present NM and the NLLSQ to solve NonLinear Problems (NLPs) in EMC. We first describe both techniques, then present numerical illustrations in lossless and lossy networks to show their applicability with different attenuation levels. As NM and the NLLSQ may be applied to any nonlinear system, their general principles are presented for any nonlinear mapping between the inputs and the outputs.

4.1.1 Theory: Newton's method and the NLLSQ solver

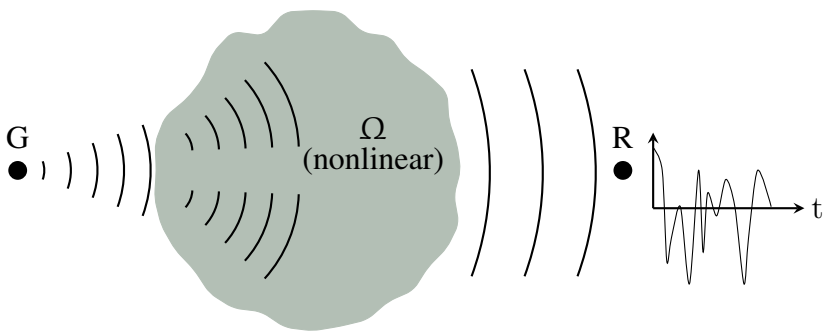

Figure 4.1: *Schematic setup of the general nonlinear problem.*

To grasp the main lines of Newton's Method (NM) and the NonLinear Least SQuares (NLLSQ) solver, we consider the schematic setup of Figure 4.1. Let $[0, t_n]$ be the time interval during which a signal is emitted and received, where $t_n = n\Delta t > 0$ $(n \in \mathbb{N}^*)$ is the last instant of time to be specified. For all $t \in [0, t_n]$, the source generator G emits a discrete signal $\mathbf{x} = [x(0), x(1), \cdots, x(n)] \in \mathbb{R}^{n+1}$ that propagates, interferes, and may be distorted due to discontinuities and inhomogeneities in the nonlinear medium Ω. A receiver R placed at a fixed point records the detected discrete signal $\mathbf{y} = [y(0), y(1), \cdots, y(n)] \in \mathbb{R}^{n+1}$ over $[0, t_n]$. Similar

to the LCCF method in linear systems, the aim of NM and the NLLSQ is to identify the temporal source $\mathbf{x}$ that may control $\mathbf{y}$ at a predefined target time $[t_q, t_f]$ in the nonlinear Ω. The source $\mathbf{x}$ is emitted from 0 to $t_p = p\Delta t$ ($x(j) = 0$, for all $j > p \in \mathbb{N}$) and controls $\mathbf{y}$ over $[t_q, t_f]$, i.e., $\mathbf{y}_{/\left[t_q, t_f\right]} = [y(q), \cdots, y(f)] = \mathbf{v}$, where $\mathbf{v} = [v(q), \cdots, v(f)]$ is the target field to be imposed over $[t_q, t_f]$.

The nonlinear transformation between the G-point over $[0, t_p]$ and the R-point over $[t_q, t_f]$ may be represented by the following nonlinear function:

$$\begin{aligned} \varphi \colon \mathbb{R}^{p+1} &\to \mathbb{R}^{f-q+1} \\ \mathbf{x} &\mapsto \varphi(\mathbf{x}) = [y(q), \cdots, y(f)]\,. \end{aligned} \tag{4.1}$$

We solve the NLP to compute the source $\mathbf{x}$ that produces a given $\mathbf{v}$ at the R-point over $[t_q, t_f]$. For this purpose, we formulate the problem to determine $\mathbf{x}$ such that $\varphi(\mathbf{x}) = \mathbf{v}$. More precisely, if we denote by $\mathbf{F}(\mathbf{x}) = \varphi(\mathbf{x}) - \mathbf{v}$, we calculate the amplitudes $x(0), \cdots, x(p)$, such that $\mathbf{F}(\mathbf{x}) = [F_0, \cdots, F_{f-q}] = \mathbf{0}$, explicitly written as

$$\begin{cases} F_0 = y(q) - v(q) = 0, \\ \vdots \\ F_{f-q} = y(f) - v(f) = 0. \end{cases} \tag{4.2}$$

Newton's method

The system (4.2) may be solved using NM for general NLPs. Assume that we have a starting point $\mathbf{x}^{(0)}$ not too far from the unknown solution $\mathbf{x}$, then the algorithm writes

$$\begin{cases} \mathbf{J}\left[\mathbf{x}^{(\xi)}\right] \Delta\mathbf{x} = -\mathbf{F}\left[\mathbf{x}^{(\xi)}\right], \\ \mathbf{x}^{(\xi+1)} = \mathbf{x}^{(\xi)} + \Delta\mathbf{x}, \end{cases} \tag{4.3}$$

where

1. $(\mathbf{J})_{0 \le i \le f-q, 0 \le j \le p}$ is the Jacobian matrix defined by

$$(\mathbf{J})_{ij} = \frac{\partial F_i}{\partial [x(j)]}(\mathbf{x})\,,$$

2. $\Delta\mathbf{x}$ is the vector to be calculated by solving a linear system,

3. $\mathbf{x}^{(\xi)}$ is the sequence of vectors that converges to the solution $\mathbf{x}$.

At the iteration ξ, each entry of the Jacobian matrix $(\mathbf{J})_{ij}$ is the directional derivative of $F(i)$ along $x(j)$. This derivative is computed by taking the limit as $\epsilon \to 0$ of the difference quotient between the fields produced by injecting $\mathbf{x}^{(\xi)}$ and $\mathbf{x}_\epsilon^{(\xi)} = \left[x(0)^{(\xi)}, \cdots, x(j)^{(\xi)} + \epsilon, \cdots, x(p)^{(\xi)}\right]$,

$$(\mathbf{J})_{ij} = \frac{\partial F_i}{\partial [x(j)]}\left[\mathbf{x}^{(\xi)}\right] = \lim_{\epsilon \to 0} \frac{F_i\left[\mathbf{x}_\epsilon^{(\xi)}\right] - F_i\left[\mathbf{x}^{(\xi)}\right]}{\epsilon}. \tag{4.4}$$

The iterative algorithm may be stopped when $\|\Delta\mathbf{x}\|_2$ is less than a given threshold ε_{tol}, indicating its convergence to the solution $\mathbf{x}$. In general, the system (4.3) is not square; however, it may be solved in the least-squares sense. We note that such problems are usually ill-posed, and accordingly require to be regularized. Here, Tikhonov regularization for nonlinear ill-posed problems [147] is used and the system (4.3) becomes

$$\begin{cases} \left[\phi_\xi \mathbf{I} + \mathbf{J}^T\left[\mathbf{x}^{(\xi)}\right]\mathbf{J}\left[\mathbf{x}^{(\xi)}\right]\right]\Delta\mathbf{x} = -\mathbf{J}^T\left[\mathbf{x}^{(\xi)}\right]\mathbf{F}\left[\mathbf{x}^{(\xi)}\right] - \phi_\xi \mathbf{x}^{(\xi)}, \\ \mathbf{x}^{(\xi+1)} = \mathbf{x}^{(\xi)} + \Delta\mathbf{x}, \end{cases} \tag{4.5}$$

where $\mathbf{I}$ is the identity matrix of size p and (ϕ_ξ) is a real decreasing sequence with $\lim_{\xi \to 0} \phi_\xi = 0$.

The nonlinear least squares solver

An optimization problem may be used to find the solution $\mathbf{x}$ of the nonlinear system of equations $\mathbf{F}(\mathbf{x}) = \mathbf{0}$. The NLLSQ method is used to fit a set of $(f - q + 1)$ observations $F_0, \cdots, F_{f-q}$ with a nonlinear model in $(p + 1)$ unknown parameters $x(0), \cdots, x(p)$. The solution $\mathbf{x} = [x(0), x(1), \cdots, x(n)]$ produces, when injected, the target voltage $\mathbf{v}$ at $[t_q, t_f]$. The minimization problem to be solved is: find $\mathbf{x} \in \mathbb{R}^{p+1}$ that minimizes $\|\mathbf{F}(\mathbf{x})\|_2^2 = \left[F_0^2(\mathbf{x}) + \cdots + F_{f-q}^2(\mathbf{x})\right]$. In fact, the NLLSQ relies on the Levenberg-Marquardt algorithm to solve the nonlinear undeter-

mined problem.

Remark: In this chapter, voltage signals are considered for illustrations and applications in wiring networks; however, current signals could be considered in a similar way.

4.1.2 Numerical illustrations in wiring networks

We first show the inapplicability of the LCCF method when applied to simple nonlinear systems, such as a nonlinear network with matched resistive loads. Alternatively, NM and the NLLSQ are used to identify the temporal sources, even when losses are introduced to the wiring network lines. Then, we go further and consider a more complex network with unmatched resistive loads to illustrate the fact that NM and the NLLSQ are still applicable in the occurrence of multiple reflections. Eventually, we compare NM and the NLLSQ solver to reveal the superiority of the latter over the former after taking the accuracy and the CPU time as criteria.

Problem settings

We consider an unshielded coaxial network Ω of arbitrary topology and characteristics (number, lengths, impedance, and loads of lines, etc.). For illustration purposes, let us consider the network of Figure 4.2 composed of two nodes and five point-to-point TLs. Table 4.1 displays their respective number l, length z, characteristic impedance (Z_{C}^{l}), and load impedance (Z_{L}^{l}) for $l \in \{1, ..., 5\}$. The load placed at the termination of each line may be a resistor $Z_{\mathrm{L}}^{l} = 50\,\Omega$, diode, or varistor. To further complicate the problem, arbitrary losses are introduced to the lines of Ω ($R = 0.025\,\Omega/\mathrm{m}$, for example). The considered value of resistance causes 5.36% information losses. In general, any attenuation level may certainly be selected, as we will see later in this chapter.

An RLCG model of Ω is considered in which the telegrapher's equations are solved using a standard one-dimensional FDTD scheme (see Chapter 1 Section 1.3.2). The total duration of the simulations is $[0, t_n] = [0, 1422\Delta t]$. The time step $\Delta t = 3.904 \times 10^{-9}\,\mathrm{s}$ and the space step $\Delta z = 0.1\,\mathrm{m}$ are selected in a way that satisfies the stability criterion (1.38). In what follows,

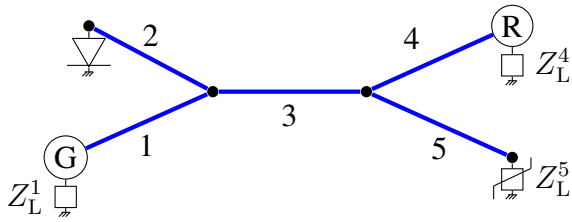

Figure 4.2: *Nonlinear network configuration.*

Line Nb. l	z (in m)	Z_{C}^{l} (in Ω)	Load
1	1	50	Resistor
2	3	50	Diode
3	4	50	-
4	5	50	Resistor
5	8	50	Varistor

Table 4.1: *Characteristics of the nonlinear network.*

we assume that a source generator G is placed at the first node of line 1 and a receiver R is placed at the termination of 5, although they could still be placed anywhere on the network. The target time $[t_q, t_f]$ may be any time interval after the signal $\mathbf{x}$ reaches the receiver R, for example, $t_q = 500\Delta t$ and $t_f = 620\Delta t$. The target $\mathbf{v}$ is chosen to be a sinusoidal signal $\mathbf{S}_{0.1}$ (2.10) of maximum amplitude $+0.1\,\mathrm{V}$, such that $\not{f} = 6.3\,\mathrm{MHz}$.

To guarantee a nonlinear behavior of Ω, two electronic components, a diode and a varistor, are respectively placed at the terminations of lines 2 and 5. The current-voltage $(\mathbf{I} - \mathbf{V})$ characteristic of the diode is $\mathbf{I} = I_s \exp(\mathbf{V}/V_T - 1)$, where I_s is the reverse bias saturation current and V_T is the thermal voltage. The $(\mathbf{I} - \mathbf{V})$ characteristic of the varistor is $\mathbf{I} = I_0 \mathbf{V}^{\gamma}$, where I_0 is a constant and γ is the nonlinear voltage exponent. For instance, the diode parameters are chosen to be $I_s = 10^{-12}\,\mathrm{A}$ and $V_T = 0.026\,\mathrm{V}$, whereas the varistor parameters are set to $I_0 = 0.1\,\mathrm{A}$ and $\gamma = 5$. We note that the chosen characteristics of Ω may not correspond to a practical approach for testing networks as we suppose that all the network's extremities are accessible (placement of generators, receivers, diodes, varistors and matched loads); however, any other network of different

characteristics and cartography could be considered, as shown later. Here, the aim is nothing else than illustrating and comparing NM and the NLLSQ solver.

To test the nonlinearity level of the system, two independent simulations are carried out by injecting a Gaussian pulse $\mathbf{G}_2$ (resp. $\mathbf{G}_1$) (2.6) of maximum amplitude $+2\,\mathrm{V}$ (resp. $+1\,\mathrm{V}$), where $t_c = 40\Delta t$ and $\sigma = 8\Delta t$. The output voltages recorded by R are denoted by $\mathbf{y}_2$ for $\mathbf{G}_2$ and $\mathbf{y}_1$ for $\mathbf{G}_1$. Figure 4.3 represents the quotient $|\mathbf{y}_2/\mathbf{y}_1|$ and shows that they are disproportional, indicating a high nonlinear level of the considered case. If the system is linear, we would obtain two proportional voltage signals at the R-point with a ratio $r = 2$, i.e., $\mathbf{y}_2 = 2\mathbf{y}_1$. In Figure 4.3, we notice that the quotient value $|\mathbf{y}_2/\mathbf{y}_1|$ for the nonlinear case is constant at the beginning, indicating a linear output. This is due to the signal propagating directly from the G-point to the R-point before reflections and re-reflections occur once reaching the diode and the varistor. Such reflections enable the nonlinearity of the system.

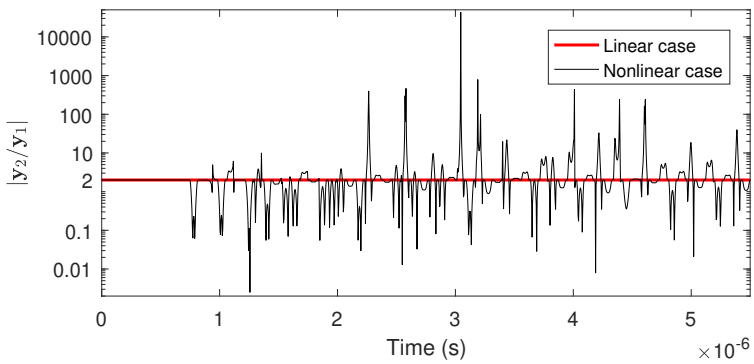

Figure 4.3: *Amplitude ratios of* $|\mathbf{y}_2/\mathbf{y}_1|$ *to show the nonlinearity of the system.*

Newton's iterative algorithm (4.5) is solved by taking $\mathbf{x}^{(0)} = \mathbf{0}$ as an initial guess, $\phi_\xi = 10^{-2(\xi+1)}$ as the real sequence of regularization, and a stopping criterion $\varepsilon_{\mathrm{tol}} = 10^{-10}$. Similarly, the initial guess of the optimizing NLLSQ solver is set to zero, whereas its function tolerance is chosen to be 10^{-6}.

Malfunctioning of the LCCF method

The LCCF method is no longer efficient at handling nonlinear problems; thus, its performance starts to deteriorate once nonlinear elements are introduced to the system. Here, we apply the LCCF method to the nonlinear network Ω and show that the LCCF is inefficient when it comes to controlling the voltage at the R-point. By solving the linear system $\mathbf{Ax} = \mathbf{S}_{0.1}$, the source $\mathbf{x}$ is computed. As expected, $\mathbf{x}$ fails in producing $\mathbf{S}_{0.1}$ at the level of R over $[t_q, t_f]$, as seen in Figure 4.4, where $\mathbf{y}_{/[t_q,t_f]} \neq \mathbf{S}_{0.1}$.

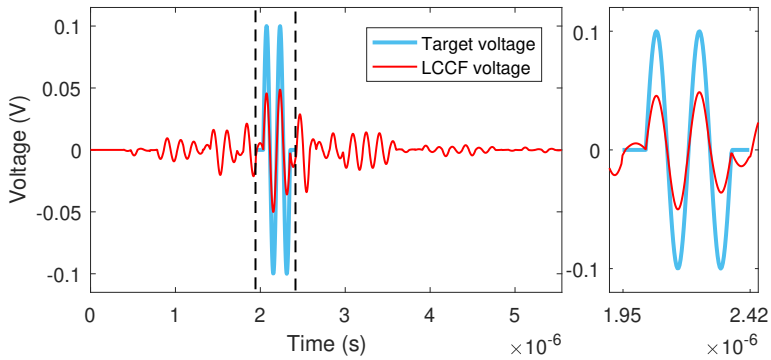

Figure 4.4: *In nonlinear systems, the LCCF fails in identifying the temporal source that produces the desired target voltage at the target time.*

Lossy network

Two different sources $\mathbf{x}_{\text{NM}}$ and $\mathbf{x}_{\text{NLLSQ}}$ are respectively computed by NM and the NLLSQ, then represented in Figure 4.5a. The two techniques compute different nontrivial solutions for the same emission duration, $t_p = 520\Delta t$. The separate injection of these two signals by G generates the output signals $\mathbf{y}$, where $\mathbf{y}_{/[t_q,t_f]} = \mathbf{S}_{0.1}$ at $[t_q, t_f]$, as shown in Figure 4.5b. For $t \in [0, t_n] \setminus [t_q, t_f]$, the signals are uncontrolled.

To carry out a comparison between NM and the NLLSQ solver, in this case, we consider as criteria the number of iterations for convergence, the Intel® Core™ i7 CPU time, and the Relative Error (RE) (2.8) between $\mathbf{S}_{0.1}$

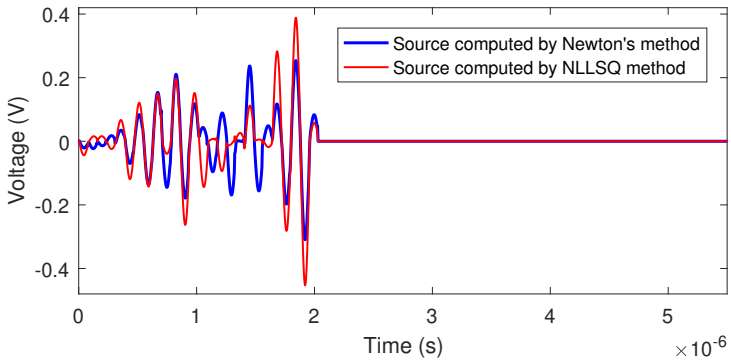

(a) Sources $\mathbf{x}_{\mathrm{NM}}$ and $\mathbf{x}_{\mathrm{NLLSQ}}$ computed respectively by NM and the NLLSQ.

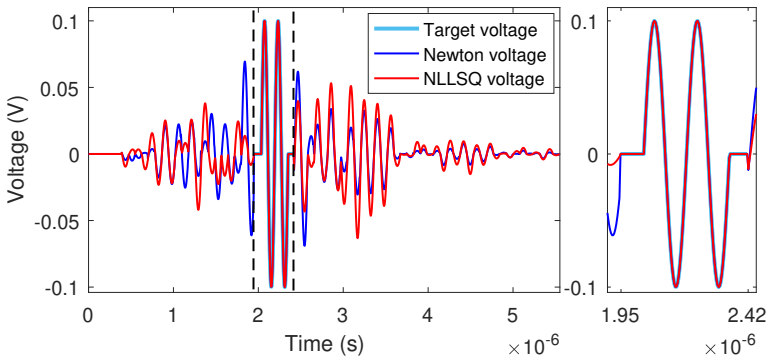

(b) Voltage signals recorded after injecting $\mathbf{x}_{\mathrm{NM}}$ and $\mathbf{x}_{\mathrm{NLLSQ}}$.

Figure 4.5: *Signals* $\mathbf{x}_{\mathrm{NM}}$ *and* $\mathbf{x}_{\mathrm{NLLSQ}}$ *propagate through the network to control the voltage at the termination of line* 4*. After their separate emissions, the receiver R records the signals* $\mathbf{y}$ *where the desired target voltage* $\mathbf{S}_{0.1}$ *is obtained at the target time* $[t_q, t_f] = [1.95 \times 10^{-6}, 2.42 \times 10^{-6}]$ *lying between the two dashed lines.*

and $\mathbf{y}_{/[t_q,t_f]}$. The studied case corresponds to the second row of Table 4.2 for an attenuation level $R = 0.025$. NM requires 7 iterations for an estimated time $15.53\,\mathrm{min}$ to achieve convergence with an RE $= 4.94 \times 10^{-11}$ (2.8). Otherwise, the NLLSQ takes $13.15\,\mathrm{min}$ to converge with fewer iterations (6 iterations) and higher accuracy RE $= 9.38 \times 10^{-14}$ (2.8).

Attenuation level (in Ω/m)	Losses percentage (in %)	RE $\left(\mathbf{S}_{0.1}, \mathbf{y}_{/\left[t_q, t_f\right]}\right)$		CPU time (min)	
		NM	NLLSQ	NM	NLLSQ
$R = 0\ (*)$	0	$1.2 \times\ 10^{-11}$	$2.69 \times\ 10^{-14}$	14.82	12.01
$R = 0.025$	5.36	$4.94 \times\ 10^{-11}$	$9.38 \times\ 10^{-14}$	15.53	13.15
$R = 0.04$	8.34	$1.43 \times\ 10^{-11}$	$5.32 \times\ 10^{-14}$	15.58	13.17
$R = 0.5$	56.51	$1.73 \times\ 10^{-10}$	$1.97 \times\ 10^{-13}$	15.5	13.89
$R = 0.8$	70.07	$1.14 \times\ 10^{-10}$	$3.89 \times\ 10^{-13}$	15.44	14.3
$R = 3$	95.39	$1.09 \times\ 10^{-4}$	$2.93 \times\ 10^{-6}$	15.81	15.55

$(*)$: lossless network

Table 4.2: *Comparing the results of Newton's method and the NLLSQ solver with respect to the different attenuation levels.*

In Figures 4.6 and 4.7, we see that NM and the NLLSQ solver always succeed in generating $\mathbf{S}_{0.1}$ independently of the attenuation levels. In Figures 4.6a and 4.7a, we respectively plot the sources $\mathbf{x}_{\mathrm{NM}}$ and $\mathbf{x}_{\mathrm{NLLSQ}}$, while their output voltage signals are represented in Figures 4.6b and 4.7b. Table 4.2 illustrates that both techniques are independent of any low, average, or high attenuation level, where they still produce the desired $\mathbf{S}_{0.1}$ at $[t_q, t_f]$ with a quite low RE. It should be noted that the relation between the sources seems to be linear from the first sight, but this is not true in general.

The NLLSQ solver seems to be more efficient than NM at imposing a specified target voltage over a fixed target time as it provides higher accuracy with less CPU time. Moreover, NM requires a starting point not too far from the solution; otherwise, the algorithm diverges. Often, the computed signal is characterized by its complex profile, making it difficult to guess the starting point.

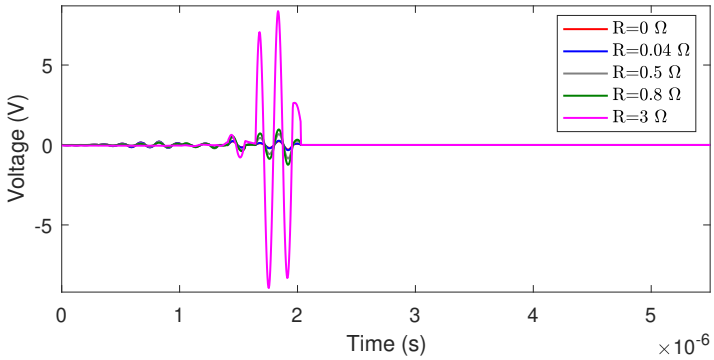

(a) Sources $\mathbf{x}_{\mathrm{NM}}$ computed by NM.

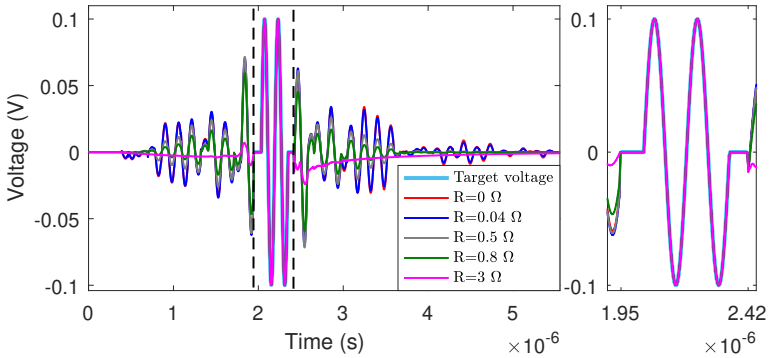

(b) Voltage signals $\mathbf{y}$ recorded after separately injecting the sources $\mathbf{x}_{\mathrm{NM}}$ at different attenuation levels.

Figure 4.6: *After Newton's simulations at different attenuation levels, the signals* $\mathbf{x}_{\mathrm{NM}}$ *separately propagate through the lossy network to control the voltage at the termination of line* 4*. After their emissions, the receiver R records the signals* $\mathbf{y}$*, where the desired target voltage* $\mathbf{S}_{0.1}$ *is obtained at the target time* $[t_q, t_f] = [1.95 \times 10^{-6}, 2.42 \times 10^{-6}]$ *lying between the two dashed lines.*

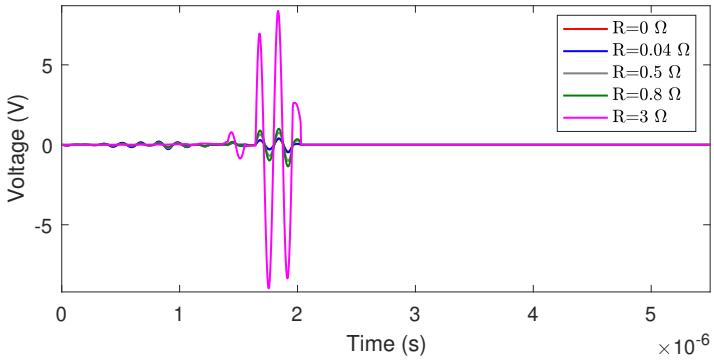

(a) Sources $\mathbf{x}_{\text{NLLSQ}}$ computed by the NLLSQ.

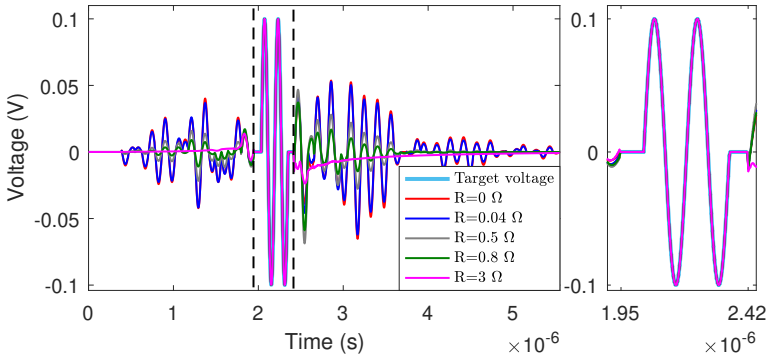

(b) Voltage signals $\mathbf{y}$ recorded after separately injecting the sources $\mathbf{x}_{\text{NLLSQ}}$ at different attenuation levels.

Figure 4.7: *After NLLSQ's simulations at different attenuation levels, the signals* $\mathbf{x}_{\text{NLLSQ}}$ *separately propagate through the lossy network to control the voltage at the termination of line* 4. *After their emissions, the receiver R records the signals* $\mathbf{y}$, *where the desired target voltage* $\mathbf{S}_{0.1}$ *is obtained at the target time* $[t_q, t_f] = [1.95 \times 10^{-6}, 2.42 \times 10^{-6}]$ *lying between the two dashed lines.*

Multiple reflections

In the previous section, we focused on the applicability of NM and the NLLSQ solver in the presence of losses. For illustration purposes, a network with matching resistive loads was considered. As aforementioned, this network may not refer to a practical approach since not all the network's

extremities may be accessible in reality. To clear up all the doubts concerning the applicability of NM and the NLLSQ in the presence of multiple reflections, we keep the same network as described in the problem settings of this section with two additional lines connected to its second node, where the voltage perfectly reflects when reaching their terminations. The new network Ω along with its new characteristics are represented in Figure 4.8 and Table 4.3.

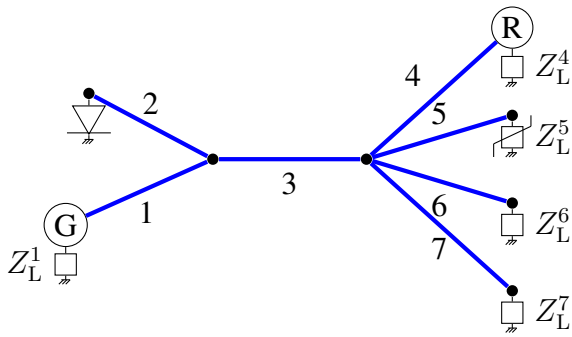

Figure 4.8: *Configuration of the nonlinear network with multiple reflections.*

Line Nb.	z (in m)	Z_{C}^{l} (in Ω)	Z_{L}^{l} (in Ω)
1	1	50	50
2	3	50	Diode
3	4	50	-
4	5	50	50
5	8	50	Varistor
6	1	50	0
7	3	50	∞

Table 4.3: *Characteristics of the nonlinear network with multiple reflections.*

The results are represented in Figure 4.9, where both techniques successfully generate the desired target voltage $\mathbf{S}_{0.1}$ at $[t_q, t_f]$. Increasing the complexity of the system does not enhance the divergence of NM or the NLLSQ. Otherwise, both approaches are independent of the topology of the network as well as its nonlinearity level. This implies that the two algorithms do not

rely on either the complexity of the network (number of lines and junctions, characteristics, loads, etc.), the multiple reflections occurring during propagation, or the level of attenuation. We note that the dispersion is treated in the same way as the attenuation for which NM and the NLLSQ continue to work properly for any level of dispersion. On the other hand, the applicability of both techniques always requires a free extremity to branch a receiver.

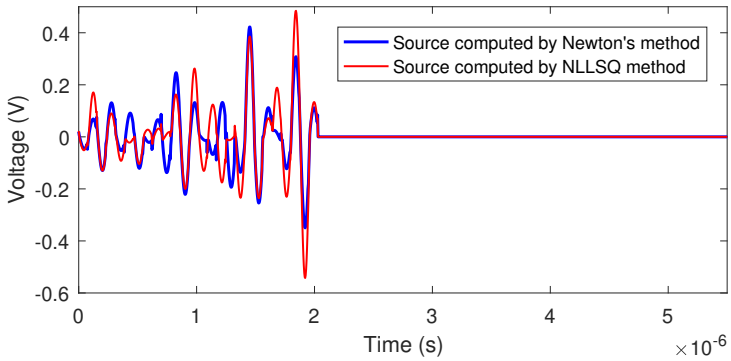

(a) Sources $\mathbf{x}_{\mathrm{NM}}$ and $\mathbf{x}_{\mathrm{NLLSQ}}$ computed respectively by NM and the NLLSQ.

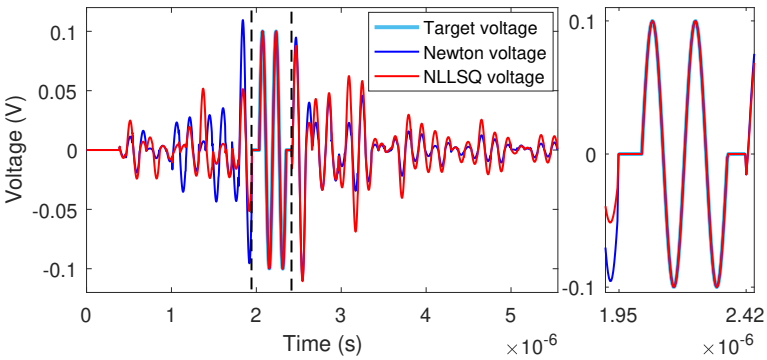

(b) Voltage signals recorded after injecting $\mathbf{x}_{\mathrm{NM}}$ and $\mathbf{x}_{\mathrm{NLLSQ}}$.

Figure 4.9: *Signals* $\mathbf{x}_{\mathrm{NM}}$ *and* $\mathbf{x}_{\mathrm{NLLSQ}}$ *propagate through the complex network (Figure 4.8) to control the voltage at the termination of line* 4. *After their separate emissions, the receiver* R *records the signals* $\mathbf{y}$, *where the desired target voltage* $\mathbf{S}_{0.1}$ *is obtained at the target time* $[t_q, t_f] = [1.95 \times 10^{-6}, 2.42 \times 10^{-6}]$ *lying between the two dashed lines.*

4.2 Software Correction of Faulty Lossy Nonlinear Networks

In Chapter 3 Section 3.2, a detailed description of the Software Correction (SC) process was given, where it was introduced to compensate for the effects of the faults in faulty communication systems. Earlier in this chapter, we have shown that the LCCF is inefficient at controlling the voltage/current in nonlinear networks; consequently, it is not designed to bring an SC to nonlinear networks. As an alternative solution, NM and the NLLSQ may be used as they have shown high efficiency at controlling the voltage/current in nonlinear networks in Section 4.1. However, as demonstrated, the latter is more efficient than the former both from accuracy and computational point of view; as a result, we rely on the NLLSQ solver only to bring an SC to faulty lossy nonlinear wiring networks. Although NM requires an initial guess not too far from the real solution, which is not always easy for assumption, NM may also bring an SC to faulty lossy nonlinear networks when the initial guess may be hypothesized.

We discuss the SC process in networks presenting soft, hard, and multiple faults (soft and hard) such as the complex network Ω of Figure 4.8. Furthermore, we examine how we can bring an SC to Ω when exposed to external defects coupling Ω at unshielded parts. To show the impact of the fault(s) or defect(s), we record the voltage signals at the R-point after two separate injections of the initial Gaussian pulse $\mathbf{G}_2$ (2.6) ($t_c = 40\Delta t$ and $\sigma = 8\Delta t$) of maximum amplitude $+2\,\mathrm{V}$ in the healthy Ω and its faulty version Ω'. We denote by $\mathbf{V}_\mathrm{H}$ the healthy voltage signal recorded by R after the injection of $\mathbf{G}_2$ in Ω and by $\mathbf{V}_\mathrm{F}$ the faulty voltage signal recorded by R after the injection of $\mathbf{G}_2$ in Ω'. The effects of the fault(s) or defect(s) are represented by the differences between the two outputs $\mathbf{V}_\mathrm{H}$ and $\mathbf{V}_\mathrm{F}$.

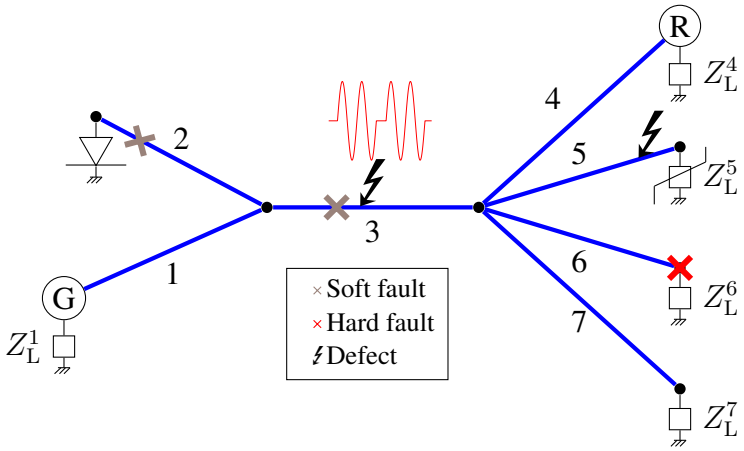

Figure 4.10: *Configuration of the nonlinear network used during the SC process.*

4.2.1 Soft fault

The soft fault is simulated at $2.5\,\mathrm{m}$ distance from the first junction along line 2 and represented by the gray X-mark in Figure 4.10. After injecting $\mathbf{G}_2$, the healthy and the faulty signals, $\mathbf{V}_\mathrm{H}$ and $\mathbf{V}_\mathrm{F}$, recorded at the R-level are respectively displayed in green and blue in Figure 4.11b. Slight output distortions are noticed as a result of the soft fault. Using the NLLSQ solver, we identify the new the source $\mathbf{x}$ represented in Figure 4.11a that minimizes $\|\mathbf{F}(\mathbf{x})\|_2^2 = \left[F_0^2(\mathbf{x}) + \cdots + F_{n-1}^2(\mathbf{x})\right]$. After the injection of $\mathbf{x}$ in Ω', the corrected voltage signal $\mathbf{V}_\mathrm{C}$ is recorded by R, then represented in red in Figure 4.11b. The signal $\mathbf{V}_\mathrm{C}$ is similar to $\mathbf{V}_\mathrm{H}$ with an $\mathrm{RE}\left(\mathbf{V}_\mathrm{H}, \mathbf{V}_\mathrm{C}\right) = 4.17 \times 10^{-4}$ (2.8).

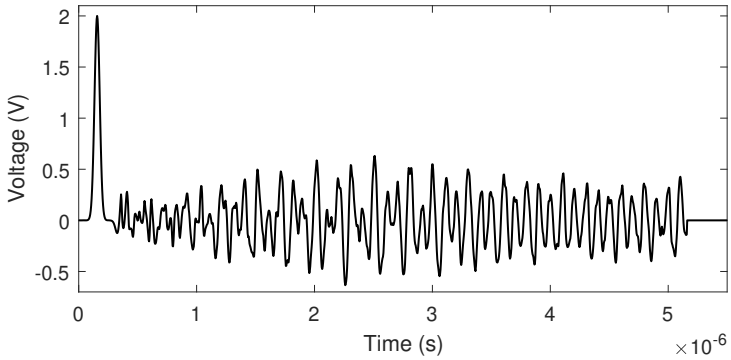

(a) Source $\mathbf{x}$ to tolerate the soft fault.

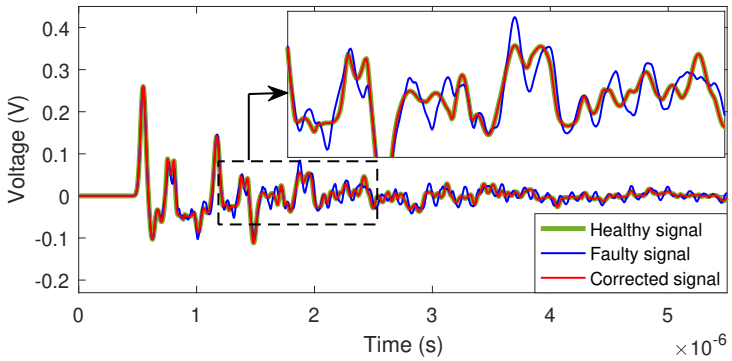

(b) Healthy, faulty and corrected voltage signals recorded by R.

Figure 4.11: *Software correction of the nonlinear faulty network presenting a single soft fault.*

4.2.2 Hard fault

The hard fault is simulated by an open circuit at the termination of line 6 represented by the red X-mark in Figure 4.10. The simulated fault is implemented by modifying the load impedance from 0 to $\infty\,\Omega$. After injecting $\mathbf{G}_2$, the healthy $\mathbf{V}_\mathrm{H}$ and the faulty $\mathbf{V}_\mathrm{F}$ signals are respectively displayed in green and blue in Figure 4.12b. Using the NLLSQ solver, the new source $\mathbf{x}$ is identified (see Figure 4.12a) and sent down in Ω' to generate the corrected signal $\mathbf{V}_\mathrm{C}$. We note that $\mathbf{V}_\mathrm{H}$ and $\mathbf{V}_\mathrm{C}$ are almost identical with an $\mathrm{RE}\left(\mathbf{V}_\mathrm{H}, \mathbf{V}_\mathrm{C}\right) = 2.77 \times 10^{-4}$ (2.8).

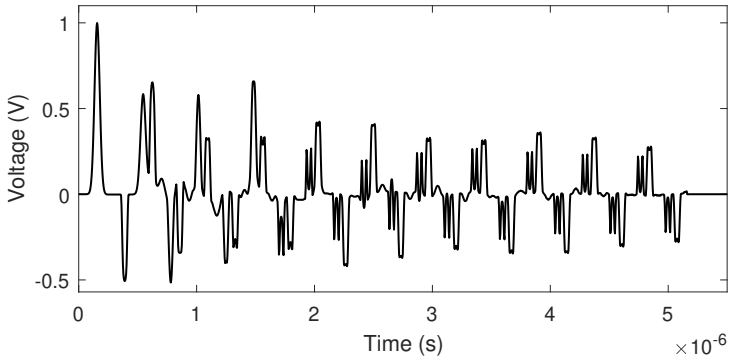

(a) Source $\mathbf{x}$ to tolerate the hard fault.

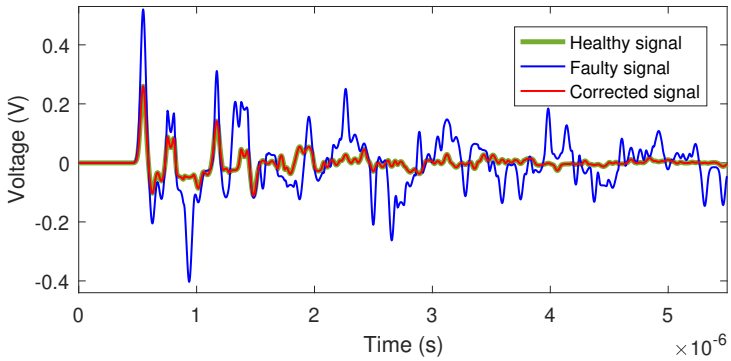

(b) Healthy, faulty and corrected voltage signals recorded by R.

Figure 4.12: *Software correction of the nonlinear faulty network presenting a single hard fault.*

4.2.3 Multiple faults

Two soft faults are respectively simulated along the lines 2 and 3 at $2.5\,\mathrm{m}$ and $1.5\,\mathrm{m}$ distance from the first junction. Also, a hard fault (open circuit) is simulated at the termination of line 6. The faults are represented by the gray and red X-marks in Figure 4.10. By the NLLSQ method, the new source $\mathbf{x}$ is computed and displayed in Figure 4.13a. Its injection in Ω' leads R to recording the corrected signal $\mathbf{V}_\mathrm{C}$. Remarkably, $\mathbf{V}_\mathrm{H}$ and $\mathbf{V}_\mathrm{C}$ are indistinguishable for the entire time domain with an $\mathrm{RE}\left(\mathbf{V}_\mathrm{H}, \mathbf{V}_\mathrm{C}\right) = 2.92 \times 10^{-4}$ (2.8).

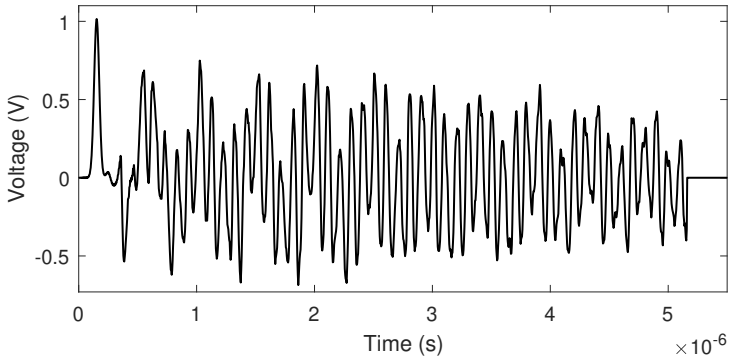

(a) Source $\mathbf{x}$ to tolerate the multiple faults.

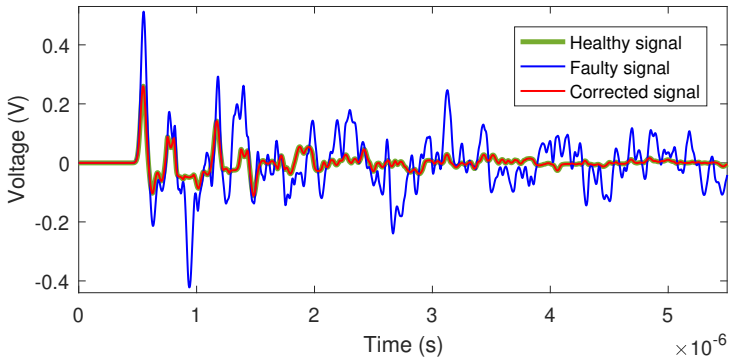

(b) Healthy, faulty and corrected voltage signals recorded by R.

Figure 4.13: *Software correction of the nonlinear faulty network presenting multiple faults of different nature (soft and hard).*

4.2.4 External defect

In what preceded, we applied the SC process using the NLLSQ method to the faulty network behaving nonlinearly with faults inherent in its lines. However, in many cases, wiring networks may be distorted by external defects resulting from radiating sources that couple the network along an unshielded length of its cables. In the following, we deal with a network exposed to a defect to show that the SC process is still applicable in such a case. We note that the treated defects are constant signals resulting from an external radiator without changing their profiles. The defect signal may take any form; we may consider the red signal represented in Figure 4.10, for example.

Assume that the coupling occurs at the midpoint of line 3. This interference distorts the output signals, as represented in Figure 4.14b. By the NLLSQ, the outputs are corrected after identifying the correcting source $\mathbf{x}$ represented in Figure 4.14a. The relative error (2.8), in this case, is RE $= 7.26 \times 10^{-5}$.

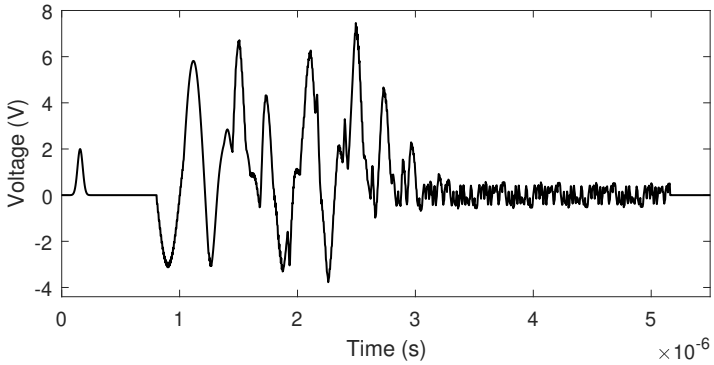

(a) Source $\mathbf{x}$ to tolerate the defect.

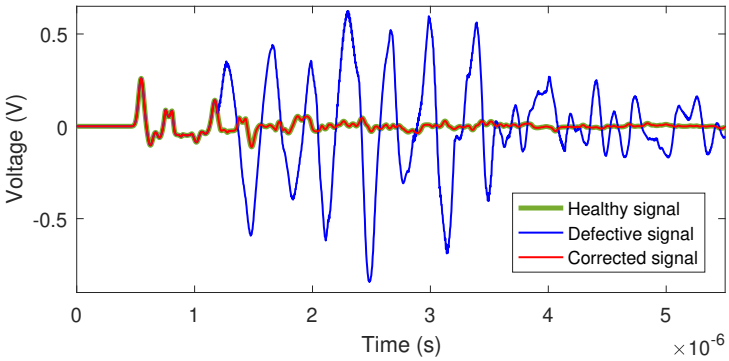

(b) Healthy, defective and corrected voltage signals recorded by R.

Figure 4.14: *Software correction of a nonlinear defective network coupled by an external interfering signal.*

4.2.5 Multiple faults and external defects

Even if faults and external defects distort the network Ω at the same time, the SC remains applicable. Here, we assume that Ω is distorted by the multiple

faults described earlier as well as the two defects coupling Ω at the midpoint of line 3 and $6\,\mathrm{m}$ distance from the second junction along the fifth line. The occurring distortions are represented in Figure 4.15b. Using the NLLSQ, we correct the outputs by identifying the new source to be injected by G (see Figure 4.15a). After its emission, the receiver R records the corrected signal displayed in red in Figure 4.15b. The relative error (2.8) between $\mathbf{V}_{\mathrm{H}}$ and $\mathbf{V}_{\mathrm{C}}$ is RE $= 6.28 \times 10^{-3}$.

The SC process may be applied to any defective communication system regardless of the number, nature (soft/hard or external), and position of the faults or defects [148]. The SC in nonlinear systems encounters the same limitations as in the linear case. It always requires prior knowledge of the healthy output and the need for a free extremity to branch a receiver. It is worth mentioning that when a hard fault appears on the linking path between the source point and the receiver point, the SC does not work anymore as no signal is reaching the receiver. For example, if line 3 is cut at any of its points, then the SC process is not efficient anymore in such a particular case.

4.3 Conclusion

We used NM and the NLLSQ solver to identify the temporal profile of an electromagnetic source that produces a predefined voltage/current or field at a single spatial point of the nonlinear network over a fixed time interval. After considering a wiring network, we showed that the LCCF method malfunctions when nonlinear elements are introduced to the system. As an alternative solution, we demonstrated the applicability of NM and the NLLSQ in nonlinear lossy and lossless wiring networks. For any chosen level of attenuation, it was shown that the applicability of the nonlinear techniques is not affected at all. In a second step, NM and the NLLSQ were compared in terms of accuracy and CPU time to show the superiority of the latter over the former. Due to its excellent performance, the NLLSQ was then used to bring a software correction to a faulty nonlinear complex network with losses introduced to its lines. We removed all the doubts concerning the capability of the software correction process to correct the faulty outputs regardless of the number, position, and nature of the potential faults. Furthermore, we also demonstrated that the software correction might equally be applied when

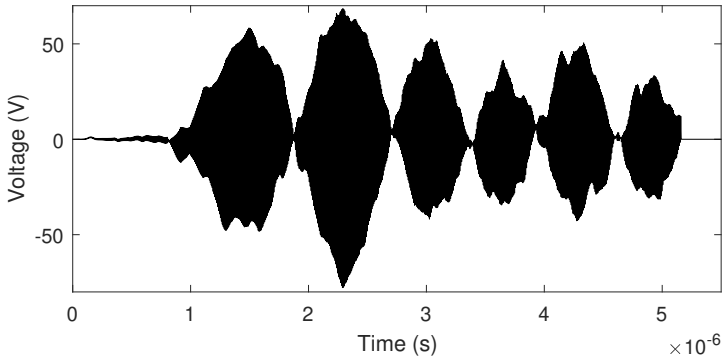

(a) Source $\mathbf{x}$ to tolerate the inherent faults and the external defects.

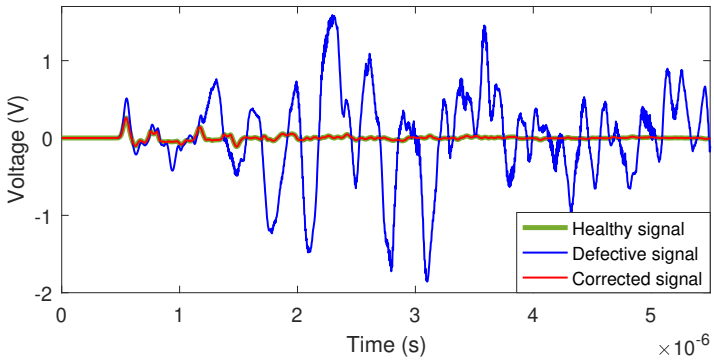

(b) Healthy, defective and corrected voltage signals recorded by R.

Figure 4.15: *Software correction of a nonlinear defective network coupled by two external interfering signals with multiple faults inherent in its lines.*

signals caused by a radiating source couple the network at unshielded parts. A general example was presented for a quite complex network presenting two soft faults, one hard fault, and two defects where the obtained results were always satisfactory.

The next chapter is devoted to validating the results of Chapter 3 experimentally; however, nonlinear experiments will not be considered. Adding constraints to the nonlinear problem is an essential step before conducting experimental trials. Such constraints may modify the source properties (frequencies, amplitudes, etc.) witnessed during experiments; otherwise, the ex-

perimental realizations are not possible. As a proactive step, it seems necessary to reduce the high frequencies and amplitudes of the computed source to become experimentally achievable. For example, the rapid oscillations of the source of Figure 4.15b generate high frequencies that may not be included in the bandwidth of the devices used in experiments. On the other side, the nonlinear tests may require modeling the tested network to calculate the Jacobian matrix derivatives. Once these gaps are filled, experimental tests for nonlinear networks will then be possible.

5

Experimental Validation: The LCCF Method

THIS chapter is dedicated to applying the Linear Combination of Configuration Field (LCCF) method experimentally after it was described, developed, and numerically illustrated in previous chapters. Yet, the LCCF method, as previously presented, is not ready for practical applications due to some physical limitations. Firstly, we upgrade the LCCF to satisfy such limitations. After describing the equipment used in testings, the LCCF method, in its upgraded version, is invested in carrying out experiments in wiring networks and a reverberant cavity. This chapter is divided into two main parts.

The first part determines the temporal sources in wiring networks. In simple and complex network configurations, we identify the sources that impose any desired target signal at one or more spatial points during a given time interval. Sometimes, built-in equipment or budget limitations prevent the upgraded LCCF method from generating the target output; therefore, constraints are added to the problem to overcome these limitations. Furthermore, we experimentally show the applicability of the LCCF method to bring a software correction to faulty communication networks when single or multiple faults appear in their lines regardless of their nature and position.

The second section is the result of a collaboration between Clermont Auvergne University (Institut Pascal) and Paul Sabatier University in Toulouse, France (LAPLACE and ISAE-SUPAERO laboratories). This work shows that the LCCF method could also fit three-dimensional applications in a reverberant cavity. In this part, we apply the Time-Reversal (TR) and the LCCF

methods to enhance the spatial control of nanosecond microwave plasma by controlling the electromagnetic fields inside the cavity. After comparing the results, we illustrate the superiority of the LCCF method over the TR to generate plasma at specified positions only, unlike the TR, where unintentional parasitic discharges appear elsewhere.

5.1 Experimental LCCF method

In Chapters 2 and 3, we presented and developed the LCCF method before it was illustrated numerically. As previously described, the LCCF may not be considered to conduct experimental tests due to physical limitations encountered during experiments. These experiments may not be carried out unless the LCCF is modified to comply with such limitations. Indeed, the recorded impulse responses used to build the LCCF characterization matrix $\mathbf{A}$ may be theoretically and numerically convenient, but not experimentally. The emission of the unit impulse $\mathbf{e}_1$ is impractical for experimental tests. As an alternative solution, $\mathbf{A}$ is built by considering the responses of any incident signal $\boldsymbol{\alpha} = [\alpha(0), \cdots, \alpha(n)] \neq \mathbf{e}_1$ that could experimentally be realized. Let $\tilde{\mathbf{A}}$ be the matrix constructed exactly in the same way as $\mathbf{A}$ (2.4), but this time, based on the responses of $\boldsymbol{\alpha}$ and not the impulse responses. Using the new notation, the LCCF system becomes after regularization

$$\left(\tilde{\mathbf{A}}^T\tilde{\mathbf{A}} + \epsilon\mathbf{I}\right)\tilde{\mathbf{x}} = \tilde{\mathbf{A}}^T\mathbf{F}. \tag{5.1}$$

The system (5.1) is solved and the sources $\tilde{\mathbf{x}} = (\tilde{\mathbf{x}}_1, \cdots, \tilde{\mathbf{x}}_N)$ are computed. For all $j = \{1, \cdots, N\}$, each source $\tilde{\mathbf{x}}_j$ is the expression of the corresponding solution $\mathbf{x}_j$, a source associated with $\mathbf{A}$ characterizing the real system, computed in another basis. Injecting the sources $\tilde{\mathbf{x}}_j$ simultaneously, each by its generator, does not produce the target signals $\mathbf{F}_1, \cdots, \mathbf{F}_M$ (M is the number of the receiver points) at the levels of the receivers since $\tilde{\mathbf{A}}$ is not the characterization matrix of the system. That is why it is necessary to compute $\mathbf{x}_j$ from $\tilde{\mathbf{x}}_j$ using basic concepts of linear algebra. For all $k \in \{1, \cdots, f+1\}$, let $\boldsymbol{\alpha}_k$ be a signal, such that $\boldsymbol{\alpha}_k = [\mathbf{0}_{k-1}, \alpha(0), \cdots, \alpha(f-k+1)]$, where $\mathbf{0}_k$ is the zero-vector of length k. We denote by $\mathscr{C} = \{\mathbf{e}_1, \cdots, \mathbf{e}_{f+1}\}$ the canonical basis of the vector space $\mathbb{R}^{f+1}$. Assuming that $\mathscr{B} = \{\boldsymbol{\alpha}_1, \cdots, \boldsymbol{\alpha}_{f+1}\}$ forms also a basis of $\mathbb{R}^{f+1}$, then there exists an invertible matrix $\mathbf{P}$ called the

transition matrix from $\mathscr{C}$ to $\mathscr{B}$, such that $\boldsymbol{\alpha}_k = \mathbf{P}\mathbf{e}_k$, where

$$\mathbf{P} = \begin{bmatrix} \boldsymbol{\alpha}_1 & \cdots & \boldsymbol{\alpha}_{f+1} \end{bmatrix} = \begin{pmatrix} \alpha(0) & 0 & \cdots & 0 \\ \vdots & \ddots & \ddots & \vdots \\ \vdots & & \ddots & 0 \\ \alpha(f) & \cdots & \cdots & \alpha(0) \end{pmatrix}. \tag{5.2}$$

Each vector $\mathbf{x}_j$ is a linear combination of $\tilde{x}_j(0), \cdots, \tilde{x}_j(f)$ in $\left(\mathbb{R}^{f+1}, \mathscr{B}\right)$ and may be written in $\left(\mathbb{R}^{f+1}, \mathscr{C}\right)$ as

$$\begin{aligned} \mathbf{x}_j = \sum_{k=1}^{f+1} \tilde{x}_j(k-1)\boldsymbol{\alpha}_k = \mathbf{P}\sum_{k=1}^{f+1} \tilde{x}_j(k-1)\mathbf{e}_k = \mathbf{P}\tilde{\mathbf{x}}_j \\ \implies \mathbf{x} = \begin{pmatrix} \mathbf{P} & & \\ & \ddots & \mathbf{0} \\ & \mathbf{0} & \ddots \\ & & & \mathbf{P} \end{pmatrix} \tilde{\mathbf{x}}. \end{aligned} \tag{5.3}$$

Note that, if $\boldsymbol{\alpha} = \mathbf{e}_1$, then $\mathbf{P}$ is the identity matrix and $\mathbf{x} = \tilde{\mathbf{x}}$.

Sometimes, before switching to the canonical basis, the elements of the matrices cannot be stored in the memory because of their large dimensions. To address this problem, we can use the convolution product to build the LCCF system (5.1). Let $\mathbf{u}$ and $\mathbf{v}$ be two vectors in $\mathbb{R}^n$ and $\mathbb{R}^m$, respectively. Then, $\mathbf{w} = conv(\mathbf{u}, \mathbf{v})$ is the vector of length $m+n-1$ whose kth element is

$$w(k) = \sum_{l=\max(1,k+1-n)}^{\min(k,m)} u(l)v(k-l+1). \tag{5.4}$$

For the sake of simplicity, we show how to build the LCCF matrix using the convolution product in the case of one generator and one receiver. That is to say, we solve the large-scale linear system (5.1) with $\tilde{\mathbf{x}} = \tilde{\mathbf{x}}_1$, and $\mathbf{F} = \mathbf{F}_1$,

and $\tilde{\mathbf{A}} = \tilde{\mathbf{A}}_{11}$, knowing that

$$\tilde{\mathbf{A}} = \begin{pmatrix} h_{\boldsymbol{\alpha}}(q) & h_{\boldsymbol{\alpha}}(q-1) & \cdots & h_{\boldsymbol{\alpha}}(0) & 0 & \cdots & 0 \\ \vdots & h_{\boldsymbol{\alpha}}(q) & & \vdots & h_{\boldsymbol{\alpha}}(0) & \ddots & \vdots \\ \vdots & \vdots & & \vdots & \vdots & \ddots & 0 \\ h_{\boldsymbol{\alpha}}(f) & h_{\boldsymbol{\alpha}}(f-1) & \cdots & h_{\boldsymbol{\alpha}}(f-q) & h_{\boldsymbol{\alpha}}(f-q-1) & \cdots & h_{\boldsymbol{\alpha}}(0) \end{pmatrix}, \tag{5.5}$$

where $h_{\boldsymbol{\alpha}}$ is the response recorded after the emission of $\boldsymbol{\alpha}$. Explicitly, for the right side of the LCCF system (5.1), we have

$$\begin{aligned} \tilde{\mathbf{A}}^T \mathbf{F} &= \begin{pmatrix} h_{\boldsymbol{\alpha}}(q) \cdot F_0 + \cdots + h_{\boldsymbol{\alpha}}(f) \cdot F_{f-q} \\ h_{\boldsymbol{\alpha}}(q-1) \cdot F_0 + \cdots + h_{\boldsymbol{\alpha}}(f-1) \cdot F_{f-q} \\ \vdots \\ h_{\boldsymbol{\alpha}}(0) \cdot F_{f-q-1} + h_{\boldsymbol{\alpha}}(1) \cdot F_{f-q} \\ h_{\boldsymbol{\alpha}}(0) \cdot F_{f-q} \end{pmatrix} \\ &= \begin{pmatrix} \sum_{l=q}^{f} h_{\boldsymbol{\alpha}}(l) F_{l-q} \\ \sum_{l=q-1}^{f-1} h_{\boldsymbol{\alpha}}(l) F_{1+l-q} \\ \vdots \\ \sum_{l=0}^{1} h_{\boldsymbol{\alpha}}(l) F_{f-1+l-q} \\ \sum_{l=0}^{0} h_{\boldsymbol{\alpha}}(l) F_{f+l-q} \end{pmatrix} \\ &= conv^{\leftarrow}\left(\mathbf{h}_{\boldsymbol{\alpha}}, \mathbf{F}^{\leftarrow}\right), \text{ for } 1 \leq k \leq f+1, \end{aligned} \tag{5.6}$$

where for any vector $\mathbf{a}$, $\mathbf{a}^{\leftarrow}$ is the same vector as $\mathbf{a}$ reversed with the order of elements. Similarly, for the left side of the system (5.1), we first use the

convolution product to compute the vector

$$\begin{aligned}\tilde{\mathbf{A}}\tilde{\mathbf{x}} &= \begin{pmatrix} h_{\boldsymbol{\alpha}}(q)\cdot x(0) + h_{\boldsymbol{\alpha}}(q-1)\cdot x(1) + \cdots + h_{\boldsymbol{\alpha}}(0)\cdot x(q) \\ h_{\boldsymbol{\alpha}}(q+1)\cdot x(0) + h_{\boldsymbol{\alpha}}(q)\cdot x(1) + \cdots + h_{\boldsymbol{\alpha}}(0)\cdot x(q+1) \\ \vdots \\ h_{\boldsymbol{\alpha}}(f)\cdot x(0) + h_{\boldsymbol{\alpha}}(f-1)\cdot x(1) + \cdots + h_{\boldsymbol{\alpha}}(0)\cdot x(f) \end{pmatrix} \\ &= \begin{pmatrix} \sum_{l=0}^{q} h_{\boldsymbol{\alpha}}(l)x(q-l) \\ \sum_{l=0}^{q+1} h_{\boldsymbol{\alpha}}(l)x(q-l+1) \\ \vdots \\ \sum_{l=0}^{f} h_{\boldsymbol{\alpha}}(l)x(f-l) \end{pmatrix} \\ &= conv(\mathbf{h}_{\boldsymbol{\alpha}}, \mathbf{x}), \text{ for } q \leq k \leq f. \end{aligned} \tag{5.7}$$

Then, the resulting vector reversed with the order of elements $conv^{\leftarrow}(\mathbf{h}_{\boldsymbol{\alpha}}, \mathbf{x})$ is convolved with $\mathbf{h}_{\boldsymbol{\alpha}}$, for $1 \leq k \leq f+1$, to compute $\tilde{\mathbf{A}}^T\tilde{\mathbf{A}}\tilde{\mathbf{x}}$. The Linear Least SQuares (LLSQ) method is used with a function handle to solve this large-scale linear system. The function handle computes $\tilde{\mathbf{A}}^T\tilde{\mathbf{A}}\tilde{\mathbf{x}}$ using convolution products. As a result, we just need to store the vectors $\mathbf{h}_{\boldsymbol{\alpha}}$ and $\tilde{\mathbf{A}}^T\mathbf{F}$. Then, the LLSQ solver finds a least squares solution for $\tilde{\mathbf{x}}$ that minimizes $\left\| \left(\tilde{\mathbf{A}}^T\tilde{\mathbf{A}} + \epsilon\mathbf{I}\right)\tilde{\mathbf{x}} - \tilde{\mathbf{A}}^T\mathbf{F} \right\|_2^2$.

5.2 Source Identification in Wiring Networks

The experimental setup and the equipment used in testings are first presented. Then, we apply the LCCF method with and without constraints to identify the temporal voltage source that would produce a specified target signal at a single point of the network. After that, we test more complex and ramified networks for imposing the same or different target signals at two points over a given target time.

5.2.1 Experimental setup

To test the LCCF method experimentally, any network of any arbitrary topology can be considered. In this section, we select two different network cartography made up of standard $50\,\Omega$ coaxial cables as transmission lines. Although coaxial cables are not routinely found in practical networks, they were chosen due to their excellent stability to ensure the reproducibility of the results. However, the LCCF process is general and independent of the type of lines used; therefore, the derived conclusions are not related to the type of lines.

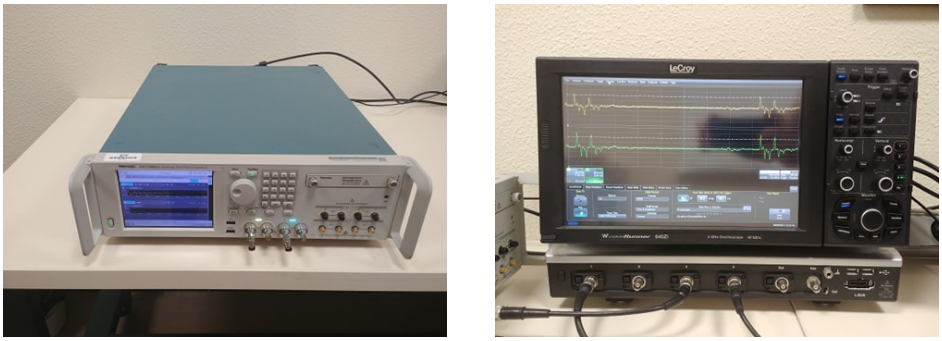

(a) Arbitrary waveform generator. (b) Oscilloscope.

Figure 5.1: *Equipment used in experiments.*

A Tektronix AWG70002A Arbitrary Waveform Generator (AWG) [1] (Figure 5.1a) is connected to the network at one of its ports to generate any arbitrary shape signal of amplitudes varying between $-250\,\mathrm{mV}$ and $+250\,\mathrm{mV}$. The receiver points are represented by the terminations of the network and connected to the channels of the oscilloscope. The oscilloscope used is a LeCroy WaveRunner 640Zi (Figure 5.1b) with a frequency range from $400\,\mathrm{MHz}$ to $4\,\mathrm{GHz}$. It is responsible for displaying the variation of the voltage signals as a function of time. The signal emissions and recordings are synchronized using a trigger signal.

[1] The AWG was supported by the CPER MMASYF of the Auvergne-Rhône Alpes Region and the European Commission (FEDER Auvergne Fund).

As reported earlier, it is not possible to record the impulse response experimentally due to the impractical excitation of a Dirac signal. However, we may rely on the response of any other incident pulse $\boldsymbol{\alpha}$. As an example, the chosen pulse is a double Gaussian $\boldsymbol{\alpha}$ that obeys the amplitude limits of the AWG. The signal $\boldsymbol{\alpha}$ is represented in Figure 5.2 and satisfies the following formula:

$$\alpha(t) = +0.25 \exp\left[-\left(\frac{t - t_{c_1}}{\sigma}\right)^2\right] - 0.25 \exp\left[-\left(\frac{t - t_{c_2}}{\sigma}\right)^2\right], \quad (5.8)$$

where $t_{c_1} = 25\Delta t$, $t_{c_1} = 75\Delta t$, $\sigma = 7\Delta t$, and $\Delta t = 3.9 \times 10^{-9}$. The responses of $\boldsymbol{\alpha}$ at the receiver points must be recorded again once the network undergoes any single modification.

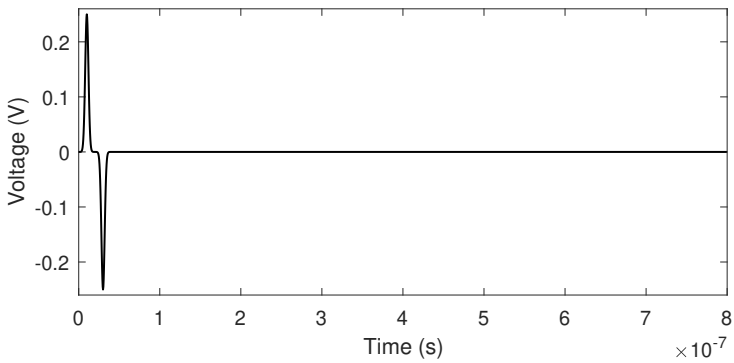

Figure 5.2: *Incident signal $\boldsymbol{\alpha}$ used instead of the Dirac signal.*

5.2.2 Simple network configuration

The first configuration of the network Ω considered in our experiments is represented in Figure 5.3a. Figure 5.3b shows the schematic diagram of Ω composed of four coaxial cables with perfectly matched loads at all its terminations.

The termination of the 1-meter cable is the receiver point connected to the first channel of the oscilloscope and denoted by CH1. The coupling at CH1 is chosen to be $1\mathrm{DC}\,\mathrm{M}\Omega$. In fact, any other coupling may certainly

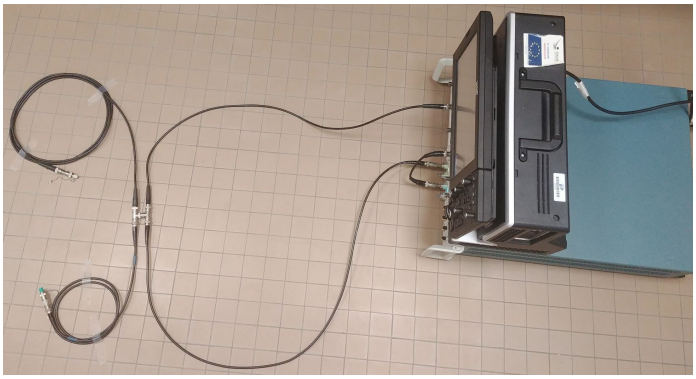

(a) Simple network configuration used in experiments.

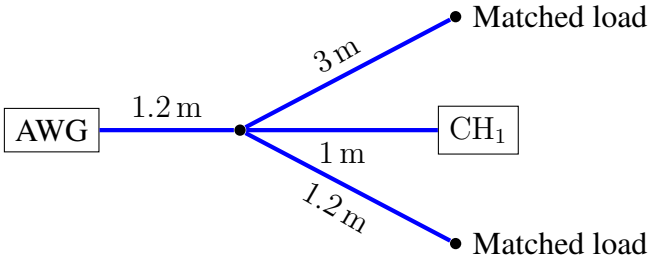

(b) Schematic diagram of the network.

Figure 5.3: *Simple experimental configuration of the network with matched loads.*

be selected as it is included in the network's characteristics of which the LCCF is independent. The idea behind starting from a simple example is the ease of guessing the solution before running any simulation. After applying the LCCF method, we compare and show that the computed solution perfectly matches our expectations. Obviously, a simple analysis of the wave propagation in Ω shows that multiple reflections do not occur in the cables due to the matched loads at all the extremities of Ω. As a result, the only signal reaching the oscilloscope is the one propagating directly through the linking path between the AWG and CH1.

As an example, we seek to identify the source $\mathbf{x}$ that generates the sinusoidal target signal $\mathbf{F}$ represented in green Figure 5.4 over the target time $[t_q, t_f] = [0.2 \times 10^{-7}, 2.16 \times 10^{-7}]$. Theoretically, it is sufficient to inject a signal $\mathbf{x}$ having the same profile as $\mathbf{F}$, but with higher amplitudes,

i.e., $\mathbf{x} = \gamma\mathbf{F}$ $(\gamma > 1)$. The increase in the amplitudes will be reduced during propagation due to the inevitable losses presented in the lines of Ω.

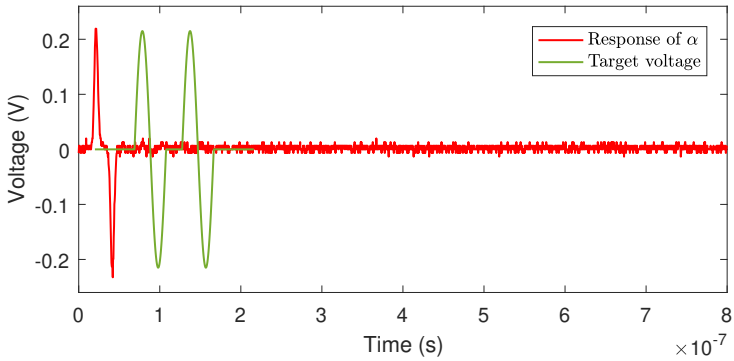

Figure 5.4: *Response of $\boldsymbol{\alpha}$ used instead of the impulse response to characterize the network of Figure 5.3 at CH1.*

After injecting $\boldsymbol{\alpha}$, the signal recorded by the oscilloscope at CH1 is displayed in red in Figure 5.4 and used to construct the matrix $\tilde{\mathbf{A}} = \tilde{\mathbf{A}}_{11}$. Two computational steps are required in Matlab to compute the new source $\mathbf{x}$. At first, we solve the linear system (5.1) for the source $\tilde{\mathbf{x}}$ in the noncanonical basis. Secondly, using the formula (5.3), the multiplication of $\tilde{\mathbf{x}}$ by the corresponding transition matrix $\mathbf{P}$ yields the computation of the desired source $\mathbf{x}$ represented in Figure 5.5a. Injecting $\mathbf{x}$ by the AWG leads the oscilloscope to recording the signal $\mathbf{y}$ for the entire time interval (see Figure 5.5b). Notably, $\mathbf{y}$ is almost the sinusoidal target signal over $[t_q, t_f]$. As expected, the source $\mathbf{x}$ is simple and trivial with the same profile as $\mathbf{F}$ but with higher amplitudes to compensate for the losses in Ω.

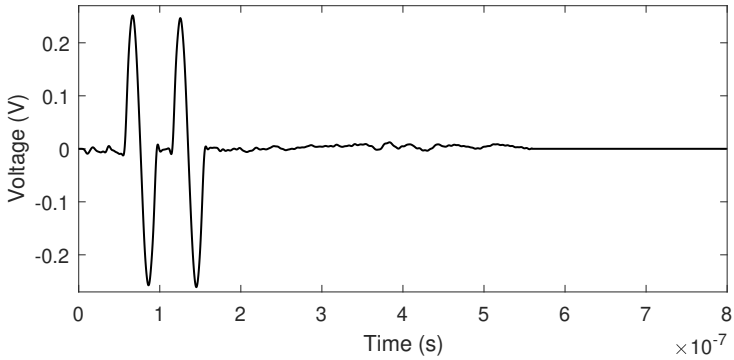

(a) Source computed by the LCCF method.

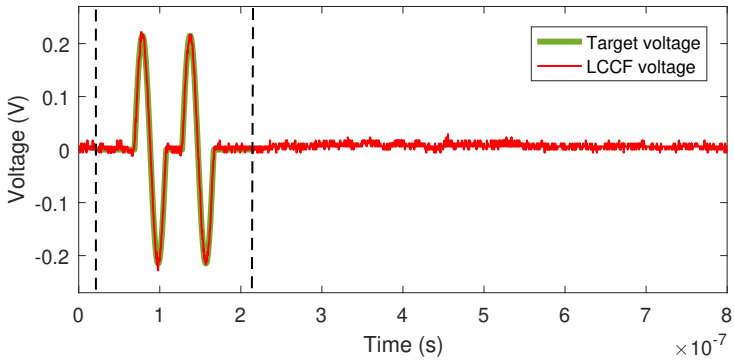

(b) Voltage signal $\mathbf{y}$ recorded at CH_1 after injecting $\mathbf{x}$.

Figure 5.5: *Signal* $\mathbf{x}$ *propagates through the network (Figure 5.3b) to control the voltage at CH1. After its emission, the oscilloscope records the signal* $\mathbf{y}$*, where the sinusoidal target signal is obtained at the target time* $[t_q, t_f] = [0.2 \times 10^{-7}, 2.16 \times 10^{-7}]$ *lying between the two dashed lines.*

Amplitude constraints

Considering now the same network cartography but with more complex characteristics, we assume that the loads at the terminations of the 3-meter and 1.2-meter lines are open circuits (see the images of Figure 5.6). Assume that we look for the source $\mathbf{x}$ that generates the new target Gaussian signal $\mathbf{F}$ represented in green in Figure 5.7 over $[t_q, t_f] = [0.8 \times 10^{-7}, 2 \times 10^{-7}]$. We note that the multiple reflections occurring in Ω make it difficult to guess the solution. After re-characterizing the system by the new response of $\boldsymbol{\alpha}$ (see

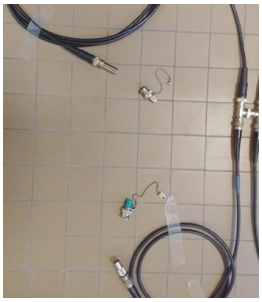

(a) Open circuits.

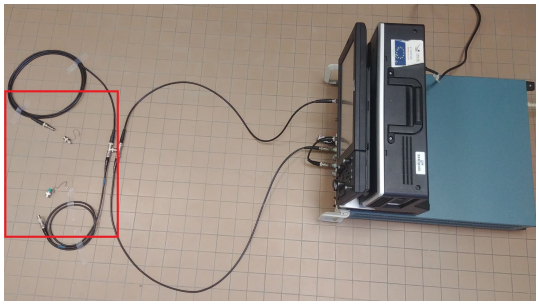

(b) Simple network configuration used in experiments.

Figure 5.6: *Simple experimental configuration of the network with open-circuited loads. Figure 5.6a is the zoom of Figure 5.6b over the red-bordered area.*

the red signal in Figure 5.7), we compute the source $\mathbf{x}$ represented in red in Figure 5.8a. Injecting $\mathbf{x}$ in Ω drives the oscilloscope to record the signal $\mathbf{y}$ at CH1 for the entire time interval, as shown by the red signal in Figure 5.8b.

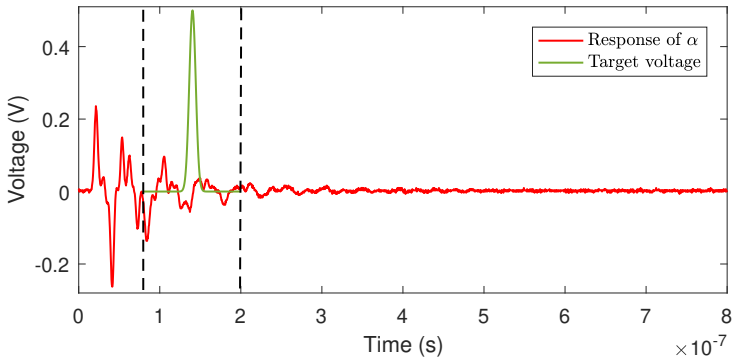

Figure 5.7: *Response of $\boldsymbol{\alpha}$ used instead of the impulse response to characterize the network of Figure 5.6 at CH1.*

Over $[t_q, t_f]$, the output signal $\mathbf{y}$ has the same profile as the target signal $\mathbf{F}$, but with lower amplitudes. This may be explained by the fact that the maximum amplitude of the LCCF computed source $\mathbf{x}$ ($+0.3\,\mathrm{V}$) exceeds the maximal limit of the AWG ($+0.25\,\mathrm{V}$). In this case, the AWG multiplies $\mathbf{x}$ by

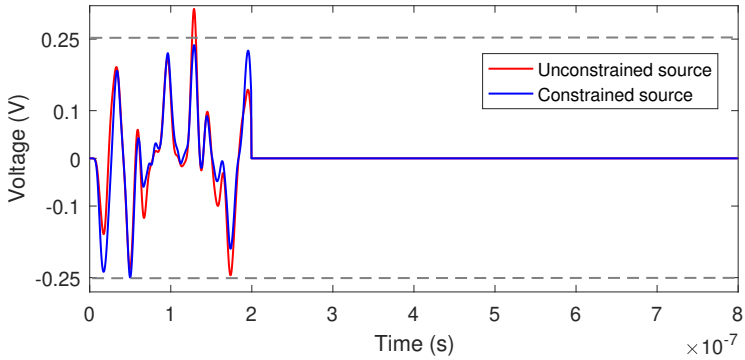

(a) Source $\mathbf{x}$ before and after adding amplitude constraints.

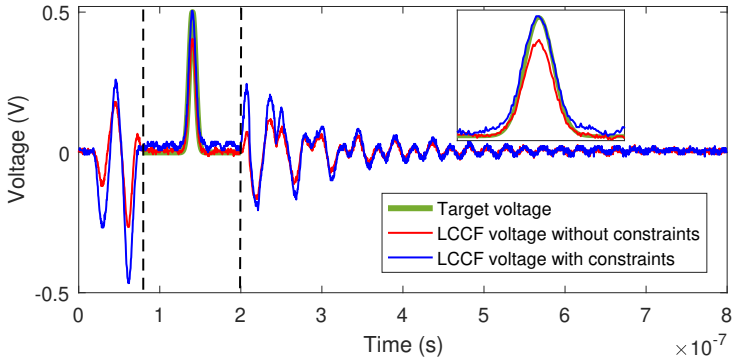

(b) Voltage signals $\mathbf{y}$ and $\mathbf{y}_{\mathrm{CSTR}}$ recorded after injecting $\mathbf{x}$ and $\mathbf{x}_{\mathrm{CSTR}}$, respectively.

Figure 5.8: *Unconstrained LCCF problem: after the emission of the unconstrained source* $\mathbf{x}$*, the oscilloscope records the signal* $\mathbf{y}$ *similar to the Gaussian target signal over* $[t_q, t_f]$ *but with lower amplitudes due to equipment limitations. Constrained LCCF problem: after the emission of the amplitude-constrained source* $\mathbf{x}_{\mathrm{CSTR}}$*, the oscilloscope records the signal* $\mathbf{y}_{\mathrm{CSTR}}$ *that almost coincides with the Gaussian target signal over* $[t_q, t_f]$*. The target time* $[t_q, t_f] = [0.8 \times 10^{-7}, 2 \times 10^{-7}]$ *is the interval between the two dashed lines.*

the scalar $c = 0.25/\max(\mathbf{x})$ $(c < 1)$ before emitting the new rescaled source $\mathbf{x}' = c\mathbf{x}$. After its emission, the amplitudes of $\mathbf{y}$ proportionally decrease due to the linearity of Ω, i.e., $\mathbf{y} \approx c\mathbf{F}$. This explains the difference in amplitudes between $\mathbf{F}$ and $\mathbf{y}$ over $[t_q, t_f]$. A solution would be to use an amplifier to amplify the amplitudes of $\mathbf{x}'$ after its emission by the AWG. As an alternative

solution, we seek to identify a new source $\mathbf{x}_{\text{CSTR}}$ that generates $\mathbf{F}$, such that the amplitudes of $\mathbf{x}_{\text{CSTR}}$ do not exceed the maximal and the minimal limits of the AWG. In what follows, we add amplitude constraints described in Chapter 2 Section 2.3.3 to treat this problem.

For this purpose, we use the LLSQ method to solve the constrained LCCF system. As the solution is not unique, the LLSQ solver computes a new source $\mathbf{x}_{\text{CSTR}}$ with a different energy distribution, such that $\mathbf{x}_{\text{CSTR}}$ satisfies the constraint condition $-\mathbf{0.25} \leq \mathbf{x}_{\text{CSTR}} \leq +\mathbf{0.25}$. In Figure 5.8a, the source $\mathbf{x}_{\text{CSTR}}$ and its output voltage signal $\mathbf{y}_{\text{CSTR}}$ are represented in blue. As noticed, the amplitudes of $\mathbf{y}_{\text{CSTR}}$ over $[t_q, t_f]$ are almost the same as $\mathbf{F}$.

5.2.3 Complex network configuration

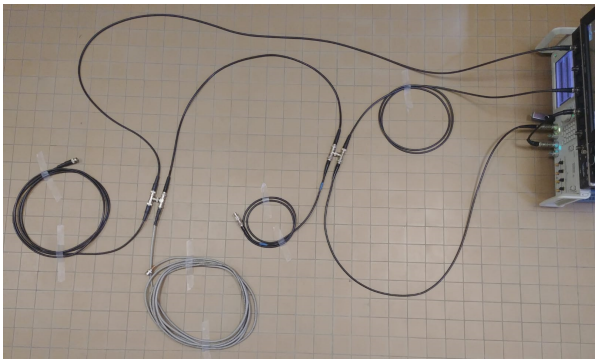

(a) Ramified network configuration used in experiments.

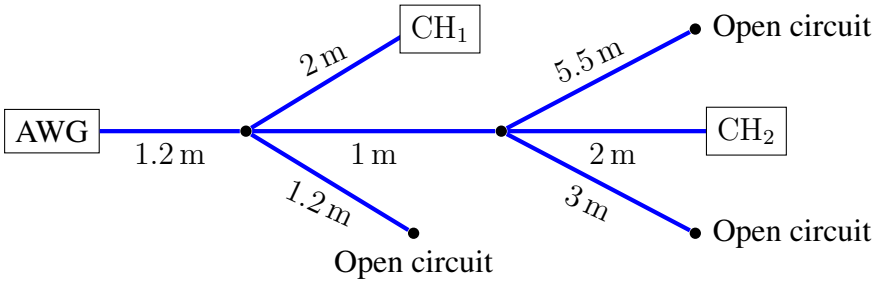

(b) Schematic diagram of the network.

Figure 5.9: *More complex experimental configuration of the network with more ramifications.*

Let Ω be the complex ramified network represented in Figure 5.9. In addition to the complex configuration of Ω, its chosen characteristics enhance its complexity due to the occurring multiple reflections.

Same target signals $(\mathbf{F}_1 = \mathbf{F}_2)$

In this section, we simultaneously apply the LCCF method to impose the target Gaussian signal $\mathbf{F}_1$ represented in green in Figure 5.10 at the two terminations, CH1 and CH2, over $[t_q, t_f] = [4 \times 10^{-7}, 4.8 \times 10^{-7}]$. After injecting $\boldsymbol{\alpha}$, its responses are recorded at CH1 and CH2 and respectively displayed in red and blue in Figure 5.10.

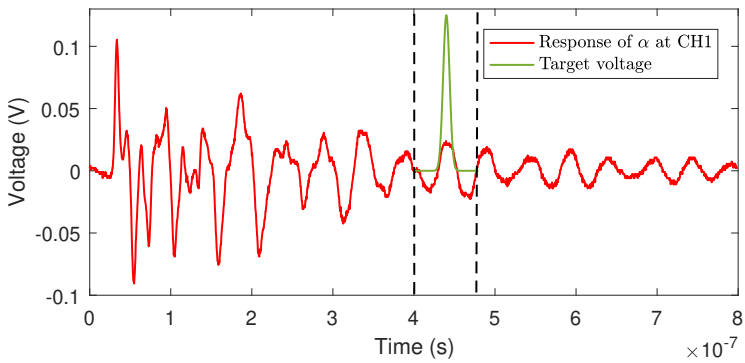

(a) Response of $\boldsymbol{\alpha}$ at CH_1.

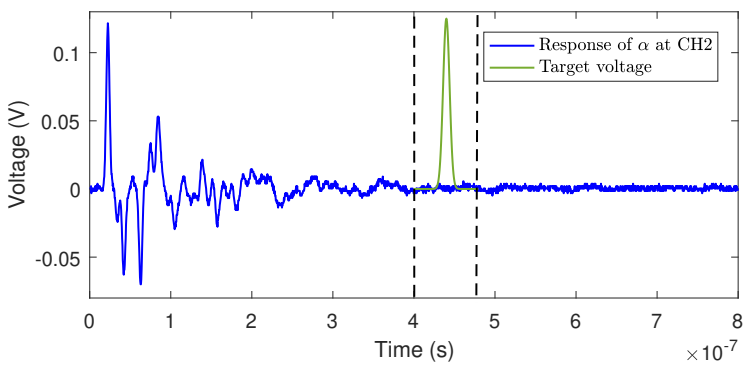

(b) Response of $\boldsymbol{\alpha}$ at CH_2.

Figure 5.10: *Response of $\boldsymbol{\alpha}$ used instead of the impulse response to characterize the network of Figure 5.9 at CH1 and CH2.*

The two responses are used to construct the LCCF transfer matrices $\tilde{\mathbf{A}}_{11}$ and $\tilde{\mathbf{A}}_{21}$ between the AWG and the receiver points. Then, we solve the LCCF system (5.1) after switching to the canonical basis through the formula (5.3). The source $\mathbf{x}$ is computed and represented in Figure 5.11a. The emission of $\mathbf{x}$ leads the oscilloscope to recording the signals $\mathbf{y}_1$ and $\mathbf{y}_2$ at CH1 and CH2 represented in red and blue in Figures 5.11b and 5.11c, respectively. As expected, $\mathbf{y}_1$ and $\mathbf{y}_2$ are almost the Gaussian signal $\mathbf{F}_1$ over $[t_q, t_f]$.

Different target signals $(\mathbf{F}_1 \neq \mathbf{F}_2)$

Considering the same setup and settings as Ω, assume that we want to identify the temporal source that imposes two distinct target signals $\mathbf{F}_1$ and $\mathbf{F}_2$ at CH1 and CH2, respectively, over $[t_q, t_f] = [4 \times 10^{-7}, 4.8 \times 10^{-7}]$. Let $\mathbf{F}_1$ be the Gaussian signal represented in green in Figure 5.12b and $\mathbf{F}_2 = \mathbf{0}$. As Ω does not undergo any modification, then the same matrices $\tilde{\mathbf{A}}_{11}$ and $\tilde{\mathbf{A}}_{21}$ could still be used in the LCCF system (5.1). Solving again this system with the new targets gives the source $\mathbf{x}$ represented in Figure 5.12a. After its emission, the oscilloscope records the signals $\mathbf{y}_1$ and $\mathbf{y}_2$ that are almost identical to $\mathbf{F}_1$ and $\mathbf{F}_2$ over $[t_q, t_f]$, as shown in Figures 5.12b and 5.12c.

In this part of the chapter, we have adapted the LCCF method to pave the way for experimental implementations. Then, the LCCF has been illustrated experimentally to identify the temporal profile of a source that would generate the same or distinct target voltage signals at one or more terminations of the network over a predefined target time. In Chapters 2 and 3, we stated that the LCCF method relies on the impulse response of the network whose geometry and characteristics may be chosen arbitrarily. This may be generalized to say that the LCCF is uniquely dependent on the response of any nonnull signal and not necessarily the Dirac excitation. After that, we also showed how the constrained LCCF method could be applied when limited equipment or budget abilities are encountered during testings. In the next part, we will experimentally show the applicability of the software correction process when one or more faults of any nature appear at any point on the wiring network lines.

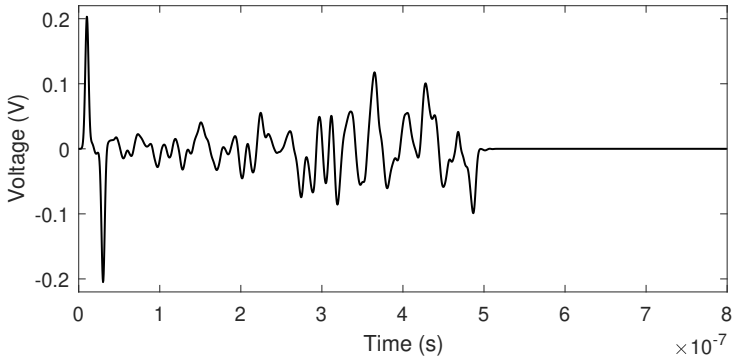

(a) Source $\mathbf{x}$ computed by the LCCF method.

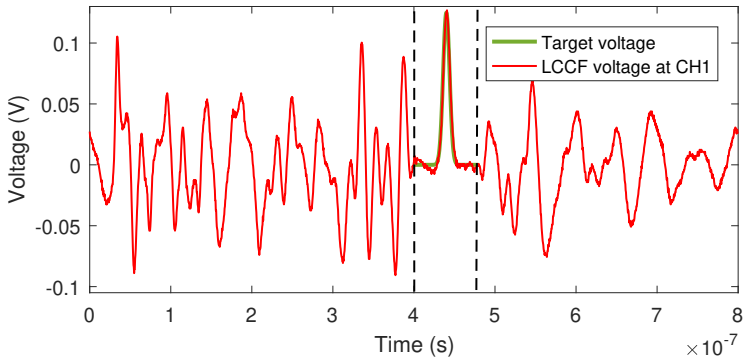

(b) Voltage signal $\mathbf{y}_1$ recorded at CH_1 after injecting $\mathbf{x}$.

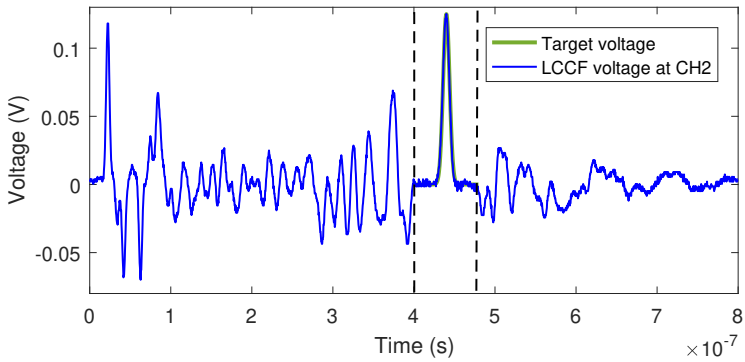

(c) Voltage signal $\mathbf{y}_2$ recorded at CH_2 after injecting $\mathbf{x}$.

Figure 5.11: *Signal* $\mathbf{x}$ *propagates through the network (Figure 5.9) to control the voltage at CH1 and CH2. After its emission, the oscilloscope records the signal* $\mathbf{y}_1$ *and* $\mathbf{y}_2$*, where the Gaussian target signals are obtained at the target time* $[t_q, t_f] = [0.2 \times 10^{-7}, 2.16 \times 10^{-7}]$ *lying between the two dashed lines.*

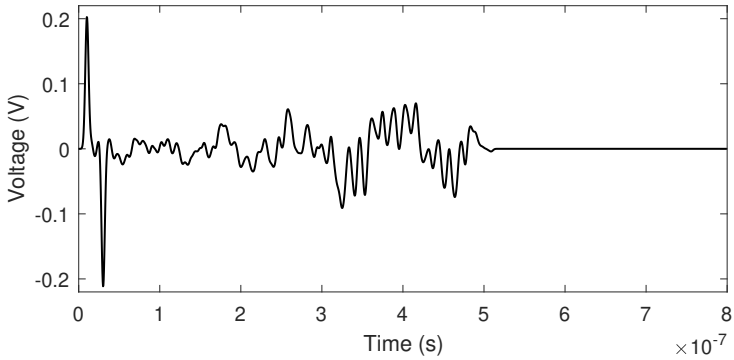

(a) Source $\mathbf{x}$ computed by the LCCF method.

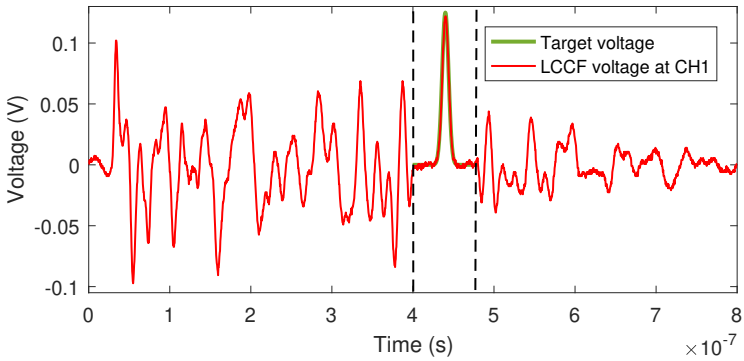

(b) Voltage signal $\mathbf{y}_1$ recorded at CH_1 after injecting $\mathbf{x}$.

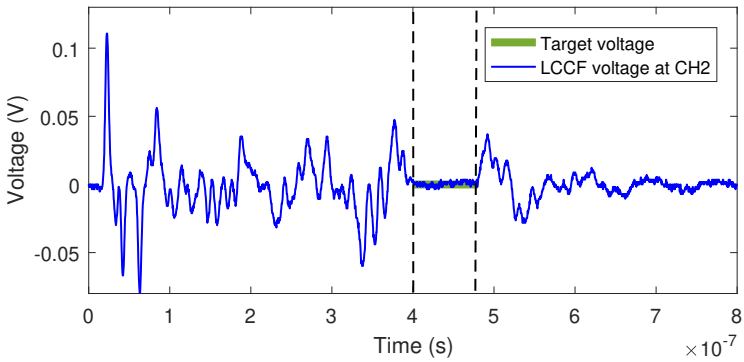

(c) Voltage signal $\mathbf{y}_2$ recorded at CH_2 after injecting $\mathbf{x}$.

Figure 5.12: *Signal* $\mathbf{x}$ *propagates through the network (Figure 5.9) to control the voltage at CH1 and CH2. After its emission, the oscilloscope records the signal* $\mathbf{y}_1$ *and* $\mathbf{y}_2$*, where different target signals are obtained at the target time* $[t_q, t_f] = [0.2 \times 10^{-7}, 2.16 \times 10^{-7}]$ *lying between the two dashed lines.*

5.3 Software Correction in Wiring Networks

In the following, we experimentally apply the LCCF method to bring a Software Correction (SC) to a faulty network regardless of the number, nature, and position of the presented faults. A detailed description of the SC process can be found in Chapter 3 Section 3.2. Here, we keep the same experimental setup and equipment as that of Section 5.2.1. For the sake of clarity, we consider the same notation as the numerical examples in Chapters 3 and 4 for the signals: $\mathbf{V}_{\mathrm{H}}$ (healthy), $\mathbf{V}_{\mathrm{F}}$ (faulty), and $\mathbf{V}_{\mathrm{C}}$ (corrected). We also recall that Ω and Ω' are the notation of the healthy and faulty networks, respectively. The network Ω' differs from Ω in the fault(s) presented in its lines. As a first step, we record the healthy voltage signals of Ω, $\mathbf{V}_{\mathrm{H}}^{1}$ and $\mathbf{V}_{\mathrm{H}}^{2}$, at the channels CH_1 and CH_2 after injecting $\boldsymbol{\alpha}$.

We start by testing the SC process in a simple network presenting a single soft fault. Afterward, we go further in our experiments to test a complex network with a hard fault introduced at one of its terminations. The last experiment is quite general and shows the applicability of the SC in the presence of multiple faults regardless of their number, nature, and position. The distortions resulting from the fault(s) after successively injecting $\boldsymbol{\alpha}$ in Ω and Ω' are examined as the differences between $\mathbf{V}_{\mathrm{H}}^{\lambda}$ and $\mathbf{V}_{\mathrm{F}}^{\lambda}$ $(\lambda = 1, 2)$ displayed in green and blue, respectively, in the figures corresponding to each of the three addressed cases.

5.3.1 Soft fault

The same simple network as that of Figure 5.3b is considered, but, this time, the oscilloscope is connected to two of its terminations, as shown in Figure 5.13. A soft fault has been simulated by locally modifying the matched load impedance at the end of the 3-meter cable (see the gray X-mark in Figure 5.13). This modification is modeled by replacing the $50\,\Omega$ resistor by an $82.5\,\Omega$ resistor, as shown in the images of Figure 5.14. Such implementation creates a soft fault without deforming any cable, even though the soft fault may still be located anywhere in the network. For illustration purposes, this case is quasisymmetric, so the signals obtained at CH_1 and CH_2 are almost similar.

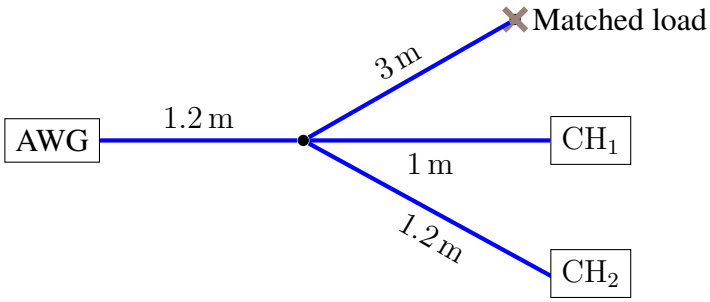

Figure 5.13: *Configuration of the network used for the SC process of the single soft fault.*

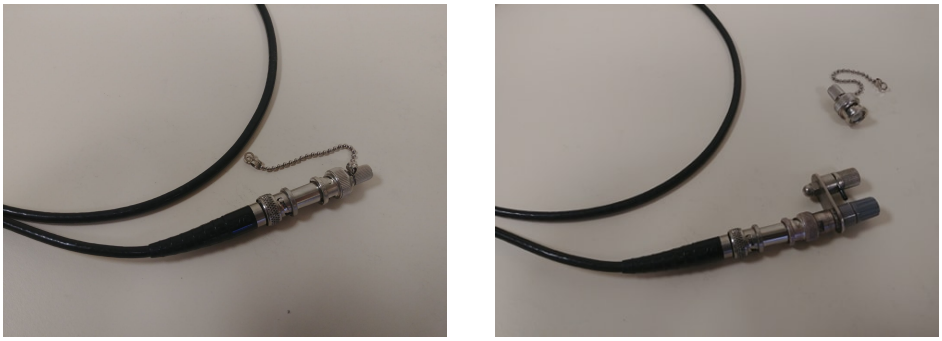

(a) Healthy termination. (b) Faulty termination.

Figure 5.14: *Simulating a soft fault at the termination of the cable by replacing the* $50\,\Omega$ *resistor by an* $82.5\,\Omega$ *one.*

In Figures 5.15b and 5.15c, the soft fault slightly distorts the outputs at CH_1 and CH_2. Apparently, these simple distortions, represented by the small blue peaks, facilitate the prediction of the correcting source $\mathbf{x}$. Logically, $\mathbf{x}$ is the initial signal $\boldsymbol{\alpha}$ with additional peaks opposite to the sign of the distortion, i.e., $\mathbf{x} = \boldsymbol{\alpha} - \left(\mathbf{V}_{\mathrm{F}}^{\lambda} - \mathbf{V}_{\mathrm{H}}^{\lambda}\right)$. In fact, the added peaks and the distortions intersect at the appropriate instants of time to cancel one another out according to the superposition theorem. After solving the LCCF system (5.1), the source $\mathbf{x}$ represented in Figure 5.15a perfectly meets our expectations. After its injection, the corrected signals $\mathbf{V}_{\mathrm{C}}^{1}$ and $\mathbf{V}_{\mathrm{C}}^{2}$ are recorded and found to match the healthy outputs. In the next section, we show that the SC is not restricted to simple cases.

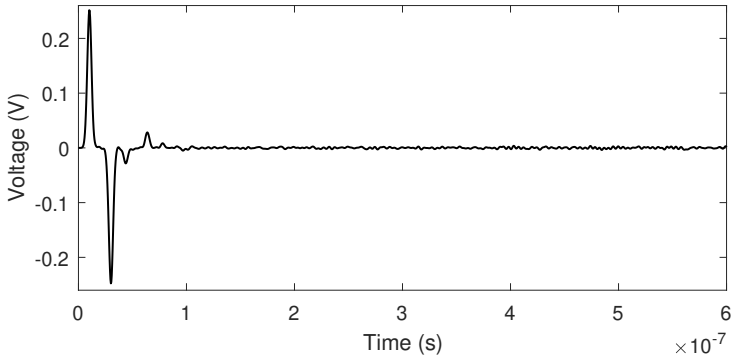

(a) Source $\mathbf{x}$ to tolerate the soft fault.

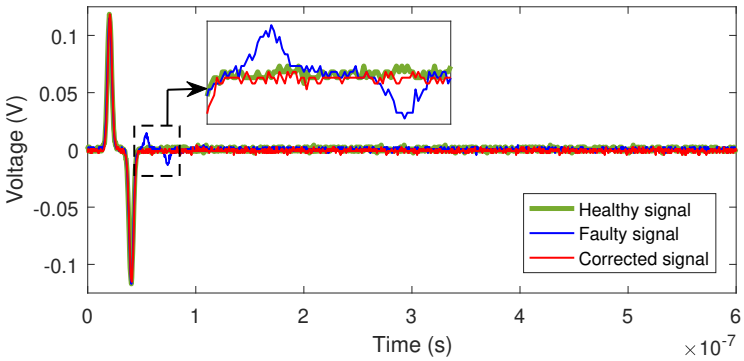

(b) Healthy, faulty and corrected voltage signals at CH_1.

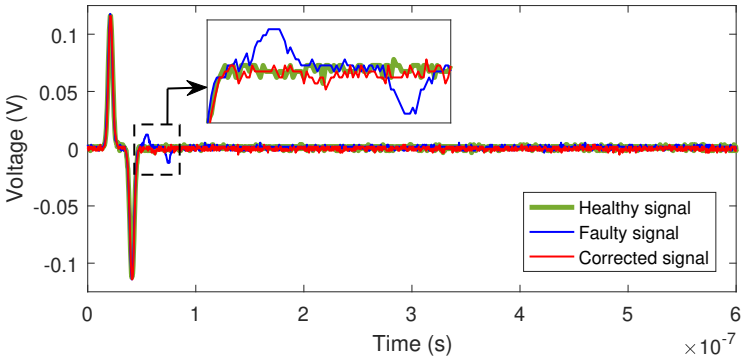

(c) Healthy, faulty and corrected voltage signals at CH_2.

Figure 5.15: *Experimental software correction of the faulty network presenting a single soft fault.*

5.3.2 Hard fault

To show that the SC process *via* the LCCF method is applicable to more complex cases, we consider the network of Figure 5.16 composed of nine cables and three junctions.

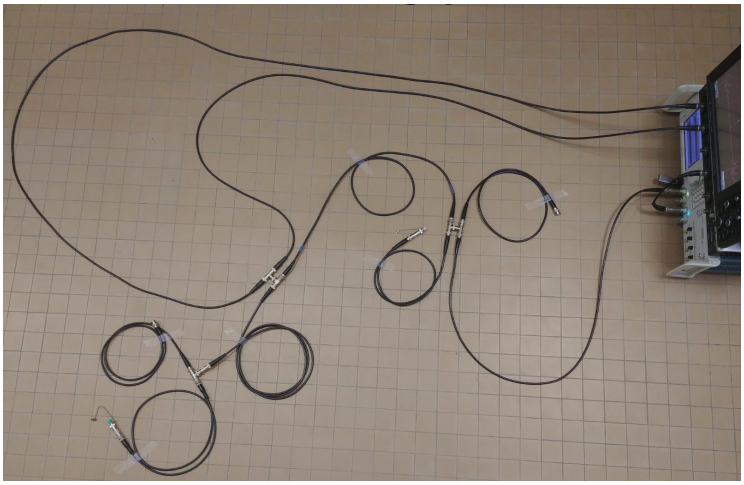

(a) Complex network configuration.

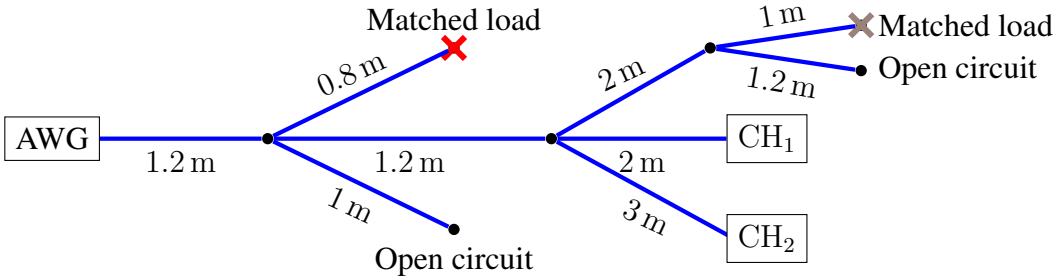

(b) Schematic diagram of the network.

Figure 5.16: *Configuration of the network used during the SC process of a single hard fault and multiple faults.*

Also, a stiffer fault, ultimately a hard one, is implemented by removing the $50\,\Omega$ resistor at the extremity of the 0.8-meter cable, as shown in Figure 5.17. The fault position is represented by a red X-mark in Figure 5.16b.

(a) Healthy termination. (b) Faulty termination.

Figure 5.17: *Simulating a hard fault at the termination of the cable by removing the* $50\,\Omega$ *resistor.*

The hard fault strongly distorts the outputs between the healthy and the faulty states, as illustrated in Figures 5.18b and 5.18c. The SC correction is then repeated to correct the outputs at CH_1 and CH_2 despite this disconnection. The computed source $\mathbf{x}$ of Figure 5.18a is complex and may not be predicted due to the multiple reflections resulting from the complexity of the studied network. After generating $\mathbf{x}$ by the AWG, the outputs are properly corrected, as seen in Figures 5.18b and 5.18c.

5.3.3 Multiple faults

To illustrate the case of multiple faults, we keep the same setup and settings as that of Section 5.3.2. In addition to the hard fault, a soft fault located at the extremity of the 1-meter cable is added by modifying the load impedance from $50\,\Omega$ to $82.5\,\Omega$ (see the gray X-mark in Figure 5.16b). The results in Figure 5.19 show that the SC process efficiently cancels the effects of the multiple faults. It should be emphasized that it is still possible to introduce faults of any nature at any position on the lines of the network as long as the oscilloscope receives signals.

We have experimentally validated the SC process when faults appear in linear faulty communication networks regardless of their topology as well as the number, nature, and position of the potential faults. Not only the LCCF may be applied to wiring networks, but also it may tackle three-dimensional problems to control the electromagnetic fields inside a cavity. Next, we present a three-dimensional application of the LCCF method to control the

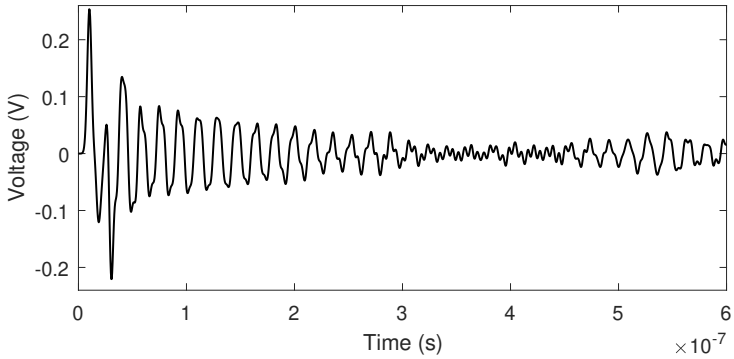

(a) Source $\mathbf{x}$ to tolerate the hard fault.

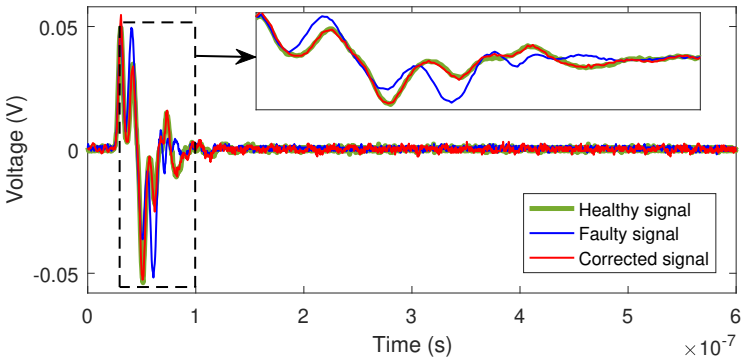

(b) Healthy, faulty and corrected voltage signals at CH_1.

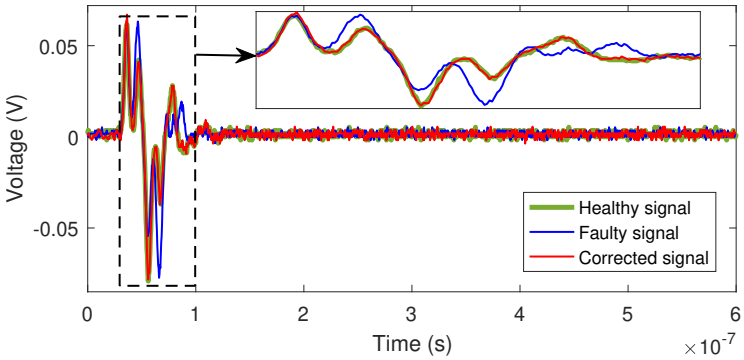

(c) Healthy, faulty and corrected voltage signals at CH_2.

Figure 5.18: *Experimental software correction of the faulty network presenting a single hard fault.*

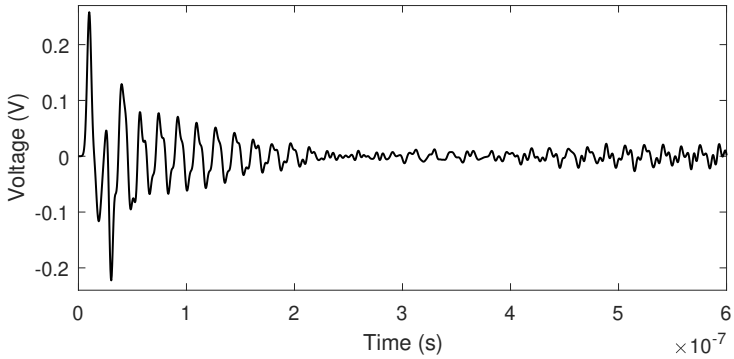

(a) Source $\mathbf{x}$ to tolerate the multiple faults.

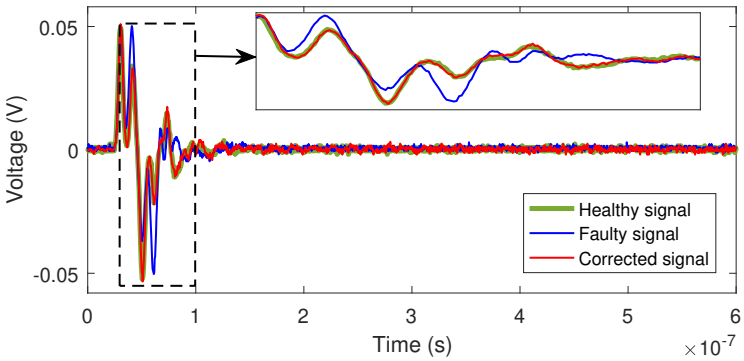

(b) Healthy, faulty and corrected voltage signals at CH_1.

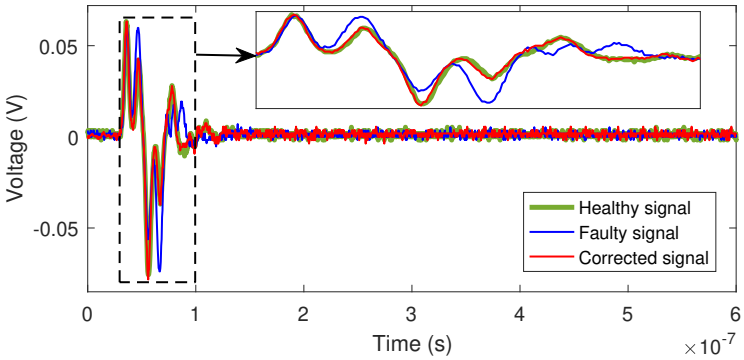

(c) Healthy, faulty and corrected voltage signals at CH_2.

Figure 5.19: *Experimental software correction of the nonlinear faulty network presenting multiple faults of different nature (soft and hard).*

electric fields inside a reverberant cavity in order to enhance the control of microwave plasma. More details are discussed in the next part.

5.4 Enhanced Spatial Control of Microwave Plasma in a Reverberant Cavity

This work was accomplished through collaborative work with Paul Sabatier University in Toulouse, France (LAPLACE and ISAE-SUPAERO laboratories). In [13], they have proposed a novel paradigm to develop a new kind of microwave plasma source called the *plasma brush*. As opposed to many existing microwave plasma sources [14–24], the idea is not to create a plasma occupying the entire volume of a large plasma vessel, but rather to generate a local plasma whose position is controlled in real-time for local material processing of large objects. Thus, practical implementation requires generating and controlling arbitrarily shaped electromagnetic fields in the plasma vessel. In the following, we briefly explain how the Time-Reversal (TR) method could be used to generate plasma at a fixed position. The reader may refer to [13] for further explanations.

Later, we show that some limitations may deteriorate the performance of the TR process when plasma breakdown occurs at other neighboring points, namely parasitic discharges. As an alternative solution, the LCCF method is used to generate plasma at the desired position and prevent the appearance of discharges elsewhere. These discharges result from the enhancement of the electric field by the geometry of some elements inside the cavity, such as the corners and wedges of the sample holder, or the presence of screws, defects, gaps, and metallic grids. First, we present the experimental setup of the problem, then we show that the TR and the LCCF can be used together to efficiently activate plasma at a fixed point. On the other hand, we illustrate the superiority of the proposed method over the TR when it comes to preventing the appearance of parasitic discharges at the neighboring points.

5.4.1 Experimental setup

This experiment takes place in a $0.6\,\mathrm{m} \times 0.6\,\mathrm{m} \times 0.3\,\mathrm{m}$ plasma reactor, called a reverberant metallic cavity, filled with argon at a working pressure $133\,\mathrm{Pa}$.

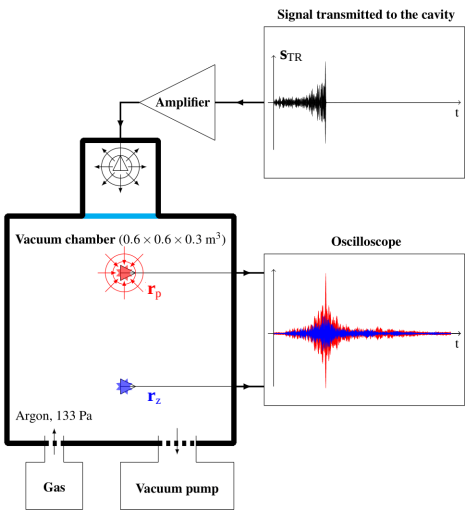

(a) Schematic diagram of the TR experiment at $\mathbf{r}_p$. The time-reversed experimental impulse response $\mathbf{s}_{\mathrm{TR}}$ between $\mathbf{r}_p$ and $\mathbf{r}_0$ allows to obtain an $8\,\mathrm{ns}$ peak at $\mathbf{r}_p$. In this experiment, the level of the signal transmitted to the cavity is high enough to obtain plasma breakdown near $\mathbf{r}_p$. Unfortunately, parasitic discharges are simultaneously generated near $\mathbf{r}_z$. In fact, the microwave level at $\mathbf{r}_z$ is high enough to reach the microwave plasma breakdown threshold.

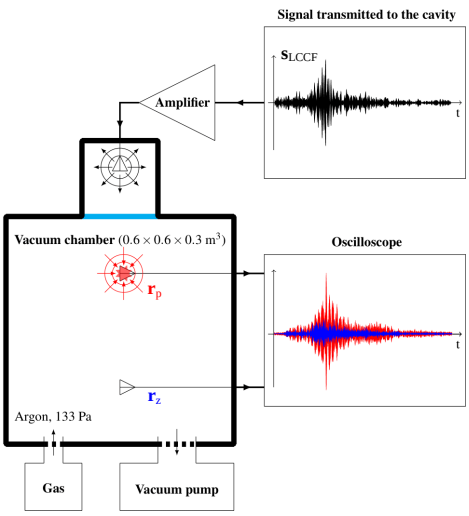

(b) Schematic diagram of the LCCF experiment at $\mathbf{r}_p$ and $\mathbf{r}_z$. After injecting the source $\mathbf{s}_{\mathrm{LCCF}}$, the received signal at $\mathbf{r}_p$ corresponds to the target signal $\mathbf{E}_{\mathrm{TR}}$ measured at the same monopole during the TR experiment. However, the target signal at $\mathbf{r}_z$ is set to zero. As desired, the peak obtained at $\mathbf{r}_p$ is similar to $\mathbf{E}_{\mathrm{TR}}$. Interestingly, the signal level at $\mathbf{r}_z$ is reduced enough when compared to the signal obtained at the $\mathbf{r}_z$ during the TR experiment.

Figure 5.20: *TR and LCCF experimental results to enhance the spatial control of microwave plasma.*

The cavity dimensions are about $5\lambda_0 \times 5\lambda_0 \times 2.5\lambda_0$ at the microwave carrier frequency $f_0 = 2.45\,\mathrm{GHz}$. The microwave devices controlling the signal waveform manipulate high power microwave signals with a maximum bandwidth of $0.25\,\mathrm{GHz}$ on either side of f_0. The plasma discharges and the electrical feedthroughs of the microwave signals are observed through a faradized window.

Considering Figure 5.20a, two coaxial probes acting as monopoles are inserted into the cavity and represented in black and red. The black monopole is located in an appendix connected to the cavity by a glass window at the atmospheric pressure to prevent the gas breakdown in its vicinity while emitting high power signals. The termination of the black monopole, denoted by $\mathbf{r}_0$, represents the source, whereas the termination of the red monopole, located anywhere in the main cavity, is denoted by $\mathbf{r}_p$ and represents the receiver point. The reason behind employing the notation $\mathbf{r}_p$ refers to our purpose of generating plasma at the red monopole, where the subscript 'p' refers to "plasma". Doing so, we use the TR technique, as illustrated in the next section.

5.4.2 Plasma control by the TR method

The spatial control of microwave plasma using the TR method has already been presented in [13]. Firstly, the experimental impulse response $\mathbf{s}_{\mathrm{TR}}$ is recorded between $\mathbf{r}_p$ and $\mathbf{r}_0$, then reversed in time (see the black signal in Figure 5.20a). This signal is amplified using a $2\,\mathrm{kW}$ traveling wave tube pulsed power amplifier (TMD PTC7353) with a repetition period of $16.6\,\mu\mathrm{s}$ and transmitted to the cavity by $\mathbf{r}_0$. After emitting $\mathbf{s}_{\mathrm{TR}}$, it finally generates a spatio-temporal refocusing of the electromagnetic energy at $\mathbf{r}_p$ represented by the red signal $\mathbf{E}_{\mathrm{TR}}$ in Figure 5.20a. Generating an electric signal of such a peaky form leads to plasma activation at $\mathbf{r}_p$.

Unfortunately, when increasing the power injected by the amplifier, the TR inevitably leads to a relative increase in the electric field magnitude in the neighborhood of $\mathbf{r}_p$, causing parasitic discharges or plasma breakdowns at undesired positions. These discharges may result from the presence of screws, defects, gaps, or metallic grids in the cavity [149]. Assume that a third coaxial probe or monopole is inserted near $\mathbf{r}_p$. Its termination is denoted by $\mathbf{r}_z$ and represented in blue in Figure 5.20a. In this case, $\mathbf{r}_z$ is chosen with a sharp tip to model an irregularity inside the cavity; thus, it allows the monitor of the temporal field evolution at its position.

Repeating the same process, the TR refocuses the electromagnetic energy again at $\mathbf{r}_p$; meanwhile, the magnitudes of the electric field are high enough at $\mathbf{r}_z$ to reach the plasma breakdown condition. The electric field at $\mathbf{r}_z$ is

represented by the blue signal in Figure 5.20a. This implies that plasma is activated at $\mathbf{r}_p$ and undesired parasitic discharges also appear at $\mathbf{r}_z$ at the same time. Figure 5.21a better visualizes the signals received at $\mathbf{r}_p$ and $\mathbf{r}_z$ after the TR process. Signals of such profiles activate plasma at $\mathbf{r}_p$ and result in the appearance of parasitic discharges at $\mathbf{r}_z$, as illustrated in Figure 5.21b.

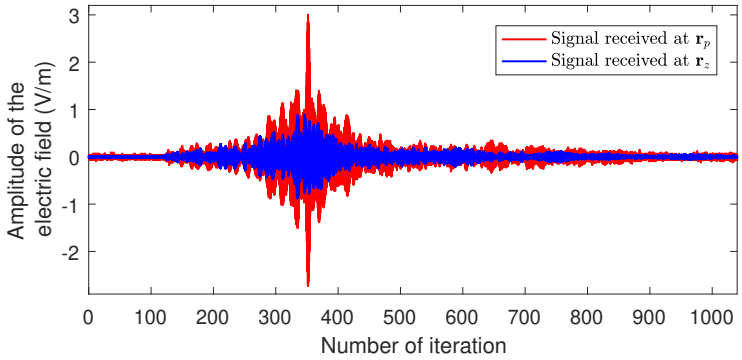

(a) Signals received at $\mathbf{r}_p$ and $\mathbf{r}_z$.

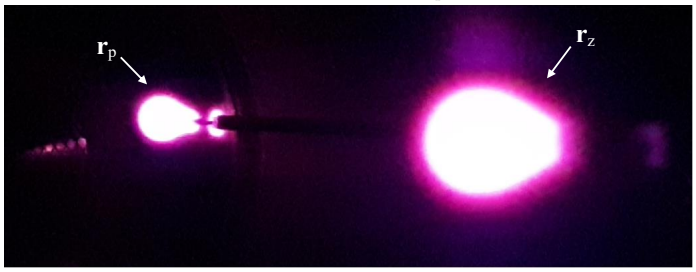

(b) Plasma is activated at $\mathbf{r}_p$ and parasitic discharges appear at $\mathbf{r}_z$.

Figure 5.21: *TR Experimental results: the TR succeeds in activating plasma at* $\mathbf{r}_p$*, while it fails in preventing the appearance of parasitic discharges at* $\mathbf{r}_z$ *during the entire time of the experiment.*

Using the TR technique, the position of the plasma $\mathbf{r}_p$ may be controlled by manipulating the signal waveform only. Although the TR is efficient at controlling the position of the microwave plasma inside the cavity, it inevitably leads to an increase in the magnitude of the electric fields elsewhere. This increase may be high enough to reach the plasma breakdown condition causing the appearance of parasitic discharges. Avoiding such discharges re-

quires advanced transient electric field shaping methods to cancel or at least reduce the electric field at $\mathbf{r}_z$ during the entire time of the experiment. An effective way is to use the LCCF method due to its ability to control the electric field at several spatial points simultaneously as described in Chapter 3 Section 3.1.2 [150].

5.4.3 Plasma control by the LCCF method

The LCCF method was described for any linear function, mapping the inputs and the outputs. In this application, the operator is represented by the linear time-dependent Maxwell's equations

$$\varepsilon \frac{\partial \mathbf{E}}{\partial t} = \nabla \times \mathbf{H} - \sigma \mathbf{E} - \mathbf{J}, \tag{5.9}$$

$$\mu \frac{\partial \mathbf{H}}{\partial t} = -\nabla \times \mathbf{E}, \tag{5.10}$$

that govern the evolution of the electric $\mathbf{E} = \mathbf{E}(\mathbf{r}, t)$ and the magnetic $\mathbf{H} = \mathbf{H}(\mathbf{r}, t)$ fields at any point $\mathbf{r}$ in the cavity and instant t. The parameters $\varepsilon = \varepsilon(\mathbf{r})$, $\mu = \mu(\mathbf{r})$, and $\sigma = \sigma(\mathbf{r})$ are the local permittivity, permeability, and conductivity of Ω, respectively. The boundary conditions are defined by the walls of the cavity, but generally, arbitrary boundary conditions may be considered as the LCCF is independent of the topology of the medium. The LCCF method identifies a temporal current density source $\mathbf{J}$ to control $\mathbf{E}$ at the two spatial points $\mathbf{r}_p$ and $\mathbf{r}_z$ over the target time $[t_q, t_f]$.

We recall that the LCCF has been presented to control the voltage and/or current in wiring networks, or any electric (E_x, E_y, E_z) and/or magnetic (H_x, H_y, H_z) field in free space environments. To remove the parasitic discharges, we are interested in controlling the component E_x. Then we look for the source $\mathbf{J}_x$ that controls the electric fields at $\mathbf{r}_p$ and $\mathbf{r}_z$. For the sake of simplicity, the source $\mathbf{J}_x$ is denoted by $\mathbf{s}_{\mathrm{LCCF}}$.

Generating plasma at $\mathbf{r}_p$ usually requires imposing the target electric signal denoted by $\mathbf{E}_x^p = [0, \ldots, 0, a_1, \ldots, a_m, 0, \ldots, 0]$, where $a_1, \ldots, a_m \gg 0$. The signal $\mathbf{E}_x^p$ is a null except for a short interval of time, where it reaches a peak at $a_{m/2}$. Meanwhile, we prevent the appearance of any parasitic discharges at $\mathbf{r}_z$, i.e., the electric field at $\mathbf{r}_z$ denoted by $\mathbf{E}_x^z$ is set to $\mathbf{0}$. It is

easily conceivable that this configuration may not be realized in practice, at least in our experimental conditions, as it would come up against some physical limitations. For this application, the wave refocusing is crucial to obtaining a local electric field strong enough to generate plasma at $\mathbf{r}_p$. In the time domain, it is complicated, if not impossible, to understand the spatial refocusing of the waves on the shape of the measured signals. For this reason, we proceed from imposing the signal $\mathbf{E}_{\mathrm{TR}}$ obtained by the TR at $\mathbf{r}_p$, i.e, $\mathbf{E}_x^p = \mathbf{E}_{\mathrm{TR}}$. The signal $\mathbf{E}_x^p$ may suit a refocusing of the waves and fit the physical constraints of the experiment.

After specifying the target signal $\mathbf{E}_x^{p,z} = \begin{pmatrix} \mathbf{E}_x^p \\ \mathbf{E}_x^z \end{pmatrix} = \begin{pmatrix} \mathbf{E}_{\mathrm{TR}} \\ \mathbf{0} \end{pmatrix}$, we construct the LCCF matrix $\tilde{\mathbf{A}} = \begin{pmatrix} \tilde{\mathbf{A}}_{11} \\ \tilde{\mathbf{A}}_{21} \end{pmatrix}$, where $\tilde{\mathbf{A}}_{11}$ (resp. $\tilde{\mathbf{A}}_{21}$) is the transfer matrix between $\mathbf{r}_0$ and $\mathbf{r}_p$ (resp. $\mathbf{r}_z$). The matrix $\tilde{\mathbf{A}}$ is built by recording the responses of a Sine-Gaussian signal, for example, at $\mathbf{r}_p$ and $\mathbf{r}_z$. Then, the LCCF system to be solved is

$$\tilde{\mathbf{A}}\tilde{\mathbf{s}}_{\mathrm{LCCF}} = \mathbf{E}_x^{p,z}. \tag{5.11}$$

We use the LLSQ solver with function handle to solve this large-scale linear system for $\tilde{\mathbf{s}}_{\mathrm{LCCF}}$, as described in Section 5.1, then we switch to the canonical basis to compute $\mathbf{s}_{\mathrm{LCCF}}$. We note that the electric field behavior inside the cavity may be controlled or monitored through the voltage signals measured at $\mathbf{r}_p$ and $\mathbf{r}_z$ in our experimental setup. By solving the above system, the source $\mathbf{s}_{\mathrm{LCCF}}$ is computed and represented in black in Figure 5.20b. After its injection, the output signals recorded at $\mathbf{r}_p$ and $\mathbf{r}_z$, $\mathbf{y}_p$ and $\mathbf{y}_z$, are represented in red and blue in Figure 5.20b. Indeed, the outputs $\mathbf{y}_p$ and $\mathbf{y}_z$ are satisfactory to activate plasma at $\mathbf{r}_p$ and prevent the appearance of parasitic discharges at $\mathbf{r}_z$. The advantage that the LCCF method could bring over the TR is its capability to produce a signal similar to $\mathbf{E}_{\mathrm{TR}}$ at $\mathbf{r}_p$ and simultaneously reduce the signal magnitude at $\mathbf{r}_z$ for the entire time interval. As a result, plasma is activated at $\mathbf{r}_p$ and parasitic discharges are avoided at $\mathbf{r}_z$ during the entire time of the experiment. Figure 5.22a shows again the signals received at $\mathbf{r}_p$ and $\mathbf{r}_z$ after the LCCF process. Signals of such profiles activate plasma at $\mathbf{r}_p$ and prevent the appearance of parasitic discharges at $\mathbf{r}_z$, as illustrated in Figure 5.22b.

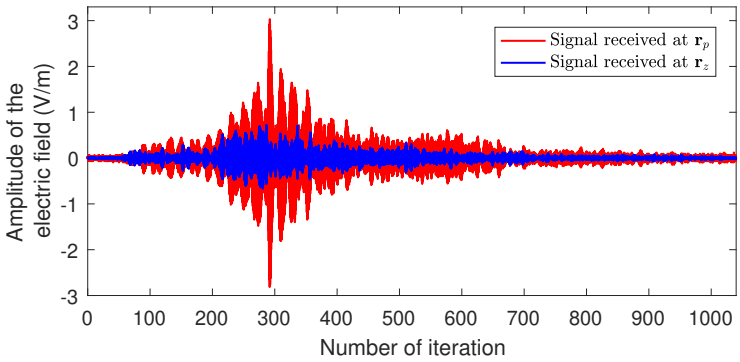

(a) Signals received at $\mathbf{r}_p$ and $\mathbf{r}_z$.

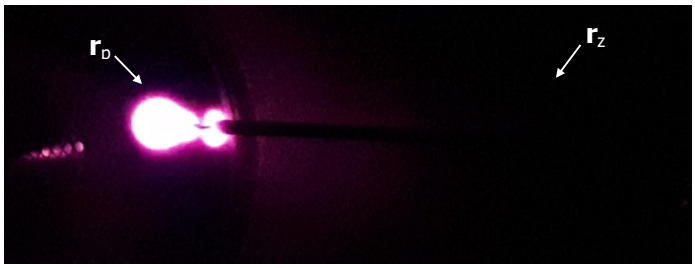

(b) Plasma is activated at $\mathbf{r}_p$ without parasitic discharges appearing at $\mathbf{r}_z$.

Figure 5.22: *LCCF Experimental results: the LCCF simultaneously succeeds in activating plasma at* $\mathbf{r}_p$ *and preventing the appearance of parasitic discharges at* $\mathbf{r}_z$ *during the entire time of the experiment.*

Obviously, as the waves propagate inside the cavity, they often hit $\mathbf{r}_z$, so it would certainly be physically impossible to impose an identical zero signal during the entire time of the process. However, the LCCF method gives a configuration close to the identical zero signal in the least square sense, as long as it is physically realizable. Accordingly, the LCCF method synchronously generates $\mathbf{y}_p$ similar to $\mathbf{E}_{\mathrm{TR}}$ at $\mathbf{r}_p$ and $\mathbf{y}_z$ with the lowest possible level at $\mathbf{r}_z$. The most important point is that the microwave power contained in the peak of $\mathbf{y}_p$ is high enough to reach plasma breakdown condition, whereas the microwave power of $\mathbf{y}_z$ is quite low to prevent the appearance of parasitic discharges. The difference between the target signals and the obtained ones is due to the use of the LLSQ solver to compute the optimal $\mathbf{s}_{\mathrm{LCCF}}$ after regularizing the problem. In fact, we look for the optimal

source $\mathbf{s}_{\mathrm{LCCF}}$ that minimizes the quantity $\left\|\left(\mathbf{A}^T\mathbf{A}+\epsilon\mathbf{I}\right)\mathbf{s}_{\mathrm{LCCF}}-\mathbf{A}^T\mathbf{E}_x^{p,z}\right\|_2^2$. We note that such a difference is also enhanced by the inevitable noises one encounters during experiments.

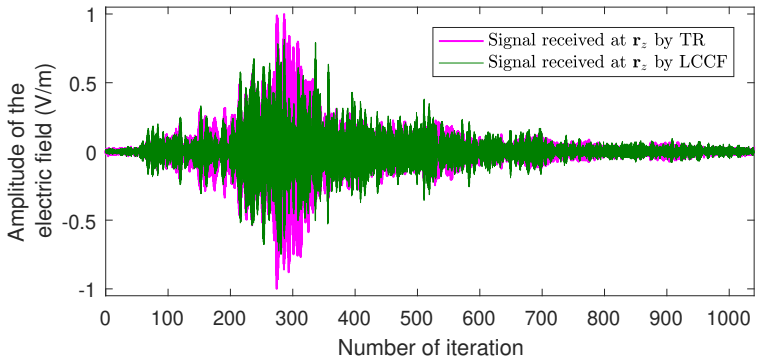

(a) Signals received at $\mathbf{r}_z$ after the TR and LCCF experiments.

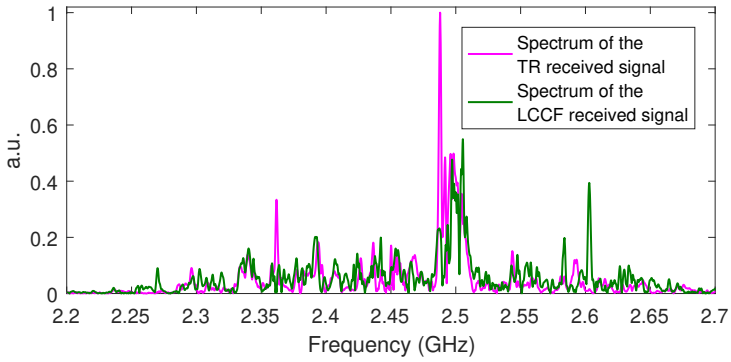

(b) Spectra of the received signals at the used bandwidth.

Figure 5.23: *After separate TR and LCCF experiments, the signal received at $\mathbf{r}_z$ for the TR process is higher in magnitude than the signal received by the LCCF at $\mathbf{r}_z$. This implies that parasitic discharges appear during the TR process, unlike the LCCF method which prevents their appearance at $\mathbf{r}_z$. The multimodal property at the used bandwidth in the frequency domain justifies the reason behind receiving a nonidentical zero signal at $\mathbf{r}_z$ after the LCCF experiment. This is due to the many modes excited during the experiment.*

After the TR and LCCF processes, the measured signals at $\mathbf{r}_z$ are represented in Figure 5.23a. The level obtained at $\mathbf{r}_z$ during the LCCF experiment is lower than the level obtained during the TR experiment. However, both signals are far from the identical zero signal. To understand the origin of this difference, we look at these signals at the used bandwidth $[2.2\,\mathrm{GHz}, 2.7\,\mathrm{GHz}]$ in the frequency domain, as shown in Figure 5.23b. The purpose is to observe the multimodal property of the cavity for this bandwidth to check the proper functioning of the TR and the LCCF methods. Here, we notice the difficulty that prevents the LCCF from imposing an identical zero target signal. In fact, the impossible imposition of an identical zero signal is due to the many modes excited during the experiment. Nevertheless, the LCCF method manages to find a solution, where the influence of the mode with the highest amplitude, namely around $2.5\,\mathrm{GHz}$, is considerably reduced. Interestingly, we may note that the plasma breakdown is a threshold phenomenon. After emitting the LCCF source, although the level of the signal measured at $\mathbf{r}_z$ is not identically zero, its level is low enough so as not to reach the plasma breakdown condition.

In other TR and LCCF experiments, we switch the notation $\mathbf{r}_p$ and $\mathbf{r}_z$. We denote now by $\mathbf{r}_p$ the termination of the blue monopole and by $\mathbf{r}_z$ the termination of the red monopole. In other words, we carry out the same experiments, but the objective here is to activate plasma at the blue monopole and avoid discharges at the red one. Similar to what preceded, the same interpretations and analyses may be conducted. We clearly observe that the TR fails to prevent the appearance of parasitic discharges at the red monopole, unlike the LCCF that efficiently generates plasma at the blue monopole and prevents the appearance of discharges at the red one. The plasma activation of these experiments is illustrated in Figure 5.24.

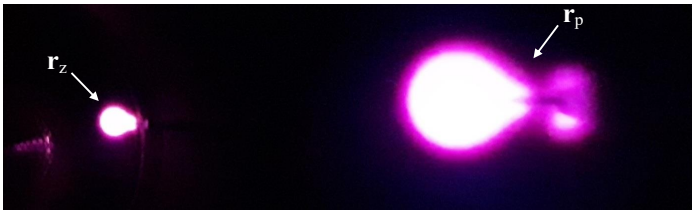

(a) TR experiment.

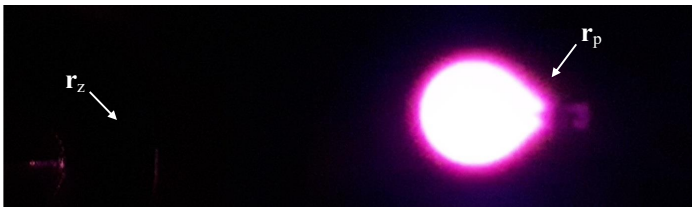

(b) LCCF experiment.

Figure 5.24: *TR fails in preventing the appearance of parasitic discharges at* $\mathbf{r}_z$*, unlike the LCCF that efficiently generates plasma at* $\mathbf{r}_p$ *and prevent the appearance of discharges at* $\mathbf{r}_z$*.*

To sum up, we compare the TR and the LCCF methods. Table 5.1 outlines their similarities and differences to enhance the spatial control of microwave plasma.

Method	TR	LCCF
Plasma activation at $\mathbf{r}_p$	✓	✓
Prevent parasitic discharges at $\mathbf{r}_z$	✗	✓
Control multiple spatial points	✗	✓

Table 5.1: *Comparison between the TR and the LCCF methods for the spatial control enhancement of microwave plasma.*

5.5 Conclusion

The LCCF method has shown remarkable robustness in the presence of noise and proved to be efficient in noisy measuring environments. In

Section 5.1, we firstly adapted the LCCF to make it experimentally feasible. Then, experimental tests were conducted in wiring networks to identify the temporal profile of the source that would impose a desired target signal at a specified target time in different network topology. Sometimes, the use of the constrained LCCF method is necessary due to built-in equipment or budget limitations for experiments. For this reason, we demonstrated the applicability of the constrained LCCF method to obey such limitations. As faults may often appear in the lines of the wiring networks, we also showed how we could experimentally bring a software correction to the faulty network regardless of the number, nature, and position of the faults. For both the source identification and the software correction experiments, simple, ramified, and complex networks were considered to prove the generality of the LCCF and its independence of the network's topology and characteristics.

In the last section, we experimentally investigated the capabilities of the LCCF method to generate and control nanosecond microwave plasma in an all-metal plasma reactor. We showed that the LCCF can prevent the appearance of parasitic discharges by controlling the electric field at several positions in the plasma reactor during the spatio-temporal focusing operation. The microwave control capabilities of the LCCF method make it a good candidate for the sophistication of the recently developed plasma source [13]. This three-dimensional transient electric field shaping method clearly pushes back the capabilities of this source as a promising microwave plasma brush. In what was reported in this chapter, the duration of the plasma generated at a single spatial point was very short; therefore, the problem was viewed as linear. Nevertheless, this will not be the case anymore for the plasma brush, where the nonlinear effects could no longer be ignored. The nonlinear methods represented in Chapter 4 to control the electromagnetic fields in nonlinear systems seem to be promising to enhance the spatial control of nanosecond microwave plasma in nonlinear cavities.

General Conclusion and Perspectives

THE research conducted in this thesis aims to develop new techniques to identify the profile of electromagnetic sources in the time domain that would shape electromagnetic fields in a zone of interest. After their emission, they propagate, interact, and finally reach the receivers with the desired field profile over a predefined time interval. The need to replace or substitute unintentional sources by desired ones, or complex sources by equivalents, has been emphasized and explained while showing the limitations that the existing methods face in the time domain.

The Time-Reversal (TR) adopted from acoustics showed its ability to shape electromagnetic fields; however, its performance starts to degrade when tackling lossy problems or performing under complex conditions. Thus other techniques are required that may overcome such limitations, such as the Linear Combination of Configuration Field (LCCF) method.

In linear media, we recall the main lines of the LCCF and its efficiency at imposing the desired field at a specific spatial point over a given time interval. The LCCF method collects all the propagative information of the medium through the impulse response recorded at the receiver point after exciting a Dirac signal at the source point. It shows to be independent of the topology of the medium, multiple reflections, losses. The LCCF was compared to the TR in one dimension to impose simple and complex target signals in a lossy network. The LCCF showed its superiority over the TR to shape electromagnetic fields in any linear medium using only one source generator.

These results incited us to improve the LCCF method to modify the temporal properties of the source in order to obey some constraints encoun-

tered during experiments. At first, we added filtration constraints to compute smooth sources, and consequently reduce its maximum frequency. Then, amplitude constraints we added to compute a source whose maximal and minimal amplitudes are included between two predefined bounds. At the end of Chapter 2, we presented an application of the LCCF method to replace one field by another.

After that, we generalized the LCCF method that became able to control several spatial points simultaneously. The generalized version of the LCCF allowed us to use several source generators to impose target fields at several receiver points. After computing the source signals, they propagate, interfere, and interact in the linear medium, ending up to the set of the receivers to impose the desired fields over the target time. Like its basic version, the generalized LCCF is also independent of the medium's topology and the physical phenomena occurring inside.

After introducing nonlinear components to the medium, we showed that the LCCF performance deteriorates in this case. Therefore, alternatives methods were required to shape electromagnetic fields in nonlinear media, such as Newton's Method (NM) and the NonLinear Least-SQuares (NLLSQ) solver. The general principles of both techniques were presented for any nonlinear problem and they showed to be independent of the medium's topology. Our nonlinear applications were restricted to impose a specific target signal at a single point of the networks over a given target time. In terms of accuracy and CPU time, NM and the NLLSQ were compared to show the superiority of the latter over the former.

We gathered all these ideas together to introduce a new process in the context of faulty wiring networks called the Software Correction (SC). The SC correction drives the system from its faulty state to the healthy state despite the presence of the faults. It identifies the new inputs added to the faulty network to recover the healthy outputs again at the receiver points. Notably, the SC is independent of the number, position, and nature of the faults. To apply the SC process, The LCCF was used in linear faulty networks, whereas the NLLSQ solver was used with faulty networks behaving nonlinearly.

The obtained results in linear wiring networks paved the way for carrying

out experimental validations. After adapting the LCCF theory to make it experimentally feasible, we considered different network topology to identify the temporal sources that impose given target signals. The LCCF experimental tests also showed the possibility of adding amplitude constraints to the computed source in order not to exceed the boundary limits of the used generator. Moreover, the SC was also applied experimentally to different network cartography presenting faults in its lines. Practical applications for the SC in the presence of soft, hard, and multiple faults were successfully conducted. In three dimensions, the LCCF method was applied to enhance the spatial control of nanosecond microwave plasma in a reverberant cavity.

These results give credibility to the practical use of the LCCF method in real-life configurations. A critical concern that might influence the practical implementation of the method in real-life applications, namely noise, is investigated. The LCCF has shown to be robust with good performances when dealing with noisy collected data.

Perspectives

We opted to work in this thesis on identifying the temporal sources that shape electromagnetic fields in a domain of interest. Efficient and significant results have been obtained in linear and nonlinear media using different numerical methods. further study could be carried out to continue or handle other features that have not been addressed in our work. Some of these perspectives are listed in the following:

- In the linear case, when modifying the temporal properties of the computed source by the constrained LCCF method, the obtained results to reduce the maximum frequency after filtering the source seem interesting. However, our work may not compute a source whose maximum frequency is specified beforehand. It would be interesting that the LCCF will be able to compute sources with frequencies lying in a predefined bandwidth.

- When testing the LCCF experimentally, experiments were applied to coaxial cables and have shown interesting and promising results. Another line of research for these methods could be conducted to bring an SC, such as twisted pair cables.

- In the nonlinear case, three-dimensional numerical applications may be simulated in the future as our simulations were only limited to wiring networks. Moreover, constraints may be added to the nonlinear problem to modify the temporal properties of the source (smoothness, amplitudes, bandwidth, etc.) to pave the way for future experimental tests. These tests may also include the SC in nonlinear faulty wiring networks.

- The active shaping in linear and nonlinear problems was solved when the topology of the medium is constant. Other studies may focus on developing the proposed methods for applications in dynamic systems.

Bibliography

[1] N. Magnoli and G. A. Viano, "The source identification problem in electromagnetic theory," *Journal of Mathematical Physics*, vol 38, no. 5, pp. 2366-2388, 1997.

[2] N. P. Valdivia, "Electromagnetic source identification using multiple frequency information," *Inverse Problems*, vol 28, no. 11, pp. 115002, 2012.

[3] D. Su, S. Xie, A. Chen, X. Shang, K. Zhu, and H. Xu, "Basic emission waveform theory: A novel interpretation and source identification method for electromagnetic emission of complex systems," *IEEE Transactions on Electromagnetic Compatibility*, vol. 60, no. 5, pp. 1330-1339, 2018.

[4] J. L. A. Quijano and G. Vecchi, "Field and source equivalence in source reconstruction on 3D surfaces," *Progress In Electromagnetics Research*, vol. 103, pp. 67-100, 2010.

[5] T. S. Sijher and A. A. Kishk, "Antenna modeling by infinitesimal dipoles using genetic algorithms," *Progress In Electromagnetics Research*, vol. 52, pp. 225-254, 2008.

[6] T. K. Sarkar and A. Taaghol, "Near-field to near/far-field transformation for arbitrary near-field geometry utilizing an equivalent electric current and MOM," *IEEE Transactions on Electromagnetic Compatibility*, vol. 47, no. 3, pp. 566-573, March 1999.

[7] M. Spirlet, C. Geuzaine, and V. Beauvois, "Optimal control theory applied to unintended source control and field shaping for time-harmonic electromagnetic waves," *IEEE Transactions on Electromagnetic Compatibility*, vol. 62, no. 1, pp. 65-73, 2020.

[8] M. Spirlet, "Correction of electromagnetic measurements and active shaping of electromagnetic fields in complex and reverberating environments," Ph.D. dissertation, University of Liège, Belgium, 2017, pp. 59-74.

[9] M. Fink, "Time reversal of ultrasonic fields: Part I. basic principles," *IEEE Transactions on Ultrasonics, Ferroelectrics, and Frequency Control*, vol. 39, no. 5, pp. 555-556, September 1992.

[10] I. El Baba, S. Lalléchère, and P. Bonnet, "Time reversal for electromagnetism: Applications in electromagnetic compatibility," in *Trends in Electromagnetism - From Fundamentals to Applications*, V. Barsan, R. Lungu, Eds., pp. 177-203, 2012.

[11] S. Lalléchère, P. Bonnet, B. Jannet, and L. Berry, "Electromagnetic time reversal robustness for EMC applications," In 1st URSI Atlantic Radio Science Conference (URSI AT-RASC), Las Palmas, Spain, 2015.

[12] P. Bonnet, S. Lalléchère, and F. Paladian, "From electromagnetic time-reversal theoretical accuracy to practical robustness for EMC applications," in *Electromagnetic Time Reversal: Application to Electromagnetic Compatibility and Power Systems*, F. Rachidi, M. Rubinstein, and M. Paolone, Eds., UK: John Wiley & Sons, Ltd, pp. 91-144, 2017.

[13] V. Mazières, R. Pascaud, L. Liard, S. Dap, R. Clergereaux, and O. Pascal, "Plasma generation using time reversal of microwaves," *Applied Physics Letters*, vol. 115, no. 15, pp. 154101, October 2019.

[14] Y. A. Lebedev, "Microwave discharges at low pressures and peculiarities of the processes in strongly non-uniform plasma," *Plasma Sources Science and Technology*, vol. 24, no. 5, pp. 053001, August 2015.

[15] H. Schlüter and A. Shivarova, "Travelling-wave-sustained discharges," *Physics Reports*, vol. 443, no. 4, pp. 121-255, May 2007.

[16] M. Moisan, Z. Zakrzewski, and R. Pantel, "The theory and characteristics of an efficient surface wave launcher (surfatron) producing long plasma columns," *Journal of Physics D: Applied Physics*, vol. 12, no. 2, pp. 219-237, February 1979.

[17] M. Moisan, Z. Zakrzewski, R. Pantel, and P. Leprince, "A waveguide-based launcher to sustain long plasma columns through the propagation of an electromagnetic surface wave," *IEEE Transactions on Plasma Science*, vol. 12, no. 3, pp. 203-214, September 1984.

[18] H. Tahara, J. Kitayama, T. Yasui, K. Onoei, Y. Tsubakishita, and T. Yoshikawa, "Long plasma generation using microwave slot antennas on a rectangular waveguide," *Review of Scientific Instruments*, vol. 65, no. 3, pp. 669-672, March 1994.

[19] F. Werner, D. Korzec, and J. Engemann, "Slot antenna 2.45 GHz microwave plasma source," *Plasma Sources Science and Technology*, vol. 3, no. 4, pp. 473-481, November 1994.

[20] F. C. Fehsenfeld, K. M. Evenson, and H. P. Broida, "Microwave discharge cavities operating at 2450 MHz," *Review of Scientific Instruments*, vol. 36, no. 3, pp. 294-298, March 1965.

[21] F. Silva, K. Hassouni, X. Bonnin, and A. Gicquel, "Microwave engineering of plasma-assisted CVD reactors for diamond deposition," *Journal of Physics: Condensed Matter*, vol. 21, no. 36, pp. 364202, August 2009.

[22] Y. F. Li, J. J. Su, Y. Q. Liu, M. H. Ding, X. L. Li, G. Wang, P. L. Yao, and W. Z. Tang, "Design of a new TM021 mode cavity type MPCVD reactor for diamond film deposition," *Diamond and Related Materials*, vol. 44, pp. 88-94, April 2014.

[23] M. Füner, C. Wild, and P. Koidl,"Novel microwave plasma reactor for diamond synthesis," *Applied Physics Letters*, vol. 72, no. 10, pp. 1149-1151, March 1998.

[24] J. J. Su, Y. F. Li, X. L. Li, P. L. Yao, Y. Q. Liu, M. H. Ding, and W. Z. Tang, "A novel microwave plasma reactor with a unique structure for chemical vapor deposition of diamond films," *Diamond and Related Materials*, vol. 42, pp. 28-32, February 2014.

[25] A. Codino, Z. Wang, R. Razzaghi, M. Paolone, and F. Rachidi, "An alternative method for locating faults in transmission line networks based on time reversal," *IEEE Transactions on Electromagnetic Compatibility*, vol. 59, no. 5, pp. 1601-1612, October 2017.

[26] R. Razzaghi, G. Lugrin, H. Manesh, C. Romero, M. Paolone, and F. Rachidi, "An efficient method based on the electromagnetic time reversal to locate faults in power networks," *IEEE Transactions on Power Delivery*, vol. 28, no. 3, pp. 1663-1673, July 2013.

[27] Z. Wang, R. Razzaghi, M. Paolone, and F. Rachidi, "Time reversal applied to fault location in power networks: Pilot test results and analyses," *International Journal of Electrical Power & Energy Systems*, vol. 114, pp. 105382, January 2020.

[28] L. El Sahmarany, L. Berry, N. Ravot, F. Auzanneau, and P. Bonnet, "Time reversal for soft faults diagnosis in wire networks," *Progress In Electromagnetics Research M*, vol. 31, pp. 45-58, 2013.

[29] C. Furse, Y. Chung, C. Lo, and P. Pendayala, "A critical comparison of reflectometry methods for location of wiring faults," *Smart Structures and Systems*, vol. 2, no. 1, pp. 25-46, 2006.

[30] P. Kralicek, W. John, and H. Garbe, "Modeling electromagnetic emission of integrated circuits for system analysis," In Design, Automation and Test in Europe, Munich, Germany, March 2001.

[31] K. Aunchaleevarapan, K. Paithoonwatanakij, W. Khan-ngern, and S. Nitta, "Novel method for predicting PCB configurations for near-field and far-field radiated EMI using a neural network," *IEICE Transactions on Communications*, vol. E86-B, no. 4, pp. 1364-1376, April 2003.

[32] P. Petre and T. K. Sarkar, "Differences between modal expansion and integral equation methods for planar near-field to far-field transformation," *Progress In Electromagnetics Research*, vol. 12, pp. 37-56, 1996.

[33] P. Petre and T. K. Sarkar, "Planar near-field to far-field transformation using an equivalent magnetic current approach," *IEEE Transactions on antennas and Propagation*, vol. 40, no. 11, pp. 1348-1355, 1992.

[34] A. Taaghol and T. K. Sarkar, "Near-field to near/far-field transformation for arbitrary near-field geometry utilizing an equivalent magnetic current," *IEEE Transactions on Electromagnetic Compatibility*, vol. 38, no. 3, pp. 536-542, August 1996.

[35] Y. Álvarez López, F. Las Heras Andrés, M. Rodríguez Pino, and T. K. Sarkar, "An improved super-resolution source reconstruction method," *IEEE Transactions on Instrumentation and Measurement*, vol. 58, no. 11, pp. 3855-3866, November 2009.

[36] Y. Vives-Gilabert, C. Arcambal, A. Louis, F. de Daran, P. Eudeline, and B. Mazari, "Modeling magnetic radiations of electronic circuits using near-field scanning method," *IEEE Transactions on Electromagnetic Compatibility*, vol. 49, no. 2, 391-400, May 2007.

[37] B. Essakhi, D. Baudry, O. Maurice, A. Louis, L. Pichon, and B. Mazari, "Characterization of radiated emissions from power electronic devices: Synthesis of an equivalent model from near-field measurement," *The European Physical Journal Applied Physics*, vol. 38, pp. 275-281, 2007.

[38] H. Shall, Z. Riah, and M. Kadi, "A 3D near-field modeling approach for electromagnetic prediction," *IEEE Transactions on Electromagnetic Compatibility*, vol. 56, no. 1, pp. 102-112, February 2014.

[39] J. R. Regué, M. Ribó, J. M. Garrell, and A. Martin, "A genetic algorithm based method for source identification and far-field radiated emissions prediction form near-field measurements for PCB characterization," *IEEE Transactions on Electromagnetic Compatibility*, vol. 43, no. 4, pp. 520-530, 2001.

[40] F. de Daran, J. Chollet-Ricard, F. Lafon, and O. Maurice, "Prediction of the field radiated at one meter from PCB's and microprocessors from near EM field cartography," In Electromagnetic Compatibility, IEEE International Symposium, vol. 1, 479-482, Istanbul, Turkey, May 2003.

[41] B. Liu, L. Beghou, and L. Pichon, "Adaptive genetic algorithm based source identification with near-field scanning method," *Progress In Electromagnetics Research*, vol 9, pp. 215-230, 2008.

[42] L. Beghou, B. Liu, L. Pichon, and F. Costa, "Synthesis of equivalent 3-D models from near field measurements– Application to the EMC of power printed circuit boards," *IEEE Transactions on Magnetics*, vol. 45, no. 3, pp. 1650-1653, March 2009.

[43] W. Abdelli, X. Mininger, L. Pichon, and H. Trabelsi, "Prediction of radiation from shielding enclosures using equivalent 3D high frequency models," *IEEE Transactions on Magnetics*, vol. 51, no. 3, May 2015.

[44] W. J. Zhao, B. F. Wang, E. X. Liu, H. B. Park, H. H. Park, E. Song, and E. P. Li, "An effective and efficient approach for radiated emission prediction based on amplitude-only near-field measurements," *IEEE Transactions on Electromagnetic Compatibility*, vol. 54, no. 5, pp. 1186-1189, October 2012.

[45] F. Benyoubi, L. Pichon, M. Bensetti, Y. Le Bihan, and Mouloud Feliachi, "An efficient method for modeling the magnetic field emissions of power electronic equipment from magnetic near field measurements," *IEEE Transactions on Electromagnetic Compatibility*, vol. 59, no. 2, pp. 609-617, 2017.

[46] R. Albanese and P. B. Monk, "The inverse source problem for Maxwell's equations," *Inverse Problems*, vol. 22, no. 3, pp. 1023-1035, May 2006.

[47] S. He and V. G. Romanov, "Identification of dipole sources in a bounded domain for Maxwell's equations," *Wave Motion*, vol. 28, no. 1, pp. 25-40, July 1998.

[48] S. Arridge, "Optical tomography in medical imaging," *Inverse Problems*, vol. 15, no. 2, pp. R41-R93, April 1999.

[49] A. Wirgin, "The inverse crime," 2004. https://hal.archives-ouvertes.fr/hal-00001084.

[50] J. Kaipio and E. Somersalo, "Statistical inverse problems: discretization, model reduction and inverse crimes," *Journal of Computational and Applied Mathematics*, vol. 198, no. 2, pp. 493-504, January 2007.

[51] N. Bleistein and J. K. Cohen, "Nonuniqueness in the inverse source problem in acoustics and electromagnetics," *Journal of Mathematical Physics*, vol. 18, pp. 194-201, 1977.

[52] A. Devaney and G. Sherman, "Nonuniqueness in inverse source and scattering problems," *IEEE Transactions on Antennas and Propagation*, vol. 30, no. 5, pp. 1034-1037, September 1982.

[53] K. H. Hauer, L. Kühn, and R. Potthast, "On uniqueness and non-uniqueness for current reconstruction from magnetic fields," *Inverse Problems*, vol. 21, no. 3, pp. 955-967, June 2005.

[54] E. Marengo and A. Devaney, "The inverse source problem of electromagnetics: linear inversion formulation and minimum energy solution," *IEEE Transactions on Antennas and Propagation*, vol. 47, no. 2, pp. 410-412, September 1999.

[55] A. J. Devaney, E.A. Marengo, and M. Li, "Inverse source problem in nonhomogeneous background media," *SIAM Journal on Applied Mathematics*, vol. 67, no. 5, pp. 1353-1378, July 2007.

[56] A. G. Ramm, *Multidimensional Inverse Scattering Problems*, Longman Scientific & Technical, New York: Wiley, Harlow, Essex, England, 1992.

[57] G. Bao, J. Lin, and F. Triki, "A multi-frequency inverse source problem," *Journal of Differential Equations*, vol. 249, no. 12, pp. 3443-3465, 2010.

[58] J. Cheng, V. Isakov, and S. Lu, "Increasing stability in the inverse source problem with many frequencies," *Journal of Differential Equations*, vol. 260, no. 5, pp. 4786-4804, March 2016.

[59] P. Li and G. Yuan, "Increasing stability for the inverse source scattering problem with multi-frequencies," *Inverse Problems and Imaging*, vol. 11, no. 4, pp. 745-759, July 2016.

[60] H. Ammari, G. Bao, and J. Fleming, "An inverse source problem for Maxwell's equations in magnetoencephalography," *SIAM Journal on Applied Mathematics*, vol. 62, no. 4, pp. 1369-1382, April 2002.

[61] M. V. Klibanov, "Inverse problems and Carleman estimates," *Inverse Problems*, vol. 11, no. 4, pp. 575-596, August 1992.

[62] S. Li, "Carleman estimates for second order hyperbolic systems in anisotropic cases and an inverse source problem. Part II: an inverse source problem," *Applicable Analysis*, vol. 94, no. 11, pp. 2287-2307, 2015.

[63] S. Li and M. Yamamoto, "An inverse source problem for Maxwell's equations in anisotropic media," *Applicable Analysis*, vol. 84, no. 10, pp. 1051-1067, 2005.

[64] M. Yamamotoo, "On an inverse problem of determining source terms in Maxwell's equations with a single measurement," *Inverse Problems, Tomography, and Image Processing*, vol. 15, pp. 241-256, 1998.

[65] G. Bao, P. Li, and Y. Zhao, "Stability for the inverse source problems in elastic and electromagnetic waves," *Journal de Mathématiques Pures et Appliquées*, vol. 134, pp. 122-178, 2019.

[66] P. Monk, *Finite Element Methods for Maxwell's Equations*, Oxford University Press, New York, 2003.

[67] J. L. Lions, "Exact controllability, stabilization and perturbations for distributed systems," *Society for Industrial and Applied Mathematics*, vol 30, no. 1, pp. 1-68, 1988.

[68] R. Glowinski, C. H. Li, and J. L. Lions, "A numerical approach to the exact controllability of the wave equation (I). Dirichlet controls: description of the numerical methods," *Japan Journal of Applied Mathematics*, vol 7, no. 1, pp. 1-76,1990.

[69] G. Lebeau and M.Nodet, "Experimental study of the HUM control operator for linear wave," *Experimental Mathematics*, vol 19, no. 1, pp. 93-120, 2010.

[70] P. C. Hansen, "Rank-deficient and discrete ill-posed problems," Society for Industrial and Applied Mathematics, 1998.

[71] G. Lerosey, "Retournement temporel d'ondes électromagnétiques et application à la télécommunication en milieux complexes," Ph.D. dissertation, University of ESPCI Paris Tech, France, 2006.

[72] G. Lerosey, J. De Rosny, A. Tourin, A. Derode, G. Montaldo , and M. Fink, "Time reversal of electromagnetic waves," *Physics Review Letters*, vol. 92, no. 19, pp. 193904, May 2004.

[73] W. Emerson, "Electromagnetic wave absorbers and anechoic chambers through the years," *IEEE Transactions on Antennas and Propagation*, vol. 21, no. 4, pp. 484-490, July 1973.

[74] M. Davy, J. de Rosny, and M. Fink, "Focusing and amplification of electromagnetic waves by time-reversal in an leaky reverberation chamber," In Antennas and Propagation Society, IEEE International Symposium, Charleston, SC, USA.

[75] D. A. Hill, "Plane wave integral representation for fields in reverberation chambers," *IEEE Transactions on Electromagnetic Compatibility*, vol. 40, no. 3, pp. 209-217, August 1998.

[76] P. Corona, J. Ladbury, and G. Latmiral, "Reverberation-chamber research-then and now: A review of early work and comparison with current understanding," *IEEE Transactions on Electromagnetic Compatibility*, vol. 44, no. 1, pp. 87-94, February 2002.

[77] E. Amador, C. Lemoine, P. Besnier, and A. Laisné, "Reverberation chamber modeling based on image theory: Investigation in the pulse regime," *IEEE Transactions on Electromagnetic Compatibility*, vol. 52, no. 4, pp. 778-789, November 2010.

[78] E. Amador, C. Lemoine, P. Besnier, and A. Laisné, "Studying the pulse regime in a reverberation chamber with a model based on image theory," In Electromagnetic Compatibility, IEEE International Symposium, Fort Lauderdale, FL, USA, July 2010.

[79] I. Scott, A. Vukovic, and P. Sewell, "Time reversal in lossy material: An assessment," In Photonics & Electromagnetics Research Symposium (PIERS 2007), vol. 3, no. 8, pp. 1259-1263, Beijing, China, 2007.

[80] J. De Rosny, "Milieux réverbérants et réversibilité," Ph.D. dissertation, University of Paris 6, France, 2000.

[81] J. Feng, C. Liao, L. L. Chen, and H. J. Zhou, "Amplification of electromagnetic waves by time reversal mirror in a leaky reverberation chamber," In Microwave and Millimeter Wave Technology (ICMMT), International Conference, Shenzhen, China, 2012.

[82] J. Benoit, "Identification de sources temporelles pour les simulations numériques des équations de Maxwell," Ph.D. dissertation, Clermont II-Université Blaise Pascal, France, 2012, pp. 36-53.

[83] H. Moussa, A. Cozza, and M. Cauteman, "Directive wavefronts inside a time reversal electromagnetic chamber," In Electromagnetic Compatibility, IEEE International Symposium, Austin, TX, USA, 2009.

[84] H. Moussa, A. Cozza, and M. Cauteman, "Experimental demonstration of directive pulsed wavefront generation in reverberation chambers," *Electronics Letters*, vol. 46, no. 9, pp. 623-624, April 2010.

[85] A. Cozza, "Emulating an anechoic environment in a wave-diffusive medium through an extended time-reversal approach," *IEEE Transactions on Antennas and Propagation*, vol. 60, no. 8, pp. 3838-3852, 2012.

[86] B. G. Moffat, E. Abraham, M. P. Y. Desmulliez, D. Koltsov, and A. Richardson, "Failure mechanisms of legacy aircraft wiring and interconnects," *IEEE Transactions on Dielectrics and Electrical Insulation*, vol. 15, no. 3, pp. 808-822, June 2008.

[87] C. Buccella, M. Feliziani, and G. Manzi, "Identification and localization of defects in shielded cables by a numerical/experimental procedure," In Electromagnetic Compatibility, IEEE International Symposium, vol. 1, pp. 213-218, 2003.

[88] C. Furse, M. Kafal, Reza Razzaghi, and Y. J. Shin,"Fault Diagnosis for Electrical Systems and Power Networks: A Review," *IEEE Sensors Journal*, pp. 1-19, April 2020. [Online]. Available doi: 10.13140/RG.2.2.24213.06882.

[89] F. Auzanneau, "Wire troubleshooting and diagnosis: Review and perspectives," *Progress In Electromagnetics Research B*, vol. 49, pp. 253-279, 2013.

[90] Cynthia Furse, "Finding fault: Locating hidden hazards on aircraft wiring," College of Engineering, University of Utah, February 2004.

[91] NASA, "Wire integrity research pilot study final report," 2000.

[92] Y. C. Chung, N. Amarnath, C. Furse, and J. Mahoney, "Capacitance and inductance sensors for location of open and short circuited wires," *IEEE Transactions on Instrumentation Measurement*, vol. 58, no. 8, pp. 2495-2502, August 2009.

[93] L. A. Griffiths, R. Parakh, C. Furse, and B. Baker, "The invisible fray: A critical analysis of the use of reflectometry for fray location," *IEEE Sensors Journal*, vol. 6, no. 3, pp. 697-706, 2006.

[94] P. Smith, "Spread spectrum time domain reflectometry," Ph.D. dissertation, Utah State University, USA, 2003.

[95] P. Smith, C. Furse, and Jacob Gunther, "Analysis of spread spectrum time domain reflectometry for wire fault location," *IEEE Sensors Journal*, vol. 5, no. 6, pp. 1469-1478, December 2005.

[96] C. Furse, P. Smith, C. Lo, Y. C. Chung, P. Pendayala, and K. Nagoti, "Spread spectrum sensors for critical fault location on live wire networks," *Structural Control and Health Monitoring*, vol. 12, no. 3-4, pp. 257-267, 2005.

[97] C. Furse, P. Smith, M. Safavi, and C. Lo, "Feasibility of spread spectrum sensors for location of arcs on live wires," *IEEE Sensors Journal*, vol. 5, no. 6, pp. 1445-1450, December 2005.

[98] C. Furse and N. Kamdar, "An inexpensive distance measuring system for navigation of robotic vehicles," *Microwave and Optical Technology Letters*, vol. 33, no. 2, pp. 84-87, 2002.

[99] Y. C. Chung, C. Furse, and J. Pruitt, "Application of phase detection frequency domain reflectometry for locating faults in an f-18 flight control harness," *IEEE Transactions on Electromagnetic Compatibility*, vol. 47, no. 2, pp. 327-334, May 2005.

[100] C. Furse, Y. C. Chung, R. Dangol, M. Nielsen, G. Mabey, and R. Woodward, "Frequency-domain reflectometery for on-board testing of aging aircraft wiring," *IEEE Transactions on Electromagnetic Compatibility*, vol. 45, no. 2, pp. 306-315, May 2003.

[101] O. Osman, S. Sallem, L. Sommervogel, M. O. Carrion, P. Bonnet, and F. Paladian, "Distributed reflectometry for soft fault identification in wired networks using neural network and genetic algorithm," *IEEE Sensors Journal*, vol. 20, no.9, pp. 4850-4858, May 2020.

[102] M. Kafal and J. Benoit, "Baselining: A critical approach used for soft fault detection in wire networks," *International Journal of Digital Information and Wireless Communications*, vol. 8, no. 1, pp. 52-57, 2018.

[103] L. Abboud, A. Cozza, and L. Pichon, "A noniterative method for locating soft faults in complex wire networks," *IEEE Transactions on Vehicular Technology*, vol. 62, no. 3, pp. 1010-1019, 2013.

[104] M. Kafal, A. Cozza, and L. Pichon, "Locating Multiple Soft Faults in Wire Networks Using an Alternative DORT Implementation," *IEEE Transactions on Instrumentation Measurement*, vol. 65, no. 2, pp. 399-406, February 2016.

[105] M. Kafal, J. Benoit, A. Cozza, and L. Pichon, "A statistical study of dort method for locating soft faults in complex wire networks," *IEEE Transactions on Magnetics*, vol. 54, no. 3, pp. 1-4, 2017.

[106] M. Kafal, A. Cozza, and L. Pichon, "Locating faults with high resolution using single-frequency TR-MUSIC processing," *IEEE Transactions on Instrumentation and Measurement*, vol. 65, no. 10, pp. 2342-2348, October 2016.

[107] M. Kafal and A. Cozza, "A heuristic approach applied to time reversal MUSIC method for soft fault location in noisy transmission line networks," In Photonics & Electromagnetics Research Symposium (PIERS 2019), Rome, Italy, 2019.

[108] M. Kafal and A. Cozza, "Multifrequency TR-MUSIC processing to locate soft faults in cables subject to noise," *IEEE Transactions on Instrumentation and Measurement*, vol. 69, no. 2, pp. 411-418, 2020.

[109] A. Taflove and S. C. Hagness, *Computational Electrodynamics: The Finite Difference Time-Domain Method*, Artech House, Norwood, MA, 2005.

[110] K. S. Yee, "Numerical solution of initial boundary value problems invlolving Maxwell's equations in isotropic media," *IEEE Transactions on Antennas and Propagation*, vol. 14, no. 3, pp. 302-307, May 1996.

[111] G. Cohen, X. Ferrières, and S. Pernet, "Discontinuous Galerkin methods for Maxwell's equations in the time domain. Une méthode Galerkin discontinu pour la résolution des équations de Maxwell en régime instationnaire," *Comptes Rendus Physique*, vol. 7, no. 5, pp. 494-500, June 2006.

[112] J. S. Hesthaven and T. Warburton, *Nodal Discontinuous Galerkin Methods*, Springer, 2008.

[113] J. S. Hesthaven and T. Warburton, "High-order nodal methods on unstructured grids I. Time-domain solution of Maxwell's equations," *Journal of Computational Physics*, vol. 181, no. 1, pp. 186-221, 2002.

[114] P. Bonnet, "Résolution des équations de Maxwell instationnaires et harmoniques par une technique de volumes finis," Ph.D. dissertation, Clermont II- Université Blaise Pascal, France, 1998.

[115] P. Bonnet, X. Ferrières, B. L. Michielsen, P. Klotz, and J. L. Roumiguières, "Finite-volume time domain method," in *Time Domain Electromagnetics*, S. M. Rao, Eds., Academic Press, San Diego, CA, 1999.

[116] F. Zheng, Z. Chen, and J. Zhang, "A finite-difference time-domain method without the Courant stability conditions," *IEEE Microwave and Guided Wave Letters*, vol. 9, no. 11, pp. 441-443, November 1999.

[117] T. Namiki, "A new FDTD algorithm based on alternating-direction implicit method," *IEEE Transactions on Microwave Theory and Techniques*, vol. 47, no. 10, pp. 2003-2007, October 1999.

[118] S. W. Staker, C. L. Holloway, A. U. Bhobe, and M. Piket-May, "Alternating-direction implicit (ADI) formulation of the finite-difference time-domain (FDTD) method: Algorithm and material dispersion implementation," *IEEE Transactions on Electromagnetic Compatibility*, vol. 45, no. 2, pp. 156-166, May 2003.

[119] C. Sun and C. W. Trueman,"Unconditionally stable Crank-Nicolson scheme for solving two-dimensional Maxwell's equations," *Electronics Letters*, vol. 39, no. 7, pp. 595-597, April 2003.

[120] J. Shibayama, M. Muraki, J. Yamauchi, and H. Nakano, "Efficient implicit FDTD algorithm based on locally one-dimensional scheme," *Electronics Letters*, vol. 41, no. 19, pp. 1046-1047, September 2005.

[121] Y. S. Chung, T. K. Sarkar, B. H. Jung, and M. Salazar-Palma,"An unconditionally stable scheme for the finite-difference time-domain method," *IEEE Transactions on Microwave Theory and Techniques*, vol. 51, no. 3, pp. 697-704, March 2003.

[122] E. L. Tan, "Fundamental schemes for efficient unconditionally stable implicit finite-difference time-domain methods," *IEEE Transactions on Antennas and Propagation*, vol. 56, no. 1, pp. 170-177, January 2008.

[123] S. Dey and R. Mittra, "A locally conformal finite-difference time-domain (FDTD) algorithm for modeling three-dimensional perfectly conducting objects," *IEEE Microwave and Guided Wave Letters*, vol. 7, no. 9, pp. 273-275, September 1997.

[124] T. Xiao and Q. Liu, "Enlarged cells for the conformal FDTD method to avoid the time step reduction," *IEEE Microwave and Wireless Components Letters*, vol. 14, no. 12, pp. 551-553, December 2004.

[125] I. Zagorodnov, R. Schuhmann, and T. Weiland, "A uniformly stable conformal FDTD-method in Cartesian grids," *International Journal of Numerical Modelling*, vol. 16, no.2, pp. 127-141, March 2003.

[126] G. Mur,"Absorbing boundary conditions for the finite-difference approximation of the time domain electromagnetic-field equations," *IEEE Transactions on Electromagnetic Compatibility*, vol. EMC-23, no. 4, pp. 377-382, November 1981.

[127] J. P. Bérenger, "A perfectly matched layer for the absorption of electromagnetic waves," *Journal of Computational Physics*, vol. 114, no. 2, pp. 185-200, October 1994.

[128] P. Holland and L. Simpson, "Finite difference analysis of EMP coupling to thin struts and wires," *IEEE Transactions on Electromagnetic Compatibility*, vol. 23, no. 2, pp. 88-97, May 1981.

[129] J. P. Parmantier, "Approche topologique pour l'étude des couplages électromagnétiques," Ph.D. dissertation, University of Lille Flandres Artois, France, 1991.

[130] C. R. Paul, *Introduction to electromagnetic compatibility*, Wiley Series in Microwave and Optical Engineering Series, Hoboken: Wiley, 2006.

[131] J. Benoit, C. Chauvière, and P. Bonnet, "Source identification in time domain electromagnetics," *Journal of Computational Physics*, vol. 231, no. 8, pp. 3446-3456, 2012.

[132] J. Benoit, C. Chauvière, and P. Bonnet, "Time-dependent current source identification for numerical simulations of Maxwell's equations," *Journal of Computational Physics*, vol. 289, pp. 116-128, 2015.

[133] B. I. Adi and T. N. E. Greville, *Generalized Inverses, Theory and Applications*, Springer-Verlag, 2003.

[134] A. N. Tychonoff, "Solution incorrectly formulated problems and the regularization method," *Soviet Mathematics*, vol. 4, pp. 1035-1038, 1963.

[135] B. Jannet, "Influence de la non-stationnarité du milieu de propagation sur le processus de Retournement Temporel (RT)," Ph.D. dissertation, Clermont II- Université Blaise Pascal, France, 2014.

[136] R. Razzaghi, G. Lugrin, F. Rachidi, and M. Paolone, "Assessment of the influence of losses on the performance of the electromagnetic time reversal fault location method," *IEEE Transactions on Power Delivery*, vol. 32, no. 5, pp. 2303-23128, October 2017.

[137] T. F. Coleman and Y. Li, "A reflective Newton method for minimizing a quadratic function subject to bounds on some of the variables," *SIAM Journal on Optimization*, vol. 6, no. 4, pp. 1040-1058, 1996.

[138] A. Al Ibrahim, C. Chauvière, and P. Bonnet, "Active shaping of voltage/current in transmission lines - EMC/SI applications," In International Conference on Electromagnetics in Advanced Applications (ICEAA), Granada, Spain, 2019.

[139] M. Kafal, N. Gregis, J. Benoit, N. Ravot, C. Lagomarsini, and G. Gobat, "Pilot tests of FasTR method for locating transient faults in medium voltage underground power networks," *IEEE Sensors Journal*, pp. 1–1, October 2020. [Online]. Available doi: 10.1109/JSEN.2020.3034465.

[140] A. Al Ibrahim, C. Chauvière, and P. Bonnet, "Identification of temporal sources for software defect correction in transmission lines," In 19ème Colloque International sur la Compatibilité ElectroMagnétique (CEM 2018), Paris, 2018.

[141] A. Al Ibrahim, C. Chauvière, and P. Bonnet, "Active electromagnetic interference control in time domain: Application to software correction of defective lossy transmission-line networks," *IEEE Transactions on Electromagnetic Compatibility*, vol. 62, no. 2, pp. 355-363, April 2020.

[142] A. Al Ibrahim, C. Chauvière, and P. Bonnet, "Software correction of defective lossy transmission line networks," In PhotonIcs and Electromagnetics Research Symposium - Spring (PIERS-Spring), Rome, Italy, 2019.

[143] J. Benoit, C. Chauvière, and P. Bonnet, "Identification de source temporelles pour des problèmes de ligne de transmission," In 17ème Colloque International et Exposition sur la Compatibilité Electromagnétique, Clermont-Ferrand, France, 2014.

[144] S. Caorsi, A. Massa, and M. Pastorino, "A numerical solution to full-vector electromagnetic scattering by three-dimensional nonlinear bounded dielectrics," *IEEE Transactions on Microwave Theory and Techniques*, vol. 43, no. 2, pp. 428-436, 1995.

[145] K. C. Lee, "Two efficient algorithms for the analyses of a nonlinearly loaded antenna and antenna array in the frequency domain," *IEEE Transactions on Electromagnetic Compatibility*, vol. 42, no. 4, pp. 339-346, 2000.

[146] T. K. Sarkar, and D. Weiner, "Scattering analysis of nonlinearly loaded antennas," *IEEE Transactions on Antennas and Propagation*, vol. 24, no. 2, pp. 125-131, 1976.

[147] Z. Y. Hou, and Q. N. Jin, "Tikhonov regularization for nonlinear ill-posed problems," *Nonlinear Analysis: Theory, Methods & Applications*, vol. 28, no. 11, pp. 1799-1809, 1997.

[148] A. Al Ibrahim, C. Chauvière, and P. Bonnet, "Time Domain Software Correction of Nonlinear Faulty Lossy Transmission-Line Networks," *IEEE Transactions on Electromagnetic Compatibility*, vol. 62, no. 4, pp. 1304-1311, August 2020.

[149] P. M. Platzman, and E. H. Solt, "Microwave breakdown of air in nonuniform electric fields," *Physical Review*, vol. 119, no. 4, pp. 1143-1149, August 1960.

[150] V. Mazières, A. Al Ibrahim, C. Chauvière, P. Bonnet, R. Pascaud, R. Clergereaux, S. Dap, L. Liard, and O. Pascal, "Transient Electric Field Shaping with the Linear Combination of Configuration Field Method for Enhanced Spatial Control of Microwave Plasmas," *IEEE Access*, vol. 8, pp. 177084-177091, September 2020.

List of Publications

Journal Papers:

- **A. Al Ibrahim**, C. Chauvière, and P. Bonnet, "Active Electromagnetic Interference Control in Time Domain: Application to Software Correction of Defective Lossy Transmission-Line Networks," *IEEE Transactions on Electromagnetic Compatibility*, vol. 62, no. 2, pp. 355- 363, April 2020. [Click here]

- **A. Al Ibrahim**, C. Chauvière, and P. Bonnet, "Time Domain Software Correction of Nonlinear Faulty Lossy Transmission-Line Networks," *IEEE Transactions on Electromagnetic Compatibility*, vol. 62, no. 4, pp. 1304-1311, August 2020. [Click here]

- V. Mazières, **A. Al Ibrahim**, C. Chauvière, P. Bonnet, R. Pascaud, R. Clergereaux, S. Dap, L. Liard, and O. Pascal, "Transient Electric Field Shaping with the Linear Combination of Configuration Field Method for Enhanced Spatial Control of Microwave Plasmas," *IEEE Access*, vol. 8, pp. 177084-177091, September 2020. [Click here]

Conference Papers:

- **A. Al Ibrahim**, C. Chauvière, P. Bonnet, S. Lalléchère, and F. Paladian, "Identification of Temporal Sources for Transmission Lines Applications," 2nd URSI Atlantic Radio Science Conference (URSI AT-RASC), 1 page, Gran Canaria, Spain, 2018. [Click here]

- **A. Al Ibrahim**, C. Chauvière, and P. Bonnet, "Identification of Temporal Sources for Software Defect Correction in Transmission Lines," 19ème Colloque International et Exposition sur la Compatibilité Electromagnétique, 6 pages, Paris, France, 2018. [Click here]

- **A. Al Ibrahim**, C. Chauvière, and P. Bonnet, "Software Correction of Defective Lossy Transmission Line Networks," PhotonIcs and Electromagnetics Research Symposium - Spring (PIERS-Spring), 7 pages, Rome, Italy, 2019. [Click here]

- **A. Al Ibrahim**, C. Chauvière, and P. Bonnet, "Active Shaping of Voltage/Current in Transmission Lines - EMC/SI Applications," International Conference on Electromagnetics in Advanced Applications (ICEAA), 5 pages, Granada, Spain, 2019. [Click here]

- **A. Al Ibrahim**, C. Chauvière, P. Bonnet, and E. Tefouet Donjo "Identifications de Sources Temporelles. Applications Pratiques à un Réseau de Lignes de Transmission," 20ème Colloque International et Exposition sur la Compatibilité Electromagnétique, 4 pages, Lyon, France, 2021. (Accepted)